Collisionless Relaxation in Beam-Plasma Systems

by

Ekaterina Yu. Backhaus

M.A. (University of Texas in Austin) 1995

A dissertation submitted in partial satisfaction of the
requirements for the degree of
Doctor of Philosophy

in

Physics

in the

GRADUATE DIVISION
of the
UNIVERSITY of CALIFORNIA at BERKELEY

Committee in charge:

Professor Jonathan S. Wurtele, Chair
Professor Roger W. Falcone
Professor Charles K. Birdsall

Spring 2001

The dissertation of Ekaterina Yu. Backhaus is approved:

Chair Date

Date

Date

University of California at Berkeley

Spring 2001

Collisionless Relaxation in Beam-Plasma Systems

by
Ekaterina Yu. Backhaus

Abstract

Collisionless Relaxation in Beam-Plasma Systems

by

Ekaterina Yu. Backhaus

Doctor of Philosophy in Physics

University of California at Berkeley

Professor Jonathan S. Wurtele, Chair

This thesis reports the results from the theoretical investigations, both numerical and analytical, of collisionless relaxation phenomena in beam-plasma systems. Many results of this work can also be applied to other lossless systems of plasma physics, beam physics and astrophysics.

Different aspects of the physics of collisionless relaxation and its modeling are addressed. A new theoretical framework, named Coupled Moment Equations (CME), is derived and used in numerical and analytical studies of the relaxation of second order moments such as beam size and emittance oscillations. This technique extends the well-known envelope equation formalism, and it can be applied to general systems with nonlinear forces. It is based on a systematic moment expansion of the Vlasov equation. In contrast to the envelope equation, which is derived assuming constant rms beam emittance, the CME model allows the emittance to vary through coupling to higher order moments. The CME model is implemented in slab geometry in the absence of return currents. The CME simulation yields rms beam sizes, velocity spreads and emittances that are in good agreement with particle-in-cell (PIC) simulations for a wide range of system parameters.

The mechanism of relaxation is also considered within the framework of the CME system. It is discovered that the rapid relaxation or beam size oscillations can be attributed to a resonant coupling between different modes of the system. A simple analytical estimate of the relaxation time is developed.

The final state of the system reached after the relaxation is complete is investigated. New and accurate analytical results for the second order moments in the phase-mixed

state are obtained. Unlike previous results, these connect the final values of the second order moments with the initial beam mismatch. These analytical estimates are in good agreement with the CME model and PIC simulations. Predictions for the final density and temperature are developed that show main important features of the spatial dependence of the profiles. Different aspect of the final coarse-grained state such as its non-thermal nature, the appearance of 'hot' regions on the periphery and the core-halo character of the density are investigated.

Professor Jonathan S. Wurtele
Dissertation Committee Chair

To my grandmothers, whose different lives were always an inspiration...

Contents

List of Figures

Acknowledgements

This work would never be possible without the help and support of so many people. I will try to mention all of you, but even if I forget, please, accept my gratitude.

First of all, my sincere thanks go to my supervisor, Prof. J.S. Wurtele. Jonathan, the time well spent in long discussions in your office, your desire to always push all of your students even higher, and endless interest in new problems have helped me to turn into the scientist that I am now. In addition to the great pleasure of working with you, your mentoring made life so much more pleasant and warm.

Many researchers and students contributed to this work through numerous discussions, questions and comments. Brad Shadwick, Andy Charman, Carl Schroeder, Richa Govil and many others, thank you for all the helpful input. Andy, thank you also for being a great officemate and sharing some good and bad days together. Brad, I can not thank you enough for all the computer support, for sharing your knowledge and expertise. Carl, thanks for being a great friend.

One person, who helped tremendously in my life of a graduate student was Anne Takizawa. Dearest Anne, your support, confidence in all students of the Physics department, your hard work, and kind heart made a real difference in my life. From the bottom of my heart - thank you.

Professors J. Fajans, C.K. Birdsall, R. Littlejohn, A. Kaufman and others, thank you for influencing my path and sharing your knowledge. Thank you Eric Gilson, Dan Durkin, Anita Reimann, Kristine Lang and so many others for friendship, support and help.

This work would never happen without the help and influence of Dr. Scott Backhaus. His realistic viewpoint of an experimentalist, incredible intuition, and ability to come up with simplest explanations have changed the way I view Physics. His everyday support of a devoted husband helped to never give up even when problems seemed unsolvable.

Em and Wilson, your everyday support and love helped me start and finish this work.

Thank you, my dear parents, for making me do this. Thank you for introducing me to the beautiful world of Physics, for always being my science as well as life teachers. For all the love and care, thank you.

Chapter 1

Introduction

The relaxation of a multi-particle system with interparticle interactions toward a final, equilibrium state has been a topic of many investigations in both linear and nonlinear dynamics as well as in statistical physics. The details of this relaxation in systems with losses or collisions are very well understood, and such properties as relaxation time and final equilibrium state can be easily evaluated. The physical nature of the relaxation has also been thoroughly studied and is now fully understood on both microscopic and macroscopic levels. The knowledge of underlying physical principle allows one to determine which equilibrium state is realized asymptotically out of a set of possible stationary states. Predictions that avoid the intermediate dynamical stage become even more important for large statistical systems due to difficulties with numerical simulations.

Despite the significant progress in understanding physics of systems with dissipative forces, the relaxation toward a stationary state of collisionless or lossless systems is still under investigation. Many physical systems that are of interest in the fields of plasma physics, fluid mechanics, astrophysics and beam physics, to name a few, belong to a class of systems with many degrees of freedom in which dissipative processes are insignificant. As is known from experiments and numerical simulations, arbitrary initial particle distributions never settle into a final equilibrium state but, instead, develop a complex structure of filaments in phase-space. However, the averaged, or so-called coarse-grained, distribution finally reaches a stationary state. This process is usually referred to as collisionless relaxation. While the physical mechanism of collisionless decay is usually attributed to the mixing of different initial regions of the distribution in the phase-space, the description of the process with a simplified model still constitutes a challenge to research. A number of

theoretical investigations aimed at a deeper understanding of the process can be found in the literature. For example, Kadomtsev and Pogutse in Ref. [3] analyzed the relaxation using two-particle correlations and concluded that the decay leads to a Lynden-Bell distribution with an additional high-energy tail. Yet, no single theory presents a consistent, simple picture of the relaxation process with correct predictions for the asymptotic final state and the scale of the relaxation process. Possible descriptions with a mathematical model containing a smaller number of equations than the exact particle system or a full kinetic model still remain an active area of research. Simple estimates of the relaxation time or predictions of the final coarse-grained distribution continue to attract the interest of many researchers.

One such area of interest is the prediction of the final asymptotic state of the system. A significant amount of analytical and numerical work on the topic can be found in the astrophysics literature concerning the dynamics of self-gravitating stellar systems and formation of galaxies. A clear relaxation of a collisionless self-gravitating galactic systems toward some asymptotic final state was demonstrated in a variety of different numerical simulations. [4, 5] While a number of different predictions of the final state were developed (see, for example, Refs. [6], [7] and [8]), no conclusive agreement with numerical results was achieved.

This thesis presents a new understanding of the collisionless relaxation phenomena. It is simpler to study the physics of collisionless relaxation using a particular physical system rather than a generic set of equations. Different aspects of the relaxation are investigated here using the system of a beam propagating through a plasma. The beam parameters are such that the collisions do not play a role in the dynamics of particles on the time scales considered. The plasma is assumed to be overdense – its density exceeds the beam density. The plasma particles charge neutralize the beam resulting in the cancellation of the electric field inside the beam. Under the assumption of a plasma with no return currents, motion of the beam particles is governed solely by the focusing force from the self-magnetic field. This force is determined by the density profile of the beam and usually depends nonlinearly on the spatial coordinate x. Due to this nonlinearity of the force, filamentation of the distribution takes place in the phase-space, leading to a relaxation of the coarse-grained distribution to a final state. This simple system shows all the important features of a collisionless system that relaxes towards a stationary state in the averaged sense, and it is chosen as a working example in this thesis. The essential features of this system are reviewed in Chapter 2.

The beam-plasma system is the subject of many recent investigations motivated by applications such as plasma wakefield acceleration schemes [9], including the most recent E-157 experiment [10, 11], the use of plasma lenses for beam focusing [12, 13, 14, 15], applications of intense beams for plasma heating [16, 17], microwave generation [18] and ion acceleration [19]. Different aspects of beam dynamics in a plasma have been investigated including detailed calculations of the induced return plasma currents without [20] and with [21, 22] the effect of collisions between plasma electrons and ions, with and without an externally applied static magnetic field [23]. Some results were compared with experiments. [24, 25] Beam pinching in an overdense plasma was analyzed. [26] Much attention was devoted in the past to the possiblity of plasma heating with a relativistic electron beam, and interesting results on two-stream instability in beam -plasma systems were obtained in the course of these studies. [27, 28, 29, 30, 31] A review of basics of beam-plasma interactions is presented Ref. [32]. A general review of topics such as equilibrium beam configurations, injection of beams into plasma, injection and propagation of a beam through a neutral gas, and acceleration of ions by the electron beam can be found in Ref. [33].

Under the approximations used in this thesis (an overdense plasma with no return currents), the physics in the system is similar to that of beam-beam interactions in linear colliders [1, 2]. Therefore, many results of this work find a direct application in the field of beam physics.

Another application, perhaps of greater interest to a broad scientific community, is evident from the isomorphism of the paraxial beam propagation in the overdense plasma with no return currents with the astrophysical problem of self-gravitating systems. The studies of the galactic formation have been an active topic of research for the last thirty years (see, for example Refs. [34, 35]). For mathematical simplicity, we consider the problem of beam-plasma interaction in one-dimensional systems with a slab geometry.

Understanding collisionless relaxation logically breaks down into two main studies. First is the grasp of the dynamics and development of estimates of the relaxation time and a description of the dynamics with a set of equations that is simpler than the original dynamical set governing the evolution of the individual particles in the system. For example, a derivation of a closed form equation governing the evolution of the beam temperature or derivation of an operator responsible for the relaxation of the coarse-grained distribution could be very useful. The second study is in deeper understanding of the asymptotic properties of the relaxed state. Answers to the questions of the dependence of the final

state on the initial conditions, of the existence of a variational principle that determines the asymptotic state should be considered. This thesis provides fresh insights and theoretical advances in both of these tasks.

The process of relaxation of the initial oscillations in the bulk beam properties is studied first using a new model developed in Chapter 3 and named Coupled Moment Equations (CME). The CME models the evolution of the beam using an expansion of the beam phase-space distribution over a basis related to the moments of the distribution. The exact evolution of the beam involves the dynamics of all its constituent particles charged particles. Therefore, numerical integrations can be computationally intensive, and the basic understanding of physical processes becomes very difficult. In practice, we are often interested in global aspects of the beam propagation, which provide general kinematic and morphological properties of the system. A widely used technique that provides such global aspects of the dynamics is the well-known envelope equation [36, 37], which is used to determine the change in the root-mean-square (rms) beam size as the beam propagates under the influence of external and self-fields. The envelope model is particularly useful for systems with linear forces, where the dynamics of the rms-beam properties decouple from the evolution of higher order moments and the beam emittance remains constant. In reality, of course, not all forces acting on the beam can be modeled as linear. In fact, many external and space-charge forces exhibit spatial nonlinearities. As a consequence, beam distribution moments become coupled. Additional approximations, which often lead to poor agreement with experiments, are required to model such systems with the envelope equation. For example, emittance growth is often observed both experimentally and numerically but it can not be modeled within the traditional envelope formalism. This problem of emittance growth in high brightness beams due to the nonlinearity of space-charge forces has been considered extensively theoretically [38], and many predictions are available for the final values of the beam emittance. A better understanding (compared to the current understanding of analogous effects in beam-plasma systems) is achieved in the connection between the emittance growth and relaxation of rms beam properties. [39, 40] However, many analytical results still need numerical verification, and a simple reduced model (of the envelope equation type) would be very helpful.

Some attempts were made in the past to incorporate emittance growth into the envelope equation. A simple phenomenological model developed by Lee and Yu in Refs. [41] and [42] for beam propagation through plasma showed the dynamics similar to that observed

in numerical simulations. The drawback of this model was in its use of an adjustable parameter in the emittance growth equation. This parameter is connected to the evolution of the density profile. A new description, presented in this thesis, makes efficient predictions for the self-consistent beam evolution without any use of adjustable parameters. The technique is based on the systematic inclusion of the couplings between beam moments (without any use of free parameters) at the expense of a slightly larger resulting system of equations then the envelope model.

Just as the envelope equation reduces the number of degrees of freedom for linear systems, the CME technique provides us with similar simplifications for nonlinear systems through the evolution of the beam moments. The idea of incorporating higher order moments in the description of the dynamics is not new. Previous attempts were made by Channell[43, 44] and recently by Shadwick and Wurtele[45] to include the coupling of the second order moments to higher orders directly by integrating the equations for a finite number of distribution moments. The direct application of the method suggested in Ref. [43] to our case, which includes a space-charge force, is rather difficult because of the problems arising in the calculation of the force and truncation of the system.

The CME model uses a different approach to obtain a reduced model for the beam evolution. The phase-space distribution function is expanded over a Hermite polynomial basis in both velocity and spatial variables. This approach is similar to that used in Vlasov simulations of plasma systems[46, 47] where the Hermite polynomial basis was used to represent the velocity dependence. This basis is especially convenient due to the simple relations between the expansion coefficients of the distribution function and the beam moments. The propagation equations for these expansion amplitudes are obtained, and we refer to this dynamical system as CME model. The resulting infinite CME system is exact. For the purpose of numerical integration it is later truncated and only a finite number of expansion coefficients is kept in the analysis. The model is used to study the dynamics of the rms beam moments and nonlinear emittance growth. Even though the derivation of the CME model is presented for the particular example of a beam propagating through an overdense plasma, a similar approach can be used for other systems with nonlinear forces.

Comparisons with PIC simulations are used throughout this thesis to test the results of the theory. Predictions of CME for the dynamical evolution of the second and fourth order space-velocity moments of the distribution as well as results for the change of density and temperature profiles are compared against PIC simulations. A wide range of

initial conditions corresponding to gaussian and uniform in phase-space beams are considered. Extensive numerical tests are carried out to assess the performance of the theoretical model. The CME model is in good agreement with PIC simulations.

An analysis of the CME model yields a better understanding of the physics of collisionless relaxation. The complex nature of the phase mixing and filamentation make quantitative analysis of relaxation difficult to characterize. In this work, we present a new description of the relaxation process that can be considered as a reduced model for the relaxation dynamics. The relaxation is attributed to a resonant coupling between different modes of the system that arise naturally in the context of the CME expansion of the distribution function. The relation between the nonlinearity of the force and the strength of this resonant coupling is studied. In particular, details of the relaxation of the beam size oscillations are investigated.

Further analysis of the CME model yields a simple analytical estimate of the decay time of the rms-oscillations which can be used as a measure of τ_r defining the relaxation time. Other theoretical results for τ_r can be found literature. For example, an order of magnitude estimate for the relaxation scale caused by the violent relaxation can be found in Ref. [6] or a detailed statistical calculation based on the coarse-grained dynamics is presented in Ref. [48]. All estimates that we were able to find in the literature are either based on dimensionless analysis, and thus are not very accurate, or involve quantities that are hard to evaluate for the system, like the unknown equilibrium coarse-grained distribution function. The estimate of the relaxation time presented in this thesis is easy to evaluate, based on first principles, and the results are in the satisfactory agreement with dynamical simulations.

The problem of predicting the final coarse-grained equilibrium state of the system is addressed in Chapter 5 of this thesis. Interest in asymptotic system properties stimulated many theoretical and numerical studies of the final state of self-gravitating collisionless systems. To clarify the present state of the theoretical understanding, we compare different analytical results with numerical results obtained using PIC simulations. Many current theoretical investigations can be traced back to the classical work of Lynden-Bell [6]. There, the term violent relaxation was first introduced, the physics of relaxation due to rapid variations of the self-gravitating potential was discussed, and a statistical prediction for asymptotic coarse-grained equilibrium function was obtained. The theory was presented for the astrophysical self-gravitating system in the attempt to predict the final distribution

of mass in galaxies. Some further modifications and refinements of the theory together with additional proofs of some aspects of the derivation subsequently appeared in the work of Shu [49]. Numerous numerical works followed in an attempt to verify the prediction of Ref. [6] for different geometries, including slab systems [50, 51] and three dimensional [52, 53] galactic systems. Most of the numerical simulations indicated that the final coarse-grained distributions are significantly different from the prediction of Lynden-Bell. For example, the general shape of the density distribution usually reveals a core-halo structure with a general spatial dependence different from the analytical prediction. Additional theoretical predictions followed in an attempt to remedy these problems. In spite of the large amount of litterature devoted to the theory of Lynden-Bell, the author could not find any clear, explicit and case-by-case comparisons between numerical and analytical results. The comparisons for one-dimensional slab system are presented in this thesis and show significant discrepancies between the theory and PIC simulations.

The second prominent theory for the final state developed to overcome the difficulties with Lynden-Bell's prediction was presented by Wiechen et al. in Refs. [7] and [8]. Its foundations, assumptions, and physical justifications are significantly different from those of Ref. [6]. The method of Ref. [7] is based on the assumption that the relaxation process depends on the amount of the available free energy, and that it ceases as soon as all the free energy is used. With this premise, the final state is calculated as the lowest energy state consistent with a set of constraints determined by dynamics. The technique was later extended to make predictions of the final state achieved in collisionless plasmas [54] and ideal fluids. Numerical studies were used to attempt to verify the predictions of the theory. While numerical results for initial states not far from equilibrium distributions showed good agreement with the theoretical predictions [55], simulations with highly mismatched initial conditions indicated significant qualitative discrepancies. The difficulties with the model are only compounded by a certain degree of uncertainty inherent in the theory. The model is based on the calculation of the lowest energy state accessible from a given initial condition. The concept of a memory function, containing the information about the details of the initial distribution and its subsequent smoothing (or loss of some of the information) due to filamentation and phase-mixing, is used to model the coarse-grained dynamics. The exact mechanism of smoothing is not known at the present, and the effect can at best be described by different operators acting on the memory function. However, as reported in Ref. [8], different choices of smoothing operators for the memory function result in different

predictions for the stationary state. Thus, no first principles predictions have been obtained for the final state based on the theory of Refs. [7] and [8]. Other approaches can be found in the astrophysics literature devoted to self-gravitating collisionless systems, as, for example, one presented in Ref. [56]. The restriction on the asymptotic coarse-grained equilibrium state and its connection to the initial state are discussed in Ref. [57].

Some theoretical progress was made independently by researchers in other fields with collisionless systems. In the field of beam-plasma physics, the theoretical investigations of beam equilibria begin with the classical work of Bennett. [58, 59] There, predictions for the self-pinched beam in thermal equilibrium were presented. Some results can also be found in the literature for the hydrodynamic equilibrium of a beam in different geometries [60] and including the effect of return plasma currents. [61] The approach to the thermal state of the initially mismatched beam propagating in the overdense plasma without induced return currents in the presence of collisions was considered in Ref. [62]. In the case of collisionless beam-plasma systems (overdense plasma, no return currents), predictions of the final state for given initial beams were also developed. An analytical model was proposed by Rosenzweig and Chen in Ref. [2]. The coarse-grained distribution was assumed to be in thermal equilibrium form, and the equilibrium condition and conservation of the number of particles at the phase-space origin were used to specify the beam parameters. No direct systematic comparisons with computations were reported. However, only a limited agreement with numerical simulations is expected based on PIC results presented in this thesis. These simulations indicate a non-thermal character of the final state. Comparisons of the results of theory of Ref. [2] with numerical results are presented in this thesis. Theoretical predictions, based on the radial envelope equation, and their comparisons with PIC simulation were presented in Ref. [63]. In that work, no results for fluid beam profiles were presented. The value of the theoretical predictions for the asymptotic beam state achieved after the relaxation process is completed is even increased by the existing time-consuming, complex dynamical simulations of the long term beam behavior. [64] Theories for nonlinear beam and electromagnetic wave equilibrium in plasmas can also be found in the literature. [65] These are beyond the scope of this thesis.

The discussion herein of the existing theories and comparisons with numerical results show that the exact mechanism that determines the selection of the asymptotic coarse-grained equilibrium state is still not well-understood. Simple analytical estimates for final values of beam size, temperature and emittance are developed in this thesis. These

can be used to predict these important parameters for future experiments. To gain a deeper comprehension of the collisionless equilibrium, we investigate analytically important features as the non-thermal character of the distribution and the presence of space-velocity correlations in the final state. Due to the complexity associated with the nonlinearity and self-consistency of the problem, we predict the asymptotic state of a system with a lesser degree of intricacy in the attempt to shed light to the physics of the full system. The final state of a system with a spatially nonlinear but fixed in time force is investigated and compared with the numerical simulations.

This thesis is organized as follows. First, the physical system consisting of the beam propagating through a plasma is introduced in Chapter 2. The geometry and assumptions used in this work are discussed. A general illustration of the collisionless relaxation of the betatron oscillations of the beam size is presented using a result of the PIC simulation. The difficulties associated with the use of a traditional envelope equation are reviewed using a particular simulation result. Analytical estimates for the final values of the beam second order moments are also presented in Chapter 2. The Chapter 3 is devoted to the derivation and numerical tests of a new model, namely CME, that can be used to predict the dynamics of low order beam moments such as beam size and temperature. Numerical issues, such as conservation of dynamical invariants and Casimirs in the process of CME integration, useful normalization parameters, are also discussed. Numerous comparisons with PIC simulations are presented for initially gaussian and uniform beams with a different degree of the mismatch. Chapter 4 is dedicated to the investigation of the physical mechanism of collisionless relaxation within the framework of CME model. The time needed for the relaxation of the rms beam oscillations is estimated. The asymptotic coarse-grained equilibrium state is studied in Chapter 5. A detailed comparisons and discussions of previous theories with PIC simulations for slab systems are presented. Theoretical insights are also gained into the aspects of the equilibrium distribution and new predictions for the final state of a system with a spatially nonlinear but not self-consistent force are obtained.

Chapter 2

Illustration of Beam Propagation Through Long Plasma Systems

We begin our analysis with a short description of the physical system consisting of the beam propagation through a long plasma. A long plasma is defined as a plasma with a length comparable to or larger than the betatron wavelength of the beam. Due to the spatial nonlinearity of the space-charge force acting on the beam particles, a rich set of different phenomena is expected to take place in this system including the decay of the amplitude of the betatron oscillations, emittance growth and the relaxation of the coarse-grained distribution towards an equilibrium state. Modeling and understanding of these phenomena are the topics of this thesis.

In this Chapter we set the stage for the theoretical modeling of the relaxation of the rms oscillations. We begin with a brief description of the physical system under consideration. The approximations made in the theoretical analysis are discussed. To prepare grounds for the study, a numerical illustration of the rms beam dynamics in a long plasma system is presented in Sec. 2.1 using a result of the PIC simulation. The traditional envelope equation with constant emittance is shown to make poor predictions, and problems associated with this model are discussed. The asymptotic values of the beam size, temperature and emittance, reached after the decay of the betatron oscillations, are derived in Sec. 2.3.

This Chapter and Chapter 3 are an extension of the paper titled 'Coupled Moment Expansion Model for the Dynamics in a Beam-Plasma System' by E. Yu. Backhaus and J.

S. Wurtele [66].

2.1 Numerical Example

The physical system is illustrated in Fig. 2.1. It consists of a continuous warm beam of particles, each with charge q_b and mass m_b. Both electrons and ions can constitute the beam. The beam is characterized spatially by the number density n_b. It propagates with relativistic velocity v_z along the z-axis in an infinite plasma of density n_p. For simplicity, we assume that the beam is a sheet of charge which is infinite in y-direction and the motion of the beam particles is well described by the paraxial limit. Using this common beam physics approximation, the longitudinal velocity $v_z \approx c$ remains unchanged, and the transverse and longitudinal motion decouple. Combining the assumption of the infinite extent in y-direction with the paraxial limit approximation, we may characterize the system as one-dimensional with a slab geometry.

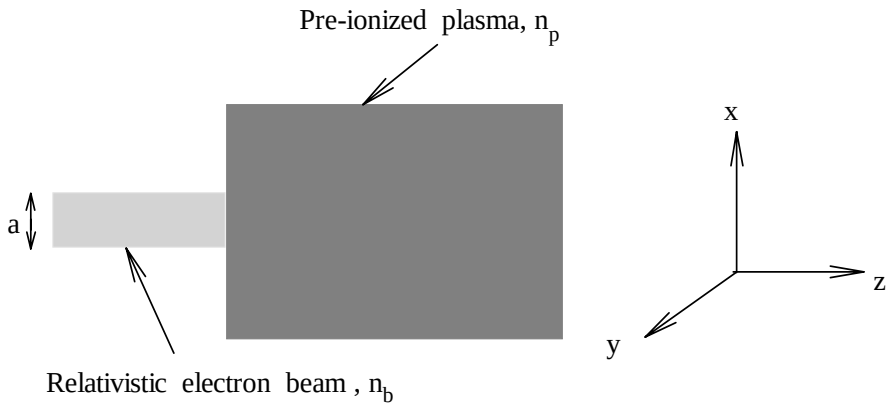

Figure 2.1: The setup of the system

Some further assumptions are made to simplify the mathematics of the analysis. The plasma is taken to be overdense, so that the plasma density $n_p \gg n_b$. Under this approximation, complete charge neutralization takes place in the beam as plasma particles move to cancel the beam-generated electric field. Thus, no electric field is present in the beam. We also assume that the transverse beam size is much smaller than the plasma skin depth c/ω_p, where $\omega_p = \sqrt{n_p e^2/\varepsilon m}$ denotes the plasma frequency and c is the speed of light

in vacuum. This regime corresponds to the absence of return plasma currents within the beam [67]. Since no current neutralization takes place, the self-magnetic field is not reduced by the plasma, and the only force acting on the beam particles is the Lorentz force due to the magnetic field. Combining all the approximations, the governing equation of motion for beam particles can be written as

$$m_b\gamma\frac{dv_x}{dt} = -q_b v_z B_y, \tag{2.1}$$

$$B_y = q_b v_z \mu_0 \int_0^x dx'\, n_b(x'), \tag{2.2}$$

where γ is the relativistic factor and μ_0 is the permeability of the free space. Due to the paraxial approximation, $\gamma = Const$ in Eq. (2.2). Now the dynamics of beam particles is modeled as one-dimensional, and Eq. (2.1) can be used to advance the transverse velocity of the particles with the force computed using Eq. (2.2). Then, transverse displacements (displacements along x-axis) of the particle can be computed as well. The longitudinal velocity v_z remains constant, and it is equal to c. Thus, the longitudinal displacement of a beam slice can be computed as $z = ct + z_0$, where z_0 is the initial displacement. This linear relation between the horizontal position of the beam slice and time is useful to translate the transverse dynamics of the beam in time into evolution of the beam slice as it propagates along the z-axis.

We begin our discussion of the beam transport with a numerical illustration obtained using a PIC simulation. The PIC code *xpdp1*, used throughout this paper, was written and supported by the UC Berkeley EECS Plasma Simulation Group [68]. It is a one-dimensional electrostatic code for systems with a slab geometry. More information on the original code can be found in Ref. [69]. Our system, described by Eqs. (2.1)- (2.2), is one-dimensional in x variable, as variations along y axis are neglected. Therefore, x is taken as the axis of *xpdp1* simulation. The fact that the force on the beam particles is determined by the self-magnetic field as in Eq. (2.2) is used directly in the PIC simulations. The simulation is set up as to compute the dynamics of a warm electron beam (no plasma is explicitly present in the simulation as its effect is accounted for in the force acting on the electrons). The initial distribution of the beam in the simulation is varied depending on the initial condition of interest. Only beam particles are loaded in the simulation, and the force is computed from the solution of Poisson's equation for the vector potential with the sign of the source term corresponding to the attraction of particles as in Eq. (2.2). Note that Eq. (2.2) for the force acting on beam particles can be considered as a solution of Poisson's

equation for one-dimensional system with an attractive force. Thus, an electrostatic model can be used if the repellent electric force is replaced by an attractive electrostatic force. To accommodate the set-up of the simulation, walls are placed above and below the plasma at a distance much larger than the plasma size. The external circuit is taken as a short as no external circuit is present in the problem. A typical simulation is performed using 6×10^4–10^5 particles. We use the results of PIC simulations as a baseline to test the applicability of our theoretical models.

In this first illustration, the initial phase-space distribution is taken to be of the form

$$f_0(x, v_x) = \frac{n_0}{\sqrt{2\pi}\sigma_{vo}} e^{-x^2/2\sigma_{xo}^2} e^{-v_x^2/2\sigma_{vo}^2}, \tag{2.3}$$

where σ_{xo} and σ_{vo} characterize the initial beam size and temperature, and $n_b(x = 0, t = 0) = n_0$. The initial beam density n_b corresponding to Eq. (2.3) has a gaussian spatial dependence. The initial condition given by Eq. (2.3) is used in other examples in this thesis. The second initial condition used in numerical illustrations corresponds to a uniform phase-space density given by

$$f_0(x, v_x) = \begin{cases} \dfrac{n_0}{2\sqrt{3}\sigma_{vo}} & , \quad |x| \le \sqrt{3}\sigma_{xo}, |v_x| \le \sqrt{3}\sigma_{vo} \\ 0 & , \quad \text{otherwise.} \end{cases} \tag{2.4}$$

It is convenient to quantify the initial deviation of the rms beam properties from their equilibrium values and the size of the rms oscillations by the value of the mismatch coefficient

$$\alpha \equiv |U/2T|. \tag{2.5}$$

Here, $T = m_b\gamma\langle v_x^2\rangle/2$ stands for the kinetic energy of the transverse motion and $U = q_b v_z \langle x B_y\rangle$ is the virial integral of the force. The notation $\langle\rangle$ stands for the average over the distribution and is defined as

$$\langle ...\rangle \equiv \frac{1}{N} \int\int dx dv_x \, ... f(x, v_x), \tag{2.6}$$

where

$$N = \int_{-\infty}^{\infty} dx \, n_b(x). \tag{2.7}$$

Using Eq. (2.6), the virial integral can be written explicitly as

$$U = \frac{q_b v_z}{N} \int_{-\infty}^{\infty} dx \, n_b x B_y. \tag{2.8}$$

As can be seen from the envelope equation presented below, the rms size of a beam with an initial value of $\alpha = 1$ does not change in time (at least within the framework of the envelope formalism) and, therefore, it is called matched. If initially $\alpha \neq 1$, the beam is mismatched, and rms oscillations occur due to the interplay between the focusing magnetic force and the defocusing effect of the pressure. Thus, α serves as a measure of the initial beam mismatch and the amplitude of the rms oscillations.

For the initial distribution given by Eq. (2.3), the mismatch parameter is explicitly found to be

$$\alpha = 2\sqrt{\pi}\frac{q_b v_z N \sigma_{xo}}{I_A}\frac{v_z^2}{\sigma_{vo}^2}, \tag{2.9}$$

where $I_A = 4\pi\varepsilon_0 m_b c^2 v_z \gamma / q_b$ is the Alfven current and $N = \sqrt{2\pi} n_0 \sigma_{xo}$. A similar calculation for the initial mismatch parameter of the initially uniform distribution of Eq. (2.4) gives

$$\alpha = \frac{2\pi}{\sqrt{3}}\frac{q_b v_z N \sigma_{xo}}{I_A}\frac{v_z^2}{\sigma_{vo}^2}. \tag{2.10}$$

Consider, for example, an initial electron beam with the distribution given by Eq. (2.3) with $\sigma_{xo} = 3.4\text{mm}$, $\sigma_{vo} = 1.7 \times 10^6 \text{m/s}$, $\gamma = 100$ and $n_0 = 5.9 \times 10^{16} \text{m}^{-3}$ corresponding to $\alpha = 5$. PIC generated propagation curves for the bulk properties of the beam (*i.e.* $\sigma_x = \sqrt{\langle x^2 \rangle}$, $\sigma_v = \sqrt{\langle v_x^2 \rangle}$ and the beam emittance $\varepsilon = \sqrt{\langle x^2 \rangle \langle x'^2 \rangle - \langle x x' \rangle^2}$ with $x' = v_x / v_z$) are plotted in Fig. 2.2. At the initial stages of the propagation, betatron oscillations are induced by the initial beam mismatch due to the interplay between the defocusing pressure of the warm beam and the focusing effect of the self-magnetic field. However, a rapid relaxation of the motion is observed, and oscillations cease after just a few betatron periods. This first stage of the relaxation process is usually referred to as a period of violent relaxation in astrophysics literature [35, 6]. Small residual oscillations still persist with non-decaying amplitude after this initial relaxation stage. A significant emittance growth, which can be attributed to the nonlinearity of the self-magnetic force, is also observed in the process. A similar dynamical picture for the rms beam properties is also obtained for a beam with a uniform initial phase-space distribution.

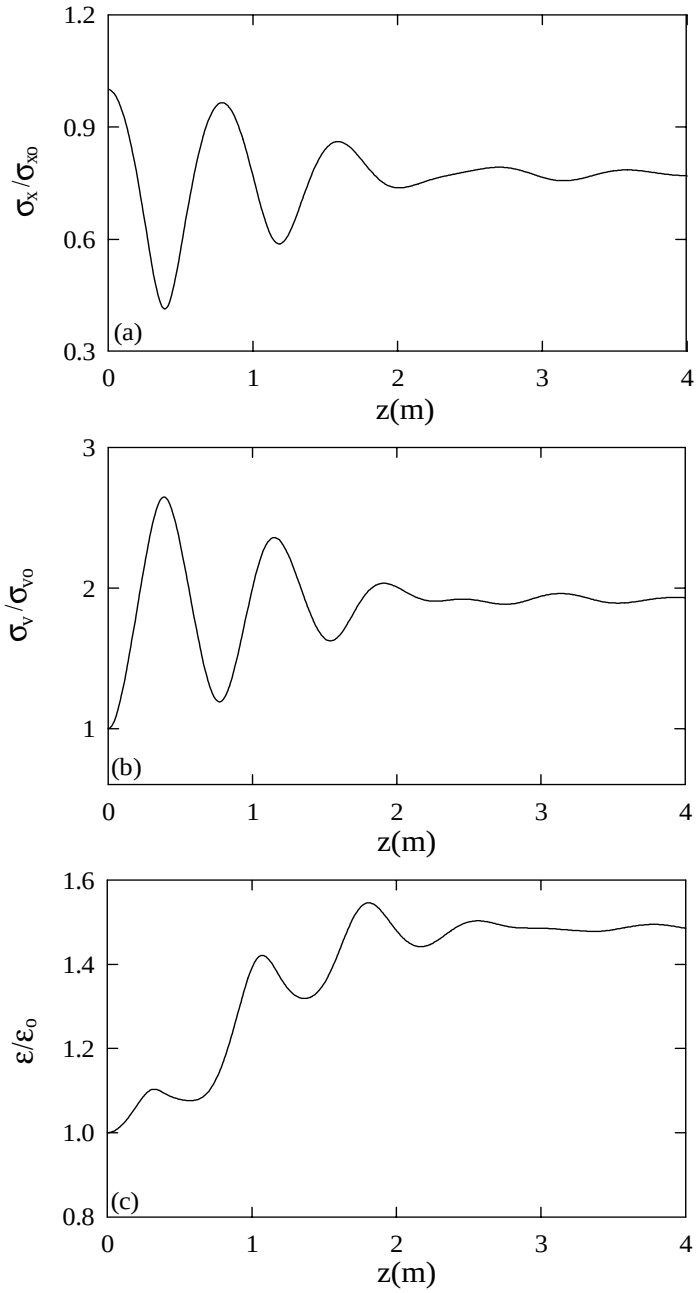

Figure 2.2: PIC propagation curves for the beam with the initial gaussian distribution and the mismatch of $\alpha = 5$ for (a) rms beam size, (b) rms velocity and (c) the emittance. All quantities are normalized to their initial values.

2.2 Predictions for the Rms Dynamics Using the Traditional Envelope Equation

In this thesis, we attempt to model accurately the dynamics of the rms beam properties using a reduced model, *i.e.* by integrating a relatively small system of dynamical equations. The simplest model of this type that can be used to predict the evolution of the beam size is the traditional envelope equation, which assumes the emittance of the beam to remain constant. The envelope equation was already used in our studies of beam focusing by a thin plasma lens and was in good agreement with experimental data. Therefore, it is a logical starting point for the investigation of dynamics in long plasma systems. The general form of the envelope equation for the evolution of the rms beam size σ_x in a one-dimensional system with a slab geometry can be written as [38]

$$\frac{d^2\sigma_x}{dz^2} = \frac{\varepsilon^2}{\sigma_x^3} + \frac{1}{m_b\gamma v_z^2}\frac{\langle xF_x\rangle}{\sigma_x}. \tag{2.11}$$

Here, F_x is the total force acting on the beam particles in the transverse direction including any external and self forces. If F_x depends linearly on x, as it is the case in some other beam physics applications such as quadrupole focusing and propagation in a long solenoid, it can be easily shown that the emittance of the beam remains constant and a closed form equation for σ_x is immediately obtained. However, in the case of a nonlinear force the beam emittance increases in the course of the beam propagation, and the evolution of the beam size becomes coupled to the dynamics of higher order distribution moments. In addition to these complications, the self-consistency of the force requires an assumption about the functional dependence of $n_b(x)$ in order to evaluate the force and the average $\langle xF_x\rangle$.

To close the system describing the evolution of the rms beam size, we first assume that the change in a beam emittance can be ignored. This approximation is commonly made in the envelope equation models. The initial density, corresponding to the distribution function given by Eq. (2.3), has a gaussian shape. As the change in the density profile is unknown, we assume that $n_b(x)$ can be modeled as a gaussian in the course of the beam propagation for the initial condition considered. Equation (2.11) is supplemented with the initial condition for the rms beam size and its slope and is integrated numerically. The predicted evolution of the rms beam size (——) is compared with the result of the PIC simulation ($\cdot\ \cdot\ \cdot$) in Fig. 2.3 for the case with the same parameters as used in the example presented in Fig. 2.2 corresponding to $\alpha = 5$. The envelope equation prediction is in the

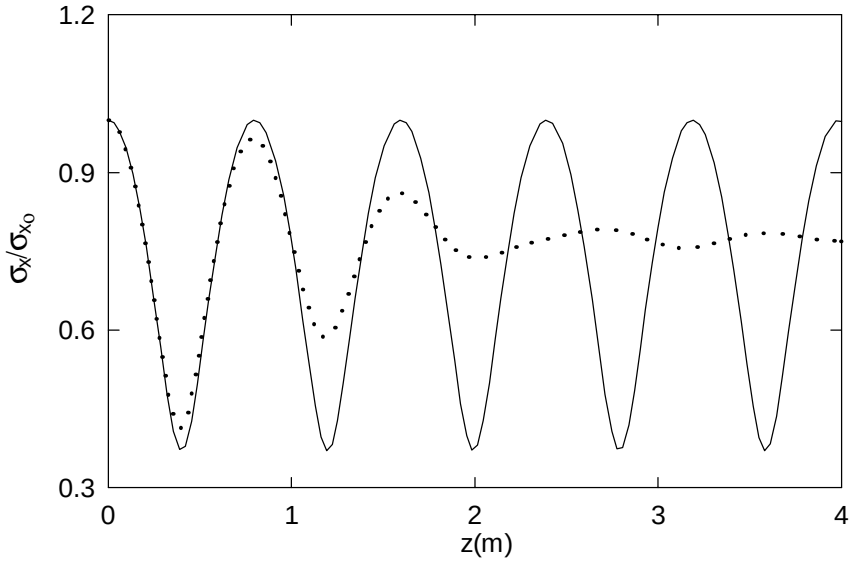

Figure 2.3: Comparison between propagation curves for the rms beam size generated by the envelope equation (——) and PIC simulation ($\cdot\ \cdot\ \cdot$) for the initial mismatch of $\alpha = 5$.

agreement with the PIC dynamics for about half of a betatron period, but no relaxation of the oscillations is seen. The other shortcoming of the model is in the assumption of the emittance invariance (which does grow due to the spatial nonlinearity of F_x). We conclude that the envelope equation can be used to predict the short-term evolution of the beam size, which explains the success of the model for thin plasma lenses. However, it does not provide adequate predictions for the propagation farther than one half of a betatron wavelength.

The intimate connection between the emittance growth and the relaxation of the rms oscillations was recognized in the past by many authors, see for example Refs. [41, 38, 39, 40]. For example, an attempt was made by Lee and Yu [41] to include the effect of the emittance growth into the beam size dynamics. In their theory, the evolution of the cylindrical beam was described by two coupled equations given by

$$\begin{aligned} \frac{d^2\sigma_r}{dz^2} &= \frac{\varepsilon^2}{\sigma_r^3} - \frac{\langle k_\beta^2 r^2 \rangle}{\sigma_r}, \\ \frac{d\varepsilon^2}{dz} &= -2\alpha_r \frac{\langle k_\beta^2 r^2 \rangle \sigma_r^2}{(\varepsilon/\sigma_r + \langle k_\beta^2 r^2 \rangle \sigma_r/\varepsilon)} \frac{d^2\sigma_r}{dz^2}, \end{aligned} \tag{2.12}$$

where the notation σ_r is used for $\sqrt{\langle r^2 \rangle}$ and $\langle k_\beta^2 r^2 \rangle \equiv q_b B_\theta / \beta\gamma m_b c^2 r$. The notations and geometry of Ref. [41] are used here. In cylindrical geometry, $\langle k_\beta^2 r^2 \rangle$ is calculated to be $\langle k_\beta^2 r^2 \rangle = I/I_A$, where I stands for the net beam current. Note that a free parameter α_r, which is connected to the unknown and changing density profile of the beam, is included in the dynamics of the beam emittance. When Eqs. (2.12) are supplemented with initial conditions and integrated forward in z, the relaxation of the rms oscillations and emittance growth result. While the model of Lee and Yu clearly illustrates the connection between the emittance growth and relaxation of rms oscillations, it can not be used to make first principle predictions for the beam dynamics due to the unknown and possibly changing value of the parameter α_r. In the next chapter, we derive an alternative set of equations that can be used to model the rms dynamics without any use of adjustable parameters.

2.3 Estimates of Equilibrium Bulk Properties

As the example of Sec. 2.1 demonstrates, the oscillations of the rms beam size and temperature subside after a few betatron periods. The estimates of resulting stationary values can be quite useful for practical applications. They can also be used as normalization parameters for the numerical simulations of the rms dynamics. An estimate for the equilibrium size of a pinched cylindrical beam was previously obtained using the energy conservation relation in Refs. [42, 70] for small amplitude betatron oscillations. Instead of re-deriving the result for a slab beam using the approach of Ref. [70], the analysis is extended here to make predictions for beams with a significant initial mismatch. Some predictions for the coarse-grained equilibrium can also be found in Refs. [1] and [2] where the final distribution is assumed to be thermal. There, two relations are used to determine the beam size and temperature after the decay of the oscillations is completed: the equilibrium condition and the conservation of the distribution function at the origin in the phase-space ($f(x = 0, v_x = 0, t) = Const$). Applying the results of Refs. [1] and [2] to a beam with the initial condition given by Eq. (2.3), we obtain the following estimates for the stationary values written in notations of this thesis:

$$\sigma_{x,eq}^{g,old} = \frac{\pi^{7/6}}{2\sqrt{3}} \frac{1}{\alpha^{1/3}} \sigma_{xo}, \tag{2.13}$$

$$\sigma_{v,eq}^{g,old} = \frac{\pi^{1/3}}{\sqrt{2}} \alpha^{1/3} \sigma_{vo}. \tag{2.14}$$

The change of the emittance can be evaluated also as $\varepsilon_{eq}^{old} = \sigma_{x,eq}^{old}\sigma_{v,eq}^{old}$, and it is given by

$$\varepsilon_{eq}^{g,old} = \frac{\pi\sqrt{\pi}}{2\sqrt{6}}\varepsilon_0 \approx 1.14\varepsilon_0, \tag{2.15}$$

where ε_0 stands for the initial value. In Eq. (2.15) it is implicitly assumed that $\langle xv_x \rangle = 0$ in the asymptotic state. It can be readily seen that the prediction given by Eq. (2.15) for the emittance growth is independent of the initial mismatch parameter α. This result contradicts the intuitive expectations (which were verified numerically) of larger emittance growth in systems with more effective phase mixing (*i.e.* larger α for $\alpha > 1$ or larger $1/\alpha$ for $\alpha < 1$). Thus, Eqs. (2.13) and (2.14) can be used for rough estimates of the rms beam size and velocity dispersion in the final state but a significant discrepancy is expected in comparisons with the PIC simulation results. The asymptotic values of the rms properties of the beam with a uniform initial distribution (given by Eq. (2.4)) are also calculated. Using results of Refs. [1] and [2], the following results are obtained

$$\sigma_{x,eq}^{u,old} = \frac{\pi^{2/3}}{2^{1/3}}\frac{1}{\alpha^{1/3}}\sigma_{xo}, \tag{2.16}$$

$$\sigma_{v,eq}^{u,old} = \frac{\sqrt{3}}{(2\pi)^{1/6}}\alpha^{1/3}\sigma_{vo}, \tag{2.17}$$

$$\varepsilon_{eq}^{u,old} = \sqrt{\frac{3\pi}{2}}\varepsilon_0 \approx 2.17\varepsilon_0. \tag{2.18}$$

The comparisons between the analytical predictions and results of PIC simulations for both initial distributions are presented below.

To derive alternative expressions for the asymptotic values, a procedure similar to that of Ref. [1] is used here. The main difference is in the use of a different constraint to find the equilibrium state - the constraint of the energy conservation is utilized instead of the conservation of $f(0,0,t)$ employed in Ref. [1]. The use of the macroscopic energy conservation relation allows to derive an exact expression for the final velocity spread while the technique of Ref. [1] results in an approximate result. The difficulty encountered here reflects the fact that the assumed form of the equilibrium distribution (*i.e.* the thermal profile) is not the exact coarse-grained equilibrium achieved by the system in the process of collisionless relaxation. Numerical studies indicate significant differences between the final coarse-grained distribution and a true thermal equilibrium. This fact is reflected in the larger number of conservation constraints than the number of parameters needed to be specified in the thermal distribution. However, for the sake of an estimate, the final

distribution function will be assumed thermal with a choice of constraints resulting in better predictions for the rms beam properties.

We now derive the predictions for the rms beam properties reached after the relaxation process is complete. Unnormalized, physical variables are used in this section. The particle equation of motion, $m_b\gamma dv_x/dt = -q_b v_z B_y$, with $\gamma = Const$ in accordance with the paraxial approximation, can be used to easily derive the following equations for the dynamics of the second order moments:

$$\frac{d\langle x^2\rangle}{dt} = 2\langle x v_x\rangle, \tag{2.19}$$

$$\frac{d\langle x v_x\rangle}{dt} = \langle v_x^2\rangle - \frac{q_b v_z}{m_b\gamma}\langle x B_y\rangle, \tag{2.20}$$

$$\frac{d\langle v_x^2\rangle}{dt} = -2\frac{q_b v_z}{m_b\gamma}\langle v_x B_y\rangle. \tag{2.21}$$

Under the assumption that phase mixing results in a coarse-grained distribution function with the symmetry $f(x,v_x) = f(-x,v_x) = f(x,-v_x)$, all moments $\langle x^p v_x^q\rangle$ with p and q odd vanish in the asymptotic state. Thus, the stationary forms of Eqs. (2.19) and Eq. (2.21) are satisfied. The remaining Eq. (2.20) results in the equilibrium condition

$$m_b\gamma\langle v_x^2\rangle_{eq} = q_b v_z\langle x B_y\rangle_{eq}, \tag{2.22}$$

where $\langle ...\rangle_{eq}$ stands for the average evaluated using the asymptotic coarse-grained distribution. This is essentially the same relation as the equilibrium condition used in Ref. [1]. It reflects the balance between the focusing magnetic force and defocusing pressure term in the stationary state.

Equation (2.22) represents one relation that can be used to find estimates for the stationary values of the beam size and temperature. A second relation between moments is needed and can be obtained from the energy conservation for the transverse motion. The conservation relation can be readily derived from Eq. (2.21). Substituting $B_y = -\partial A_z/\partial x$ and integrating by parts, Eq. (2.21) yields

$$\frac{d\langle v_x^2\rangle}{dt} = -2\frac{q_b v_z}{N m_b\gamma}\int dx dv_x\ A_z v_x\frac{\partial f}{\partial x} = 2\frac{q_b v_z}{N m_b\gamma}\int dx\ A_z\frac{\partial n_b}{\partial t}, \tag{2.23}$$

where the Vlasov equation is used, the common boundary condition $f|_{v_x\to-\infty}^{\to+\infty} = f|_C = 0$ is applied, and an integration over v_x is performed. Here, the notation C denotes the spatial boundary of the system. Using Ampere's law relation for the one-dimensional slab

system ($\partial^2 A_z/\partial x^2 = -q_b v_z \mu_0 n_b$) for $n_b(x)$ and integrating by parts, the last equation can be rewritten as

$$\frac{d}{dt}\left(\frac{m_b\gamma\langle v_x^2\rangle}{2}\right) = -\frac{1}{\mu_0 N} A_z \frac{\partial^2 A_z}{\partial t \partial x}\bigg|_C + \frac{1}{2\mu_0 N}\frac{d}{dt}\int dx \left(\frac{\partial A_z}{\partial x}\right)^2. \tag{2.24}$$

Assuming the boundary condition $A_z|_C = 0$ and integrating the remaining term by parts again, we obtain

$$\frac{d}{dt}\left(\frac{m_b\gamma\langle v_x^2\rangle}{2}\right) = -\frac{1}{2\mu_0 N}\frac{d}{dt}\int dx A_z \frac{\partial^2 A_z}{\partial x^2}. \tag{2.25}$$

Using Ampere's law once again now for $\partial^2 A_z/\partial x^2$, the last equation takes the form

$$\frac{d}{dt}\left(\frac{m_b\gamma\langle v_x^2\rangle}{2}\right) = \frac{d}{dt}\left(\frac{q_b v_z}{2N}\int dx A_z n_b\right). \tag{2.26}$$

Equation (2.26) reflects the desired conservation of transverse energy. The right-hand side of the last equation can be rewritten in a more useful form. Consider the virial integral

$$q_b v_z \langle x B_y\rangle \equiv \frac{q_b v_z}{N}\int dx\ x B_y n_b. \tag{2.27}$$

Using Ampere's law for n_b and the relation for the vector potential $B_y = -\partial A_z/\partial x$, the virial integral can be written as follows

$$q_b v_z \langle x B_y\rangle = \frac{1}{N\mu_0}\int dx\ x\left(-\frac{\partial A_z}{\partial x}\right)\left(-\frac{\partial^2 A_z}{\partial x^2}\right) = \frac{1}{2N\mu_0}\int dx\ x\frac{\partial}{\partial x}\left(\frac{\partial A_z}{\partial x}\right)^2. \tag{2.28}$$

Performing the integration by parts twice, we obtain

$$q_b v_z \langle x B_y\rangle = C_0 - \frac{q_b v_z}{2N}\int dx A_z n_b. \tag{2.29}$$

The constant C_0 arises from the boundary term, and it does not depend on time if the boundary of the system is located outside of the beam. Substituting Eq. (2.29) into Eq. (2.26) we obtain

$$\frac{d}{dt}\left(\frac{m_b\gamma\langle v_x^2\rangle}{2}\right) = -\frac{d}{dt}\left(q_b v_z\langle x B_y\rangle\right), \tag{2.30}$$

and $q_b v_z\langle x B_y\rangle$ can now be identified with the potential energy. Finally, the conservation of energy for the initial and final beam can be expressed as

$$\frac{m_b\gamma}{2}\langle v_x^2\rangle_{eq} + q_b v_z\langle x B_y\rangle_{eq} = \frac{m_b\gamma}{2}\langle v_x^2\rangle_o + q_b v_z\langle x B_y\rangle_o, \tag{2.31}$$

where $\langle ... \rangle_o$ stands for the average evaluated in the initial state.

Combining Eq. (2.22) with Eq. (2.31), the velocity dispersion in the equilibrium state can be expressed as

$$\langle v_x^2 \rangle_{eq} = \frac{\sigma_{vo}^2}{3} + \frac{2}{3} \frac{q_b v_z}{m_b \gamma} \langle x B_y \rangle_o. \tag{2.32}$$

Using the definition of the mismatch parameter $\alpha = U/2T$, the initial potential energy can be expressed as $q_b v_z \langle x B_y \rangle_o = \alpha m_b \gamma \sigma_{vo}^2$. Substitution of this relation into Eq. (2.32) results in the prediction for the velocity spread $\sigma_{v,eq} \equiv \sqrt{\langle v_x^2 \rangle_{eq}}$ in the stationary state

$$\sigma_{v,eq} = \sqrt{\frac{1+2\alpha}{3}} \sigma_{vo}. \tag{2.33}$$

This is the first estimate of the rms beam properties in the asymptotic state. Note that the result for $\sigma_{v,eq}$ is exact, as no approximation is made beyond equilibrium and the symmetry relations. It also holds for any initial beam distribution.

This analysis also yields a value for the virial integral in equilibrium, which we write explicitly as

$$q_b v_z \langle x B_y \rangle_{eq} = (1+2\alpha) m_b \gamma \sigma_{vo}^2 / 3. \tag{2.34}$$

Unfortunately, the functional dependence of the density profile in equilibrium is needed to deduce an expression for the beam size $\sigma_{x,eq}$ from the virial integral. For the sake of an estimate, we approximate the asymptotic coarse-grained phase-space density by a thermal equilibrium distribution. A measure of the sensitivity of this approximation on the predicted asymptotic beam size is investigated below by comparison with the result when the asymptotic final state is taken as a gaussian.

The thermal equilibrium for the one-dimensional magnetic pinch in a slab geometry is given in Refs. [1, 59] by a modified Bennett distribution:

$$f_B(x,v) = \frac{N}{2\sqrt{2\pi} u_B b} \frac{1}{\cosh^2 x/b} e^{-v^2/2u_B^2}. \tag{2.35}$$

The distribution is characterized by two parameters b and u_B which define the spatial and velocity scales of the beam. The corresponding density is

$$n_B(x) = \frac{N}{2b} \frac{1}{\cosh^2 x/b}. \tag{2.36}$$

Assuming the asymptotic coarse-grained distribution to have the form of Eq. (2.35), the value of the velocity dispersion $u_B = \sigma_{v,eq}$ can be evaluated using Eq. (2.33). Using the

explicit expression for $n_B(x)$, the magnetic field of the beam can now be easily calculated together with the virial integral. Using the equilibrium value of $qv_z\langle xB_y\rangle_{eq}$ and the relation $\sqrt{\langle x^2\rangle} = \pi b/2\sqrt{3}$ for the Bennett profile, the estimate of the asymptotic value of the rms beam size $\sigma_{x,eq} \equiv \sqrt{\langle x^2\rangle_{eq}}$ becomes

$$\sigma_{x,eq} = (1+2\alpha)\frac{1}{6\sqrt{3}}\frac{I_A}{Nq_bv_z}\frac{\sigma_{vo}^2}{v_z^2}. \tag{2.37}$$

The prediction for $\sigma_{x,eq}$ given by Eq. (2.37) can be used for any initial density profile. For the initially gaussian beam, it simplifies to

$$\sigma_{x,eq}^g = \sqrt{\frac{\pi}{3}}\frac{(1+2\alpha)}{3\alpha}\sigma_{xo}. \tag{2.38}$$

The analogous expression for the asymptotic size of the beam with the initially uniform density has the form

$$\sigma_{x,eq}^u = \frac{\pi}{3}\frac{(1+2\alpha)}{3\alpha}\sigma_{xo}. \tag{2.39}$$

We now have estimates for the desired values of the asymptotic beam size and the beam temperature for both initial distributions of interest.

The asymptotic emittance growth can also be computed. Substituting the values for $\langle x^2\rangle_{eq}, \langle v_x^2\rangle_{eq}$ and $\langle xv\rangle_{eq}$ into the definition of the emittance, $\varepsilon^2 = \langle x^2\rangle\langle v_x'^2\rangle - \langle xv_x'\rangle^2$, we obtain for the initially gaussian beam

$$\varepsilon_{eq}^g = \sqrt{\frac{\pi}{3}}\frac{(1+2\alpha)^{3/2}}{3\sqrt{3}\alpha}\varepsilon_0, \tag{2.40}$$

and for the initially uniform beam

$$\varepsilon_{eq}^u = \frac{\pi}{3}\frac{(1+2\alpha)^{3/2}}{3\sqrt{3}\alpha}\varepsilon_0. \tag{2.41}$$

The analysis above predicts that the emittance growth depends on the initial mismatch parameter α. Note that $\varepsilon_{eq} > \varepsilon_0$ in both cases, and the minimum emittance growth is achieved for a matched beam with $\alpha = 1$. The value of the minimum emittance change is equal to $(\varepsilon_{eq}^g/\varepsilon_0)^{min} \simeq 1.023$ for the initially gaussian beam and is given by $(\varepsilon_{eq}^u/\varepsilon_0)^{min} \simeq 1.047$ for a beam with a uniform initial profile.

To test the accuracy of the estimates, the analytical predictions for the final rms beam properties and emittance growth are compared with the PIC simulation and previous estimates of Ref. [1], given by Eqs. (2.13)-(2.15) for the initially gaussian beam and

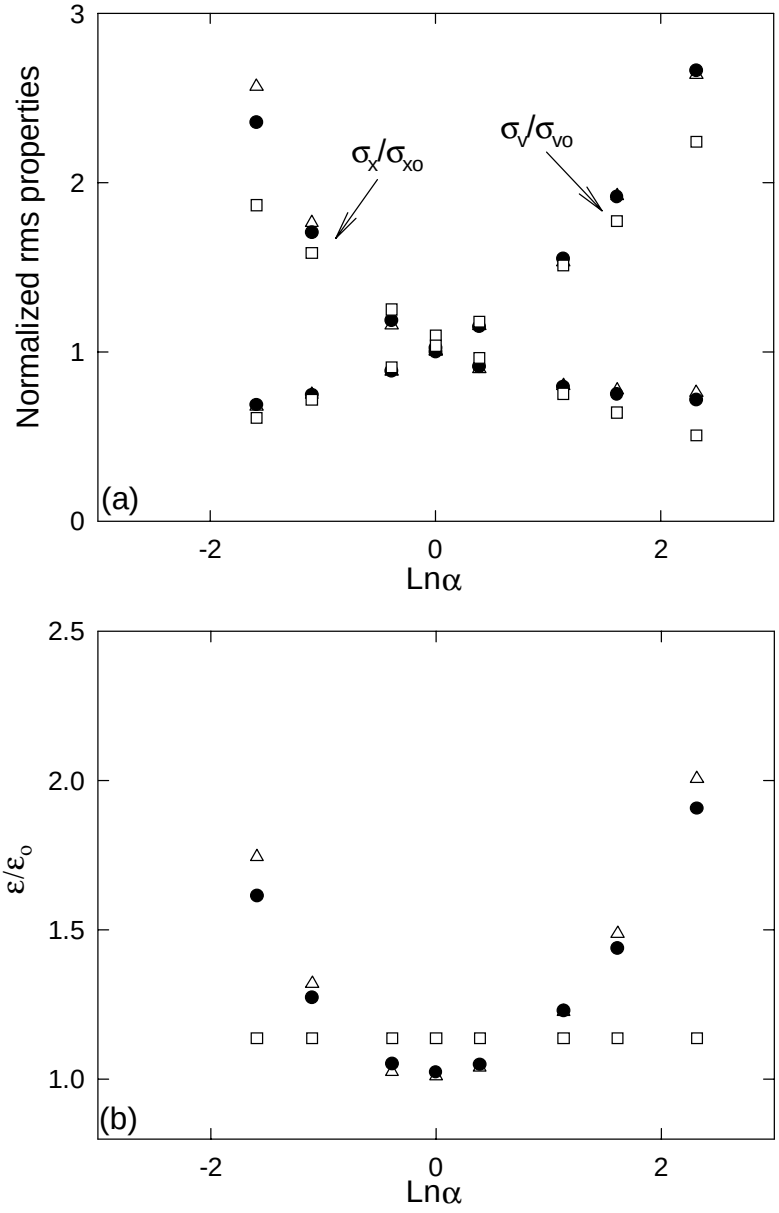

Figure 2.4: Comparison between the new analytical predictions (•) given by Eqs. (2.33), (2.38) and (2.40), predictions of Ref. [1] (□) given by Eqs. (2.13)-(2.15) and PIC results (△) for (a) the rms beam properties and (b) the emittance *vs* the initial mismatch α of the initially gaussian beam.

Eqs. (2.16)-(2.18) for the uniform distribution. The results, obtained for beams with initially gaussian profiles but with various degrees of the mismatch, are presented in Fig. 2.4. The mismatch parameter is varied in a wide range of $0.2 < \alpha < 10$. The initial emittance and the number of particles per unit area are taken the same for all cases and are equal to $\varepsilon_0 = 19.7$ mm-mrad and $N \equiv n_0\sqrt{2\pi}\sigma_{xo} = 5.05 \times 10^{14}\mathrm{m}^{-2}$ respectively. As expected, a discrepancy between predictions of Ref. [1] and PIC results can be seen. The discrepancy is especially significant for the emittance growth results. Good agreement between these new theoretical predictions and PIC results is observed for the rms beam size, thermal spread and emittance growth.

The results for the asymptotic values of the initially uniform beam are presented in Fig. 2.5 in the same range of the initial mismatch. The initial emittance and the number of particles per unit area are taken equal to $\varepsilon_0 = 20.1$ mm-mrad and $N \equiv n_0 2\sqrt{3}\sigma_{xo} = 5.05 \times 10^{14}\mathrm{m}^{-2}$. Even a more significant discrepancy between the estimates of Ref. [1] and PIC results for the asymptotic rms values is observed in this case. Good agreement between the predictions given by Eqs. (2.33), (2.39) and (2.41) and PIC values is observed.

To investigate the dependence of the estimate for $\sigma_{x,eq}$ on the assumed density profile, the calculation of asymptotic properties is also performed for a beam with a gaussian final density profile. Specifically, the density dependence is assumed to be of the form

$$n_b(x) = \frac{N}{\sqrt{2\pi}\sigma_{x,eq}} e^{-x^2/2\sigma_{x,eq}}. \tag{2.42}$$

Evaluating the magnetic field and the virial integral and using Eq. (2.34) for the stationary value of $\langle xB_y \rangle$, an estimate for the asymptotic beam size of the initially gaussian beam is obtained

$$\sigma^{g,g}_{x,eq} = \frac{(1+2\alpha)}{3\alpha}\sigma_{xo}. \tag{2.43}$$

Comparing Eq. (2.43) with the estimate based on the Bennett density assumption given by Eq. (2.38), we see that, at least for these two density profiles, the very similar estimates for $\sigma_{x,eq}$ are related by

$$\sigma^{g,g}_{x,eq} = \sqrt{\frac{3}{\pi}}\sigma^{g}_{x,eq}, \tag{2.44}$$

and they differ by less than 3%. This result suggests that the relation between the virial integral and the beam size is somewhat insensitive to the assumed density profile.

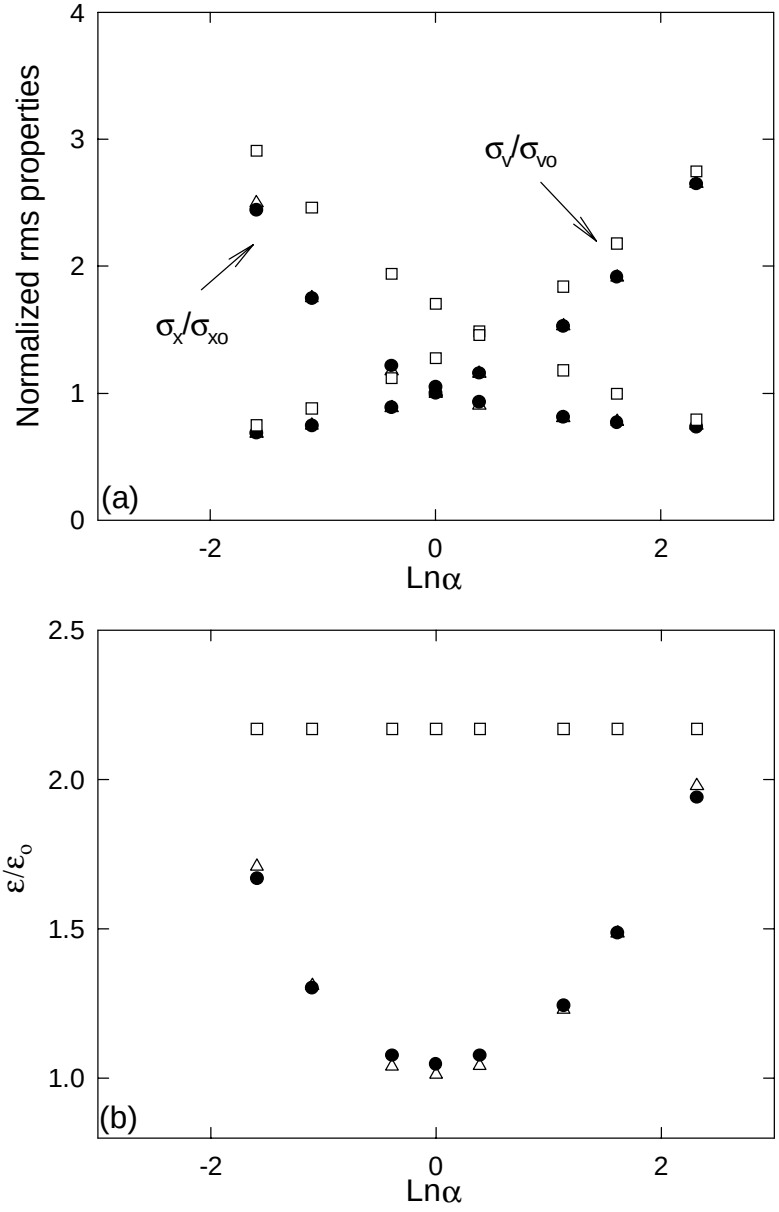

Figure 2.5: Comparison between the new analytical predictions (•) given by Eqs. (2.33), (2.39) and (2.41), predictions of Ref. [1] (□) given by Eqs. (2.16)-(2.18) and PIC results (△) for (a) the rms beam properties and (b) the emittance *vs* the initial mismatch α of the initially uniform beam.

Chapter 3

Coupled Moment Equation Model

3.1 Derivation of the Coupled Moment Equations

The interesting dynamics of the second order moments observed in beam propagation through a long plasma system was illustrated in the previous Chapter. A rapid relaxation of the rms oscillations to an almost stationary state was observed. The effect of the decay of the betatron oscillations during the beam propagation is one manifestation of the so-called process of collisionless relaxation. The relaxation, which takes place in systems with no dissipation or viscous forces present, is attributed to the phase mixing induced by the nonlinearity of the forces. The goal of this work is to correctly predict the decay of the betatron oscillations and the accompanying emittance growth with a model that allows for a significant reduction in the number of equations compared to what is needed in a PIC simulation. The use of fewer equations results in the loss of information about some finer details of the evolution of the distribution. The results of Sec. 2.2 show that the simple envelope equation model, which uses the approximation of a constant emittance and an assumed density profile, does not provide adequate predictions of the rms dynamics. Due to the unsatisfactory results from the envelope simulation, a new model, named Coupled Moment Equations (CME), is developed in this thesis.

The technique is presented in Sec. 3.1, when the governing equations are derived. The model uses the expansion of the phase-space distribution function over the asymmetrically weighted Hermite polynomial basis. The task of the numerical integration of the CME system is addressed in the next Section. Predictions of the CME system for the dynamics of rms properties, the evolution of 4^{th} order moments and the change in the beam density and

temperature are compared with the results of PIC simulations for various different initial conditions. The numerical model is discussed in the Sec.3.2. The non-conservation of the invariants of the dynamical system in the course of the simulation of a truncated CME model is studied in Sec. 3.3.1. Then a discussion of the numerical instability encountered in the course of the integration of CME and the method of its suppression based on the introduction of an artificial attenuation is presented. Sensible choices for normalization scales are also discussed. To illustrate the advantages of the use of the asymmetrically weighted Hermite polynomial basis, a brief description of the beam dynamics in a different Hermite polynomial representation which is now symmetrically weighted is presented in the last Section.

To overcome the difficulties encountered in the envelope models, the description of the dynamics is extended to include the evolution of higher order moments of the phase-space distribution function. We begin our derivation with the Vlasov equation for the distribution function $f(x, v_x, t)$ of the one-dimensional slab system:

$$\frac{\partial f}{\partial t} + v_x \frac{\partial f}{\partial x} - \frac{q_b v_z B_y}{m_b \gamma} \frac{\partial f}{\partial v_x} = 0, \tag{3.1}$$

where the self-magnetic field B_y is computed as

$$B_y(t) = q_b v_z \mu_0 \int_{-\infty}^{\infty} dv_x \int_0^x dx'\, f(x', v_x, t). \tag{3.2}$$

For convenience, the dimensionless variables

$$X = x/\sqrt{2}a, \qquad V = v_x/\sqrt{2}u, \qquad \tau = tu/a, \qquad g = 2\pi f a u/N \tag{3.3}$$

are introduced. Here, a and u are characteristic spatial and velocity dimensions respectively, and N is defined by Eq. (2.7). The possible choices of a and u that can be used in numerical simulations are discussed in the following Section. In dimensionless form, Eq. (3.1) becomes

$$\frac{\partial g}{\partial \tau} + V \frac{\partial g}{\partial X} + \kappa F \frac{\partial g}{\partial V} = 0, \tag{3.4}$$

with

$$\kappa = 2\sqrt{2} \frac{q_b v_z N a}{I_A} \frac{v_z^2}{u^2}. \tag{3.5}$$

The normalized force $F(X, \tau)$ is given by

$$F(X, \tau) = -\int_{-\infty}^{\infty} \int_0^X dV\, dX'\, g(X', V, \tau). \tag{3.6}$$

The normalization parameter κ is related to the mismatch coefficient α defined by Eq. (2.5). Explicitly, for a beam with an initial gaussian density (Eq. (3.5), it can be written as

$$\kappa = \alpha \sqrt{\frac{2}{\pi}} \frac{a}{\sigma_{xo}} \frac{\sigma_{vo}^2}{u^2}. \tag{3.7}$$

Thus, up to a numerical coefficient, κ is equal to the mismatch parameter α for a beam with the size a and the temperature u that are used to normalize the system (Eq. (3.3)).

The goal of this work is to model the evolution of the rms beam properties. The use of the simple envelope equation model has demonstrated that the coupling between different distribution moments is essential and needs to be accounted for to accurately describe the dynamics of the rms beam size. Models which accounted for this coupling were developed previously by Channell [43, 44] and more recently by Shadwick and Wurtele [45]. In their work, the dynamical equations were derived directly for different distribution moments. The application of the similar approach to our problem encounters some difficulties associated with the evaluation of the self-consistent force. Therefore, some alternative technique should be used. We choose an approach similar to that used in some Vlasov simulations (see for example Ref. [47]), which requires an expansion of the distribution function over a basis.

We begin by expanding the normalized distribution function g over a basis. Due to the localized nature of the phase-space distribution, which persists during the beam evolution, a localized basis is a good choice for the representation of the distribution function. In particular, an asymmetrically weighted Hermite polynomial basis for both spatial and velocity variables is used with the basis functions given by

$$\Psi_m^{(x)}(X) = C_m H_m(X) e^{-X^2}, \tag{3.8}$$

$$\Psi_n^{(v)}(V) = C_n H_n(V) e^{-V^2}, \tag{3.9}$$

and the normalization coefficient $C_m = (\pi^{1/4}\sqrt{2^m m!})^{-1}$. In this basis the distribution function g is represented as

$$g(X, V, \tau) = \sum_{k,l=0}^{\infty} a_{kl}(\tau) \frac{H_k(X) e^{-X^2}}{\pi^{1/4}\sqrt{2^k k!}} \frac{H_l(V) e^{-V^2}}{\pi^{1/4}\sqrt{2^l l!}}. \tag{3.10}$$

The set of coefficients $\{a_{kl}\}$ is the representation of g in the new basis. In principle, expansions over different complete sets of functions can be performed. The asymmetrically weighted Hermite polynomial basis is chosen because of the convenient relations between $\{a_{kl}\}$ and moments of the distribution function, as discussed below. The basis given by

Eqs. (3.8)-(3.9) was used previously in Ref. [47] to represent the velocity dependence in Vlasov simulations of Landau damping and bump-on-tail instability. The spatial dependence was expressed using Fourier eigenfunctions. Here, Hermite polynomial bases are used for both spatial and velocity dependence. Note in passing that the typical goal of an accurate Vlasov or PIC simulation is to describe the details of the evolution of the particle distribution, the primary aim of this work is to predict the dynamics of only the rms beam properties ignoring some finer aspects of the evolution. The values of the coefficients $\{a_{kl}\}$ can be computed by inverting the representation and using the orthogonality properties of the Hermite polynomials:

$$a_{kl} = \int_{-\infty}^{\infty}\int_{-\infty}^{\infty} dXdV g(X,V,\tau)\Psi_k(X)e^{X^2}\Psi_l(V)e^{V^2}. \tag{3.11}$$

This Hermite polynomial basis is an example of a non-orthogonal representation. This fact can be seen explicitly in Eq. (3.11), as a_{kl} are evaluated using a projection with a weight $e^{X^2}e^{V^2}$. The last relation can be written as

$$a_{kl} = \int_{-\infty}^{\infty}\int_{-\infty}^{\infty} dXdV g(X,V,\tau)\frac{H_k(X)}{\pi^{1/4}\sqrt{2^k k!}}\frac{H_l(V)}{\pi^{1/4}\sqrt{2^l l!}}. \tag{3.12}$$

Integration of g over the phase-space and the orthogonality condition for $H_k(Y)$ with a weight of e^{-Y^2} yield the normalization condition

$$\int\int dXdV\, g(X,V) = a_{00}\sqrt{\pi} = \int\int dxdv_x\, f(x,v_x)\frac{\pi}{N} = \pi. \tag{3.13}$$

Thus, the normalization of the distribution function is assured by a single constant coefficient $a_{00} = \sqrt{\pi}$ in the Hermite representation of g. This coefficient a_{00} remains unchanged in the course of the beam propagation, and we will treat it as a known constant. Thus, the expansion based on the asymmetrically weighted Hermite representation guarantees the conservation of the number of particles in the system.

The remaining coefficients $\{a_{kl}\}$ with $k+l > 0$ are related to the moments of the distribution function. Using the representation of the distribution function given by Eq. (3.10), the moment $\langle X^p V^q\rangle$, with some integer p and q, is computed to be

$$\langle X^p V^q\rangle = \sum_{k,l=0}^{\infty} a_{kl}M_{pk}M_{ql}, \tag{3.14}$$

where

$$M_{pk} = \int_{-\infty}^{\infty} dY\, \frac{H_k(Y)e^{-Y^2}}{\pi^{1/4}\sqrt{2^k k!}}Y^p, \tag{3.15}$$

and the notation $\langle\rangle$ is used for the average over the distribution g

$$\langle ... \rangle \equiv \frac{1}{\pi} \int \int dX dV \, ... g(X, V). \tag{3.16}$$

Computing the integral of Eq. (3.15) explicitly, we note an important property of the matrix M_{pk}: $M_{pk} \neq 0$ only for $p \leq k$. A useful feature of the linear mapping $\{\langle X^p V^q \rangle\} \rightarrow \{a_{kl}\}$ results. Consider a set of moments $\{\langle X^p V^q \rangle\}$ with $p + q \leq j_{max}$, where j_{max} is some positive integer. The set contains $(3j_{max} + j_{max}^2)/2$ elements. It is related to the set of $(3j_{max} + j_{max}^2)/2$ coefficients $\{a_{kl}\}$ with $k + l \leq j_{max}$, $k + l \neq 0$ and a known coefficient a_{00} by the linear mapping given by Eq. (3.14). For example, the moments $\langle X^2 \rangle$, $\langle XV \rangle$ and $\langle V^2 \rangle$ are expressed through a_{20}, a_{11}, a_{02}. This relation can be written explicitly as

$$\begin{aligned} \langle X^2 \rangle &= M_{00}(M_{20} a_{00} + M_{22} a_{20}), \\ \langle XV \rangle &= M_{11}^2 a_{11}, \\ \langle V^2 \rangle &= M_{00}(M_{02} a_{00} + M_{22} a_{02}). \end{aligned} \tag{3.17}$$

This simple linear relation between the rms beam properties and only three coefficients of expansion makes the asymmetrically weighted Hermite polynomial basis very convenient to study the bulk beam dynamics. It allows for the studies of the rms dynamics and the physics of collisionless relaxation using only a modest number of the expansion coefficients.

It is useful to divide the set of moments $\{\langle X^p V^q \rangle\}$, or the set of the expansion coefficients $\{a_{kl}\}$, into orders. We refer to all $\{\langle X^p V^q \rangle\}$ (or $\{a_{kl}\}$) with $p + q = j$ (or $k + l = j$) as being of order j. For example, a_{20}, a_{11}, a_{02} are coefficients of order 2; $\langle X^4 \rangle, \langle X^3 V \rangle, \langle X^2 V^2 \rangle, \langle XV^3 \rangle, \langle V^4 \rangle$ belong to order 4, and so on.

To calculate the expression for the normalized force $F(X)$ in terms of $\{a_{kl}\}$, the expansion given by Eq. (3.10) is substituted into Eq. (3.6). Using the definition of the error function

$$\mathrm{erf}(X) = \frac{2}{\sqrt{\pi}} \int_0^X dX' \, e^{-X'^2} \tag{3.18}$$

and the integral relation for the Hermite polynomials

$$\int_0^X dX' \, e^{-X'^2} H_k(X') = H_{k-1}(0) - e^{-X^2} H_{k-1}(X), \tag{3.19}$$

the expression for the normalized force becomes

$$F(X) = -\frac{\sqrt{\pi}}{2} a_{00} \mathrm{erf}(X) + \sum_{k=1}^{\infty} a_{k0} \frac{H_{k-1}(X)}{\sqrt{2^k k!}} e^{-X^2}. \tag{3.20}$$

The dynamical system describing the evolution of the coefficients a_{kl} can now be obtained directly by expressing the Vlasov equation in the Hermite basis representation. An alternative derivation that uses the evolution of the beam moments is presented in Appendix I. While the first approach results in the explicit system for the dynamics of $\{a_{kl}\}$, the second method is sometimes more convenient such as when an external force is applied.

To obtain the dynamical equations for the evolution of the expansion coefficients a_{kl}, the distribution function of Eq. (3.10) and the normalized force from Eq. (3.20) are substituted into the Vlasov equation given by Eq. (3.4). The resulting equation is projected onto the Hermite polynomial basis using the transform given by Eq. (3.11) leading to the coupled dynamical system

$$\begin{aligned}\dot{a}_{mn} &= \sqrt{m(n+1)}a_{m-1,n+1} + \sqrt{mn}a_{m-1,n-1} - \kappa a_{00}\sqrt{2n}\sum_{k=0}^{\infty} a_{k,n-1}W_{mk} \\ &+ \kappa\sqrt{2n}\sum_{k=0}^{\infty}\sum_{j=1}^{\infty} a_{k,n-1}a_{j0}\frac{\Gamma\left(\frac{m+j-k}{2}\right)\Gamma\left(\frac{k+j-m}{2}\right)\Gamma\left(\frac{k+m-j+2}{2}\right)}{2\pi^{3/2}\sqrt{k!m!j!}}, \quad (3.21)\end{aligned}$$

where

$$W_{mk} = \frac{\sqrt{\pi}}{2}\int_{-\infty}^{\infty} dX\, \frac{H_m(X)}{\pi^{1/4}\sqrt{2^m m!}}\frac{H_k(X)}{\pi^{1/4}\sqrt{2^k k!}}e^{-X^2}\mathrm{erf}(X), \quad (3.22)$$

and $\Gamma(x)$ stands for the gamma function and $\dot{a}_{mn} \equiv da_{mn}/d\tau$. In the remainder of the thesis we refer to Eqs. (3.21)-(3.22) as the Coupled Moment Equation (CME) model. The infinite system defined by Eqs. (3.21) is exact. No approximation is made in the course of the derivation.

If a different or additional force is applied to the system, the explicit form for the force terms in the equation for $\dot{a}_{mn}$ needs to be re-evaluated. The details of couplings between different a_{mn} may then also change. For example, the formalism can be immediately used for the studies of the high brightness beam transport in a focusing channel with an externally applied linear (or nonlinear) force. The space-charge force has essentially the same functional form as in Eq. (2.2), and additional terms corresponding to the external force can be easily included in the model. The model can then be used to investigate the physics of the emittance growth in a linear focusing channel, which has been the topic of extensive studies in the last decade [38].

3.2 Numerical Integration of the Coupled Moment Equations

3.2.1 Numerical Examples

We now turn to numerical tests of the CME system derived in Sec. 3.1. The infinite series representation of the distribution function, as given by Eq. (3.10), is truncated so that a finite number of expansion coefficients is used to represent g. The truncation is performed by taking all coefficients a_{kl} with $k+l > j_{max}$ equal to zero. We refer to the value of j_{max} as the 'truncation order'.

To simplify the dynamics, symmetric systems with $f(x, v_x) = f(-x, -v_x)$ are considered. The density becomes an even function of the space variable, *i.e.* $n_b(x) = n_b(-x)$, and the motion of the center-of-charge is eliminated. The initial conditions given by Eqs. (2.3) and (2.4) are particular examples of such systems. In this case, expansion coefficients a_{kl} are non-zero only for even orders, *i.e.* when $k+l = 2, 4, ...$ This fact is used directly in the numerical computation, and only dynamics of non-zero a_{kl} is computed. It is important to emphasize that the model can be used with more general initial conditions, and it is well suited to study the center-of-charge motion.

The system given by Eq. (3.21) can be integrated numerically under different normalization parameters, *i.e.* a and u from Eq. (3.3). The choice of the normalization is made based on (1) a sensible representation of the distribution function during its evolution using a finite number of the expansion coefficients and (2) on the properties of the truncated CME system. Our experience has shown that the analytical estimates of the asymptotic rms properties (see Sec. 2.3) are a good choice for a and u. They are used in most of dynamical simulations presented in this thesis. More details on the choice of the normalization parameters can be found in Sec. 3.3.3.

We illustrate the numerical integration by simulating the familiar example already considered in Sec. 2.1 with the initial gaussian distribution given by Eq. (2.3) and a mismatch parameter of $\alpha = 5$. The system is normalized by the analytically calculated asymptotic final state. Using estimates given by Eqs. (2.38) and (2.33), the normalization parameters are taken as $a = 2.3$ mm and $u/c = 1.1 \times 10^{-2}$. The initial condition for the distribution function is taken as in Eq. (2.3), and the values of $a_{kl}(\tau = 0)$ coefficients at are computed by expanding the initial distribution over the basis using Eq. (3.11).

The sensitivity of the numerical integration to the truncation order and the number of orders sufficient to describe the rms dynamics accurately are now investigated. First, the dynamical system $\{a_{kl}\}$ is truncated at the lowest order $j_{max} = 2$ and only 3 coefficients, a_{20}, a_{11} and a_{02}, are retained in the simulation. Results for the betatron oscillations of the rms beam size are plotted in Fig. 3.1 as a solid line. Results of the numerical integration are similar to the predictions of the envelope equation. It can be readily seen that no relaxation of the oscillations takes place. Truncation of the system at the next order, $j_{max} = 4$, with

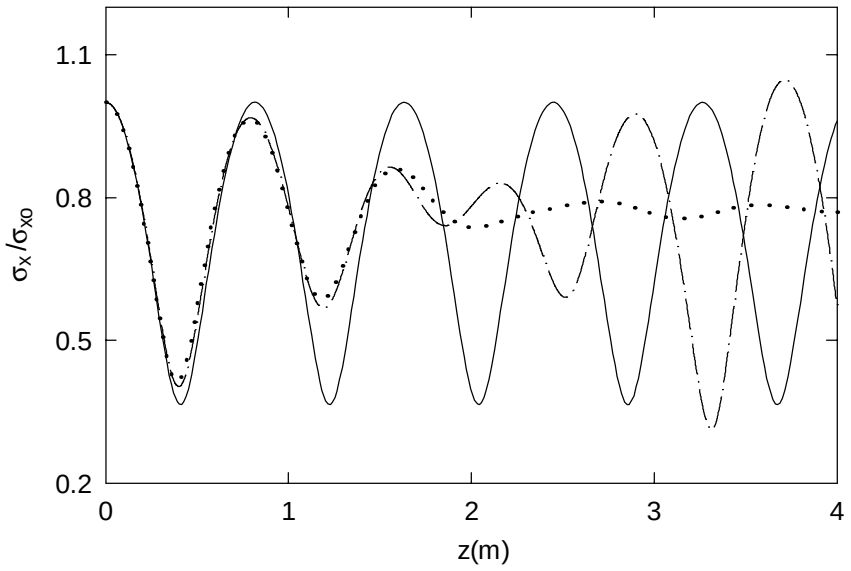

Figure 3.1: Comparison of results for the evolution of the rms beam size obtained by a PIC simulation ($\cdot\ \cdot\ \cdot$) and by a CME integration with different truncation orders $j_{max} = 2$ (——) and $j_{max} = 4$ (– · –).

8 coefficients used in the simulation, yields the dashed-dotted line plotted in Fig. 3.1. The resulting rms width of the beam shows some modulation in the amplitude of its betatron oscillations. Figure 3.1 clearly indicates that higher orders are needed to fully describe the dynamics of the relaxation.

We now truncate the system at the much higher order of $j_{max} = 20$. The direct numerical integration of the truncated system shows an unlimited growth of $\{a_{kl}\}$ coefficients in the course of the beam propagation. The prediction for the change in the rms beam size is plotted in Fig. 3.2 for the CME model (solid curve), and the result of the PIC

simulation is also plotted as a reference curve with a dotted line. As it is explained in detail

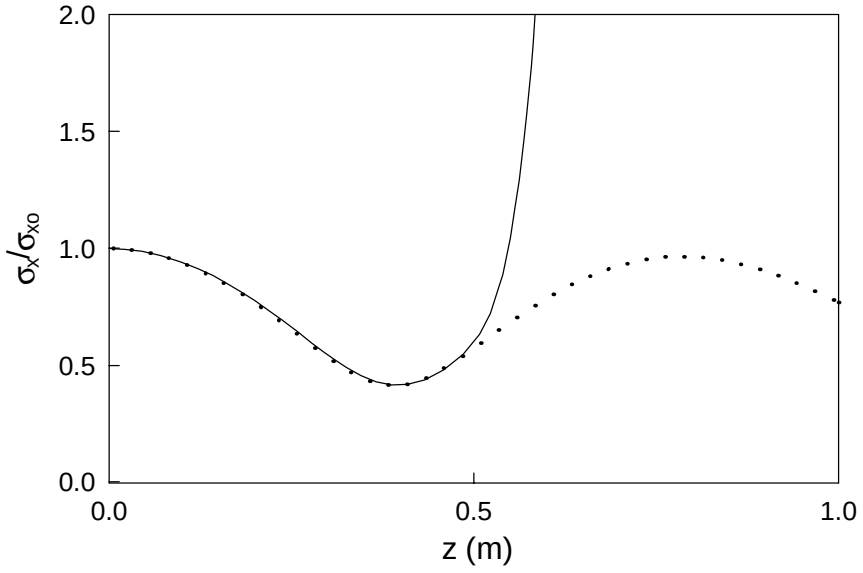

Figure 3.2: The unphysical growth of the amplitude of the rms oscillations obtained in the course of CME integration with $j_{max} = 20$ (——) together with the PIC simulation prediction ($\cdot\ \cdot\ \cdot$).

in the next section, the truncation of the infinite system results in the appearance of real eigenvalues in the spectrum of the linearized problem which correspond to the unphysical, exponentially growing solutions. The numerical problems associated with the long-term behavior are typical in Vlasov solvers which utilize the truncated expansions of the distribution function. A commonly used solution is the introduction of the artificial attenuation term of a Fokker-Planck type [46, 71]. We use a similar approach to suppress the unphysical growth and introduce an artificial attenuation term in our dynamical system. In contrast with the approach of Ref. [46, 71], a diagonal relaxation term $-\Gamma_{kl} a_{kl} \delta^{kl}_{mn}$, is introduced on the right-hand side of Eq. (3.21) with the phenomenological damping coefficient

$$\Gamma_{kl} = e^{(k+l-2)^2/\Delta^2} - 1. \tag{3.23}$$

The parameter Δ adjusts the relative strength of the attenuation of each mode. The specific form of the attenuation coefficient introduced in Eq. (3.23) has been dictated by the desire to predict the evolution of rms beam properties; these are expressed through only low order

coefficients a_{kl}. It can be easily seen that the damping is weak for low order coefficients and strong for a_{kl} with large values of $k+l$. The action of the damping term smoothes the otherwise abrupt transition to $a_{kl} = 0$ at $k + l > j_{max}$. Note that no relaxation is introduced for the lowest order coefficients, a_{20}, a_{11} and a_{02}, which correspond to the bulk beam properties σ_x, σ_v and $\langle xv_x \rangle$. Unfortunately, closed form relation was not found for the attenuation operator in the 'real' x, v_x variables.

Returning to the example of the initially gaussian distribution with $\alpha = 5$, the result of the numerical integration are compared with the PIC simulation in Fig. 3.3 for the rms beam properties. The calculation is performed with the relaxation width $\Delta = 10$ and $j_{max} = 20$. Discussion of the dependence of the results on the attenuation width and the guidelines for a sensible choice of Δ is postponed until the next section. The very good agreement between PIC results (dotted line) and predictions of the CME model (solid line) is evident, and a clear relaxation in the beam size oscillations and velocity spread is observed. The emittance growth is also predicted correctly by the CME simulation.

To compare the efficiency of PIC and CME computations for the rms beam properties, we compare the predictions for the asymptotic values obtained keeping a different number of particles in the PIC simulation and orders in the CME simulation for the same numerical example of the initial beam with $\alpha = 5$. The PIC simulation is performed with the total number of particles ranging between $200 \leq N_p \leq 50000$. The dynamical PIC results for beam size and temperature (see for example Fig. 2.2) show the decay of the initial oscillations to some small residual oscillations about the asymptotic value. The amplitude of the residual oscillations depends on the number of particles used in the simulation decreasing as N_p is increased. Therefore, we can determine the final value of the rms beam properties only to a limited precision as a mean value of σ_x with the error determined by the size of the oscillations. This error can be characterized by a standard deviation of the beam size from its average computed over many oscillations periods. The results for the beam size and temperature ($\bullet$) with the error for different values of N_p are plotted in Fig. 3.4. The figure shows that to ensure the value of the final rms properties within one percent accuracy at least 10000 should be kept in the simulation. The betatron oscillations observed in CME simulation decay to a stationary value. CME results for rms values ($\triangle$) are also plotted on the same graph for different number of orders remained in the simulation. The final beam size and temperature are presented as functions of the number of equations used in the computation. It can be seen that as few as 12 orders can used in the simulation (48

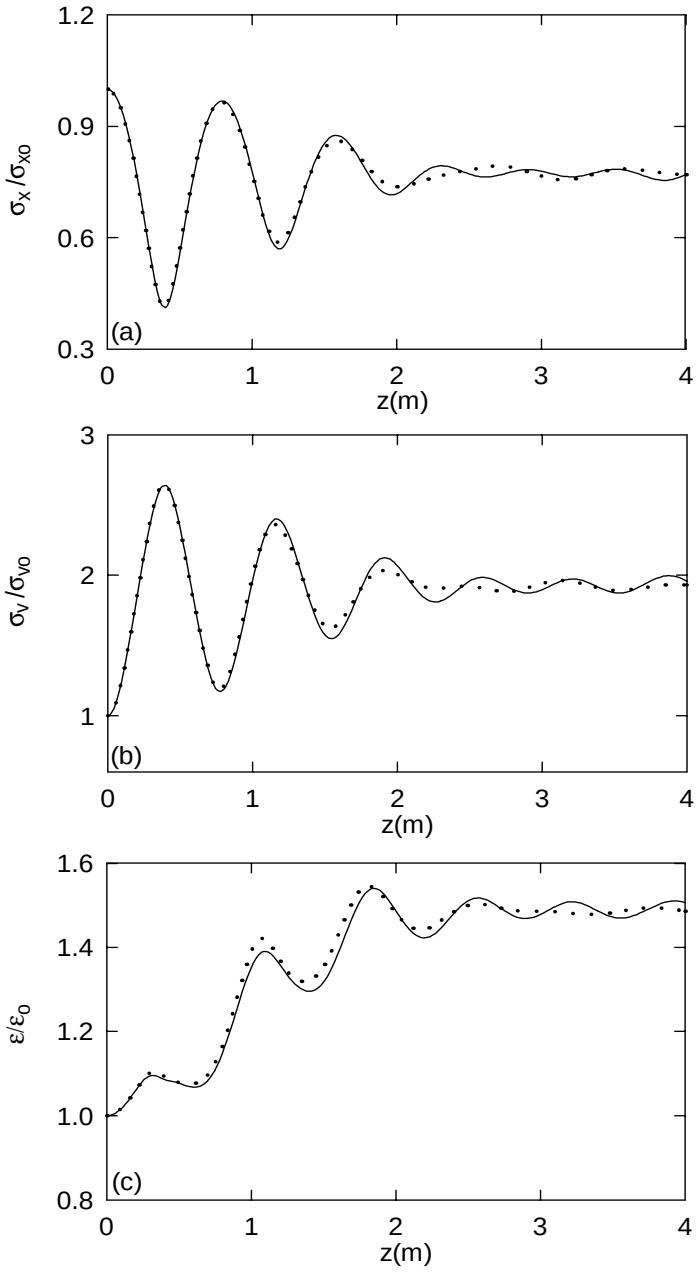

Figure 3.3: Comparisons of propagation curves for (a) rms beam size, (b) rms velocity and (c) the emittance obtained using the CME model (——) with $j_{max} = 20$, $\Delta = 10$ and a PIC simulation ($\cdot\ \cdot\ \cdot$) for the initially gaussian beam with a mismatch of $\alpha = 5$.

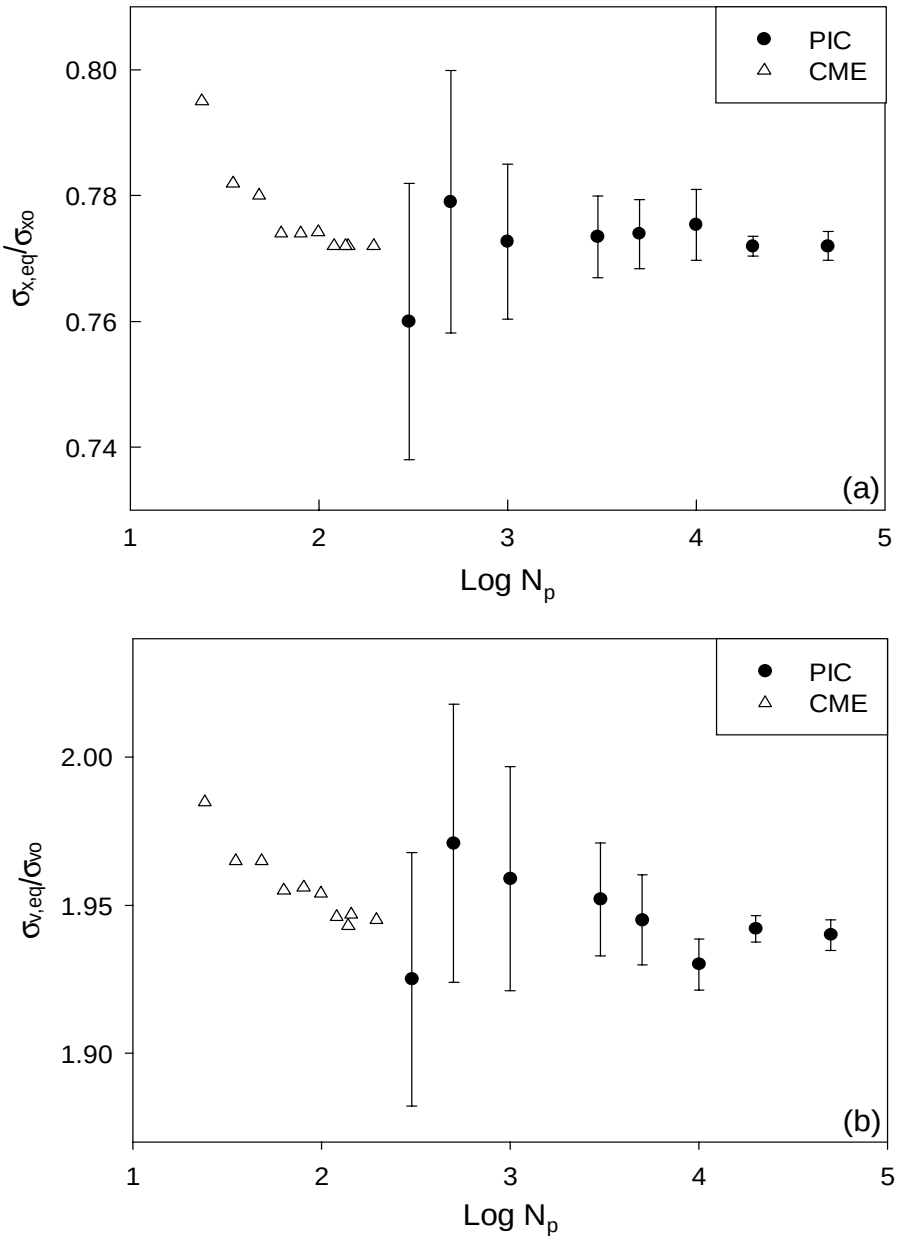

Figure 3.4: Comparisons of predictions for the asymptotic (a) rms beam size, (b) rms velocity obtained using PIC (•) and CME (△) simulations with different number of particles and equations used in the computation. An example of an initially gaussian beam with $\alpha = 5$ is used.

equations) to result in the final rms predictions within one percent from the exact value.

We now use the CME simulation to predict the dynamics of higher order beam moments. The time evolution of $\langle x^4 \rangle$, $\langle v_x^4 \rangle$ and $\langle x^2 v_x^2 \rangle$ is presented in Fig. 3.5 for the same numerical example of a gaussian distribution with $\alpha = 5$. The higher order moments of the distribution function provide valuable information on the properties of the density profile, velocity distribution and correlations in phase-space. For example, the ratio $\langle x^4 \rangle / \sigma_x^4$ indicates the relative distribution of particles in the central (core) region and the tail of the density profile. For a beam with a gaussian density $\langle x^4 \rangle / \sigma_x^4 = 3$. Values of this ratio larger than three indicate the presence of a relatively larger number of particles in the tail of the density distribution compared to a gaussian profile. As seen in Fig. 3.5, the beam density becomes significantly non-gaussian during the time evolution. For our numerical example, $\langle x^4 \rangle / \sigma_x^4 \simeq 4.5$ in the asymptotic state. Another valuable ratio of beam moments is the relative correlation $\langle x^2 v_x^2 \rangle / (\sigma_x^2 \sigma_v^2)$. Its value is a good indicator of the degree of space-velocity correlation in the phase-space distribution. The initial condition given by Eq. (2.3) corresponds to a decorrelated distribution, so that $\langle x^2 v_x^2 \rangle / (\sigma_x^2 \sigma_v^2) = 1$. Not surprisingly, the distribution becomes correlated in the process of the beam transport, and the value of the ratio significantly differs from unity. In our example with $\alpha = 5$, the value of the correlation ratio $\langle x^2 v_x^2 \rangle / (\sigma_x^2 \sigma_v^2) \simeq 1.18$ in the asymptotic state, which indicates the non-thermal character of the asymptotic distribution. Good agreement between PIC and CME results for the 4^{th} order moments is observed.

The CME model provides more information than just the dynamics of the bulk beam properties. We have already discussed the CME predictions for the forth order moments such as $\langle x^4 \rangle$, $\langle v_x^4 \rangle$ and $\langle x^2 v_x^2 \rangle$. The fluid quantities, such as the beam density and temperature, can also be reconstructed. For example, integrating the expansion given by Eq. (3.10) over velocities, the beam density can be computed as

$$n_b(X) = \frac{N}{\sqrt{2}\pi a} \sum_{k=0}^{j_{max}} a_{k0} e^{-X^2} \frac{H_k(X)}{\sqrt{2^k k!}}. \tag{3.24}$$

Defining the local temperature as

$$T_b = \frac{1}{n_b(x)} \int_{-\infty}^{\infty} f(x, v_x) v_x^2 dv_x \tag{3.25}$$

and using the expansion given by Eq. (3.10), $T_b(x)$ can be calculated as

$$T_b(X) = \frac{\sqrt{2}u^2}{\pi a} \frac{1}{n_b(X)} \sum_{k=0}^{j_{max}} (a_{k0} M_{20} + a_{k2} M_{22}) e^{-X^2} \frac{H_k(X)}{\sqrt{2^k k!}}. \tag{3.26}$$

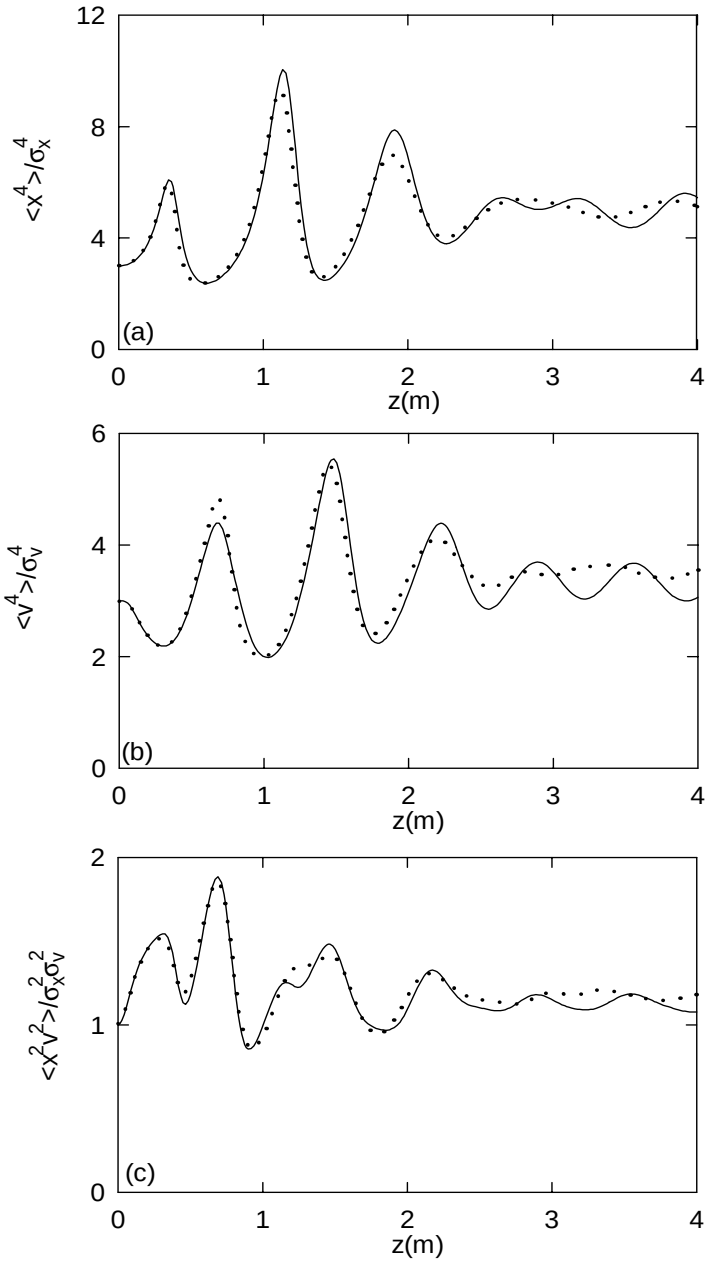

Figure 3.5: Comparisons of propagation curves for normalized 4^{th} order (a) spatial, (b) velocity and (c) correlation moments obtained using the CME model (—) with $j_{max} = 20$, $\Delta = 10$ and a PIC simulation ($\cdot \ \cdot \ \cdot$) for the initially gaussian beam with a mismatch of $\alpha = 5$

In the last equation, the definition of the coefficients M_{pk} given by Eq. (3.15) is used. Consider again the numerical example with the initial mismatch of $\alpha = 5$. Comparisons of CME and PIC predictions for the density profiles at different locations along the propagation at $z = 0$, 1.5m, 3m, 4.5m are plotted in Fig. 3.6. The local temperature profiles are compared in Fig. 3.7. The CME results are plotted as solid lines, and PIC results are presented as dotted lines. It is seen that CME profiles show very similar qualitative features as predicted by the PIC simulation: they exhibit the formation of the central core and extended tails in the beam density in the process of the propagation. The rise of the core temperature and the loss of the constancy of T_b as a function of position are also observed. Some discrepancies in CME and PIC results are also seen. Some differences can be attributed to the insufficient number of expansion coefficients kept in the CME simulation and the introduction of the artificial attenuation. Thus, we can conclude that the CME model provides general features of the evolution of beam fluid quantities, but can not be used solely for accurate predictions of the beam density (at least with the use of only few expansion coefficients).

We now apply the CME technique to a beam with $\alpha = 0.33$ and an initial distribution still given by Eq. (2.3). Explicitely, the initial parameters are given by $\sigma_{xo} = 1.38$mm, $\sigma_{vo} = 4.3 \times 10^6$ and $n_0 = 1.45 \times 10^{17}\mathrm{m}^{-3}$ while as before $\gamma = 100$. In contrast with the $\alpha = 5$ example considered above, this case corresponds to a beam with the beam pressure exceeding the magnetic focusing force at the plasma entrance. Numerical results for the rms beam properties obtained using CME equations and a PIC code are presented in Fig. 3.8 with a solid and dotted line respectively. Comparisons for the dynamics of 4^{th} order moments are presented in Fig. 3.9. Density profiles are compared in Fig. 3.10 and local temperature results are plotted in Fig. 3.11. The CME simulation is integrated with $\Delta = 8$ and $j_{max} = 20$. The estimates of the asymptotic values given by Eqs. (2.38) and (2.33) are used as normalization parameters a and u.

We now turn to the dynamical predictions for the moments of the beam with the initially uniform distribution given by Eq. (2.4) and $\alpha = 5$. Explicitely, the initial parameters are given by $\sigma_{xo} = 3.41$mm, $\sigma_{vo} = 1.8 \times 10^6$, $\gamma = 100$ and $n_0 = 4.23 \times 10^{16}\mathrm{m}^{-3}$. The equations are normalized using the estimates of the rms asymptotic values given by Eqs. (2.39) and (2.33). The initial values of a_{kl} coefficients are computed for this new initial condition and used in the CME simulation. The CME and PIC predictions for the dynamics of the rms beam properties are presented in Fig. 3.12. Twenty orders of the coefficients are retained in the simulation, and the relaxation width is chosen to be equal

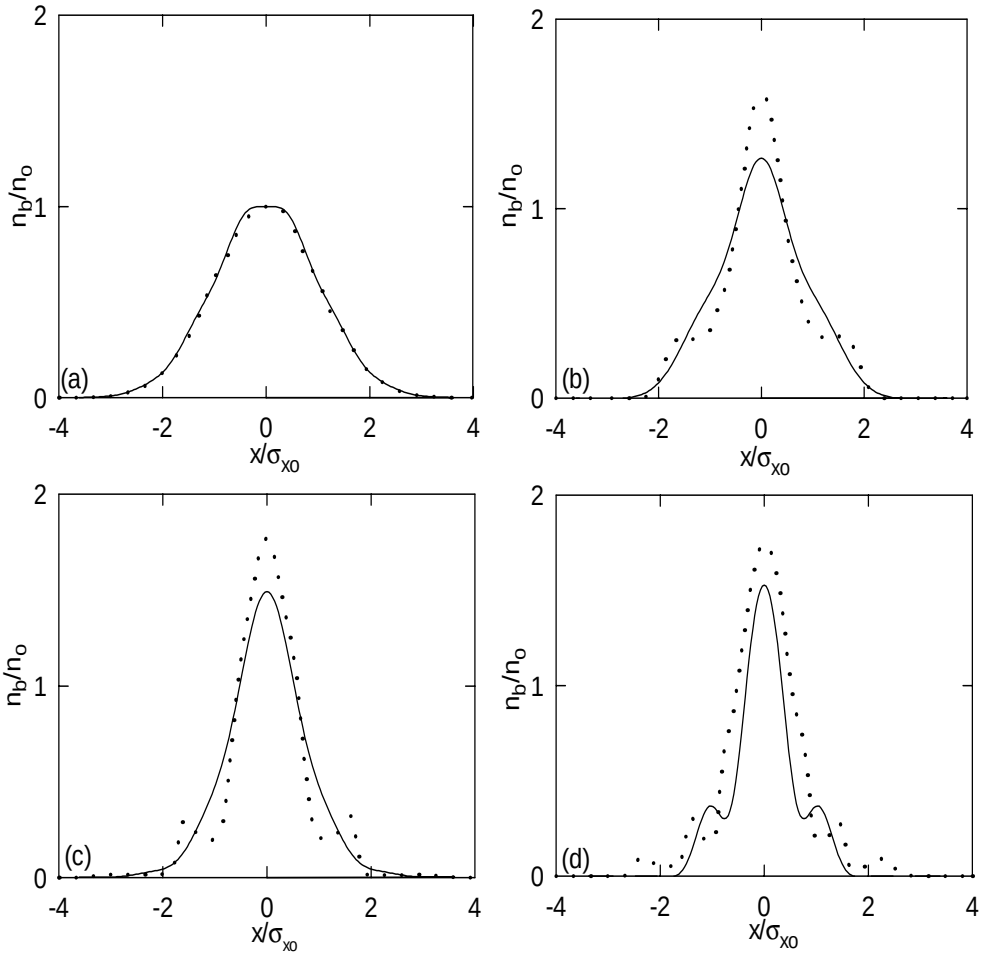

Figure 3.6: Density profiles at (a) $z = 0$, (b) $z = 1.5$m, (c) $z = 3$m and (d) $z = 4.5$m obtained by the CME integration (——) and PIC simulation ($\cdot\ \cdot\ \cdot$) for the initial gaussian beam with a mismatch of $\alpha = 5$.

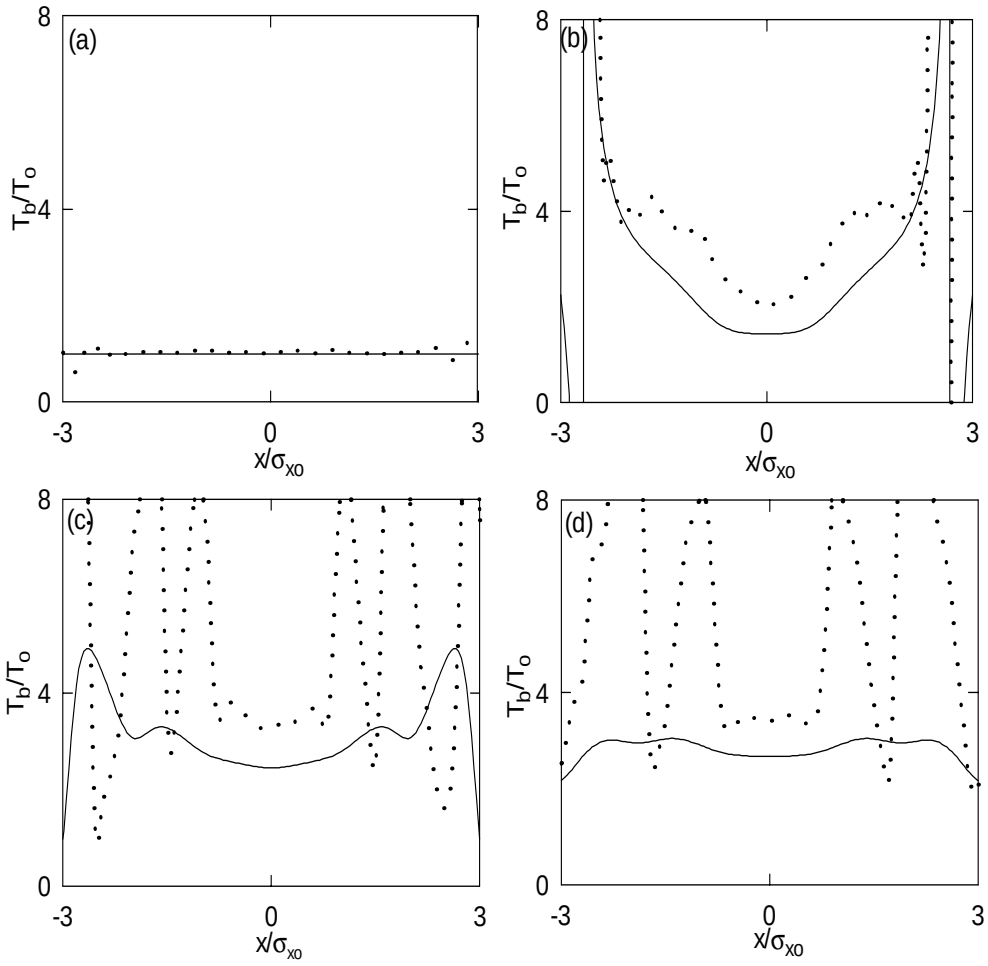

Figure 3.7: Temperature profiles at (a) $z = 0$, (b) $z = 1.5$m, (c) $z = 3$m and (d) $z = 4.5$m obtained by the CME integration (——) and PIC simulation ($\cdot\ \cdot\ \cdot$) for the initial gaussian beam with a mismatch of $\alpha = 5$.

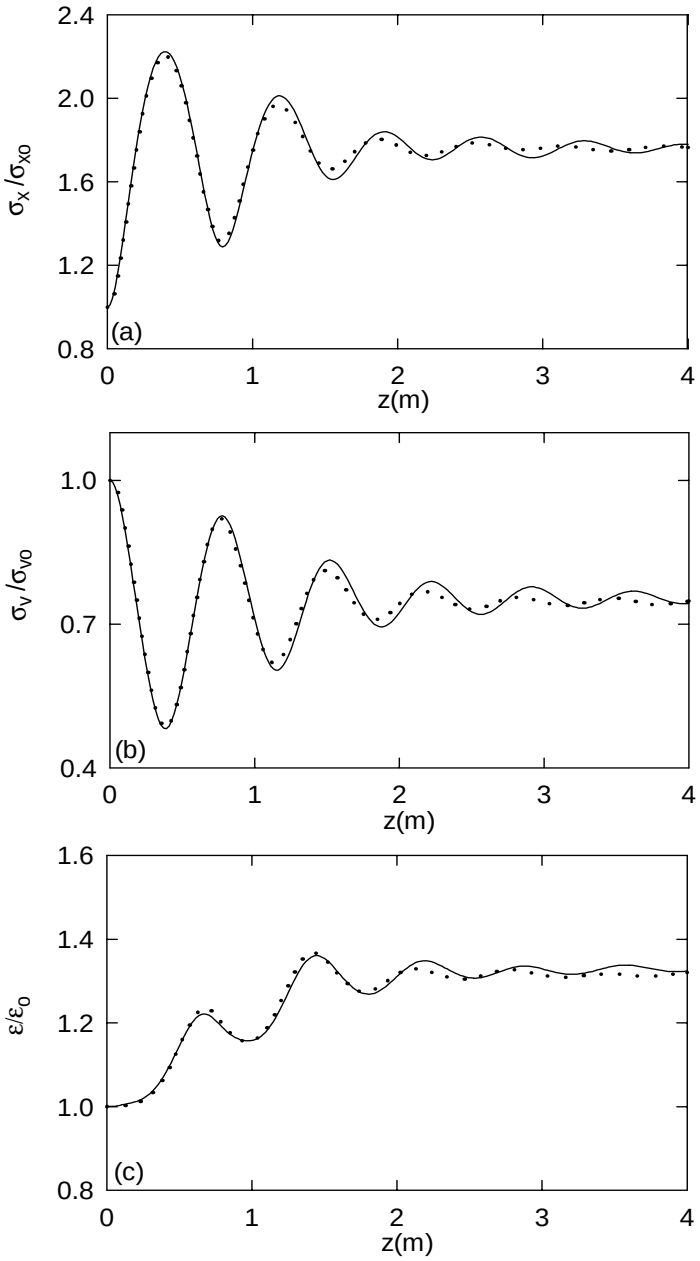

Figure 3.8: Comparisons of propagation curves for (a) rms beam size, (b) rms velocity and (c) the emittance obtained using the CME model (——) with $j_{max} = 20$, $\Delta = 8$ and a PIC simulation ($\cdot\ \cdot\ \cdot$) for the initially gaussian beam with a mismatch of $\alpha = 0.33$.

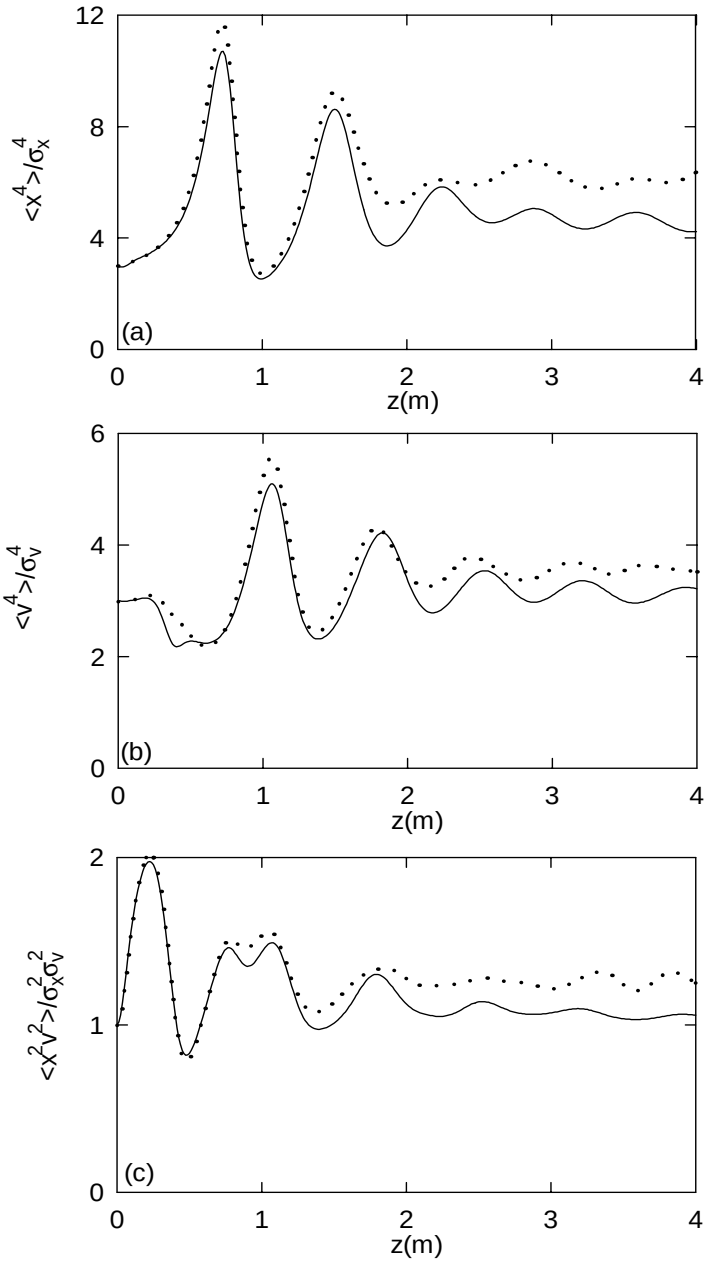

Figure 3.9: Comparisons of propagation curves for normalized 4^{th} order (a) spatial, (b) velocity and (c) correlation moments obtained using the CME model (——) with $j_{max} = 20$, $\Delta = 8$ and a PIC simulation ($\cdot \ \cdot \ \cdot$) for the initially gaussian beam with a mismatch of $\alpha = 0.33$

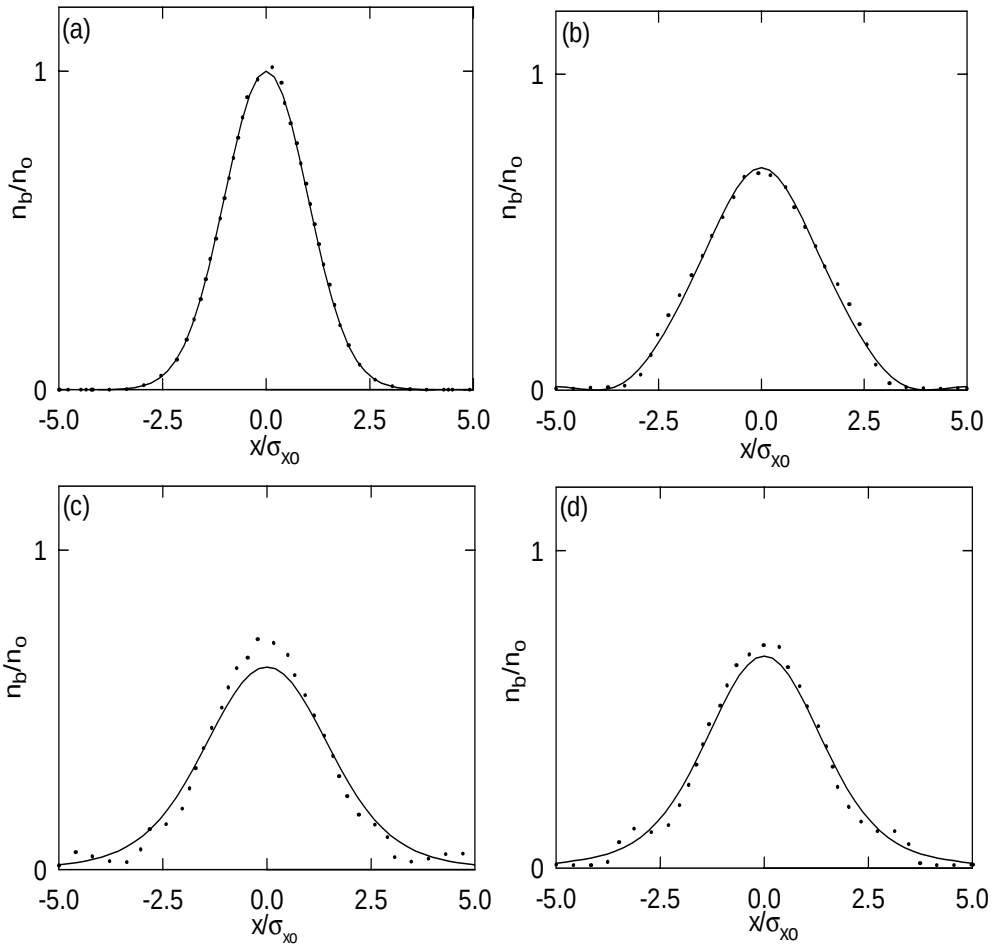

Figure 3.10: Density profiles at (a) $z = 0$, (b) $z = 1.5$m, (c) $z = 3$m and (d) $z = 4.5$m obtained by the CME integration (——) and PIC simulation ($\cdot\ \cdot\ \cdot$) for the initial gaussian beam with a mismatch of $\alpha = 0.33$.

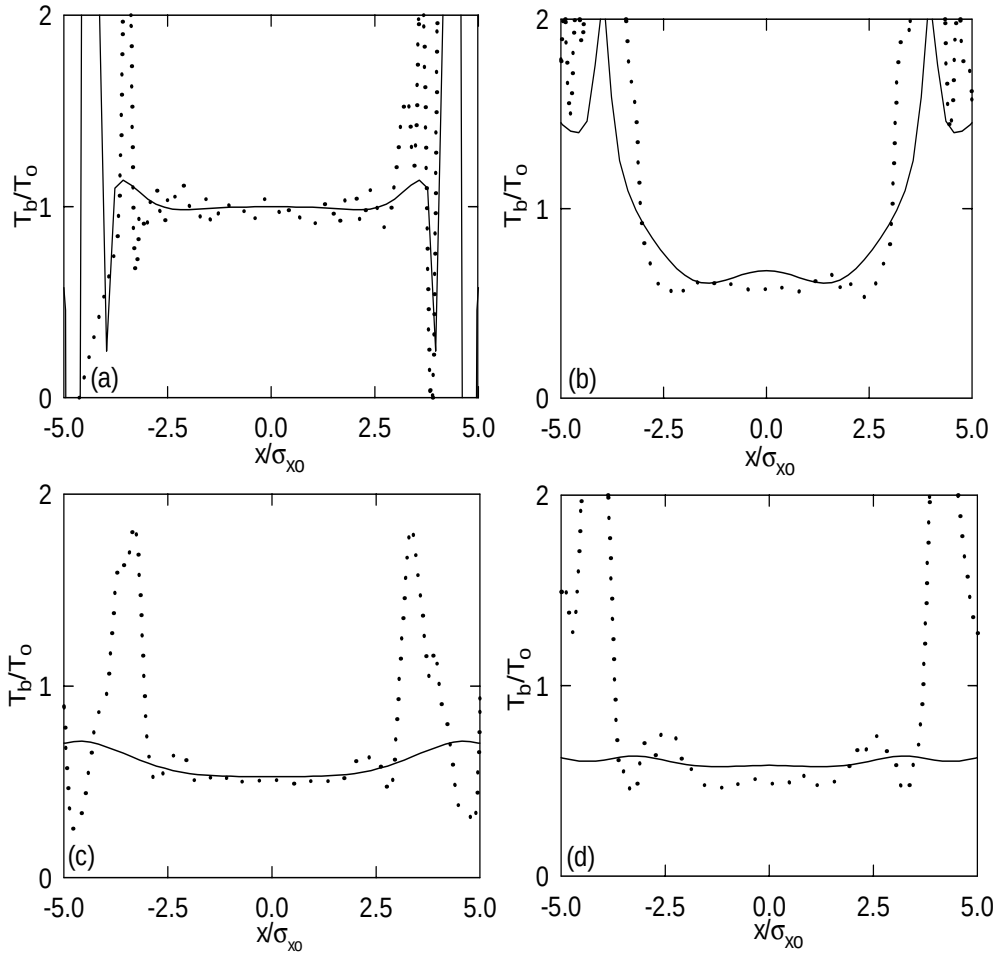

Figure 3.11: Temperature profiles at (a) $z = 0$, (b) $z = 1.5$m, (c) $z = 3$m and (d) $z = 4.5$m obtained by the CME integration (——) and PIC simulation ($\cdot\ \cdot\ \cdot$) for the initial gaussian beam with a mismatch of $\alpha = 0.33$.

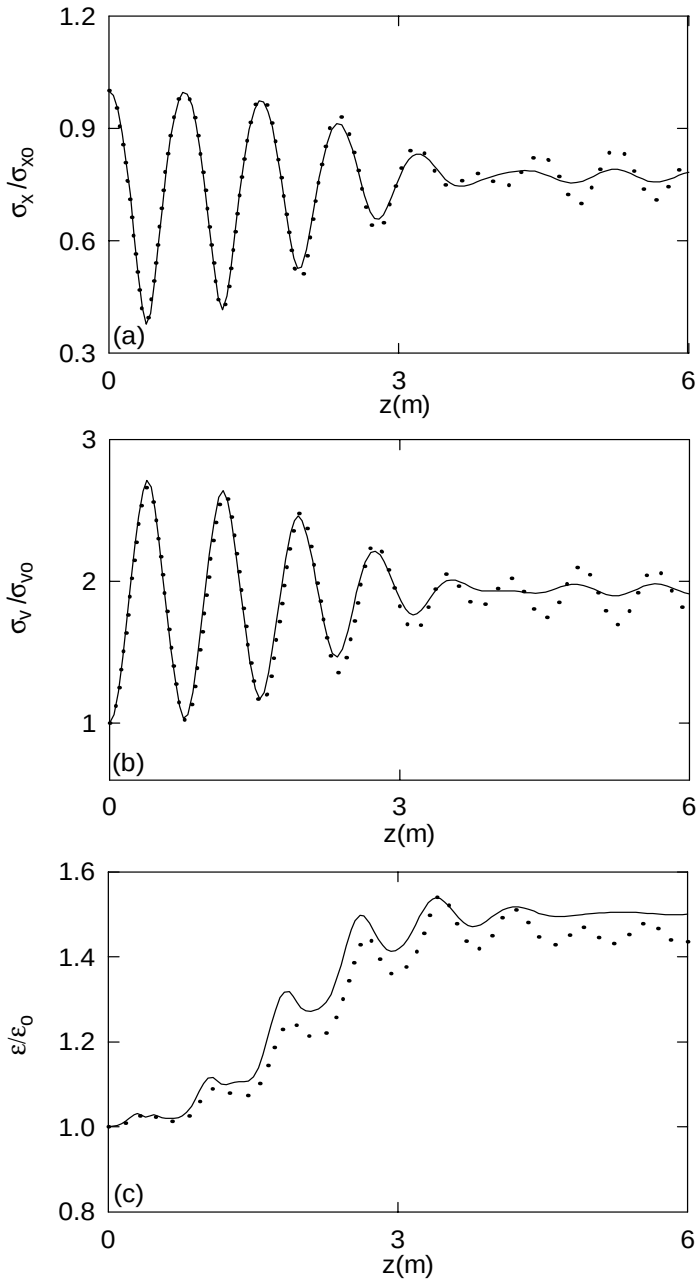

Figure 3.12: Comparisons of propagation curves for (a) rms beam size, (b) rms velocity and (c) the emittance obtained using the CME model (——) with $j_{max} = 20$, $\Delta = 10$ and a PIC simulation ($\cdot\ \cdot\ \cdot$) for the initially uniform beam with a mismatch of $\alpha = 5$.

to $\Delta = 10$. Good agreement between PIC results (dotted line) and predictions of the CME model (solid line) can be seen. The comparisons for the 4^{th} order moments is presented in Fig.3.13. Good agreement between CME and PIC results is again observed. We conclude that the numerical CME model provides us with good dynamical predictions for low order beam moments of the distributions which initial conditions differ from gaussians.

To further assess the performance of the CME model, we compare predictions for the asymptotic rms properties obtained by the time integration of the CME equations with the PIC simulation for a wide range of the initial mismatch of $0.2 < \alpha < 10$. The dynamical CME predictions ($\diamond$), theoretical estimates ($\bullet$) (given by Eqs. (2.33), (2.38) and (2.40)) and PIC results ($\triangle$) for an initially gaussian distribution are plotted in Fig. 3.14. The dynamical CME results are obtained by the numerical integration until stationary values of σ_x and σ_v are achieved. It can be seen that the dynamical CME results offer an improvement in the accuracy compared to the analytical estimates of Sec. 2.3. The numerical and analytical predictions for the asymptotic rms values of an initially uniform beam are presented in Fig. 3.15. Good CME predictions for the final values of the 2^{th} order moments are obtained. We conclude that a CME simulation can be used to obtain accurate predictions of the rms properties in the asymptotic state.

The values of the space-velocity correlation ratio $\langle x^2 v_x^2 \rangle / (\sigma_x^2 \sigma_v^2)$ in the asymptotic state are also computed over the same initial mismatch range of $0.2 < \alpha < 10$ for both initial distributions. The CME simulation results for the initially gaussian beam are plotted together with PIC predictions in Fig. 3.16. CME and PIC results agree well for all cases considered. The CME predictions for the asymptotic value of the correlation ratio for the initially uniform beam are compared with the PIC results in Fig. 3.17. The final values of the space-velocity correlation ratio becomes useful in the investigation of the properties of the final coarse-grained distribution. In particular, it can serves as a measure of the degree of thermalization of the distribution function in the course of the relaxation process. Note that the ratio takes on values both larger and smaller than unity in the range of the mismatch considered and for the initial distribution investigated. Also, for highly mismatched beams the final values of $\langle x^2 v_x^2 \rangle / (\sigma_x^2 \sigma_v^2)$ are significantly different from unity. Interestingly, the overall behavior of the correlation ratio as a function of the initial beam mismatch is very similar for both initial distributions. It has its minimum value which is smaller than one for the initially matched beam ($\alpha = 1$) and increases in value for both $\alpha > 1$ and $\alpha < 1$.

Comparisons of the propagation curves for the rms properties obtained using the

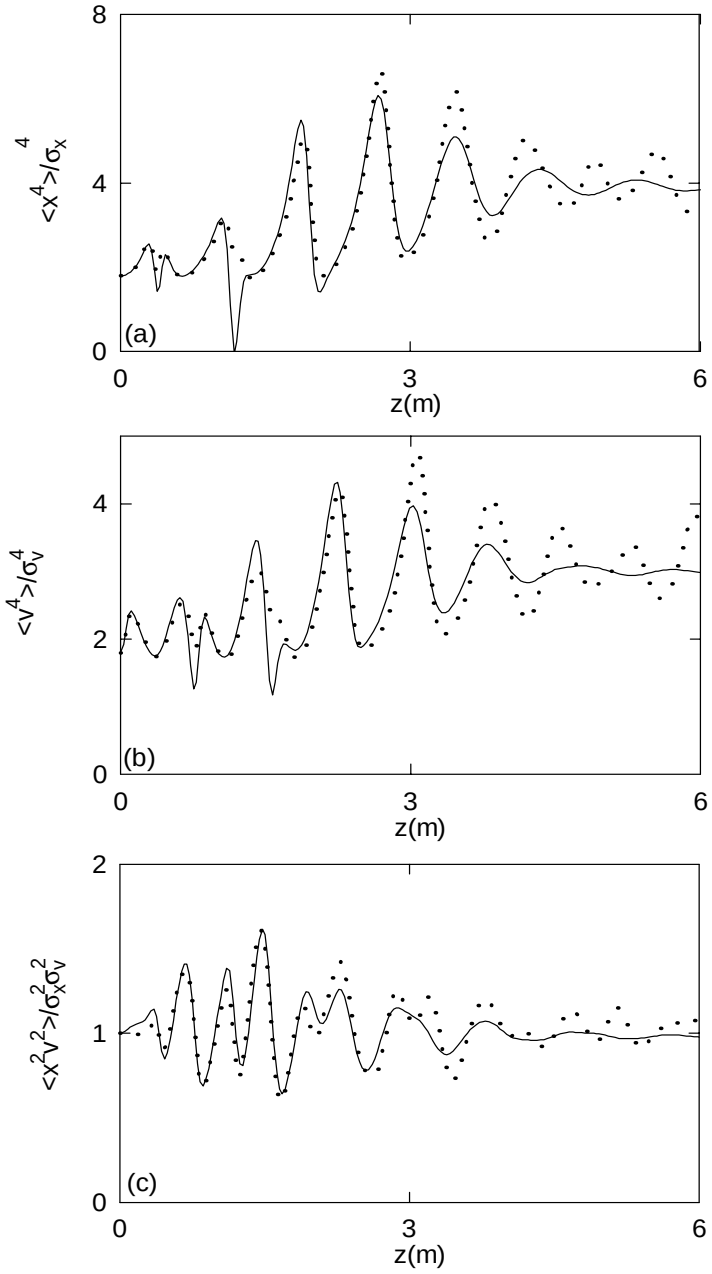

Figure 3.13: Comparison of propagation curves for normalized 4^{th} order (a) spatial, (b) velocity and (c) correlation moments obtained using the CME model (—) with $j_{max} = 20$, $\Delta = 10$ and a PIC simulation ($\cdot \ \cdot \ \cdot$) for the initially uniform beam with a mismatch of $\alpha = 5$

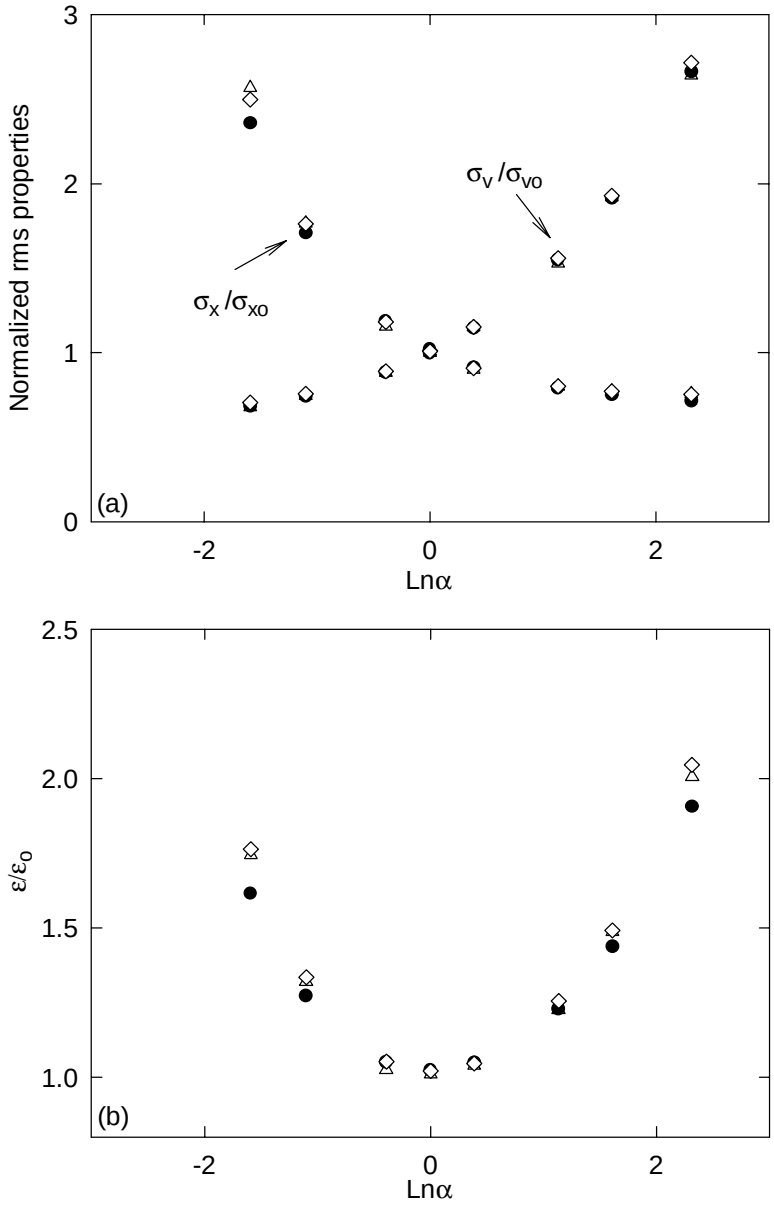

Figure 3.14: Comparison of the dynamical CME results (◇), analytical predictions (•) given by Eqs. (2.33), (2.38) and (2.40) and PIC results (△) for (a) rms beam properties and (b) the emittance of the initially gaussian beam *vs* the initial mismatch α.

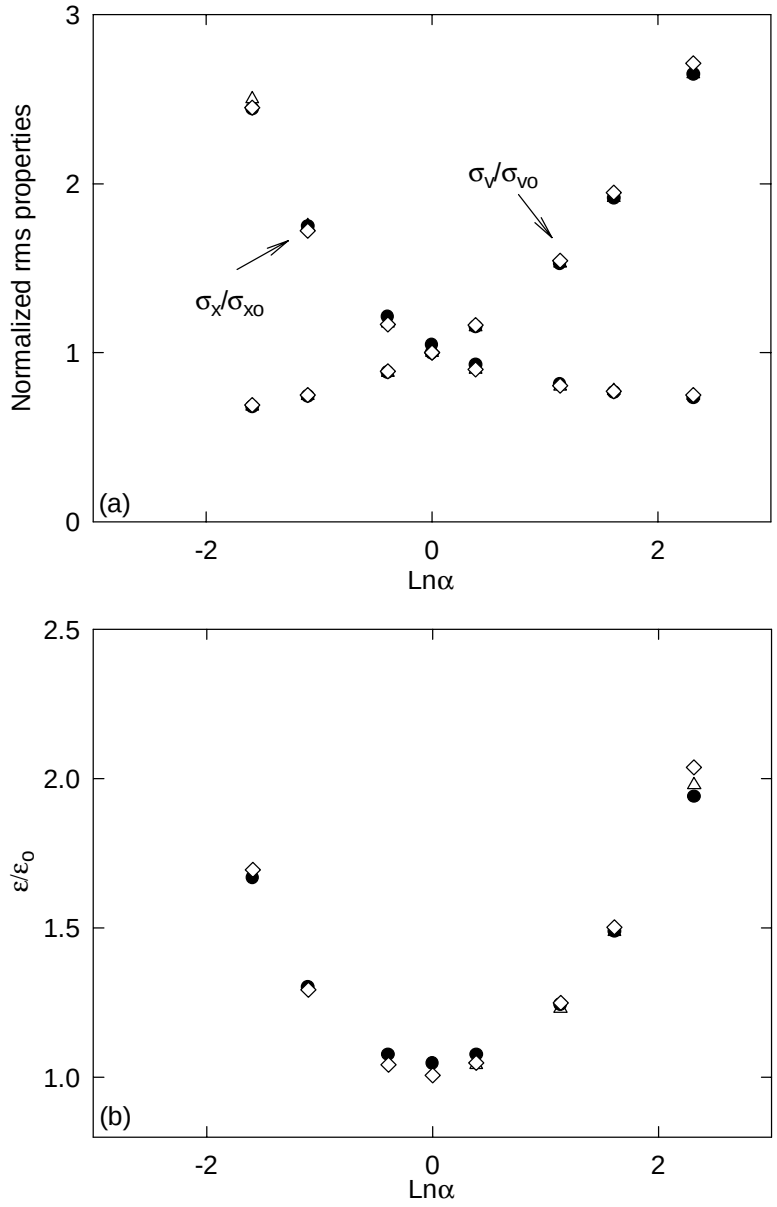

Figure 3.15: Comparison of the dynamical CME results ($\diamond$), analytical predictions ($\bullet$) given by Eqs. (2.33), (2.39) and (2.41) and PIC results ($\triangle$) for (a) rms beam properties and (b) the emittance of the initially uniform beam *vs* the initial mismatch α.

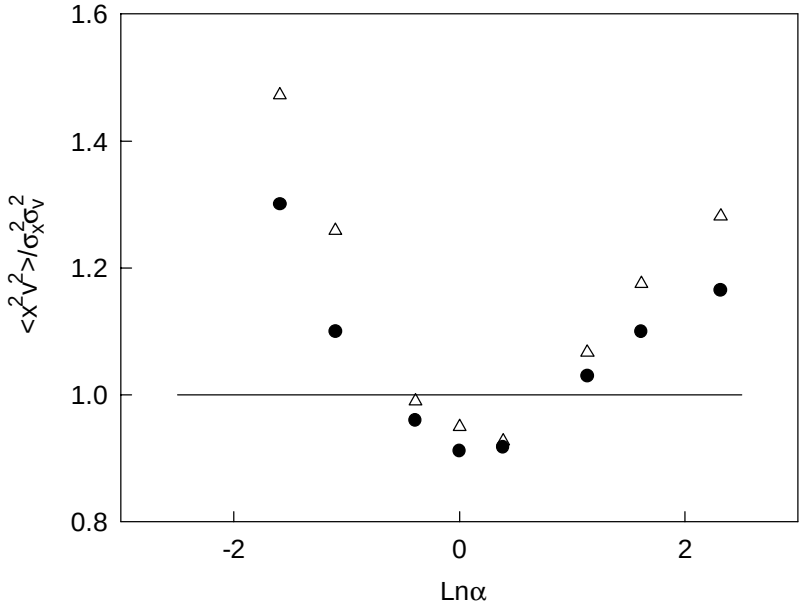

Figure 3.16: Comparison of the dynamical CME results (•) and PIC predictions (△) for the correlation ratio $\langle x^2 v_x^2 \rangle / (\sigma_x^2 \sigma_v^2)$ of the initially gaussian beam *vs* the initial mismatch α. The solid line corresponds to a fully thermalized beam and is plotted for a reference.

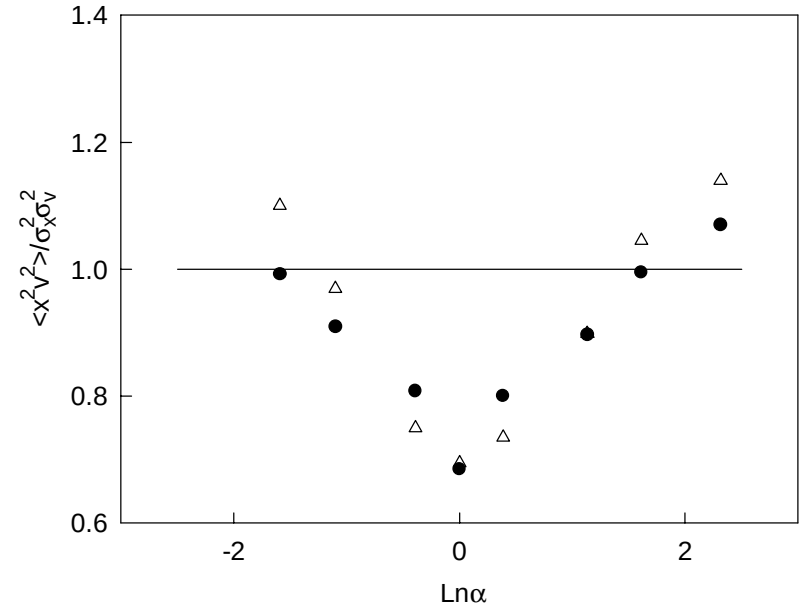

Figure 3.17: Comparison of the dynamical CME results (•) and PIC predictions (△) for the correlation ratio $\langle x^2 v_x^2 \rangle / (\sigma_x^2 \sigma_v^2)$ of the initially uniform beam *vs* the initial mismatch α. The solid line corresponds to a fully thermalized beam and is plotted for a reference.

CME and PIC simulation were also made for a wide range of the initial mismatch of $0.2 < \alpha < 10$ with the initial distribution functions given by Eqs. (2.3) and (2.4). Good agreement between CME and PIC results for the evolution of the rms beam properties is observed over this range.

3.3 Accuracy Aspects of the Numerical Model

3.3.1 CME and Conservation Laws

The exact problem of the beam evolution described by the Vlasov equation obeys a number of different conservation laws. Due to the approximations made in the numerical integration of the CME system resulting from the truncation of the infinite system and the applied artificial attenuation, the conservation constraints might become violated. In this section, we report on numerical studies that access the effects of approximations on the conservation laws.

We begin by considering the macroscopic dynamical constraints of conservation of number of particles and beam energy. The conservation of the number of particles in the beam is assured by a constant coefficient a_{00} in the expansion of the distribution function. As it was shown in Sec. 2.3, the transverse energy E of the beam given by Eq. (2.30) is conserved. Using the expression for the normalized magnetic force given by Eq. (3.20), the potential energy term is easily evaluated in terms of $\{a_{kl}\}$. The evolution of the transverse energy can then be evaluated during the numerical integration. The change of E (normalized to its initial value) is plotted in Fig. 3.18 for an initially gaussian beam with a mismatch coefficient of $\alpha = 5$. Results obtained by retaining a different number of orders in the numerical integration are presented for the lowest truncation order $j_{max} = 2$ (——), $j_{max} = 4$ (- - -) and $j_{max} = 20$ (– · –). It can be seen that when no artificial attenuation is used the energy is conserved to a good degree for the cases with $j_{max} = 2$ and $j_{max} = 4$. A simulation with $j_{max} = 8$ was also performed and showed no significant change in E. When larger number of modes are retained in the simulation and an attenuation term applied in the dynamical equations to prevent an unlimited growth of the coefficients, a change of energy is observed. For $j_{max} = 20$ and $\Delta = 10$, the relative change in E reaches 2% for the propagation ranges corresponding to the establishment of stationary rms values. Thus, the introduced artificial viscosity term results in a small change in E. The change of E can serve

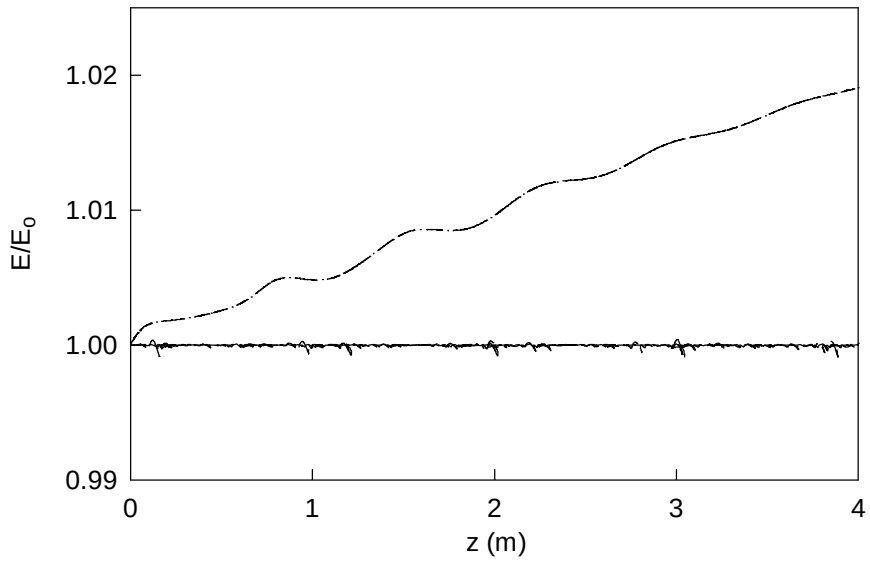

Figure 3.18: Results for the change of the beam energy in the process of the beam evolution obtained using CME integration with different truncation orders $j_{max} = 2$ (——), $j_{max} = 4$ (- - - -) and $j_{max} = 20$ (– · –). No artificial attenuation is used in the simulation with $j_{max} = 2$ and $j_{max} = 4$.

as a good numerical diagnostic of the code performance and should always be monitored in the process of numerical integration. Large values of ΔE indicate an inappropriate amount of attenuation introduced into the system resulting in a significant change of the beam dynamics. If relative changes of beam energy exceeding $10\% - 20\%$ are observed in the simulation, the amount of artificial attenuation should be decreased by increasing the value of the parameter Δ.

Due to the incompressibility of the phase-space flow described by the collisionless Vlasov equation, the system also possesses an infinite number of conservation laws of the form

$$I_n \equiv \int\int dx dv_x f^n(x, v_x) = Const. \tag{3.27}$$

We investigate the change in I_2 (given by Eq. (3.27) with $n = 2$) when the truncated CME

system is integrated. Using the definitions of Eq. (3.3), I_2 can be written as

$$I_2(\tau) = \frac{N^2}{2\pi^2 au} \int \int dX dV g^2(X, V, \tau). \tag{3.28}$$

Using the expansion for the normalized distribution function given by Eq. (3.10) and the integral relation

$$\int_{-\infty}^{\infty} dx\, H_k(x) H_l(x) e^{-2x^2} = (-1)^{\frac{(k+l)}{2}} 2^{\frac{k+l-1}{2}} \Gamma\left(\frac{k+l+1}{2}\right) \quad k+l = \text{even}, \tag{3.29}$$

the value of I_2 is

$$I_2 = \frac{N^2}{4\pi^{5/2} au} \sum_{klmn} (-1)^{\frac{(k+l+m+n)}{2}} a_{kl} a_{mn} \frac{1}{\sqrt{k!l!m!n!}} \Gamma\left(\frac{k+m+1}{2}\right) \Gamma\left(\frac{l+n+1}{2}\right). \tag{3.30}$$

The change of $I_2(\tau)$ during the beam evolution predicted by CME model is shown in Fig. 3.19 for the familiar case of an initially gaussian distribution with $\alpha = 5$. The effects of truncation and artificial attenuation on the dynamics of I_2 are seen in the results of simulations performed with $j_{max} = 2$, $j_{max} = 4$ and $j_{max} = 8$. The results for I_2 normalized to its initial value I_{20} are plotted in Fig. 3.19 with a solid line for $j_{max} = 2$, dashed curve for $j_{max} = 4$, and a dashed-dotted line for $j_{max} = 8$. No artificial attenuation is used in the simulations. From Fig. 3.19 we conclude that the relative change of I_2 in the simulation with no applied attenuation grows with increasing truncation order. If more orders are kept in the simulation and no attenuation is introduced, I_2 grows without bound reflecting the growth of the coefficients of expansion. The result for the dynamics of I_2 for a system with a large truncation order and artificial viscosity is presented in Fig. 3.20. A monotonic decay of I_2 is observed with a total decrease of about 10%. The decrease can be attributed to the suppression of higher order modes by the attenuation. This is not surprising since the artificial attenuation of higher order modes corresponds to the coarse-graining of the distribution.

3.3.2 Truncation of the Infinite CME System

We now study the effects of the truncation performed in the course of the numerical integration. We begin the analysis by linearizing Eq. (3.21).This simplification, as shown below, retains the most important features of the dynamics. The simpler linear system is then truncated at order j_{max}, and its eigenvalues are calculated numerically for a particular example. As j_{max} is increased, several of the eigenvalues gain positive real parts, indicating

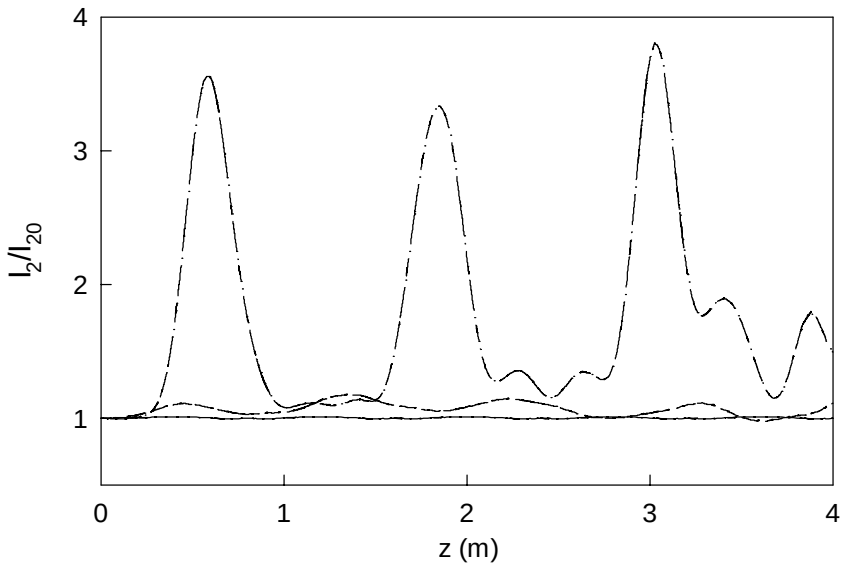

Figure 3.19: Results for the change of the normalized I_2 obtained from CME simulation with different truncation orders $j_{max} = 2$ (——), $j_{max} = 4$ (- - - -) and $j_{max} = 8$ (– · –). No artificial attenuation is used in the integration.

an exponentially growing solution. We will show how the artificial attenuation introduced in Sec. 3.2 suppresses this growth.

The right-hand side of Eqs. (3.21) contains three types of terms. Some terms do not depend on time and are determined by the normalization coefficient a_{00}. The second type depends linearly on the variables a_{kl}, and the remaining terms have a quadratic dependence on the coefficients. Symbolically, the dynamical system can be written as

$$\dot{a}_{mn} = c_{mn} + B^{kl}_{mn} a_{kl} + D^{klpq}_{mn} a_{kl} a_{pq}. \tag{3.31}$$

Here, time-independent terms are denoted by c_{mn}, and the tensors B^{kl}_{mn} and D^{klpq}_{mn} are introduced for the linear and quadratic terms respectively. The summation over repeated indices is implied.

To simplify the problem, we linearize the equations by ignoring the quadratic terms (*e.g.* set $D^{klpq}_{mn} = 0$). The physical significance of this simplification can be understood by examining the Vlasov equation. The quadratic terms in Eqs. (3.31) originate from the force term in the Vlasov equation (given by $\kappa F \partial g/\partial V$ of Eq. (3.4) in normalized variables). To

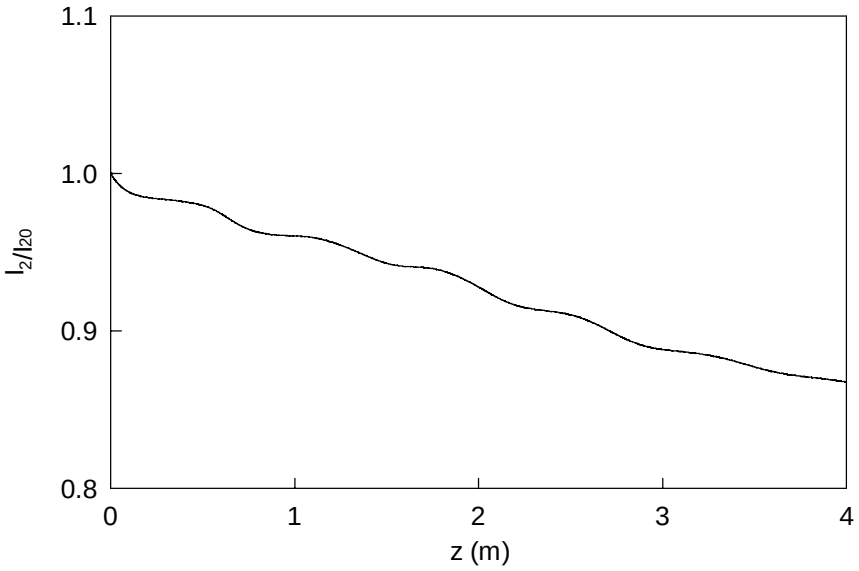

Figure 3.20: Dynamics of I_2/I_{20} obtained from CME simulation of an initially gaussian beam with $\alpha = 5$. Numerical integration is performed with $j_{max} = 20$ and $\Delta = 10$

better understand the justification for the linearization, we first represent the normalized distribution function as

$$g = g_0 + \tilde{g}, \tag{3.32}$$

where $g_0 = a_{00} H_0(X) e^{-X^2} H_0(V) e^{-V^2}/\sqrt{\pi}$ is the part of g that does not change during the beam propagation, and $\tilde{g} = g - g_0$. We next assume that $\tilde{g}$ is a small perturbation of g_0. Neglecting terms quadratic in $\tilde{g}$, the linearized force can be written as $\kappa F_0(\partial g/\partial V) + \kappa\tilde{F}(\partial g_0/\partial V)$. Here, F_0 is the self-consistent force corresponding to the distribution g_0, and $\tilde{F} = F - F_0$ originates from $\tilde{g}$. The term $\kappa F_0(\partial g/\partial V)$ is the same as would be obtained with a fixed external force equal to the self-force due to g_0. The term $\kappa\tilde{F}(\partial g_0/\partial V)$ reflects the change in F that arises from the variation in the beam density and is a consequence of the self-consistency of the force. The CME corresponding to this linearized about g_0 Vlasov system is identical to the linearized CME problem with $D_{mn}^{klpq} = 0$. Note that these approximate equations preserve the critical features the spatial nonlinearity and self-consistency of the force. Only the assumed small term $\kappa\tilde{F}(\partial\tilde{g}/\partial V)$ is neglected.

The justification for the simplification can be made as follows. If the numerical system is normalized to the initial state, the initial condition for $\{a_{kl}\}$ takes the simple form

$a_{kl}|_{\tau=0} = 0$ for $k + l > 0$, and only a_{00} has a non-zero value. Consider the propagation of a slightly mismatched beam in this normalization. Small changes in the beam parameters occur during the propagation of such a beam. Therefore, all $|a_{kl}| \ll a_{00}$ for $k, l > 0$ and $\tilde{g}$ can be considered as a perturbation of the initial g_0, resulting in insignificant nonlinear terms. If the initial mismatch is significant, the nonlinear terms might become important and dynamics can become different from the linearized problem. However, the linearized system is a very helpful tool that can be used to investigate some properties of the CME model.

To illustrate the validity of this approximation for slightly mismatched beams, we compare the predictions of the linear model with the full nonlinear simulation. An initially gaussian beam with $\sigma_{xo} = 2.28$mm, $\sigma_{vo} = 2.6 \times 10^6$, $\gamma = 100$ and $n_0 = 8.74 \times 10^{16}\,\mathrm{m}^{-3}$ is used, corresponding to a mismatch parameter of $\alpha = 1.5$. The simulation is performed with $j_{max} = 20$ and the relaxation width $\Delta = 10$. The beam is normalized to the initial state with the parameters $a = \sigma_{xo}$ and $u = \sigma_{vo}$. The propagation curves for the rms beam size and velocity dispersion are plotted in Fig. 3.21 as solid curves and compared with the full CME evolution plotted as dotted lines. The results of the linear and fully nonlinear models are very similar. The instability, observed in the dynamics of a full nonlinear CME model truncated at $j_{max} > 10$ and with no attenuation, also appears in the integration of the linearized system with $j_{max} > 12$. Thus, the instability of the full system can be studied using the simplified linearized system. The range of the normalization parameter assuring the validity of the linearized model is investigated further in Sec. 3.3.3.

We now go back to the symbolic form of the CME model given by Eq. (3.31). The linearized equations can be written as

$$\dot{a}_{mn} = c_{mn} + B^{kl}_{mn} a_{kl}. \tag{3.33}$$

We next convert Eqs. (3.33) into a more convenient vector notation. The matrix of coefficients a_{mn} is transformed into a vector $\mathbf{a}$. The coefficients are first arranged by order and then stacked into a vector. The first few components of such a vector are $\mathbf{a} = (a_{20}, a_{11}, a_{02}, a_{40}, a_{31}, ...)$. Here again we assume that $f(x, v_x) = f(-x, -v_x)$ for the system and only a_{kl} with $k + l =$ even are retained in the analysis. The system of Eqs. (3.33) can now be written in the vector form as

$$\dot{\mathbf{a}} = \mathbf{c} + \mathbf{B}\mathbf{a}, \tag{3.34}$$

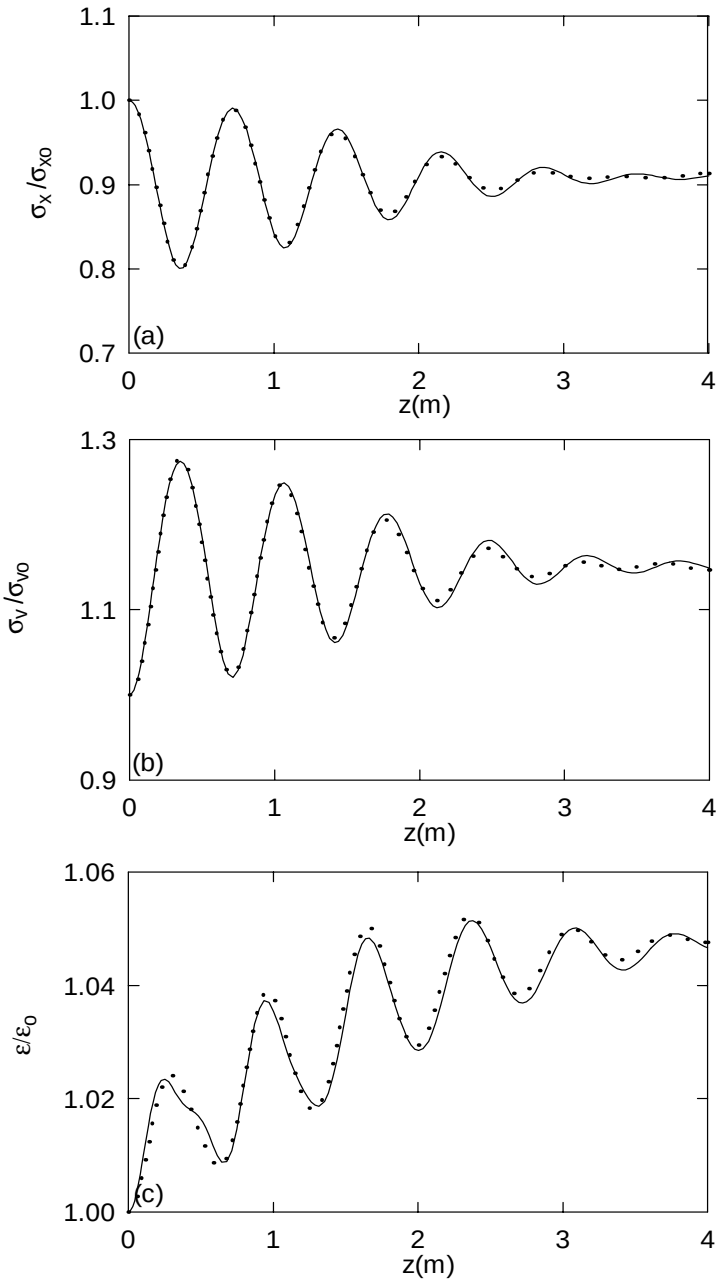

Figure 3.21: Comparisons of propagation curves for (a) rms beam size, (b) rms velocity and (c) the emittance obtained using the linearized (——) and full ($\cdot\ \cdot\ \cdot$) CME models with $j_{max} = 20$, $\Delta = 10$ for the initially gaussian distribution with a mismatch of $\alpha = 1.5$.

where, in the new notation, vector $\mathbf{c}$ and matrix $\mathbf{B}$ correspond to tensors c_{mn} and B^{kl}_{mn} of Eq. (3.33). Equation (3.34) constitutes an inhomogeneous system with constant coefficients. Its general solution is

$$\mathbf{a} = \mathbf{a_p} + \sum_{i=1}^{n_{max}} d_i \mathbf{e_i} e^{\lambda_i \tau}, \tag{3.35}$$

where $\mathbf{a_p}$ stands for a particular solution of Eqs. (3.34), $\mathbf{e_i}$ is the eigenvector of the matrix $\mathbf{B}$ that corresponds to the eigenvalue λ_i, $\mathbf{B e_i} = \lambda_i \mathbf{e}_i$, and d_i is a complex number determined by the initial conditions. The notation n_{max} is used for the total number of equations in the system. The particular solution can be chosen to be a constant-in-time vector which solves the equation $\mathbf{Ba} = -\mathbf{c}$. It can be easily verified that the matrix $\mathbf{B}$ is degenerate ($\det \mathbf{B} = 0$), and a number of solutions of the linear system $\mathbf{Ba} = -\mathbf{c}$ can be found. We choose $\mathbf{a_p}$ as one of these solutions. The coefficients d_i are found from the initial condition by solving the system

$$\mathbf{a}|_{\tau=0} = \mathbf{a_p} + \sum_{i=1}^{n_{max}} d_i \mathbf{e_i}. \tag{3.36}$$

All properties of the dynamical behavior of the truncated Eqs. (3.34) are contained in the solution given by Eq. (3.35), including the numerically observed instability. Mathematically, we expect this instability to be connected to the spectrum of the eigenvalues $\{\lambda_i\}$. In particular, if an eigenvalue with a positive real part exists in the spectrum, an unlimited growth of the solution results. Numerical methods are employed to find $\{\lambda_i\}$ and handle the algebraic complexity of the problem when $j_{max} > 2$. When the spectrum of the matrix $\mathbf{B}$ is found numerically for a particular example, it always contains zero frequencies and purely imaginary values. In some cases, eigenvalues with real parts are also present in the spectrum, indicating instability. No convergence in eigenvalues with real parts is observed as the dependence of the spectrum on the truncation order is investigated. For the example with $\alpha = 1.5$, qualitatively different behavior is observed for different truncation orders. If $j_{max} \leq 12$ all eigenfrequencies are found to be purely imaginary or zero. However, for $j_{max} > 12$, λ_i with $\mathrm{Re}(\lambda_i) \neq 0$ appear, and the largest real part of λ_i increases rapidly with j_{max}. The eigenvalues with positive real parts cause an unlimited growth of the solution given by Eq. (3.35).

An artificial attenuation term was introduced in Sec. 3.2 to suppress this exponential growth of a_{kl} coefficients. Its form was chosen in such a way that low order modes are almost unaffected by the attenuation while higher orders close to j_{max} are damped the

strongest. The purpose of this term is to smooth the truncation cutoff of the expansion series and to decrease the influence of higher orders. If the eigenvalues of the matrix $\mathbf{B}$ together with the attenuation term are computed for different values of Δ, we find that $\mathrm{Re}(\lambda_i) \leq 0$ for all modes when the attenuation width is smaller than some threshold value of Δ_{cr}. For $\Delta > \Delta_{cr}$ the applied attenuation is insufficient to suppress the instability, and some growing solutions are still observed. The value of the critical attenuation width Δ_{cr} depends on the number of orders retained in the simulation. By computing the spectrum for different Δ an optimal Δ_{cr} can be found for a given truncation order. For the example presented in Sec. 3.2, the initially gaussian beam with $\alpha = 5$ and $j_{max} = 20$, we find $\Delta_{cr} \simeq 13$. Thus, the spectrum of the linear coupled problem can be used to determine the value of the attenuation width for a dynamical simulation. Alternatively, the necessary attenuation width can be found by performing simulations with different Δ until the growth in a_{kl} is suppressed. Our experience has shown that $\Delta \approx j_{max}/2$ is usually a good starting point. It results in sufficient attenuation for all but highly mismatched cases.

Let us consider the familiar dynamical case with an initially gaussian distribution and a mismatch parameter $\alpha = 5$. The spectrum of the linearized problem reveals eigenvalues with positive real parts for truncation orders $j_{max} > 8$. We want to perform a CME simulation normalized to the asymptotic rms values and with the truncation order $j_{max} = 20$. To find the necessary attenuation width to suppress the growth, the spectrum of the linearized problem (with the attenuation term included) is found for different values of Δ for chosen normalization parameters. For $j_{max} = 20$, the threshold value is found to be $\Delta_{cr} \simeq 13$. Thus, we conclude that the CME simulation can be performed with $\Delta < 13$ and the value of $\Delta = 10$ was chosen to make comparisons with a PIC simulation. The dependence of the dynamical results on the attenuation width is illustrated in Fig. 3.22. The results for the evolution of the rms beam size obtained using different Δ are plotted for $\Delta = 12$ (dashed-dotted line), $\Delta = 10$ (solid line) and $\Delta = 8$ (dotted line). It is evident that the evolution of the rms beam properties and the asymptotic values are not sensitive to the value of Δ (for $\Delta < \Delta_{cr}$) . Thus, the applied artificial attenuation term is important for the suppression of the numerical instability but does not affect the dynamics of the quantities of interest. Two points should be kept in mind in deciding on the value of Δ for a particular simulation: (1) insufficient attenuation (Δ too large) causes a growth in the solution, (2) too much attenuation (Δ too small) results in significant numerical errors such as a change of the transverse energy E.

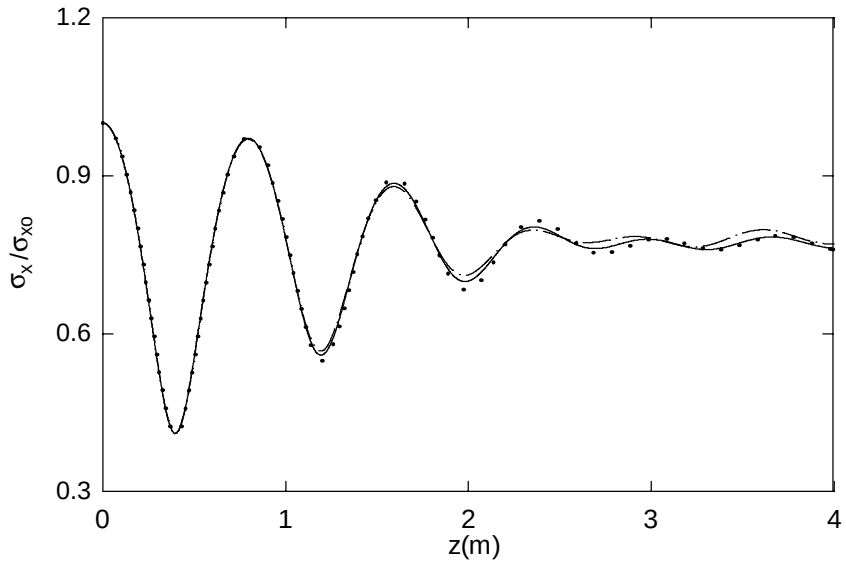

Figure 3.22: Comparison of results for the evolution of the rms beam size of the initially gaussian beam with $\alpha = 5$ obtained using $\Delta = 12$ $(- \cdot -)$, $\Delta = 10$ (——) and $\Delta = 8$ $(\cdot \cdot \cdot)$.

The linearized analysis can also be used to determine the asymptotic state of the system. The time-independent part of the general solution can be extracted by including only the particular solution $\mathbf{a_p}$ and terms that correspond to $\lambda_i = 0$ in the summation given by Eq. (3.35). This stationary non-oscillating part of the solution $\mathbf{a_s}$ can be calculated as

$$\mathbf{a_s} = \mathbf{a_p} + \sum_{i=1}^{n_{max}} d_i \eta_i \mathbf{e_i}, \tag{3.37}$$

where $\eta_i = 0$ if $\lambda_i \neq 0$ and $\eta_i = 1$ if $\lambda_i = 0$.

3.3.3 Normalization of the CME Equations

As mentioned in Sec. 3.2, there is a freedom in the choice of normalization parameters for the CME expansion. Logically, a and u (of Eq. (3.3)) should be chosen as representative space and velocity scales for the beam. The second factor that should also be considered is the optimization of the numerical model to minimize the effects of the truncation. We next study the properties of the truncated CME system properties as the normalization of the system changes. When the infinite CME system is truncated at a finite order unbounded solutions result which pose a difficulty in the numerical integration.

As we discussed above, the appearance of the growing solutions can be predicted using a simplified linearized model, and the unbounded solutions correspond to real eigenvalues in the spectrum of the dynamical matrix **B**. In choosing the normalization of the system it is desirable to minimize the growth of the solutions thus decreasing the artificial viscosity necessary to suppress this growth. Therefore, it is useful to study the change of the real eigenvalues of the matrix **B** as the values of a and u are changed.

Note that the dynamical equations do change as different normalizations are used due to a change in the parameter κ in all terms originating from the force contribution of the original Vlasov equation (given by $\kappa F \partial g/\partial V$). This implies the properties of the dynamical matrix **B** also depend on the normalization through the single parameter κ. To study the dependence of the real eigenfrequencies on the normalization, the eigenvalue problem $\mathbf{Be_i} = \lambda_i \mathbf{e}_i$ is solved for different values of κ and with different number of orders retained. The results for the maximum real eigenvalue are plotted in Fig. 3.23. It can be seen that a

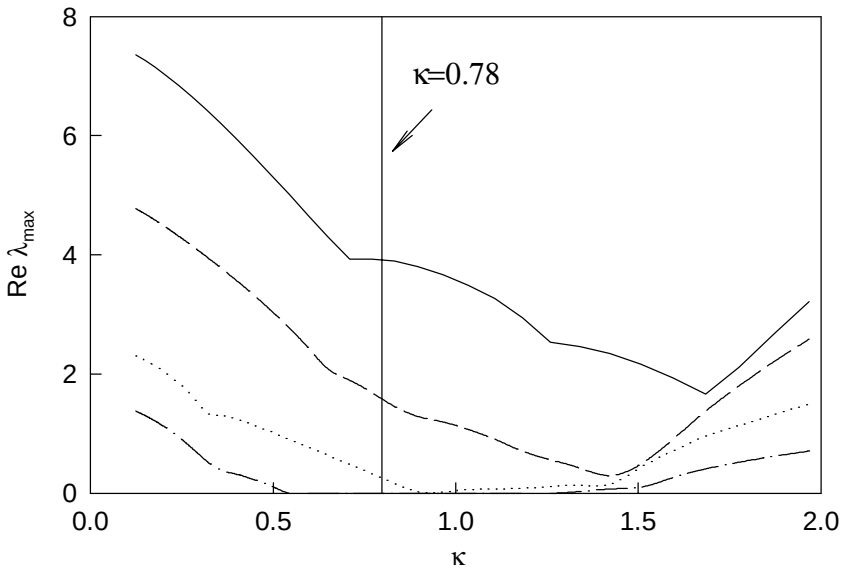

Figure 3.23: Maximum growth rates *vs* the normalization mismatch parameter κ defined by Eq. (3.5) for $j_{max} = 8$ (–·–), $j_{max} = 12$ (· · ·), $j_{max} = 20$ (- - - -) and $j_{max} = 28$ (——).

certain range of normalization exists for truncation orders $j_{max} = 8$ and $j_{max} = 12$ when no growth is observed. For truncation orders $j_{max} > 12$, instability always appears. However, a particular range of κ can be found for every truncation order which minimizes the observed

growth. For example, for the truncation order $j_{max} = 20$ the minimum growth occurs for $\kappa = 1.45$. The smaller the real eigenvalues in the spectrum of the problem the smaller artificial attenuation is required to suppress the growth. Based on Fig. 3.23, we conclude that values of κ somewhere in the range of $0.5 \leq \kappa \leq 2.5$ correspond to the significantly small real eigenvalues for the truncation orders considered. Thus, it is desirable to normalize the system using values of a and u which give κ from this range. For example, the beam can be normalized to its asymptotic rms beam size and temperature, which corresponds to the mid-range of the values realized during the evolution of the system. The value of the normalization parameter corresponding to $a = \sigma_{x,eq}$ and $u = \sigma_{v,eq}$ for the initially gaussian beam can be evaluated using estimates of Sec. 2.3, resulting in $\kappa \simeq 0.78$ which is also in the range discussed above. Thus, normalization to the analytically calculated final values of the beam size and velocity width is a sensible choice of the normalization, and it was used in most numerical cases in this thesis.

In principle, other normalizations satisfying both requirements (*i.e.* good representation of the distribution function and values of κ corresponding to a minimum of the maximum real eigenvalue) are possible. The dependence of the results on the choice of the normalization is illustrated in Fig. 3.24 using the familiar case of an initially gaussian beam with a mismatch parameter $\alpha = 5$. All numerical integrations are performed with $j_{max} = 20$ and $\Delta = 10$. The dynamical results obtained using the normalization to the final state are plotted for reference as solid curves. Other results correspond to the normalization with the optimal $\kappa = 1.45$ for $j_{max} = 20$. The propagation curves normalized to the asymptotic value of the velocity width are plotted with dotted lines. The dashed curves correspond to $a = \sigma_{x,eq}$, and the dash-dotted lines is a result for the initial beam size used as a. It can be seen that all propagation curves show similar behavior. Therefore, we conclude that a range of normalizations can be used in the numerical integration of the CME system.

The agreement between the predictions of the linearized model introduced in Sec. 3.3.2 and full system of equations also depends on the numerical normalization chosen. As the linearized system is useful to study different aspects of the problem including the relaxation time of the rms oscillations, we study the dependence of its results on the normalization parameter κ using the example of the initially gaussian beam with a mismatch of $\alpha = 5$. This investigation can serve as an illustration of the general validity of the linearized model. First, we define the relaxation time τ_r of the rms oscillations as the time it takes for the oscillation amplitude of $\langle x^2 \rangle$ to decrease by a half. The predictions of a full and

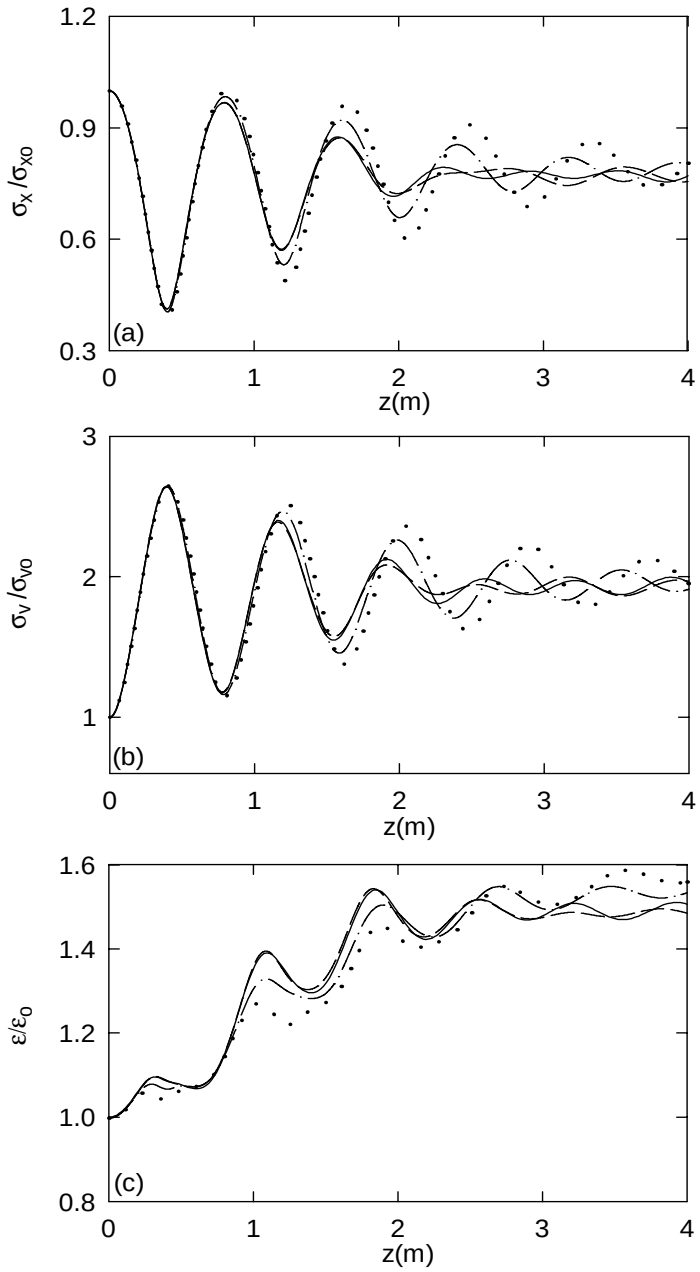

Figure 3.24: Comparisons of propagation curves for (a) rms beam size, (b) rms velocity and (c) the emittance obtained using the CME model with $j_{max} = 20$, $\Delta = 10$ and different normalization parameters. Results are for cases with $a = \sigma_{x,eq}$, $u = \sigma_{v,eq}$ (——-), $a = 1.7\sigma_{x,eq}$, $u = \sigma_{v,eq}$ ($\cdot\ \cdot\ \cdot$), $a = \sigma_{x,eq}$, $u = 0.73\sigma_{v,eq}$ (- - -) and $a = \sigma_{x,0}$, $u = 0.91\sigma_{v,eq}$ (–·–). The initial gaussian beam with a mismatch of $\alpha = 5$ is considered.

linearized models for the relaxation time normalized to the result of the PIC simulation are compared in Fig. 3.25. It can be seen that the full nonlinear model result agrees well with

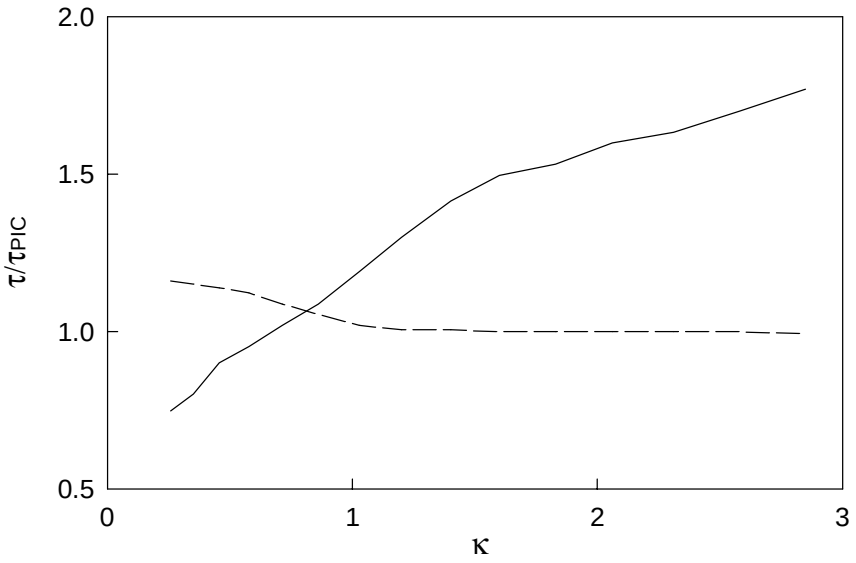

Figure 3.25: Predictions for the normalized relaxation time obtained using linearized (——–) and full (- - - -) CME model for the initially gaussian beam with $\alpha = 5$. The simulations are performed using $j_{max} = 20$ and $\Delta = 10$.

the PIC simulation especially in the wide range of $0.6 < \kappa < 1$ where agreement within 5% is observed. The prediction of the linearized set of equations depends on the normalization parameter due to a limited range of validity of the linearization approximation. The result of the linearized model for τ_r shows 10% agreement with the PIC simulation in the range of $0.45 < \kappa < 0.86$. The normalization to the analytically calculated asymptotic state ($\kappa = 0.78$) falls in this range. Without performing additional studies for other possible initial conditions, we chose $\kappa = 0.78$ as the optimal normalization for the use of the linearized model.

3.4 Description of Beam Dynamics in a Symmetrically Weighted Hermite Representation

As we emphasized above, the advantage of the use of the asymmetrically weighted Hermite polynomial basis yields a simple relation between only three expansion coefficients and the second order moments of the distribution function. This allows us to obtain accurate numerical predictions for the evolution of the second order moments retaining only few orders in the expansion of the distribution function. Some analytical predictions can also be obtained for the decay time of the betatron oscillations. This is a subject of the next chapter. In the general case of the representation of the distribution function as

$$g(X,V) = \sum_m b_{mn}(\tau)\Phi_m^{(x)}(X)\Phi_n^{(v)}(V), \tag{3.38}$$

with the inverse transform

$$b_{mn} = \int_{-\infty}^{\infty}\int_{-\infty}^{\infty} dXdV g(X,V)\Phi^{(x)m}(X)\Phi^{(v)n}(V) \tag{3.39}$$

the second order moments are expressed as a linear combination

$$\langle X^p V^q\rangle = \sum_{mn} b_{mn} Z_m^p Z_n^q, \tag{3.40}$$

where the notation

$$Z_m^p = \int_{-\infty}^{\infty}\int_{-\infty}^{\infty} dXdV X^p \Phi_m^{(x)}(X), \tag{3.41}$$

is used. The basis formed by $\Psi_k^{(x)}(X)\Psi_l^{(v)}(V)$ of Eqs. (3.8)-(3.9) allowed for good predictions of the rms dynamics for different initial conditions and only 120 coefficients retained in the simulation. The only disadvantage of the use of the asymmetrically weighted Hermite polynomial basis is in the appearance of the numerical instability appearing as an exponential growth of the coefficients of the expansion. A similar instability was also reported in Vlasov solvers which use Fourier-Hermite representations (see for example Ref. [47] where both asymmetrically and symmetrically weighted Hermite polynomials were used). The cause of the growth was attributed to the non-conservation of I_2 as defined in Eq. (3.28). The violation of the conservation of I_2 increases with the increase of the truncation order. Thus, the basis given by Eqs. (3.8)-(3.9) offers an efficient technique to model the rms beam dynamics but at the expense of the appearance of the instability. To appreciate the trade-off

between the efficiency of the method and appearance of the exponential growth, consider an alternative expansion of g over the symmetrically weighted Hermite polynomial basis given by

$$\Phi_m^{(x)}(X) = \Phi^{(x)m}(X) = C_m H_m(X) e^{-X^2/2}, \tag{3.42}$$

$$\Phi_n^{(v)}(V) = \Phi^{(v)n}(V) = C_n H_n(V) e^{-V^2/2}, \tag{3.43}$$

where the normalization constant is again taken to be equal to $C_m = (\pi^{1/4}\sqrt{2^m m!})^{-1}$. The value of C_n is chosen such that $\int_{-\infty}^{\infty} dX \Phi^{(x)m}(X)\Phi_n^{(x)}(X) = \delta_n^m$. Here, the symbol δ_n^m stands for the Kronecker delta. It was reported in Ref. [47] that the use of the Fourier-Hermite representation with the symmetrically weighted Hermite polynomials results in no instability due to the inherent conservation of I_2 by the method. The basis given by Eqs. (3.42)-(3.43) offers a solution to the problem of the unlimited growth but the second order moments are now, unfortunately, expressed through many orders of the expansion. Repeating the derivation of the dynamical equations with the basis functions given by Eqs. (3.42)-(3.43), we obtain for the time evolution of b_{mn}

$$\begin{aligned}
\dot{b}_{mn} &= 0.5(\sqrt{mn}b_{m-1,n-1} - \sqrt{(m+1)n}b_{m+1,n-1} \\
&+ \sqrt{m(n+1)}b_{m-1,n+1} - \sqrt{(m+1)(n+1)}b_{m+1,n+1}) \\
&- \kappa \sum_k \sum_{p,q=even} (\sqrt{n+1}b_{k,n+1} - \sqrt{n}b_{k,n-1}) \frac{\sqrt{q!}(p-1)!!}{\sqrt{2^{p+q-2}p!}(q/2)!} \\
&\times \left(\sum_{i=1}^{p/2} \frac{2^{i-1}}{(p-2i+1)!!} G_{p-2i+1,m,p} - 2W_{mp} \right),
\end{aligned} \tag{3.44}$$

where

$$G_{klm} = \int_{-\infty}^{\infty} dX \, \frac{H_l(X)}{\pi^{1/4}\sqrt{2^l l!}} \frac{H_m(X)}{\pi^{1/4}\sqrt{2^m m!}} H_k(X) e^{-3X^2/2}. \tag{3.45}$$

For the purposes of numerical integration, the infinite expansion of Eq. (3.38) is truncated at some $m+n = j_{max}$ and the remaining equations are supplemented with the initial condition computed using Eq. (3.39). The results for the evolution of the square of the beam size obtained for the initial gaussian distribution given by Eq. (2.3) and the mismatch of $\alpha = 5$ is presented in Fig. 3.26. The normalization to the initial state is used. To make an adequate comparison between PIC and CME simulation based on Eq. (3.44), twenty orders are retained in the simulation. No artificial attenuation is applied. Good agreement between the result of the integration of Eq. (3.44) and the PIC simulation can be seen at the initial

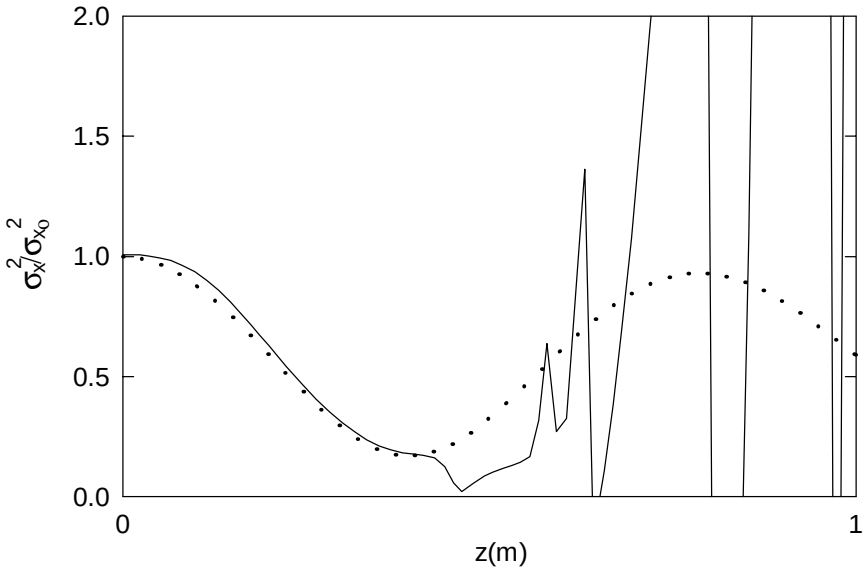

Figure 3.26: Comparison of results for the evolution of the square of the beam size of the initially gaussian beam with $\alpha = 5$ obtained using Eq. (3.44) and a PIC simulation.

stages of the propagation. A discrepancy develops after about half of a betatron period, and the prediction of Eq. (3.44) becomes drastically different from the PIC result. To investigate the nature of the discrepancy, consider the same result of the integration of Eq. (3.44) now plotted in Fig. 3.27 on a different scale. It can be seen from the graph that the nature of the discrepancy is different than the growth observed in the case of the CME simulation as presented in Fig. 3.2. No exponential growth of the beam size (or the expansion coefficients) is observed. However, the numerically obtained result for the change of $\langle x^2 \rangle$ becomes physically inapplicable after less than a betatron period due to the negativity of the second order moments. The natural cause of the discrepancy and the negativity of the moments is the use of insufficient number of the coefficients of expansion retained in the simulation. A larger number of $\{b_{kl}\}$ retained in the integration should result in the larger initial range the agreement between the simulation and PIC results. The purpose of this work, however, is to describe the rms dynamics with a reduced model with only a few equations used in the simulation. Therefore, no further investigation in the number of orders sufficient to describe the beam size evolution is performed. To obtain satisfactory predictions for the rms dynamics without the use of a large number of expansion coefficients in the simulation,

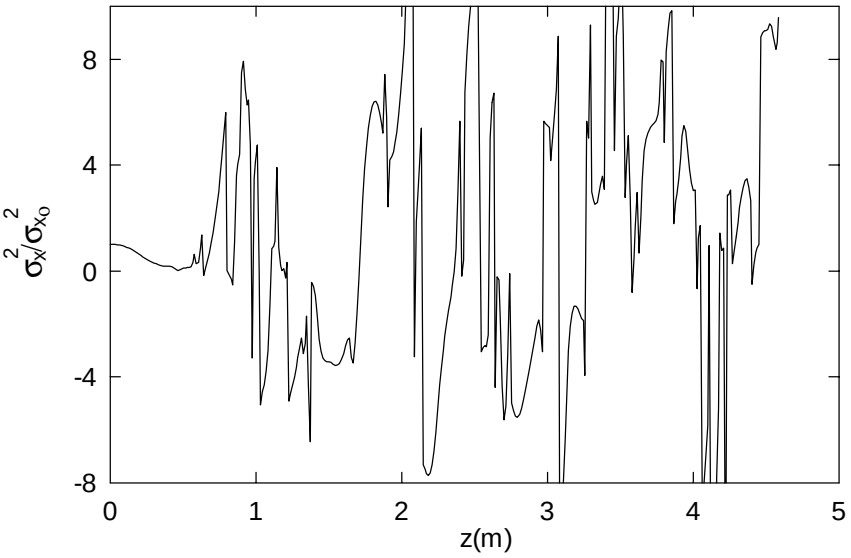

Figure 3.27: The evolution of the beam size of the initially gaussian beam with $\alpha = 5$ obtained using Eq. (3.44).

the artificial attenuation can be used to compensate for the absence of higher order b_{kl}. The relaxation term $-\Gamma_{kl} a_{kl} \delta^{kl}_{mn}$ with Γ_{kl} given by Eq. (3.23) is used. An example of the numerical prediction for the change in the second order moments obtained using Eq. (3.44) for an initially gaussian beam with $\alpha = 5$ is presented in Fig. 3.28. Due to the unsatisfactory results for the initial rms velocity using the final state normalization with twenty truncation orders, the model is normalized to the initial state. *i.e.* the scales $a = \sigma_{xo}$ and $u = \sigma_{vo}$ are used. The evolution of the second order moments qualitatively resembles that of the PIC simulation but significant quantitative differences can be seen. The cause of the discrepancy can again be traced back to the insufficient number of the expansion coefficients retained in the simulation. In contrast with the asymmetrically weighted Hermite representation, the second order moments of the distribution are determined by many orders of the expansion coefficients and are more sensitive to the truncation. Consider also the comparisons of the propagation curves with the predictions of the PIC simulation for the 4^{th} order moments. The results are presented in Fig. 3.29. Only qualitatively similar behavior is observed. Different stationary values are also achieved after the relaxation is completed.

The numerical predictions compared to the results of PIC simulations for the

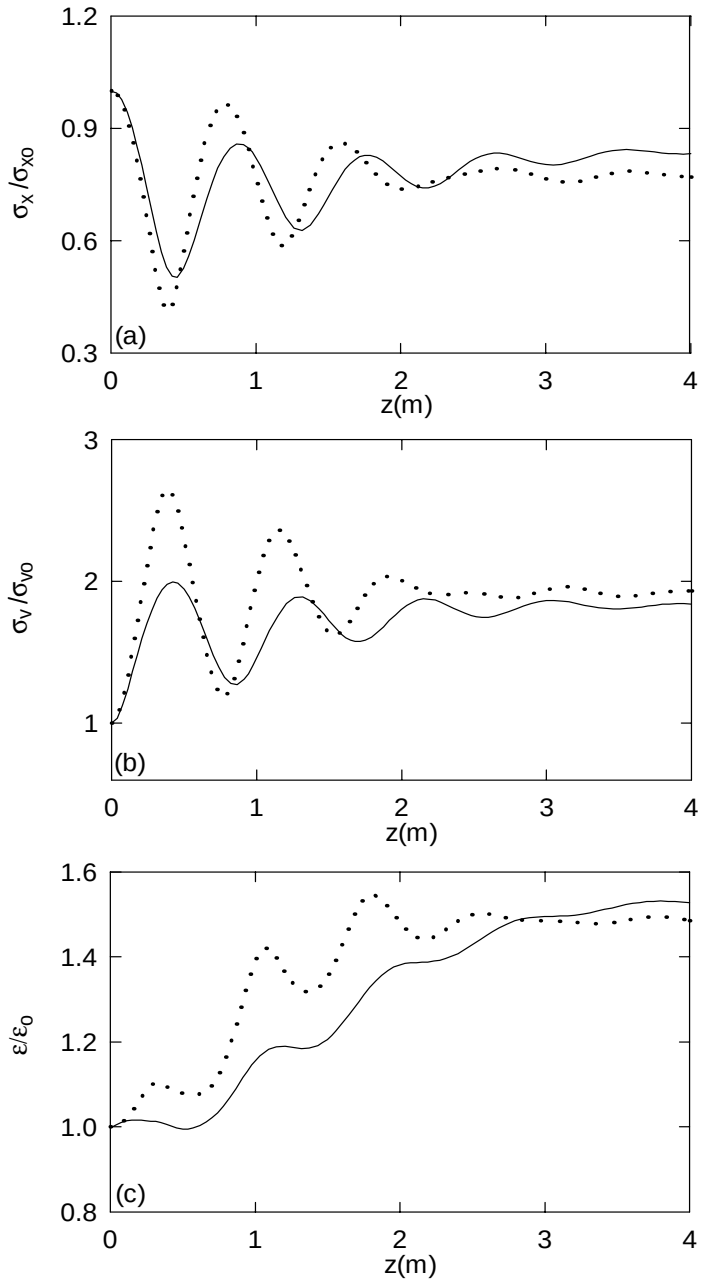

Figure 3.28: Comparisons of propagation curves for (a) rms beam size, (b) rms velocity and (c) the emittance obtained using Eq. (3.44) (——) with $j_{max} = 20$, $\Delta = 20$ and a PIC simulation ($\cdot\ \cdot\ \cdot$) for the initial gaussian beam with a mismatch of $\alpha = 5$.

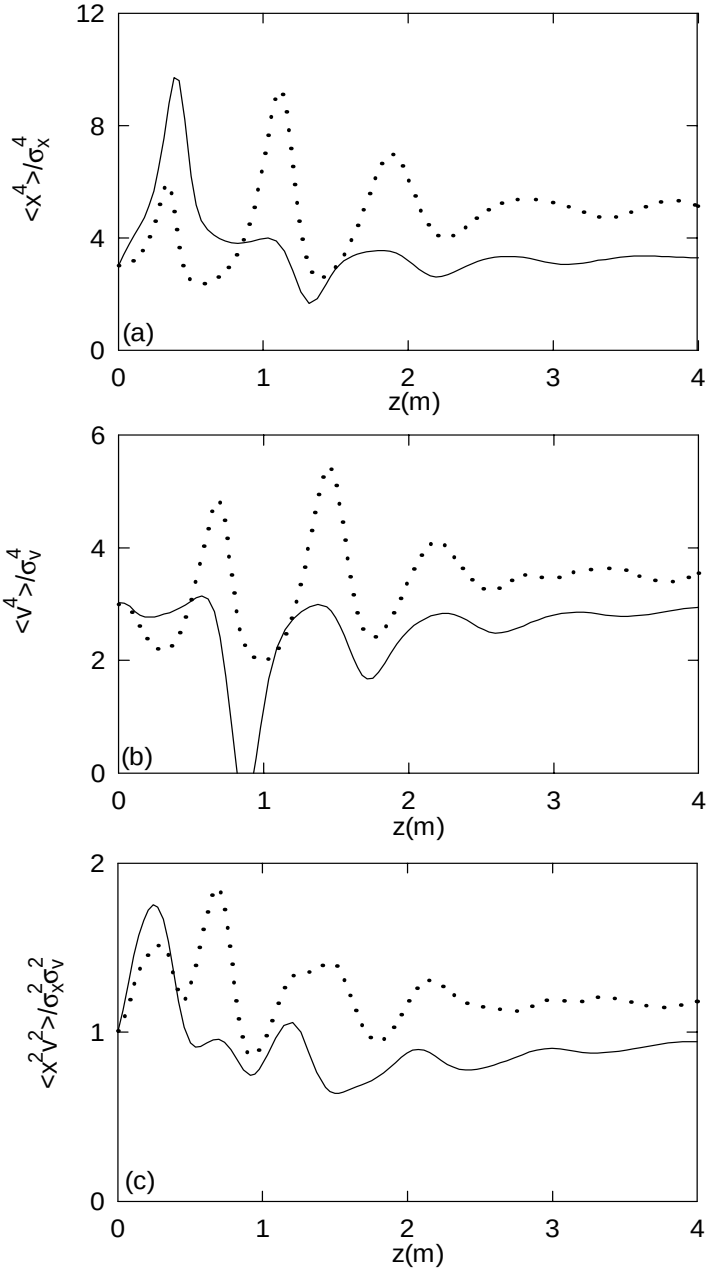

Figure 3.29: Comparisons of propagation curves for normalized 4^{th} order (a) spatial, (b) velocity and (c) correlation moments obtained using Eq. (3.44) with $j_{max} = 20$, $\Delta = 20$ and a PIC simulation ($\cdot\ \cdot\ \cdot$) for the initial gaussian beam with a mismatch of $\alpha = 5$

evolution of the beam density profile can be seen in Fig. 3.30 for the initially gaussian beam with $\alpha = 5$. The differences in the density profiles due to the insufficient number of the expansion coefficients kept in the simulation shows that accuracy requires more b_{kl} to predict the dynamics and represent the distribution function. This is also reflected in the discrepancies between the evolution of the beam moments, as they depend on all the coefficients of the expansion. An insufficient number of the expansion coefficients causes a disagreement in the behavior of the density profile at large x/σ_{xo}. This difference in turn causes a discrepancy in the result for the rms beam size.

The study of the sensitivity of the numerical predictions of Eq. (3.44) on the width of the artificial attenuation shows that the results for the rms propagation curves exhibit more dependence on Δ than the analogous results of the CME integration. As an example, consider the propagation curves for the rms beam size for the same numerical example now obtained with $\Delta = 5$ (–·–), $\Delta = 10$ (——) and $\Delta = 15$ (- - -). The results together with the PIC simulation prediction are plotted in Fig. 3.31. The investigation of the numerical model shows that while I_2 is conserved to a good degree when no artificial attenuation is used, the number of particles is not conserved.

Let us now summarize the results of this Chapter. We have shown that the representation of the distribution function in the asymmetrically weighted Hermite polynomial basis provides us with good predictions for the evolution of the rms beam properties with only about 120 coefficients of expansion retained in the simulation. The advantage of the basis is in the simple linear relation between the second order moments and the second order coefficients a_{kl}. The unphysical growth resulting from the non-conservation of I_2 invariant is suppressed by the use of the artificial attenuation. The results for the evolution of the rms properties show only a weak dependence on the width of the artificial attenuation used. While the use of symmetrically weighted Hermite polynomial representation eliminates the unlimited growth, poor predictions are obtained for the rms properties when only few orders are retained in the simulation. To be able to predict the evolution of the rms beam properties with only several orders kept in the simulation, an artificial attenuation term still has to be used. Due to the poor representation of the distribution function with only few orders, a significant disagreement with the PIC simulation is observed for the evolution of the second order moments.

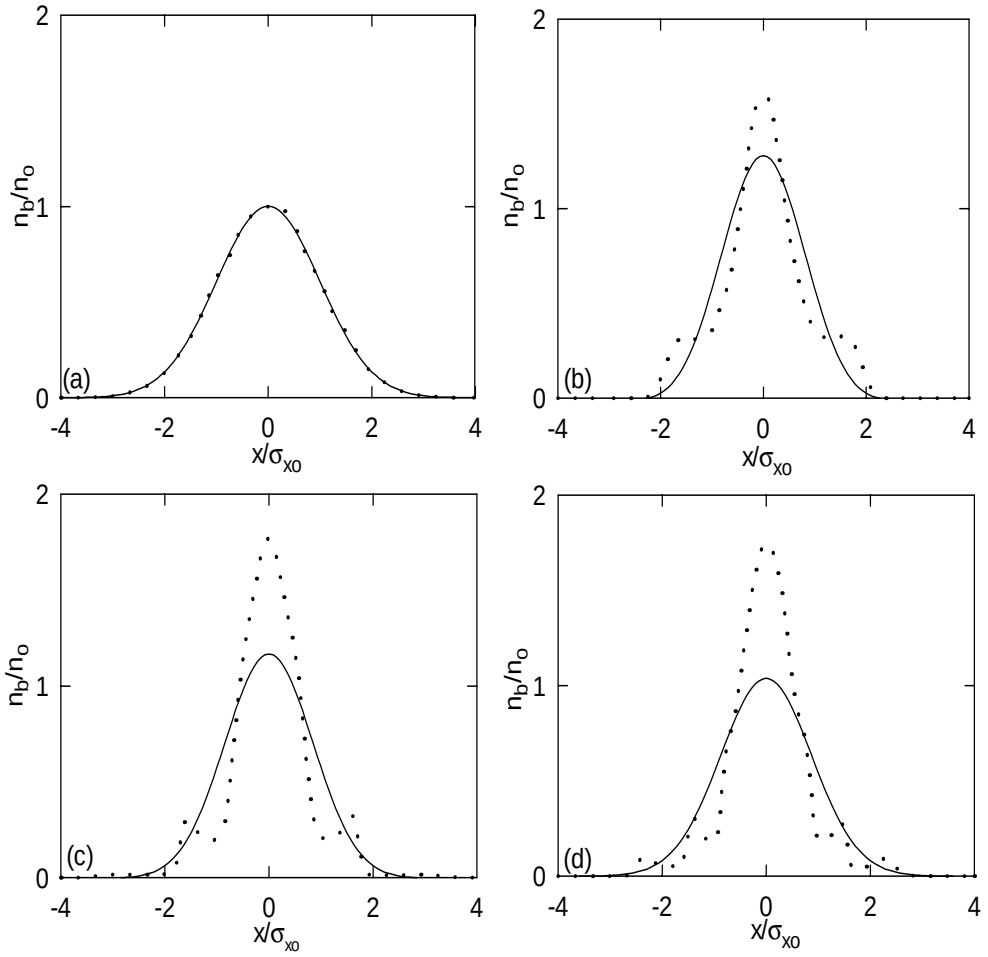

Figure 3.30: Density profiles at (a) $z = 0$, (b) $z = 1.5$m, (c) $z = 3$m and (d) $z = 4.5$m obtained by the integration of Eq. (3.44) (——) and PIC simulation ($\cdot\ \cdot\ \cdot$) for the initial gaussian beam with a mismatch of $\alpha = 5$.

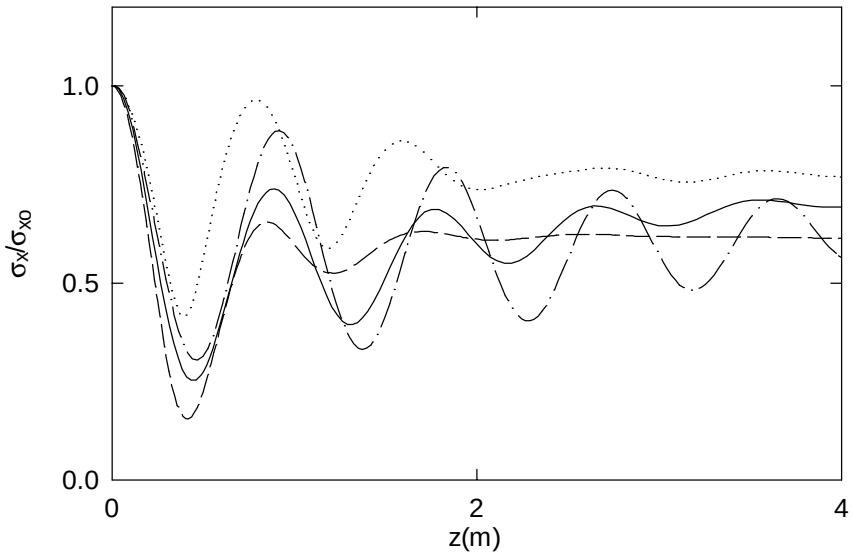

Figure 3.31: Comparison of propagation curves for the rms beam size obtained by an integration of Eq. (3.44) with $\Delta = 5$ (–·–), $\Delta = 10$ (——), $\Delta = 15$ (- - -) and a PIC simulation ($\cdot\ \cdot\ \cdot$) for the initial mismatch of $\alpha = 5$.

Chapter 4

Description of Collisionless Relaxation

As we have seen in the numerical examples of Chapters 2 and 3, the oscillations of the rms beam size e relax within a few betatron periods. More generally, the coarse-grained beam distribution rapidly relaxes toward some asymptotic state in the process of the evolution. Since no losses or collisions are present, this physics can only be attributed to the so-called collisionless relaxation process known to occur in systems containing particles which are acted upon with nonlinear forces. While the mechanism of *collisional relaxation* in different beam and plasma systems is relatively well understood (for example, it was studied for a beam propagating through a plasma in Ref. [62]) the process of collisionless relaxation is still an active topic of research in many areas of physics.

Some previous theoretical estimates for the rate of collisionless relaxation can be found in the literature. For example, an order of magnitude estimate for the decay rate caused by the violent relaxation can be found in Ref. [6] or a detailed statistical calculation based on the coarse-grained dynamics is presented in Ref. [48]. However, all previous predictions are either very approximate as they are based on the dimensionless analysis, or involve quantities that are not know analytically such as coarse-grained equilibrium distribution function. A general theory of collisionless relaxation based on the account of two-particle correlations in the evolution was developed by Kadomtsev and Pogutse [3] for systems with Coulomb-type interactions. This theory was later developed and generalized in Ref. [72] to describe the transition of the initial non-equilibrium distribution function to

the final coarse-grained equilibrium state. The theory of Refs. [3, 72] predicts a transition of any initial distribution into a Lynden-Bell equilibrium state which was not observed in our simulation that are presented in Ch. 5. In addition to apparent difficulties with the final state of the system, It is difficult to obtain estimates of the relaxation time scale from the theory.

The relaxation process in our system can be described as follows. Due to the spatial nonlinearity of the force, the initial phase-space non-equilibrium distribution becomes filamented. As the filamentation progresses to ever smaller scales, the averaged (or coarse-grained) distribution function tends to a stationary state. Nevertheless, the distribution function itself never reaches an equilibrium. This phase mixing is not the only process usually cited in the literature as responsible for the collisionless relaxation. An other physical effect, often referred to in astrophysics literature as violent relaxation, is also responsible for the decay in rms beam size oscillations.

Violent relaxation takes place in systems where particles move in time varying potentials, and relaxation occurs due to the sharp fluctuations in the self-consistent field (*e.g.* the gravitational field in the stellar system). A classical discussion of the process of violent relaxation can be found in Ref. [6]. The relation between the processes of phase mixing and violent relaxation as well as their relative importance in the decay towards the asymptotic state are still a topic of theoretical investigations (see, for example, Ref. [56] for an excellent discussion of phase mixing, violent relaxation and their relation to Landau damping in a self-gravitating system). Both of these effects are very complex and the present theory only allows for an order of magnitude estimate of bulk relaxation properties, such as its characteristic time scale.

We analyze collisionless relaxation, using the CME model, in this chapter. We begin with a study of the system properties performed in a particular basis. An eigenvalue analysis is performed, and interesting properties of the set of the eigenmodes is discovered. In particular, the existence of resonant modes in the system is shown, and the possible consequences are discussed. A simple estimate of the rms oscillations relaxation time is derived and compared with PIC simulation prediction in Sec. 4.2. To study the effects of the force nonlinearity and self-consistency on the collisionless relaxation time scale in Secs. 4.3 and 4.4, we use numerical investigations of particular examples.

4.1 Analysis of Collisionless Relaxation Using the CME Model

The numerical illustrations of the beam dynamics obtained using the CME model, presented in Ch. 3, exhibit the relaxation of rms oscillations for an initially mismatched beam. The relative simplicity (only a small set of equations has to be solved to predict the rms dynamics) of the CME model compared to a PIC simulation and simple relations between the dynamical variables and second order moments, it becomes useful for both predictions of the rms dynamics and insights into the physics of collisionless relaxation. The later is the main topic of this Chapter.

The complexity of the relaxation process is illustrated by the phase-space evolution shown in Fig. 4.1. This figure shows the results obtained using a PIC simulation for a gaussian initial condition with a mismatch of $\alpha = 5$. Four snapshots of the beam phase-space are presented at progressive points along the propagation. The plot at $z = 0$ corresponds to the initial condition given by Eq. (2.3). The initial gaussian 'ellipse' develops spiral filaments that wrap around the beam core up until the coarse-grained distribution function almost reaches a stationary state. This picture is indeed difficult to describe analytically. In this Section, we develop an alternative quantitative theoretical description of the mixing process based on the CME model.

The predictions of the linearized CME model presented in Sec. 3.3.2 contain the relaxation of the rms oscillations. Therefore, we begin our study with an analysis of this simplified system of equations. Using Eq. (3.21), the linearized CME system can be written explicitly as

$$\begin{aligned}
\dot{a}_{mn} &= \sqrt{m(n+1)}a_{m-1,n+1} + \sqrt{mn}a_{m-1,n-1} - \kappa a_{00}\sqrt{2n}\sum_{k=0}^{\infty} a_{k,n-1}W_{mk} \quad \text{for} \quad \text{n} \neq 1, \\
\dot{a}_{m1} &= \sqrt{2m}a_{m-1,2} + \sqrt{m}a_{m-1,0} - \sqrt{2}\kappa a_{00}^2 W_{m0} + \\
&+ \kappa\sqrt{2}a_{00}\sum_{k=1}^{\infty} a_{k0}\left[\frac{\Gamma\left(\frac{m+k}{2}\right)\Gamma\left(\frac{k-m}{2}\right)\Gamma\left(\frac{m-k+2}{2}\right)}{2\pi^{3/2}\sqrt{m!k!}} - W_{mk}\right].
\end{aligned} \tag{4.1}$$

Notice the coupling of a_{kl} coefficients of a particular order j (*e.g.* with $k + l = j$) to coefficients of higher orders. For example, the equation for a_{11} has the following form

$$\begin{aligned}
\dot{a}_{11} &= a_{00} - \sqrt{2}\kappa a_{00}^2 W_{10} + \sqrt{2}a_{02} + \sqrt{2}\kappa a_{00}a_{20}\left(\frac{1}{4\sqrt{2}} - W_{12}\right) \\
&+ \sqrt{2}\kappa a_{00}a_{40}\left(-\frac{\sqrt{3}}{16\sqrt{2}} - W_{14}\right) + ...
\end{aligned} \tag{4.2}$$

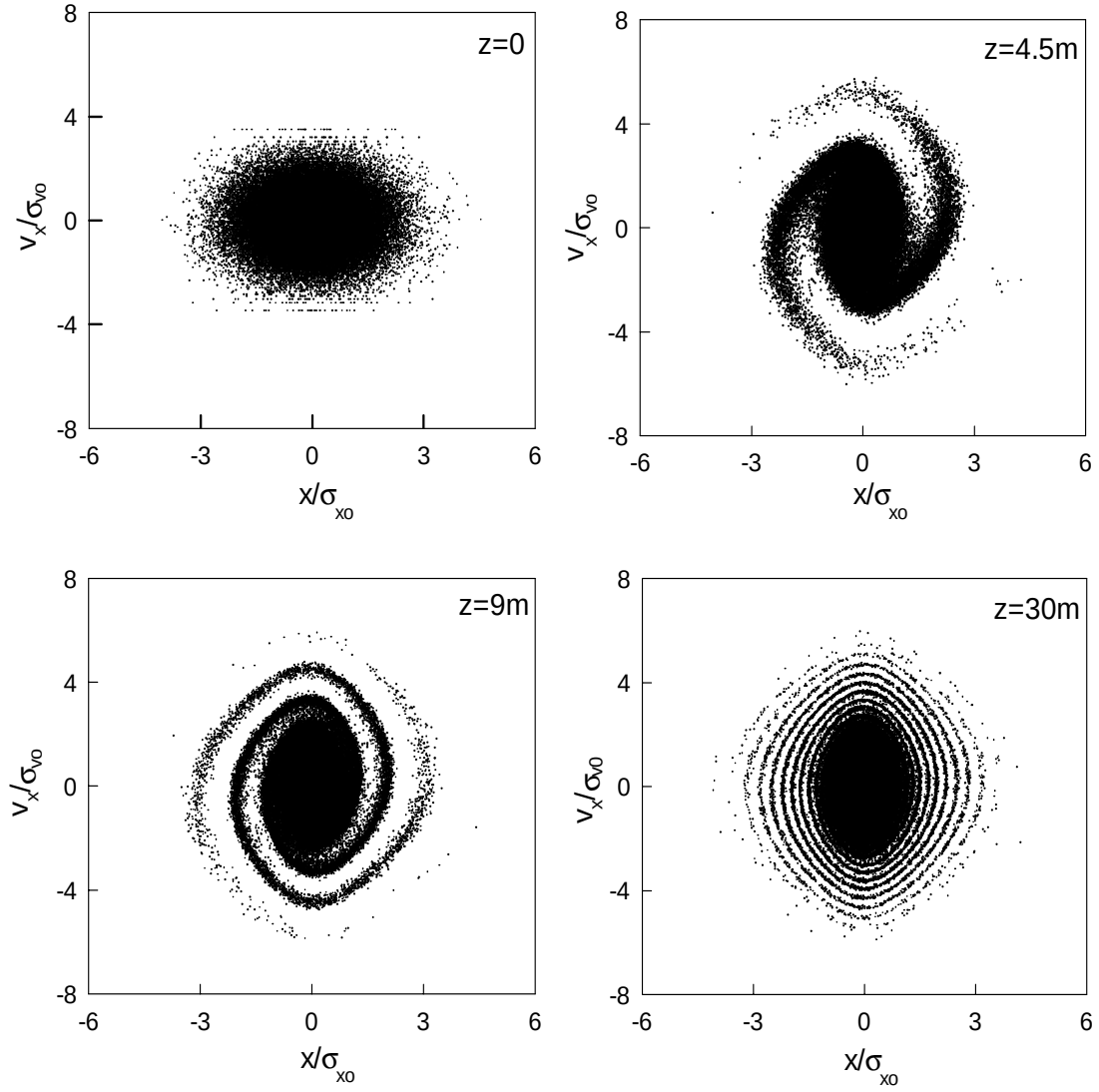

Figure 4.1: Phase-space dynamics of the initially gaussian beam with a mismatch of $\alpha = 5$.

We see that the evolution of a_{11} depends not only on the other coefficients of the second order (a_{20} and a_{02}), but also on a_{40}, a_{60}, *etc.* The coupling to higher orders is connected to the spatial nonlinearity of the force $F(X)$ defined in Eq. (3.6). Indeed, the equations for the moments $\langle X^p V^q \rangle$ are closed within each order for systems where the dynamics is governed by an $F(X)$ that depends linearly on the spatial variable X. This can be easily seen by writing the evolution equation for the moment $\langle X^p V^q \rangle$ in a system with $F = \beta X$ as

$$\dot{\langle X^p V^q \rangle} = p\langle X^{p-1} V^{q+1} \rangle + q\kappa \langle X^p V^{q-1} F \rangle = p\langle X^{p-1} V^{q+1} \rangle + q\kappa\beta \langle X^{p+1} V^{q-1} \rangle, \qquad (4.3)$$

where the equation of motion $\dot{V} = \kappa F$ for the beam particles is used. This results in the conclusion that for a particular order of a_{kl} coefficients in the Hermite polynomial representation there is no coupling to higher orders. This is evident from the properties of the linear mapping, given by Eq. (3.14), that connects the set of $\{\langle X^p V_x^q \rangle, p+q \leq j_{max}\}$ with $\{a_{mn}, m+n \leq j_{max}\}$. It is well known that systems with linear forces do not exhibit any relaxation in the rms properties and simple betatron oscillations take place. Thus, in the description of the expansion given by Eq. (3.10), the physics of the relaxation process is inherently connected with the coupling of a_{kl} coefficients of a certain order to higher orders.

We investigate the properties of this important coupling and its influence on the relaxation process through a careful analysis of the linearized system given by Eq. (4.1). To study the dynamics of the oscillating part that shows the relaxation, we explicitly separate the stationary part of the solution from its oscillating part using the notation $\mathbf{a} = \mathbf{a^{eq}} + \tilde{\mathbf{a}}$, where $\mathbf{a^{eq}}$ stands for the stationary equilibrium part of the solution and $\tilde{\mathbf{a}}$ for the oscillating part.

To make the transformation to the oscillating part of the solution, first consider the explicit linearized equations for the lowest order coefficients a_{20}, a_{11} and a_{02} which are given by

$$\begin{aligned}
\dot{a}_{20} - \sqrt{2} a_{11} &= 0, \\
\dot{a}_{11} - \sqrt{2} a_{02} - \sqrt{2}\kappa a_{00} a_{20} \left(\frac{1}{4\sqrt{2}} - W_{12}\right) &= a_{00}(1 - \sqrt{2}\kappa a_{00} W_{10}) \\
+\kappa\sqrt{2} a_{00} \sum_{k=3}^{\infty} a_{k0} \left[\frac{\Gamma\left(\frac{1+k}{2}\right)\Gamma\left(\frac{k-1}{2}\right)\Gamma\left(\frac{3-k}{2}\right)}{2\pi^{3/2}\sqrt{k!}} - W_{1k} \right], & \\
\dot{a}_{02} + 2\kappa a_{00} a_{11} W_{01} &= -2\kappa a_{00} \sum_{k=2}^{\infty} a_{k2} W_{0k}. \qquad (4.4)
\end{aligned}$$

Equations (4.4) are obtained using Eq. (4.1), and they are arranged in a special form with all a_{kl} of the order 2 written on the left-hand side. Terms that couple second to higher orders are written on the right-hand side. Making a transformation $\mathbf{a} = \mathbf{a^{eq}} + \tilde{\mathbf{a}}$ and using the relation for the stationary solution $\mathbf{B}\mathbf{a}^{eq} = -\mathbf{c}$, we can rewrite Eq. (4.4) as

$$\begin{aligned}
\dot{\tilde{a}}_{20} - \sqrt{2}\tilde{a}_{11} &= 0, \\
\dot{\tilde{a}}_{11} - \sqrt{2}\tilde{a}_{02} &- \sqrt{2}\kappa a_{00}\tilde{a}_{20}\left(\frac{1}{4\sqrt{2}} - W_{12}\right) = \\
&= \kappa\sqrt{2}a_{00}\sum_{k=3}^{\infty}\tilde{a}_{k0}\left[\frac{\Gamma\left(\frac{1+k}{2}\right)\Gamma\left(\frac{k-1}{2}\right)\Gamma\left(\frac{3-k}{2}\right)}{2\pi^{3/2}\sqrt{k!}} - W_{1k}\right], \\
\dot{\tilde{a}}_{02} + 2\kappa a_{00}\tilde{a}_{11}W_{01} &= -2\kappa a_{00}\sum_{k=2}^{\infty}\tilde{a}_{k2}W_{0k}.
\end{aligned} \tag{4.5}$$

In what follows, we often refer to the dynamics described by the left-hand side of Eqs. (4.5) as a decoupled problem for the second order variables. Introducing a matrix $\mathbf{B}^{(2)}$ as

$$\mathbf{B}^{(2)} = \begin{pmatrix} 0 & -\sqrt{2} & 0 \\ -\sqrt{2}\kappa a_{00}\left(\frac{1}{4\sqrt{2}} - W_{12}\right) & 0 & -\sqrt{2} \\ 0 & 2\kappa a_{00}W_{01} & 0 \end{pmatrix} \tag{4.6}$$

and a vector $\tilde{\mathbf{a}}^{(2)} = (\tilde{a}_{20}, \tilde{a}_{11}, \tilde{a}_{02})$, the left-hand side of Eqs. (4.5) can be expressed in the vector form as $\dot{\tilde{\mathbf{a}}}^{(2)} + \mathbf{B}^{(2)}\tilde{\mathbf{a}}^{(2)}$.

Some understanding can be gained, as will become clear from the following discussion, from considering the dynamics in the basis formed by the normal modes of the decoupled problem. The normal modes are solutions of the eigenvalue problem

$$\mathbf{B}^{(2)}\mathbf{e}^{(2)} = \lambda^{(2)}\mathbf{e}^{(2)}. \tag{4.7}$$

Equation (4.7), with $\mathbf{B}^{(2)}$ defined by Eq. (4.6), can be easily solved analytically. The resulting solution has one eigenvalue $\lambda_1^{(2)} = 0$ with a corresponding eigenvector $\mathbf{e}_1^{(2)}$ and two complex conjugate eigenfrequencies $\lambda_{2,3}^{(2)} = \pm i\omega_1^{(2)} = \pm 1.456i\sqrt{\kappa a_{00}}$ with the corresponding vectors $\mathbf{e}_{2,3}^{(2)}$. The expression for $\omega_1^{(2)}$ is obtained by a direct substitution of the numerical values for W_{12} and W_{01} into the matrix $\mathbf{B}^{(2)}$.

To perform the transformation into the basis formed by these normal modes, we first construct a matrix $\mathbf{E^{(2)}}$ out of the eigenvectors as columns as $\mathbf{E^{(2)}} = (\mathbf{e}_1^{(2)}, \mathbf{e}_2^{(2)}, \mathbf{e}_3^{(2)})$, so that

$$\tilde{\mathbf{a}}^{(2)} = \mathbf{E^{(2)}}\mathbf{q}^{(2)}. \tag{4.8}$$

Assuming that the inverse of the matrix $\mathbf{E^{(2)}}$ exists, the new variables $\mathbf{q}^{(2)}$ in the decoupled basis can be obtained using an inverse transformation as

$$\mathbf{q}^{(2)} = [\mathbf{E^{(2)}}]^{-1}\tilde{\mathbf{a}}^{(2)}. \tag{4.9}$$

We now transform the left-hand side of the evolution Eqs. (4.5) for $\tilde{a}_{20}$, $\tilde{a}_{11}$ and $\tilde{a}_{02}$ into the basis of the decoupled normal modes by multiplying the vector by $[\mathbf{E^{(2)}}]^{-1}$. As a result, the left-hand side takes the diagonal form $\dot{\mathbf{q}}_i^{(2)} + \lambda_i^{(2)}\mathbf{q}_i^{(2)}$. The transformation given by Eq. (4.8) is also used for the vector $\tilde{\mathbf{a}}^{(2)}$ appearing in equations for all orders in our dynamical system.

An analogous diagonalization procedure is used for the decoupled fourth order variables. Consider the vector of fourth order oscillating variables $\tilde{\mathbf{a}}^{(4)} = (\tilde{a}_{40}, \tilde{a}_{31}, \tilde{a}_{22}, \tilde{a}_{13}, \tilde{a}_{04})$. We extract the part of the dynamical matrix $\mathbf{B}$ that governs the evolution within the order and denote it by $\mathbf{B}^{(4)}$. It plays the role of the matrix $\mathbf{B}^{(2)}$ for fourth order variables. The eigenvalue problem governing the dynamics within the fourth order, $\mathbf{B}^{(4)}\mathbf{e}^{(4)} = \lambda^{(4)}\mathbf{e}^{(4)}$, is then solved. While it can, in principle, be solved analytically we instead resort to the numerical methods to avoid cumbersome algebra. Finally, five eigenvalues of $\mathbf{B}^{(4)}$ are obtained: one eigenvalue with a zero value $\lambda_1^{(4)} = 0$, and two complex conjugate pairs of eigenvalues $\lambda_{2,3}^{(4)} = \pm i\omega_1^{(4)}$ and $\lambda_{4,5}^{(4)} = \pm i\omega_2^{(4)}$ which are ordered with $|\omega_1^{(4)}| < |\omega_2^{(4)}|$. Numerical studies, performed for a wide range of the normalization parameter κ, indicate that in contrast with the eigenvalue problem for the coupled system considered in Sec. 3.3.2, all eigenvalues of the decoupled problem have zero real parts. The eigenvectors $\mathbf{e}^{(4)}$ are combined into a matrix $\mathbf{E^{(4)}}$. We transform into this eigenvalue basis for the 4^{th} order variables with

$$\tilde{\mathbf{a}}^{(4)} = \mathbf{E^{(4)}}\mathbf{q}^{(4)}. \tag{4.10}$$

This transformation is then used for the $\tilde{\mathbf{a}}^{(4)}$ vector in all equations of the *coupled* system.

We continue this transformation to higher orders. After the transformation is complete, our system takes on diagonal form within every order. Loosely speaking, the system is replaced by a set of harmonic oscillators that are coupled to modes of other orders. Note, however, that the coupling terms can not be obtained from a Hamiltonian, and the analogy with coupled harmonic oscillators of different natural frequencies is used only to provide intuition.

The physics of relaxation is intimately connected to the oscillator coupling to higher order modes. Naturally, we expect this coupling effect to depend on the coupling

strength and the frequency mismatch. We now investigate the decoupled eigenvalue spectrum. Specifically, we look for possible resonances that can dramatically increase the efficiency of the interaction.

The complicated form of the equations preventing a simple analytical treatment, a typical spectrum is investigated numerically. The properties of the normalized equations, such as the eigenvalues of the decoupled problem, depend on the value of the normalization coefficient κ. Consider a specific example of a case with $\kappa = 1.1$. This value of the normalization parameter is encountered in the simulation for an initially gaussian beam with $\alpha = 3$ and $\sigma_{xo} = 2.9$mm, $\sigma_{vo} = 2.1 \times 10^6$, $\gamma = 100$ and $n_0 = 7.2 \times 10^{16}\mathrm{m}^{-3}$ normalized to the analytically computed final state. Consider the sets of frequencies of the decoupled oscillators λ^j which are plotted in Fig. 4.2 *vs* their order j. The eigenvalues are normalized by $\omega_1^{(2)}$. The inspection of the spectrum shows that the system contains many oscillators

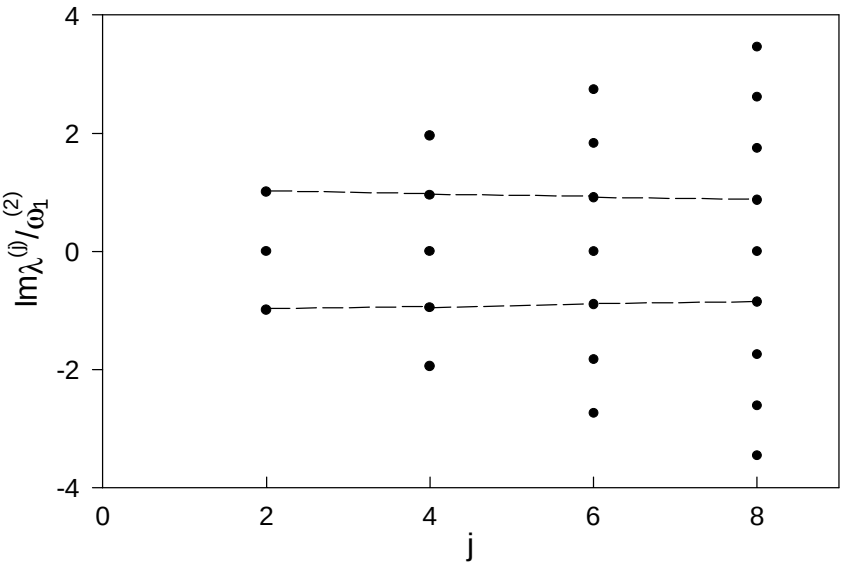

Figure 4.2: Frequency spectrum of the decoupled problem *vs* order j for $\kappa = 1.1$. The modes of the first resonant chain are connected with a dashed line for clarity.

which are nearly resonant. The eigenmodes can be grouped into chains with oscillators of almost equal frequencies with $\lambda_i^{(j)} \simeq \lambda_i^{(k)}$ and $j \neq k$. For example, every order has one eigenvector with a frequency of a numerical value close to $\omega_1^{(2)}$ (the frequency of the single oscillator of order 2). This resonant chain with $\omega_1^{(2)} \simeq \omega_1^{(4)} \simeq \omega_1^{(6)}$... can be easily seen in

Fig. 4.2. In what follows, we refer to this chain as the lowest frequency chain, or simply the lowest chain. Every order except the second order has one mode at a natural frequency almost equal to $\omega_2^{(4)}$, and a chain $\omega_2^{(4)} \simeq \omega_2^{(6)} \simeq \omega_2^{(8)}$... follows. In our example with $\kappa = 1$, the relative difference between two lowest frequencies of orders $j = 2$ and $j = 4$, i.e. $\omega_1^{(2)}$ and $\omega_1^{(4)}$ is only 5%. The difference between two lowest frequencies of orders $j = 4$ and $j = 6$ is also about 5%. A similar picture is observed upon the numerical solution of the decoupled eigenvalue problem with a wide range of the normalization parameter. These results indicate that the relative values of the frequency mismatch between resonant modes is independent of κ. For example, for two lowest order resonant modes the relative mismatch is computed to be $(\omega_1^{(2)} - \omega_1^{(4)})/\omega_1^{(2)} = 0.00495 \pm 10^{-6}$ in the range of $0.1 \leq \kappa \leq 6$.

Now we consider consequences of these resonances on the coupled system. If the couplings were absent in the system, the modes would simply oscillate in time with fixed amplitudes. For example, the variables $\mathbf{q_2^{(2)}}$ and $\mathbf{q_2^{(4)}}$ corresponding to the resonant normal modes with the eigenfrequency ω_1 and orders 2 and 4 respectively simply oscillate in time as $e^{i\omega_1 \tau}$. However, the coupling between orders allows the amplitudes to vary in time. Resonant coupling between modes can cause a rapid transfer of excitation between different oscillators assuming that the corresponding coupling strength is non-zero. We investigate the coupling between resonant modes in the next section.

To illustrate the transfer, we first consider a reduced problem where only first 6 orders (only a_{kl} with $k+l = 2, 4, 6$) are retained, and we consider an initially gaussian beam with $\alpha = 3$. The evolution of the rms-beam size obtained numerically using the linearized model is plotted in Fig. 4.3. It exhibits a modulation in the amplitude of the oscillations and not a complete relaxation which is due to an insufficient number of orders retained in the simulation. The numerical computation is performed using the normalization to the analytically calculated final state given by Eqs. (2.33) and (2.38). No artificial attenuation is used in the numerical integration. The propagation curves for the amplitudes of three resonantly coupled modes $|\mathbf{q}_2^{(2)}|$ (solid line), $|\mathbf{q}_2^{(4)}|$ (dashed line) and $|\mathbf{q}_2^{(6)}|$ (dotted line) at the lowest non-zero frequency ω_1 are presented in Fig. 4.4. It can be seen that initially $|\mathbf{q}_2^{(j)}| > |\mathbf{q}_2^{(j+2)}|$ and almost all the initial excitation is concentrated in the lowest order mode $\mathbf{q}_2^{(2)}$. A resonant driving of $|\mathbf{q}_2^{(4)}|$ and $|\mathbf{q}_2^{(6)}|$ by the initially large $|\mathbf{q}_2^{(2)}|$ can be seen at the initial stage of the propagation with a subsequent transfer of the excitation back into $\mathbf{q}_2^{(2)}$. Comparing Fig. 4.3 with Fig. 4.4, we see that the propagation range of the excitation transfer (about $\Delta z \simeq 2$m) agrees with the scale of the modulation in the rms oscillations.

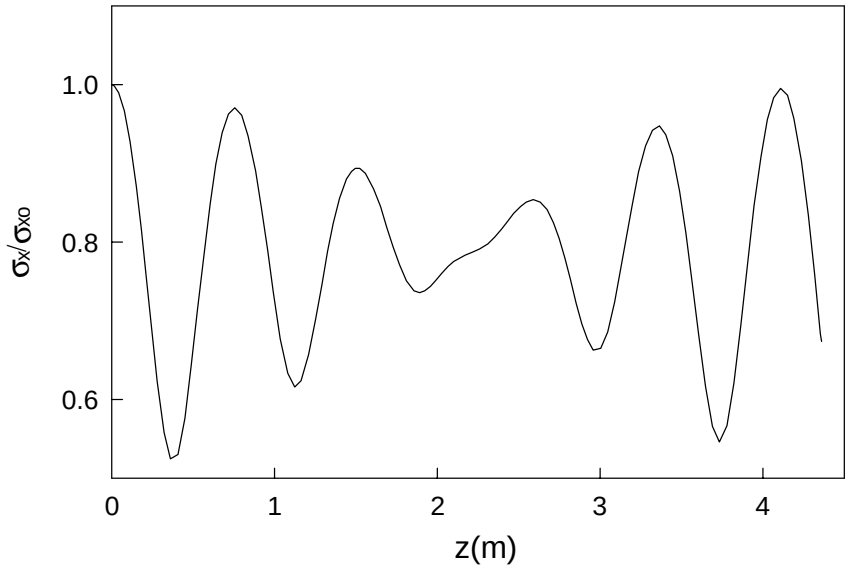

Figure 4.3: Linearized CME propagation curve for the rms beam size of the initially gaussian beam with a mismatch of $\alpha = 3$. In the simulation $j_{max} = 6$ and no artificial attenuation used.

We now retain a larger number of orders in the dynamical simulation for the same initial condition. Twenty orders are kept in the simulation, and the artificial attenuation term with the width of $\Delta = 10$ is used to compensate for the unlimited growth of higher orders. The change of the rms beam size obtained in the simulation is presented in Fig. 4.5. The beam size oscillations exhibit a complete relaxation in this case.

The corresponding evolution of $|\mathbf{q}_2^{(2)}|$, $|\mathbf{q}_2^{(4)}|$ and $|\mathbf{q}_2^{(6)}|$ obtained using the linearized equations of motion is shown in Fig. 4.6 with solid, dashed, and dotted lines, respectively. As a result of the resonance coupling, the largest amplitude $|\mathbf{q}_2^{(2)}|$ decays, $|\mathbf{q}_2^{(4)}|$ slowly grows and then decays at later times and $|\mathbf{q}_2^{(6)}|$ grows substantially and then relaxes. The decay of $|\mathbf{q}_2^{(2)}|$ in time corresponds to the relaxation of the rms oscillations as $|\mathbf{q}_2^{(2)}|$ corresponds to the amplitude of the only oscillating mode for the coefficients of the second order which in turn are connected to the rms properties of the distribution. A similar process is observed for other amplitudes $|\mathbf{q}_j^{(k)}|$. A cascading resonant driving of higher and higher modes takes place at the expense of lower order coefficients which leads to the relaxation of the oscillations. Note that the higher order modes correspond to the higher order coefficients a_{kl} which

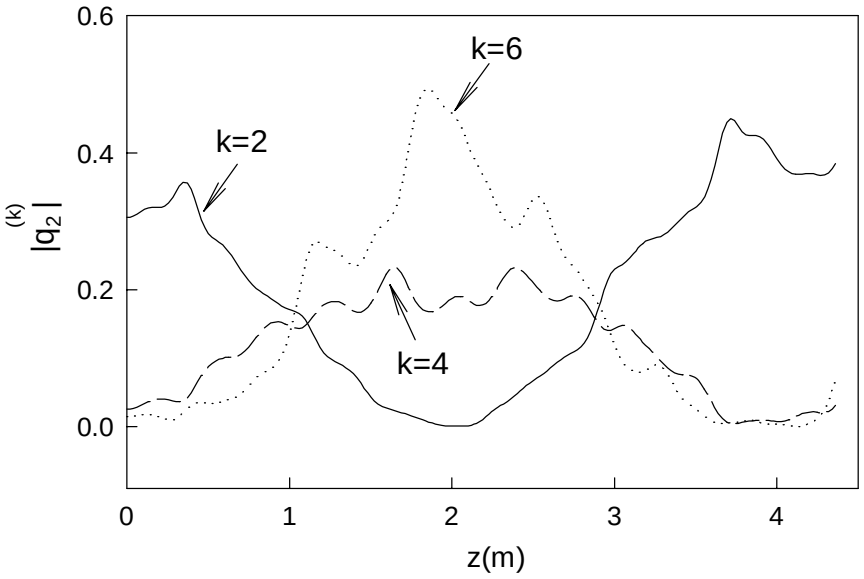

Figure 4.4: Propagation curves for the amplitudes of three lowest order resonantly coupled amplitudes obtained by a linearized simulation with $j_{max} = 6$ and no artificial attenuation.

in turn correspond to the smaller scale features of the phase-space distribution function. Indeed, the term in the expansion of the distribution function with the amplitude a_{kl} has the space-velocity dependence of the form $H_k(X)H_l(V)e^{-X^2}e^{-V^2}$ thus resolving finer scales in the phase-space as $k + l$ is increased. Therefore, the effect of the cascading transfer of excitation along the chains of resonantly coupled modes can also be interpreted as a direct manifestation of the excitation of finer and finer scales of the distribution function in the process of the phase mixing.

Our analysis so far is based on a simplified linearized system of the dynamical equations. To investigate the effect of nonlinearity in the coefficients a_{kl}, we return to the full nonlinear CME system. We perform the numerical simulation for the same initial condition of a gaussian beam with $\alpha = 3$. The solution is expanded over the decoupled basis to illustrate the effect of the nonlinearity on the resonant interactions. Results for $|\mathbf{q}_2^{(2)}|$, $|\mathbf{q}_2^{(4)}|$ and $|\mathbf{q}_2^{(6)}|$ are presented in Fig. 4.7. Qualitatively similar behavior to that observed in the linearized model can be seen with all the effects of the excitation transfer still present in the dynamics.

Another example of the amplitude dynamics is presented in Fig. 4.8. An initial

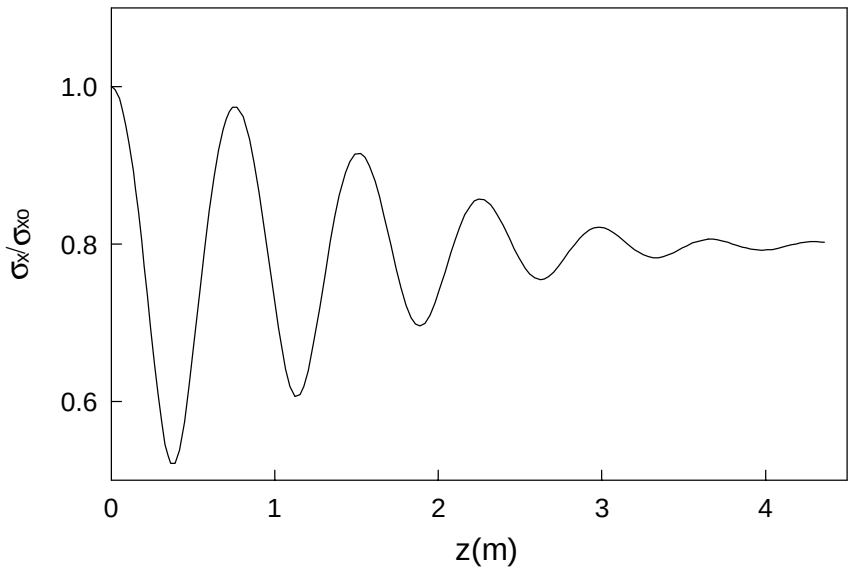

Figure 4.5: Linearized CME propagation curve for the rms beam size of the initially gaussian beam with a mismatch of $\alpha = 3$. In the simulation $j_{max} = 20$ and $\Delta = 10$.

gaussian beam with $\alpha = 0.33$ is used at start up. A full nonlinear CME simulation is performed with $j_{max} = 20$ and $\Delta = 8$. The result are similar to those obtained for a beam with an initial mismatch of $\alpha = 3$.

We further illustrate the change in the amplitudes of the resonant modes with an example of an initially uniform beam. The initial electron beam parameters are $\sigma_{xo} =$ 2.28mm, $\sigma_{vo} = 2.6 \times 10^6$, $\gamma = 100$ and $n_0 = 6.316 \times 10^{16}\mathrm{m}^{-3}$. The initial distribution is taken according to Eq. (2.4). The oscillatory part of the results of the full nonlinear CME simulation, performed with $j_{max} = 20$ and $\Delta = 10$, is expanded over the decoupled basis of the linear problem. The results for three lowest order resonant modes are presented in Fig. 4.9. The decay of $|\mathbf{q}_2^{(2)}|$ and a growth of $|\mathbf{q}_2^{(4)}|$ and especially of $|\mathbf{q}_2^{(6)}|$ can be seen. Small oscillations in the dynamics of the amplitudes that are clearly visible in the figure can be attributed to the interaction of the resonant modes with other modes. The difference in the natural frequencies of the modes gives rise to oscillations.

In all the numerical examples of the amplitude dynamics presented in this section, the initial values of $|\mathbf{q}_2^{(4)}|$ and $|\mathbf{q}_2^{(6)}|$ are significantly smaller than of $|\mathbf{q}_2^{(2)}|$. This opens the possibility of a simplified analytical model with $|\mathbf{q}_2^{(2)}|$ acting initially as a pump for $|\mathbf{q}_2^{(4)}|$.

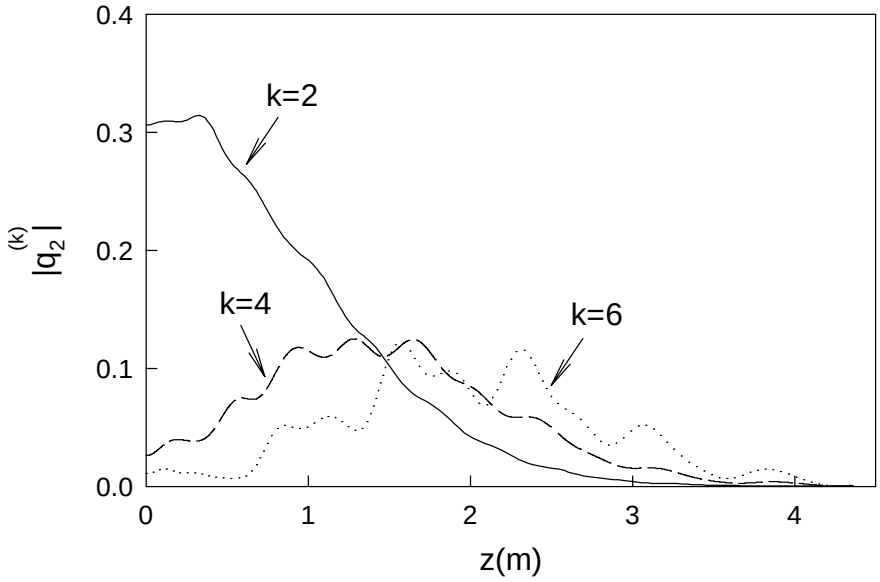

Figure 4.6: Propagation curves for the amplitudes of three lowest order resonantly coupled amplitudes obtained by a linearized CME simulation with $j_{max} = 20$.

To investigate this further, we consider the initial distribution of excitation between modes for different initial conditions. Relative amplitudes $|\mathbf{q}_2^{(4)}|/|\mathbf{q}_2^{(2)}|$ and $|\mathbf{q}_2^{(6)}|/|\mathbf{q}_2^{(2)}|$ are studied for initially gaussian and uniform beams with the mismatch in the range of $0.2 < \alpha < 10$. The computation is performed normalizing to the analytically calculated asymptotic state. The results are plotted in Fig. 4.10 for the initially gaussian beam and in Fig. 4.11 for the initially uniform distribution. This figure demonstrates that in most cases it is primarily the lowest order mode $|\mathbf{q}_2^{(2)}|$ that is excited initially. The relative amplitudes of higher order modes of the lowest chain are small for the initially gaussian beam for all but matched beams with $\alpha \simeq 1$. We thus expect a simple description of the rapid initial transfer of excitation from second order (*i.e.* with order 2 acting as a pump) to the forth order mode to be valid for all but matched beams. Fig. 4.11 shows that the relative initial amplitudes $|\mathbf{q}_2^{(4)}|/|\mathbf{q}_2^{(2)}|$ and $|\mathbf{q}_2^{(6)}|/|\mathbf{q}_2^{(2)}|$ are higher for a uniform than for a gaussian beam. The dynamical picture becomes more complicated, and an exchange between second, forth and possibly higher order modes is expected to be important in the understanding the dynamics.

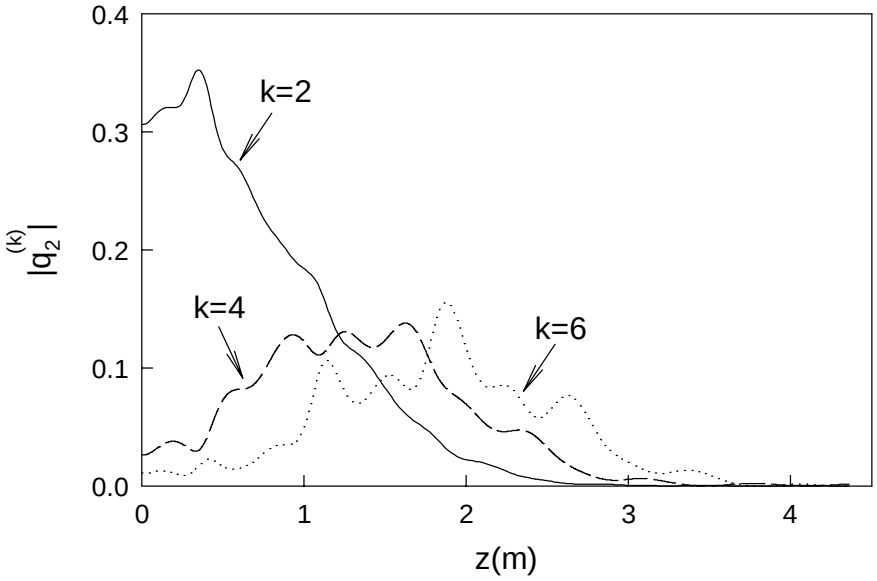

Figure 4.7: Propagation curves for the amplitudes of three lowest order resonantly coupled amplitudes obtained by a full nonlinear CME simulation with $j_{max} = 20$ and $\Delta = 10$. The initial gaussian beam with a mismatch of $\alpha = 3$ is used.

4.2 Relaxation Time Estimate

After identifying the resonant coupling as a possible source of the rapid relaxation of the rms oscillations, we now concentrate on the understanding of the oscillation decay through the study of mode coupling. We succeed in making simple estimates of the decay times for rms oscillations.

We begin with the dynamical equations for a_{kl} coefficients written in the representation of $\{\mathbf{E}^{(j)}\}$ basis introduced in Sec. 4.1. We concentrate on equations for the evolution of $\mathbf{q}_2^{(2)}$ and $\mathbf{q}_2^{(4)}$ that correspond to the resonantly coupled amplitudes of second and fourth orders which oscillate in the decoupled case at frequencies $\lambda_2^{(2)} \simeq \lambda_2^{(4)} \simeq i\omega_1$. The amplitude $\mathbf{q}_2^{(2)}$ is of interest because of its linear relation to the oscillation amplitude of the rms beam properties. After transforming into the decoupled basis, the evolution equations for these two amplitudes can be written as

$$\begin{aligned} \dot{\mathbf{q}}_2^{(2)} &= \lambda_2^{(2)}\mathbf{q}_2^{(2)} + \gamma_{24}\mathbf{q}_2^{(4)} + \text{higer order and non} - \text{resonant terms}\,, \\ \dot{\mathbf{q}}_2^{(4)} &= \lambda_2^{(4)}\mathbf{q}_2^{(4)} + \gamma_{42}\mathbf{q}_2^{(2)} + \text{higer order and non} - \text{resonant terms}\,. \end{aligned} \tag{4.11}$$

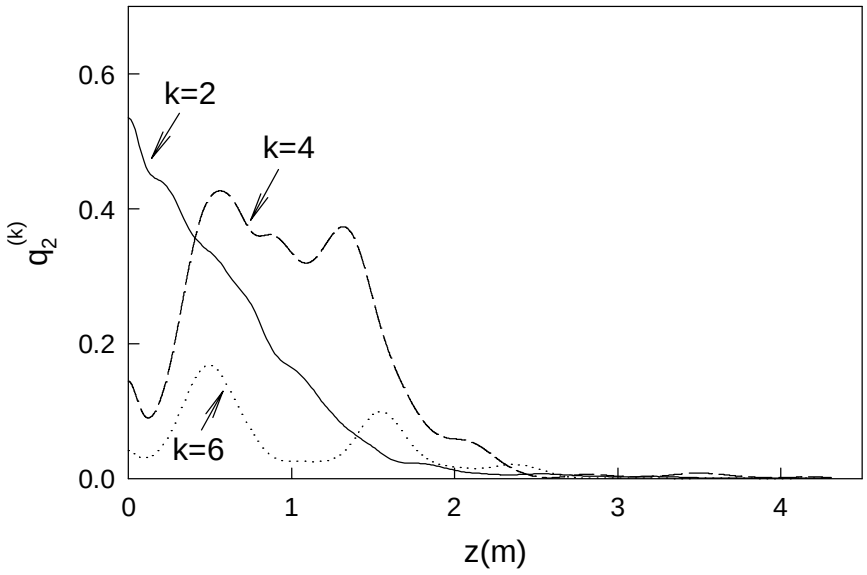

Figure 4.8: Propagation curves for the amplitudes of three lowest order resonantly coupled amplitudes obtained from a full nonlinear CME simulation with $j_{max} = 20$ and $\Delta = 10$. An initial gaussian beam with a mismatch of $\alpha = 0.33$ is used.

Notations γ_{24} and γ_{42} are used for the coupling strength of the interaction. Extracting the time dependence on its natural frequency, each mode is represented as

$$\mathbf{q}_i^{(j)} = \tilde{\mathbf{q}}_i^{(j)} e^{\lambda_i^{(j)}\tau}. \tag{4.12}$$

In the decoupled problem, the 'amplitude' of the mode $\tilde{\mathbf{q}}_i^{(j)}$ remains constant. It varies in time in the full system due to the mode coupling. We emphasize here that no assumption is made about the 'slowness' of the time dependence of $\tilde{\mathbf{q}}_i^{(j)}(\tau)$. Substitution of Eq. (4.12) into Eqs. (4.11) yields

$$\begin{aligned} \dot{\tilde{\mathbf{q}}}_2^{(2)} &= \gamma_{24}\tilde{\mathbf{q}}_2^{(4)} e^{-i\Delta\omega_{24}\tau} + \dots , \\ \dot{\tilde{\mathbf{q}}}_2^{(4)} &= \gamma_{42}\tilde{\mathbf{q}}_2^{(2)} e^{i\Delta\omega_{24}\tau} + \dots , \end{aligned} \tag{4.13}$$

where $\Delta\omega_{24} = \omega_1^{(2)} - \omega_1^{(4)}$ and $i\omega_1^{(j)} = \lambda_2^{(j)}$.

Neglecting the frequency mismatch (which is equal to about 5% of $\omega_1^{(2)}$ as it was reported in previous section), higher order couplings and non-resonant contributions, the dynamics can be approximately modeled as

$$\dot{\tilde{\mathbf{q}}}_2^{(2)} = \gamma_{24}\tilde{\mathbf{q}}_2^{(4)},$$

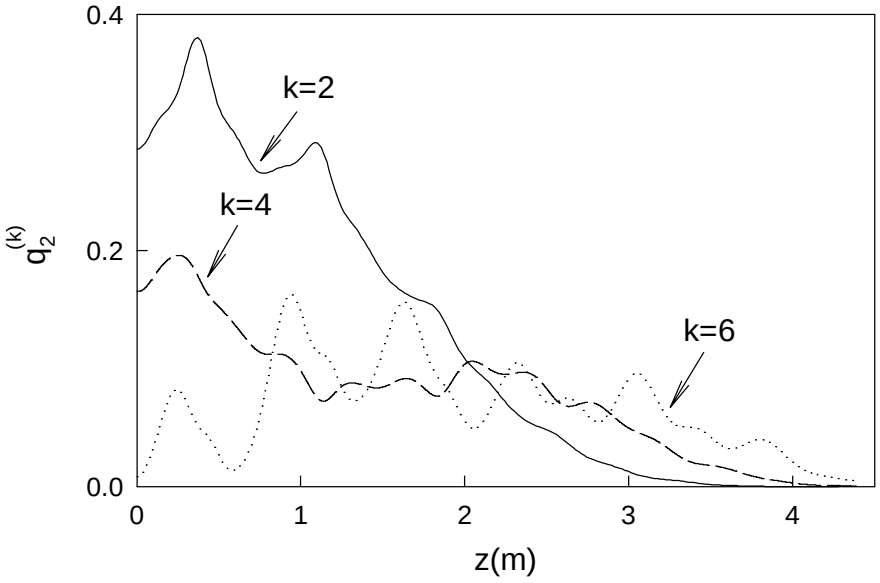

Figure 4.9: Propagation curves for the amplitudes of three lowest order resonantly coupled amplitudes obtained by a full nonlinear CME simulation with $j_{max} = 20$ and $\Delta = 10$. The initial uniform beam with a mismatch of $\alpha = 5$ is used.

$$\dot{\tilde{\mathbf{q}}}_2^{(4)} = \gamma_{42}\tilde{\mathbf{q}}_2^{(2)}. \tag{4.14}$$

To make estimates for particular examples coupling coefficients γ_{24} and γ_{42} need to be computed. In principle, the eigenvalue problem for $\mathbf{B}^{(4)}$ can be solved analytically and dynamical equations can be transformed into the desired uncoupled representation. However, to avoid cumbersome algebraic calculations the procedure is performed numerically on a case by case basis. In all cases considered, the product $\gamma_{24}\gamma_{42}$ is found to be real and with and negative ($\gamma_{24}\gamma_{42} < 0$).

The dynamical Eqs. 4.14 can be solved easily for the initial value problem with $\mathbf{q}_2^{(2)}(\tau = 0) = \mathbf{q}_{20}^{(2)}$ and $\mathbf{q}_2^{(4)}(\tau = 0) = \mathbf{q}_{20}^{(4)}$. The solution becomes

$$\begin{aligned} \tilde{\mathbf{q}}_2^{(2)} &= \mathbf{q}_{20}^{(2)}\cos(\Omega\tau) + \sqrt{\frac{\gamma_{24}}{\gamma_{42}}}\mathbf{q}_{20}^{(4)}\sin(\Omega\tau), \\ \tilde{\mathbf{q}}_2^{(4)} &= \mathbf{q}_{20}^{(4)}\cos(\Omega\tau) + \sqrt{\frac{\gamma_{42}}{\gamma_{24}}}\mathbf{q}_{20}^{(2)}\sin(\Omega\tau), \end{aligned} \tag{4.15}$$

where $\Omega = \sqrt{-\gamma_{24}\gamma_{42}}$. We implicitly assumed that $\gamma_{24}\gamma_{42} < 0$.

The energy $\mathcal{E}_2$ of the approximate 2 mode system can be identified with

$$\mathcal{E}_2 = \gamma_{42}^*|\tilde{\mathbf{q}}_2^{(2)}|^2 - \gamma_{24}|\tilde{\mathbf{q}}_2^{(4)}|^2, \tag{4.16}$$

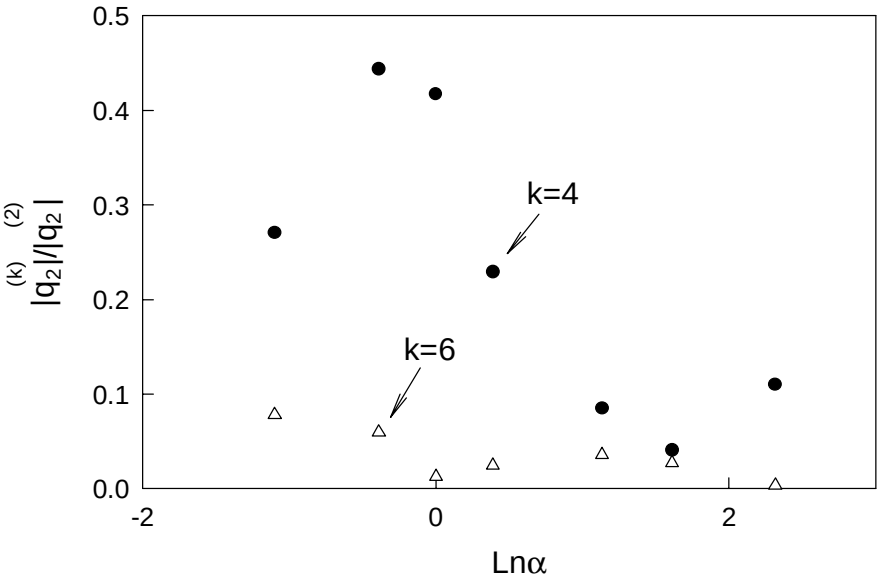

Figure 4.10: Dependence of the initial relative amplitudes $|\mathbf{q}_2^{(4)}|/|\mathbf{q}_2^{(2)}|$ (•) and $|\mathbf{q}_2^{(6)}|/|\mathbf{q}_2^{(2)}|$ (△) of a gaussian beam on the initial mismatch α.

where $*$ denotes complex conjugation. Substituting Eq. (4.16) into Eqs. (4.14) it can be easily verified that $\mathcal{E}_2$ remains constant in time within the simplified model. In this reduced model, $\gamma_{42}^*|\tilde{\mathbf{q}}_2^{(2)}|^2$ and $-\gamma_{24}|\tilde{\mathbf{q}}_2^{(4)}|^2$ can be identified with the energy of the modes $\mathbf{q}_2^{(2)}$ and $\mathbf{q}_2^{(4)}$ respectively. A continuous transfer of energy from $\mathbf{q}_2^{(2)}$ to $\mathbf{q}_2^{(4)}$ and back assures the constancy of the total energy $\mathcal{E}_2$. If higher orders are taken into account and the whole infinite chain is included, the cascade continues to $\mathbf{q}_2^{(6)}$, $\mathbf{q}_2^{(8)}$ and so on resulting in the decay of $\mathbf{q}_2^{(2)}$ and $\mathbf{q}_2^{(4)}$.

The characteristic time for the excitation transfer between lowest order modes can be estimated from this model. The relaxation time τ_r is defined as the time required for the oscillation amplitude of $\langle x^2 \rangle$ to decrease by a half. It can be estimated theoretically from Eq. (4.15) for the approximate initial condition $\mathbf{q}_{20}^{(4)} = 0$, valid in most cases with a mismatched gaussian beam (see Fig. 4.10) of $\alpha \neq 1$. Assuming that the decay of the rms amplitude follows the simplified model of 2 mode coupling at the initial stage of the propagation, the time to decrease $\tilde{\mathbf{q}}_2^{(2)}$ in half is equal to

$$\tau_{min} = \frac{\pi}{3\Omega}, \tag{4.17}$$

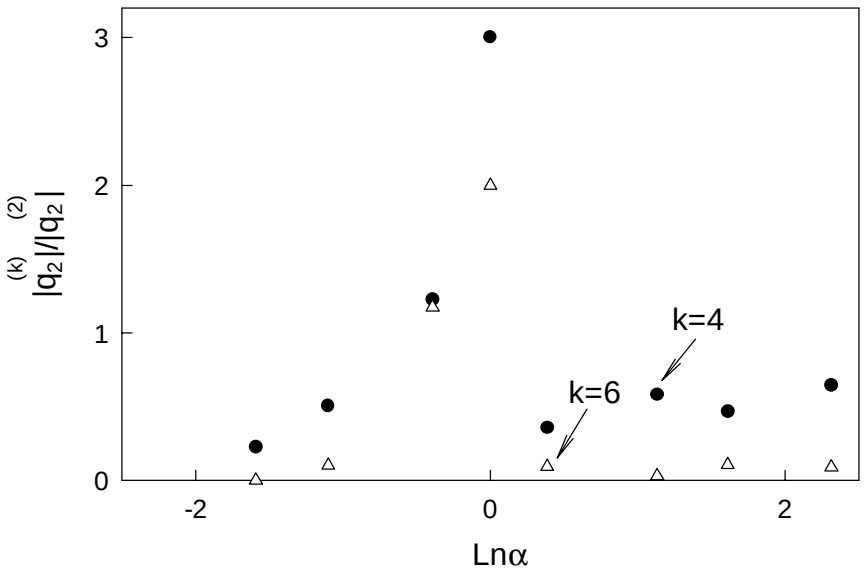

Figure 4.11: Dependence of the relative amplitudes $|\mathbf{q}_2^{(4)}|/|\mathbf{q}_2^{(2)}|$ (•) and $|\mathbf{q}_2^{(6)}|/|\mathbf{q}_2^{(2)}|$ (△) of a uniform beam on the initial mismatch α.

or, explicitly,

$$\tau_{min} = \frac{\pi}{3}\frac{1}{\sqrt{|\gamma_{24}\gamma_{42}|}}. \tag{4.18}$$

In the opposite limit of $\mathbf{q}_{20}^{(2)} = 0$ and $\mathbf{q}_{40}^{(4)} \neq 0$, an initial transfer of energy from $\tilde{\mathbf{q}}_2^{(4)}$ to $\tilde{\mathbf{q}}_2^{(2)}$ seen as a growth of the rms oscillations. In the full system, however, the transfer to higher order resonant modes takes place and the oscillations decay. An estimate of the relaxation time in this limit, valid for beams that are close to matched beams, is

$$\tau_{max} = \frac{5\pi}{6\Omega} = \frac{5\pi}{6}\frac{1}{\sqrt{|\gamma_{24}\gamma_{42}|}}. \tag{4.19}$$

For the intermediate range of the initial mismatch parameter we expect a smooth transition between the result of Eq. (4.18) to Eq. (4.19).

In general, the rms oscillation relaxation time is expected to fall in the range between the estimates given by Eqs. (4.18) and (4.19), depending on the initial condition. Note that according to our estimates, $\tau_{max} = 2.5\tau_{min}$ indicating a relatively weak dependence of the relaxation time on the initial condition. The order of magnitude of τ_r is in turn determined not by the details of the initial condition but by the values of the coupling coefficients γ_{24} and γ_{42} which are, in turn, determined by the functional dependence of the force

$F(X)$. It should be kept in mind that the estimates of Eqs. (4.18) and (4.19) depend on the normalization since the coupling strength coefficients take on different values as κ changes. Two main approximations are made in deriving Eqs. (4.18)–(4.19): (1) the linearization of the dynamical equations for a_{kl} is performed and (2) only lowest order resonant interaction for the oscillating part of $\langle x^2 \rangle$ is taken into account. As it was discussed in Sec. 3.3.3, the results of the linearized model depend on the normalization, and an optimal normalization, namely to the analytically calculated asymptotic state, was suggested. This normalization roughly corresponds to the asymptotic values of the rms beam size and velocity. It is used to determine the values of coupling strengths γ_{24} and γ_{42} to find the numerical values for the relaxation time estimates.

It is useful to estimate the relaxation time relative to the period of oscillations occurring in the rms-beam properties. The relative scale indicates the efficiency of the relaxation process compared to the betatron oscillations. The period of betatron oscillations can be estimated as $T = 2\pi/\omega_1^{(2)}$ with $\omega_1^{(2)}$ already found in the course of solving the decoupled eigenvalue problem. Substituting numerical values for γ_{24} and γ_{42} into Eqs. (4.18)-(4.19), the estimates of the normalized relaxation time are equal to $\tau_{min}/T = 1.64$ and $\tau_{max}/T = 4.1$. The comparison between these estimate and the results of the PIC simulation for different initial conditions is presented in Fig. 4.12. The predictions for the initially gaussian beams ($\triangle$) of a different initial mismatch are plotted together with the results for the initially uniform beams ($\bullet$). As expected, the result of Eq. (4.18) gives a good estimate for the oscillations relaxation time for the initially mismatched gaussian beams. The approximation of the initial dominance of the second order mode used in the derivation of Eq. (4.18) is satisfied for most cases considered (see Fig. 4.10). For the values of $\alpha \simeq 1$ a significant initial values of forth order mode can be seen in Fig. 4.10, and the larger values of τ_r for the matched beam seen in Fig. 4.12 are in approximate agreement with the estimate of Eq. (4.19). A slightly different picture is seen for the initially uniform beam. As Fig. 4.11 shows, the initial presence of the forth order mode can not be ignored for most of the range of the initial mismatch parameter, and we expect the relaxation time to be estimated by Eq. (4.19). For the almost matched beams, higher order modes also become important and the approximations of the two mode model breaks down. Indeed, the result of Fig. 4.12 for the uniform beam shows agreement with Eq. (4.19) for $\alpha > 2$ and $\alpha < 0.6$. Overall, we conclude that rms resonant time can be roughly estimated as being in the range of $1.64 < \tau_r/T < 4.1$ predicted by Eqs. (4.18) and (4.19) for most of the cases considered.

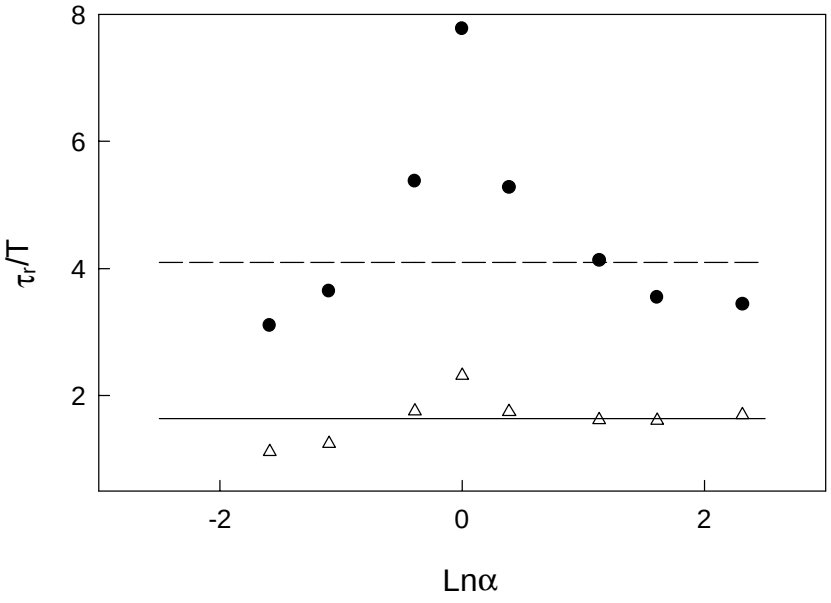

Figure 4.12: Comparison of PIC results for the relaxation time with the estimates of Eqs. (4.18) (——-) and (4.19) (- - - -) for initially gaussian (△) and uniform (•) beams.

For the same initial distribution function profile, a larger relaxation time is expected for the almost matched beams than for the highly mismatched ones.

4.3 Resonant Coupling Strength and Force Nonlinearity

The problem of the decay of betatron oscillations as a beam propagates through a plasma can also be considered in a more general context. Our picture of the relaxation process can be considered as a simplified description of the complicated phase mixing dynamics which occurs in all systems with nonlinear forces. As it is well known, a Vlasov system with a linear external force $F_x(x) \sim x$ does not exhibit any relaxation; any decay is connected to the nonlinearity of the force. At the same time, the discussion and results of Sec. 4.1 show that within the model described by the expansion of Eq. (3.10) the coupling between the modes in resonance with the second order moment variables is responsible for the rapid relaxation of the rms oscillations.

To clarify the connection between the nonlinearity of the force and resonant inter-

actions between modes, we study the relation between the nonlinearity and coupling mode parameters such as frequency mismatch and interaction strength. For this purpose, we consider a simplified example of a beam which is acted upon by an external force defined by the two parameter family

$$F_x(x) = -\nu(x - \mu x^3). \tag{4.20}$$

We again use the CME technique. We emphasize here that in the derivation of the dynamical system given by Eq. (3.21) a specific form of the force given by Eq. (3.6) is assumed. The derivation is now repeated for a force given by Eq. (4.20), and a dynamical system for the evolution of the expansion coefficients of the distribution function in the asymmetrically weighted Hermite polynomial basis is obtained. The force is external so that the Vlasov equation is linear in the distribution function f. Therefore, the resulting problem for $\{a_{kl}\}$ coefficients is also linear in a_{kl}, and no linearization is needed for the modal analysis.

Consider, as a specific example, an initial condition given by Eq. (2.3) with $\sigma_{xo} =$ 2.28mm, $\sigma_{vo} = 2.6 \times 10^6$m/s, $\gamma = 100$. The parameter ν is taken as fixed. The parameter μ is then varied to study the effect of the nonlinearity on the resonant coupling. Both positive and negative values of μ are investigated. The initial mismatch coefficient α for this distribution can be evaluated from the expression

$$\alpha \equiv \frac{\langle xF_x \rangle}{m\gamma\langle v^2 \rangle} = \nu \frac{\sigma_{xo}^2 - 3\mu\sigma_{xo}^4}{m\gamma\sigma_{vo}^2}. \tag{4.21}$$

We take a particular value of the parameter $\nu = 1.2m\gamma\sigma_{vo}^2/\sigma_{xo}^2$, resulting in $\alpha = 1.2$ for the case of a linear force ($\mu = 0$). In obtaining Eq. (4.21), we used explicitly the relation $\langle x^4 \rangle = 3\langle x^2 \rangle^2$, valid for a gaussian density profile.

An analysis similar to that of Sec. 4.1 is performed, and the decoupled problem is studied first. The beam is only slightly mismatched and normalization to either the asymptotic final or initial states can be used. We choose the initial normalization. We solve the eigenvalue problem for a decoupled case to find the natural frequencies of the modes and the basis $\{\mathbf{E}^{(i)}\}$. As in the beam-plasma case, all non-zero eigenvalues are found to be purely imaginary. There is one zero eigenvalue at each order for all the values of the nonlinearity parameter μ considered. The appearance of resonant modes again takes place. The dependence of the relative frequency mismatch for the resonant modes in second and fourth orders, $(\omega_1^{(2)} - \omega_1^{(4)})/\omega_1^{(2)}$, on the dimensionless nonlinearity parameter $2\mu\sigma_{xo}^2$ is presented in Fig. 4.13. For the range of $|2\mu\sigma_{xo}^2| \leq 0.04$ the frequency mismatch is less than

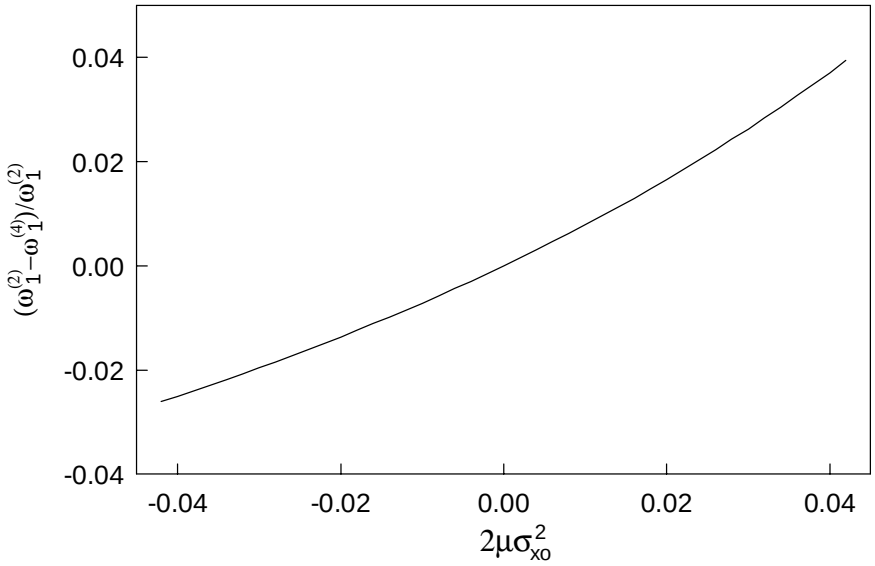

Figure 4.13: The relative frequency mismatch between the lowest order resonance modes as a function of the nonlinearity parameter for a system with $F_x(x) = -\nu(x - \mu x^3)$.

4%, thus indicating a strong resonance. The modes are in perfect resonance in the case of $\mu = 0$, *i.e.* for a linear force, and the absolute value of the mismatch increases as the nonlinearity in the force increases.

To study the dependence of the coupling strength on the force nonlinearity, the equations of motion are transformed into the $\{\mathbf{E}^{(i)}\}$ basis. The dependence of the relative initial amplitude $|\mathbf{q}_2^{(4)}|/|\mathbf{q}_2^{(2)}|$ on the nonlinearity parameter is plotted in Fig. 4.14, where it can be seen from the figure that $|\mathbf{q}_2^{(4)}| \ll |\mathbf{q}_2^{(2)}|$. Thus, Eq. (4.18) can be used to predict the rms oscillations relaxation time. The coupling coefficients γ_{24} and γ_{42} take on different values as the nonlinearity parameter μ changes. The theoretical estimate of τ_r are obtained by a numerical evaluation of the coupling strengths for each value of the nonlinearity parameter $2\mu\sigma_{xo}^2$. The estimate of τ_r is compared with the dynamical prediction from the full CME. The CME simulation is performed with $j_{max} = 20$ and $\Delta = 10$, and all variables are normalized using $a = \sigma_{xo}$ and $u = \sigma_{vo}$. The results for the relaxation time normalized to the betatron period are presented in Fig. 4.15 with the dynamically obtained τ_r plotted with symbols and the estimate Eq. (4.18) plotted as a solid curve. In the case of a linear force $\mathbf{q}_2^{(2)}$ and $\mathbf{q}_2^{(4)}$ are not coupled and $\gamma_{24} = \gamma_{42} = 0$. As a result, no relaxation in the

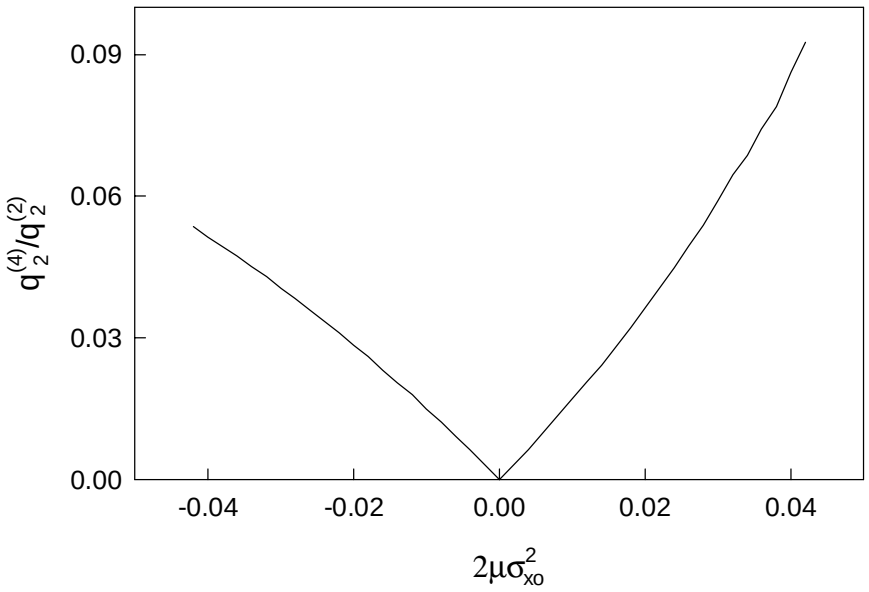

Figure 4.14: The relative amplitude $|\mathbf{q}_2^{(4)}|/|\mathbf{q}_2^{(2)}|$ as a function of the nonlinearity parameter for a system with $F_x(x) = -\nu(x - \mu x^3)$. A particular example of the initially gaussian beam with $\alpha = 1.2$ is considered.

rms size of the beam is predicted. The dynamical simulation also shows no relaxation in betatron oscillations. As the nonlinearity is increased, the coupling coefficients increase, and the relaxation takes place on an even faster scale. The theoretical estimate based on the resonant coupling gives good predictions for the observed dependence of the relaxation time on the degree of nonlinearity in the system.

To summarize, the relaxation time in the system with the force $F_x(x) = -\nu(x - \mu x^3)$ depends very strongly on the nonlinearity parameter μ, and the simple two mode model given by Eq. (4.18) provides good results for the observed relaxation. This result indicates that the order of magnitude of the relaxation time normalized to the oscillation period depends on both the functional dependence and the strength of the nonlinearity of F_x compared to the linear part of the force.

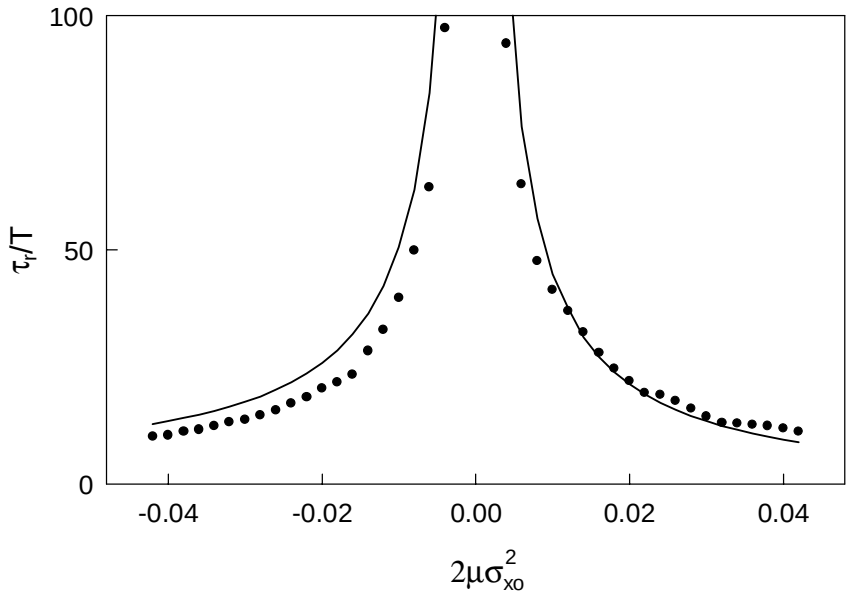

Figure 4.15: The relative rms oscillations relaxation time obtained dynamically (•) and from Eq. 4.18 (——-) as a function of the nonlinearity parameter for a system with $F_x(x) = -\nu(x - \mu x^3)$.

4.4 Resonant Coupling Strength and Self-Consistency of the Force

The previous Section investigated the dependence of the relaxation time on the spatial nonlinearity of the force. We controlled the nonlinearity of F_x by replacing the self-consistent magnetic force of our beam-plasma problem with a constant (in time) external force. The force in our beam-plasma system is, however, not only nonlinear but also self-consistent. Here, we investigate the dependence of relaxation process on the self-consistency of the force. We compare the relaxation time in our physical system with a self-consistent force and a hypothetical system that is acted upon with an external force. The external force is chosen to be equal to the initial force of the self-consistent system, but does not evolve along the beam propagation. The comparison is performed for a set of initially gaussian beams over a wide range of the mismatch parameter.

The relaxation process is studied by integrating numerically the dynamical CME with two different forces. The relaxation time is then extracted from the propagation curves

for the rms-beam size. The results for the relaxation time normalized to the betatron period are plotted in Fig. 4.16 for the full system with a self-consistent force (•) and for the system with a given external force (△). Figure 4.16 shows that the relaxation processes have very

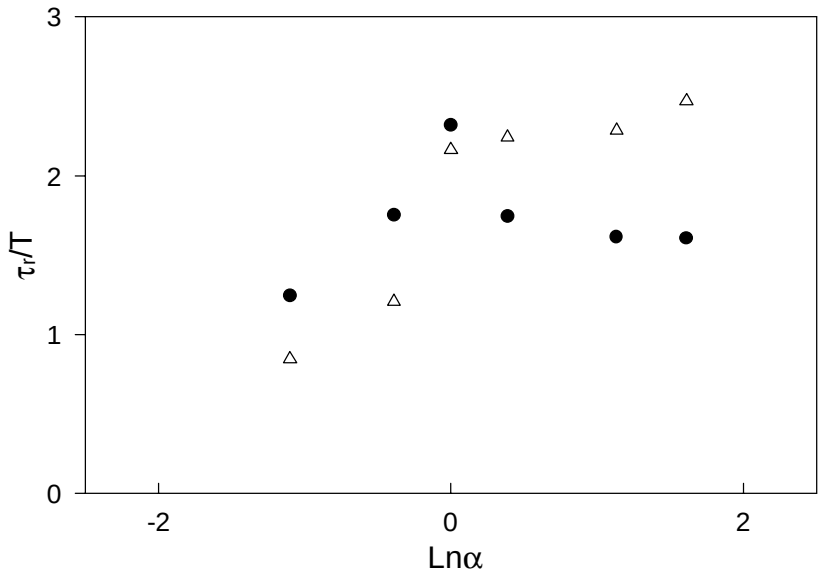

Figure 4.16: The relative rms oscillations relaxation time of initially gaussian beams with different values of the mismatch for a system with external (△) and a full self-consistent (•) force.

similar time scales. The relaxation is slower for the fixed-force system for $\alpha > 1$ (when the beam is initially wider than its equilibrium value and $\sqrt{\langle x^2 \rangle} \leq \sigma_{xo}$ at all times), and it is faster for $\alpha < 1$ (when initial beam is too narrow and $\sqrt{\langle x^2 \rangle} \geq \sigma_{xo}$ at all times).

To summarize the results of the Secs. 4.3 and 4.4, the betatron oscillation relaxation time depends greatly on the nonlinearity of the force. While no relaxation takes place in linear systems (infinite relaxation time), τ_r/T decreases as the force becomes ever more nonlinear. On the other hand, the self-consistency of the force does not effect the efficiency of the relaxation process as much.

Chapter 5

Coarse-grained Equilibrium State

The numerical illustrations of beam propagation through an overdense plasma presented in previous Chapters have demonstrated that a coarse-grained (or averaged) distribution function of the beam tends to a stationary final state at later times. The general properties of this asymptotic state and predictions of the fluid quantities, such as density and temperature, have been the subject of numerous investigations in the last four decades. The prediction of the final state for a collisionless and lossless system based on a given initial condition and avoiding the intermediate dynamics has challenged scientists from different areas of physics varying from fluid mechanics to astrophysics and plasma physics. The underlying physics that determines the selection of the asymptotic state in the process of collisionless relaxation has also been of great interest.

We begin with a quick introduction and general overview of current theoretical understanding of the final state properties. PIC results for the final beam density and temperature are presented in Sec. 5.2. Simulations are performed for different initial distributions. Features of the final distribution are discussed. A more detailed discussion of the previous results and comparisons with the numerical predictions are presented in Sec. 5.3. The results of Sec. 5.2 clearly demonstrate a non-thermal character of the beam in the stationary state. This issue is discussed further in Sec. 5.4. Some simple arguments based on the conservation of energy are used to show that the final thermal state is only accessible from a limited range of initial conditions. We then use a simplified model of the dynamics to make analytical predictions for different beam moments. The model uses more of simplifying approximations than the theory of Chapter 2 but allows to obtain predictions for moments orders higher than second. The model is presented in Sec. 5.5. The theoret-

ical results show the same dependence of the final values on the initial mismatch as the numerically obtained predictions. The model sheds light on the physics of the dependence of the asymptotic state on the initial condition. Finally, in the last section the problem of predicting the final beam density and temperature are considered. Due to the difficulties with the results for the final state for our system due to the self-consistency of the force, we consider a simpler problem of a spatially nonlinear but external force applied to the system. The force is assumed to be equal to the self-consistent force of the initial beam and taken to be time independent. This simplification allows us to make predictions for the beam density and temperature in the final state which agree with results of PIC simulations obtained for systems with external forces. An attempt is also made to predict the asymptotic density and temperature profiles of the system with a self-consistent force using a simplified method based on the results for systems with external forces.

5.1 Introduction

While the exact distribution function never reaches an equilibrium but develops finer filaments in the phase-space, the coarse-grained distribution function approaches a stationary state in a finite time. As a result, macroscopic characteristics of the beam, such as density and temperature, relax into equilibrium. A number of different attempts were made in the past to predict the final state of a collisionless system. Some studies were performed in context of both astrophysical and beam dynamics for systems with the evolution governed by Eqs. (2.2.

The first prediction dates back to the classical work of Lynden-Bell originally presented in Ref. [6] on violent relaxation, phase mixing and collisionless relaxation in self-gravitating systems. The statistical approach was used to study the evolution of the distribution function. Based on the exclusion principle imposed by the phase mixing dynamics, Lynden-Bell predicted a Fermi-Dirac distribution for the stationary coarse-grained function when the initial condition corresponds to a uniform phase density. This conclusion is reached using the maximization of the mixing entropy. The final state, characterized by two parameters, can be specified exactly using principles of conservation of mass and energy. A modification of Lynden-Bell's approach was also used by Shu [49]. Numerical work followed to verify the prediction of Ref. [6] for both slab [50, 51] and three dimensional [52, 53] systems. Numerical results indicated that a core-halo structure is frequently developed as

a result of the relaxation, but the details of the averaged distribution showed significant differences with Lynden-Bell's prediction. They also showed that the final states do not usually correspond to a thermodynamic equilibrium (*i.e.*, not thermal Maxwellian distributions), and a certain degree of memory of the initial condition is usually present. The theory of Ref. [6] was further developed by Chavanis and Sommeria [73] in an attempt to resolve the difficulties associated with Lynden-Bell's result to include the degenerate equilibrium states in the analysis resulting in a degenerate core and thermalized halo structure of the distribution.

Due to the difficulties with Lynden-Bell's prediction for the final coarse-grained distribution, another theory for self-gravitating systems was developed by Wiechen et al. (Refs. [7, 8]). In contrast with Lynden-Bell's theory of maximization of the entropy, the method of Ref. [7] is based on the premise that the relaxation process depends on the amount of energy that is free (*e.g.* non-equilibrium energy). As soon as no free energy is available for the dynamics the relaxation process seizes. The final state is calculated as the lowest energy state for a set of constraints determined by the microscopic dynamics. The technique was later extended to the description of the equilibrium state in collisionless plasmas [54] and ideal fluids. A comparison with numerical results for initial states not far from equilibrium distributions showed good agreement with the numerical predictions [55]. However, comparisons with numerical results presented in Ref.[74] for highly unmatched initial conditions indicated that only central (core) regions of the stationary distributions resemble the density profile predicted by this theory, and some significant qualitative discrepancies were also observed. The other shortcoming of the theory is in the unknown character of the degree of smoothing of the memory function related to the exact details of microscopic filamentations and coarse-graining. Different choices of smoothing operators for the memory function result in different predictions for the stationary state (more details can be found in Ref. [8]). Other approaches were also used (see for example Ref. [56]) in the field of self-gravitating collisionless systems. Some theoretical progress was also made independently in the field of beam-plasma systems. An analytical model was developed by Rosenzweig and Chen in Ref. [2] predicting the equilibrium state. Using an assumption of complete thermalization of the phase-space distribution combined with the equilibrium condition and conservation of the number of particles at the phase-space origin, a stationary coarse-grained distribution is predicted. Although no comparisons with numerical results were reported, a limited agreement with numerical results is expected based on the

numerical results for the stationary distributions for self-gravitating systems that showed non-thermal character of the final distributions.

All previously developed theoretical models show some degree of discrepancy with numerical results. Thus, no analytical prediction is available up to this date that can be used to evaluate the equilibrium coarse-grained distribution without considering the intermediate dynamical stage. The inability to predict the final state also indicates that the exact mechanism that determines the equilibrium achieved as a result of collisionless relaxation is still not well understood. Comparisons of numerical predictions obtained in this thesis with the results of existing theories allow for a better understanding of the nature of discrepancy between numerical and analytical results. Results for both beam density and temperature profiles are presented. Theoretical arguments for the non-thermal character of the final stationary state and a simple model for calculating asymptotic values of beam moments is also presented. The model further sheds light on the physical nature of the beam distribution at equilibrium. Finally, a model is developed to predict the beam fluid quantities resulting from the collisionless relaxation in a simplified case of an external, spatially nonlinear force.

5.2 Coarse-grained Equilibrium State - Numerical Examples

We return to the numerical examples of initially gaussian and uniform beams considered in Chapter 2 and 3. We previously investigated the rms beam size, temperature and correlation ratio obtained after the relaxation is completed. In this section the investigation is extended to the corresponding study of the density and temperature profiles. Propagation over only a few betatron wavelengths was sufficient for the relaxation of rms oscillations investigated in Chapter 3. Here this study is extended since a stationary density profile is usually established only after beam is propagated over 20-30 betatron wavelengths inside the plasma.

The stationary density and temperature profiles for an initially gaussian beam with a mismatch of $\alpha = 5$ are presented in Fig. 5.1. Density and temperature, normalized by their initial values on the axes ($x = 0$), respectively, are plotted with solid curves. Initial profiles are shown for reference as dotted lines. The spatial variable is normalized to the initial rms beam size, σ_{xo}. A pronounced core-halo structure can be easily identified on the density plot. The temperature results clearly indicate that the initially thermalized distribution is

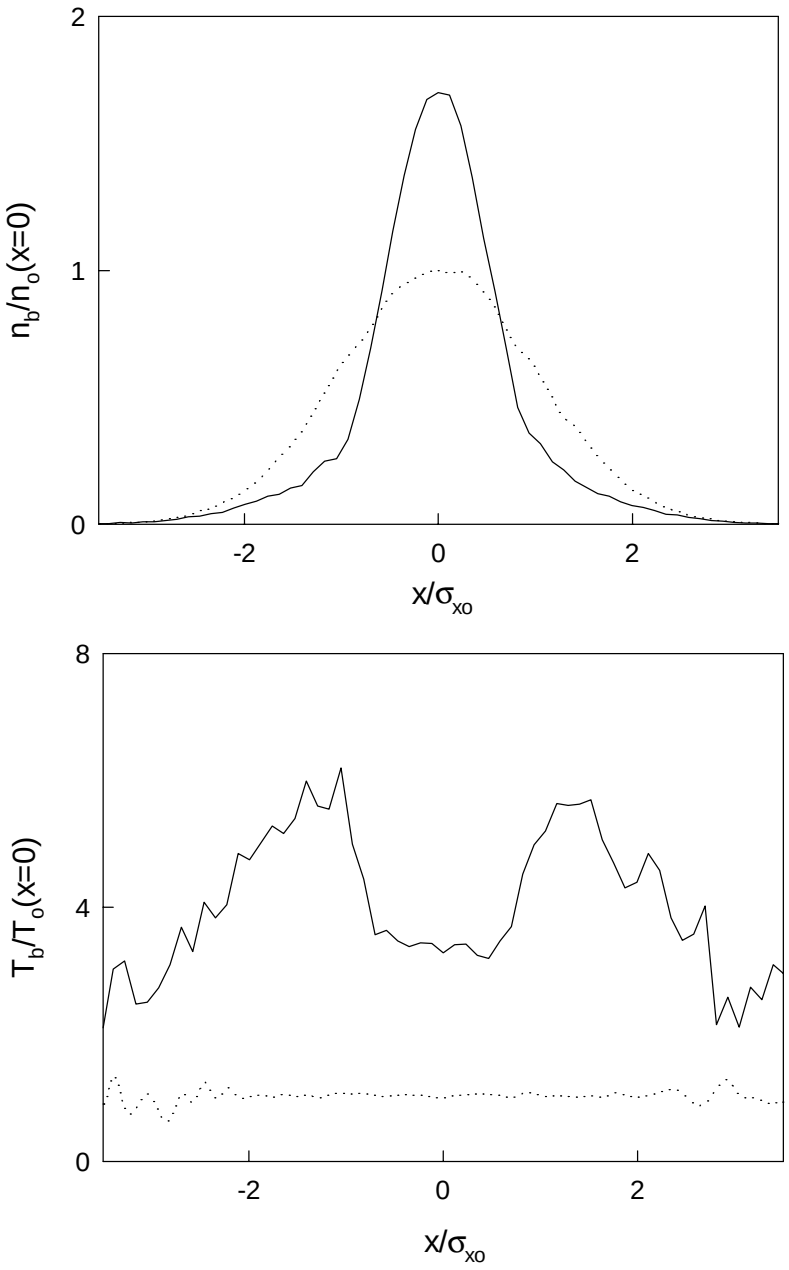

Figure 5.1: Final density and temperature profiles (——) for the initially gaussian beam with $\alpha = 5$. Corresponding initial profiles ($\cdot\cdot\cdot\cdot\cdot$) are plotted as a reference.

significantly non-thermal in the final state, as $T_b(x)$ becomes a function of position. While the core of the beam has almost a constant temperature, regions of 'hot' particles develop at the transition between the core and halo regions. Referring to the plot of the correlation ratio for initially gaussian beams presented in Fig. 3.16, we find that $\langle x^2 v_x^2 \rangle / (\sigma_x^2 \sigma_v^2) = 1.17$ in the stationary state for $\alpha = 5$. The ripples observed in the temperature plot can be attributed to the particle noise owing to the small number of particles at the density tail. To increase accuracy, more particles can be kept in the PIC simulation.

In the second example of an initially gaussian distribution, we present results for a beam with $\alpha = 0.2$. The relative strengths of the two forces acting on the beam envelope are now reversed, and the beam pressure exceeds the focusing force at the plasma entrance. Resulting stationary density and temperature profiles are plotted in Fig. 5.2 A development of a core-halo structure is again observed. Two regions with significantly different functional dependencies of density on the spatial variable can be easily seen dividing the beam into a core and halo regions. General features of the temperature profile resemble these of Fig. 5.1. A non-thermal coarse-grained distribution is reached as a result of the relaxation. The temperature in the beam core is now lower than that of the particles at the tail of the distribution. A region of hot particles coincides with the transition from the core of the beam to the halo.

After we considered the main features of the final density and temperature of an initially gaussian beam, it is informative to compare the profiles for different initial mismatches. This yields further insights and detailed understanding of the dependence of the stationary state on the initial conditions, and, therefore, the degree of the memory on the initial conditions. In other words, considering beams with the same initial dependence of the phase-space distribution on the spatial and velocity variable (*i.e.*, gaussian) but different mismatches, we investigate the changes in the functional dependence of fluid quantities $n_b(x)$ and $T_b(x)$ in the final state. Results for the density profiles are presented in Fig. 5.3. To simplify the comparison, the results are normalized to the final value of the beam density on the axis ($x = 0$). The spatial scale is also normalized, but now to the equilibrium value of the beam size for a given value of α. Density is plotted for five different cases: $\alpha = 0.2$ (- - - -), $\alpha = 0.66$ ($\cdot \cdot \cdot \cdot \cdot$), $\alpha = 1.1$ (— — —), $\alpha = 3$ (— $\cdot$ — $\cdot$ — $\cdot$) and $\alpha = 10$ (— —). Comparison of the density profiles indicates that the functional dependence of $n_b(x)$ depends on the initial conditions, and it depends on the value of the initial mismatch α for a given initial profile. While stationary densities of slightly mismatch beams ($\alpha = 0.66$ and

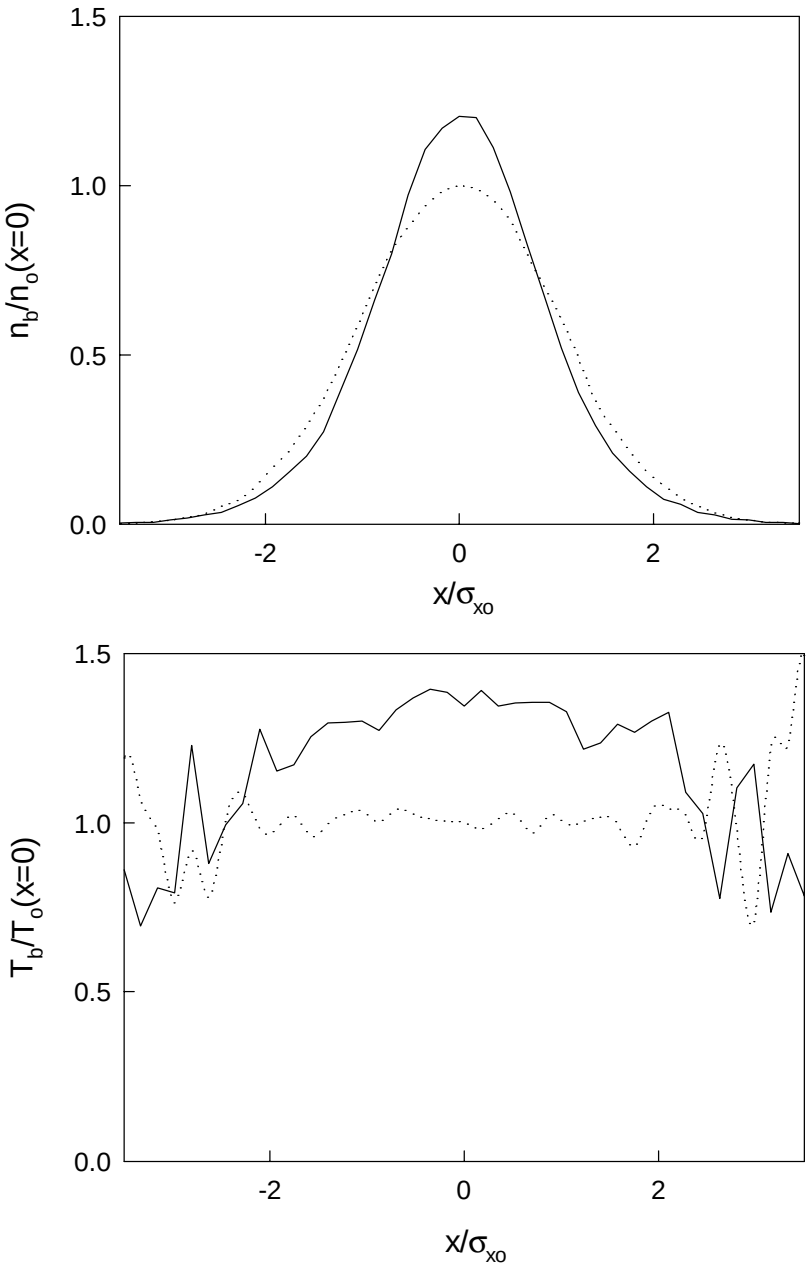

Figure 5.2: Final density and temperature profiles (——) for the initially gaussian beam with $\alpha = 0.2$. Corresponding initial profiles ($\cdot\cdot\cdot\cdot$) are plotted as a reference.

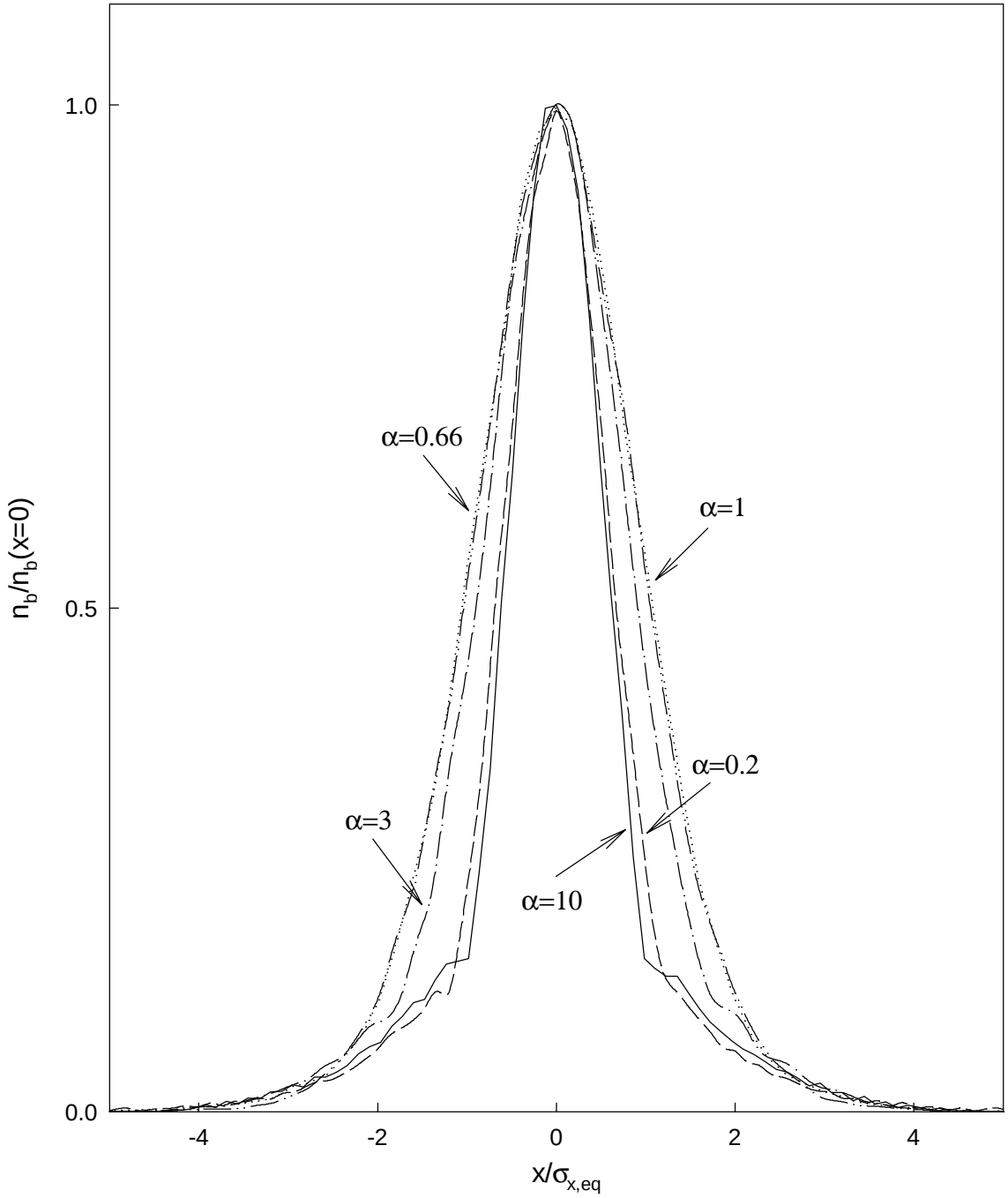

Figure 5.3: Final density profiles for the initially gaussian beam with $\alpha = 0.2$ (- - - -), $\alpha = 0.66$ ($\cdot\cdot\cdot\cdot$), $\alpha = 1.1$ (— — —), $\alpha = 3$ (— $\cdot$ — $\cdot$ — $\cdot$) and $\alpha = 10$ (——). Density is normalized to its value at $x = 0$, and spatial variable is normalized by the final beam size for each given α.

$\alpha = 1.1$) have a general bell-shape form, the highly mismatched beams ($\alpha = 0.2, \alpha = 10$) have a pronounced core-halo structure. A sharp transition between the regions is observed at about $x \simeq 1.1\sigma_{x,eq}$. The equilibrium density of highly mismatch beams has similar shape for both $\alpha > 1$ and $\alpha < 1$.

The stationary temperature profiles $T_b(x)$ are presented in Fig. 5.4. The results for the same initially gaussian beams with $\alpha = 0.2$ (- - - -), $\alpha = 0.66$ ($\cdot \cdot \cdot \cdot$), $\alpha = 1.1$ (— — —), $\alpha = 3$ (— $\cdot$ — $\cdot$ — $\cdot$) and $\alpha = 10$ (——) are plotted. The temperature is normalized to its value on the x-axis. Comparisons of the results show that drastically different temperature distributions are observed for beams with different initial mismatch. In particular, slightly mismatch beams ($\alpha = 0.66$ and $\alpha = 1.1$) evolve into distributions with a monotonically decaying temperature as a function of a distance from the center of the beam. In contrast, the final distribution of initially highly mismatched beams has hot regions at some distance from the center of the beam. The particle temperature first increases as a function of a distance from the center of the beam and then decays. The hot regions coincide with the transition from the core to the halo of the beam. Again, $T_b(x)$ shows similar behavior for $\alpha > 1$ and $\alpha < 1$. Consider the change in the dependence of $T_b(x)$ in the core of the beam. The temperature profile changes from a concave to a convex function as the mismatch increases (that is as α deviates from unity). This leads us to expect that there exists a value of α such that the temperature becomes constant with a density profile corresponding to a beam in thermal equilibrium. We return to this problem in Section 5.4, where we discuss further why the thermalization of the beam is possible for only particular values of the initial mismatch parameter.

A similar set of PIC simulations has been conducted for initially uniform beams. The final density and temperature obtained from PIC simulations for a beam with $\alpha = 5$ are presented in Fig. 5.5. The overall behavior of both density and temperature is similar to final $n_b(x)$ and $T_b(x)$ of an initially gaussian beam. A pronounced core-halo structure in the beam density can be seen. A relatively higher temperature is observed in the transition region from the beam core to the halo compared to T_b on the axis.

The collection of final density profiles obtained for initially uniform beams with different mismatch parameters is plotted in Fig. 5.6. Results are normalized to the value of the beam density on the axis ($x = 0$) with the spatial scale normalized by $\sigma_{x,eq}$ for a given value of α. The density is plotted for 5 different cases with $\alpha = 0.2$ (- - - -), $\alpha = 0.66$ ($\cdot \cdot \cdot \cdot$), $\alpha = 1.1$ (— — —), $\alpha = 3$ (— $\cdot$ — $\cdot$ — $\cdot$) and $\alpha = 10$ (——). A picture similar to

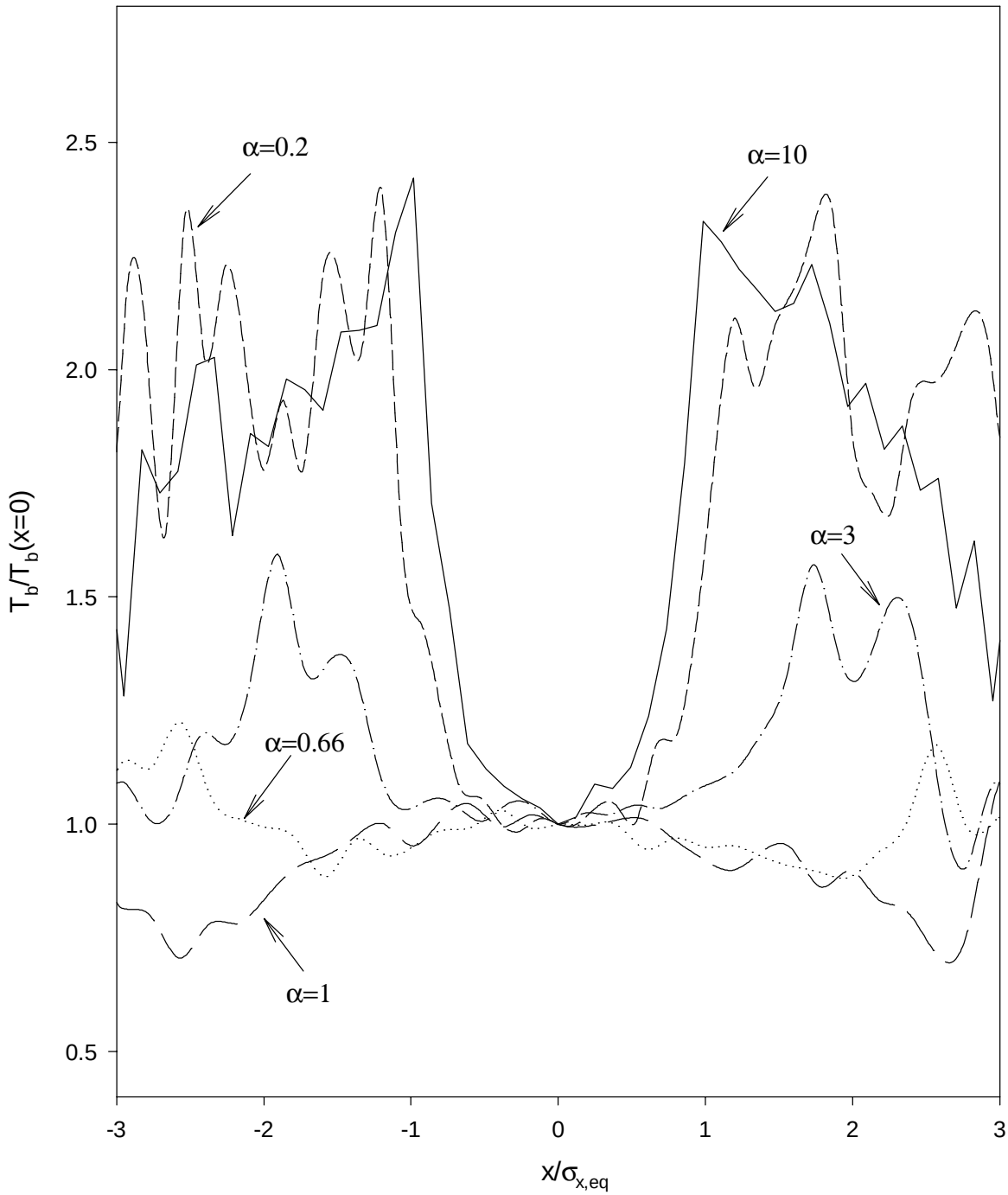

Figure 5.4: Final temperature profiles for the initially gaussian beam with $\alpha = 0.2$ (- - - -), $\alpha = 0.66$ ($\cdots\cdots$), $\alpha = 1.1$ (— — —), $\alpha = 3$ (— · — · — ·) and $\alpha = 10$ (——). Temperature is normalized to its value at $x = 0$, and spatial variable is normalized by the final beam size for each given α.

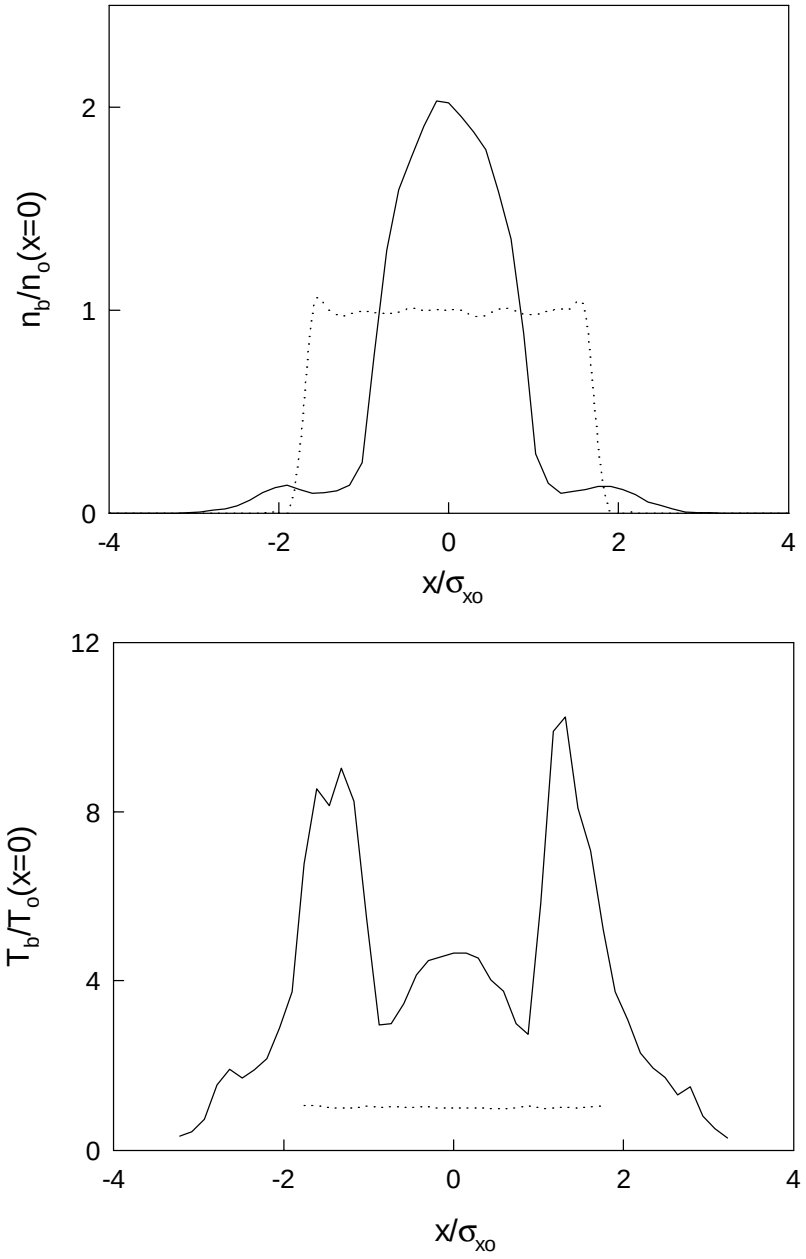

Figure 5.5: Final density and temperature profiles (——) for the initially uniform beam with $\alpha = 5$. Corresponding initial profiles ($\cdot\cdot\cdot\cdot\cdot$) are plotted as a reference.

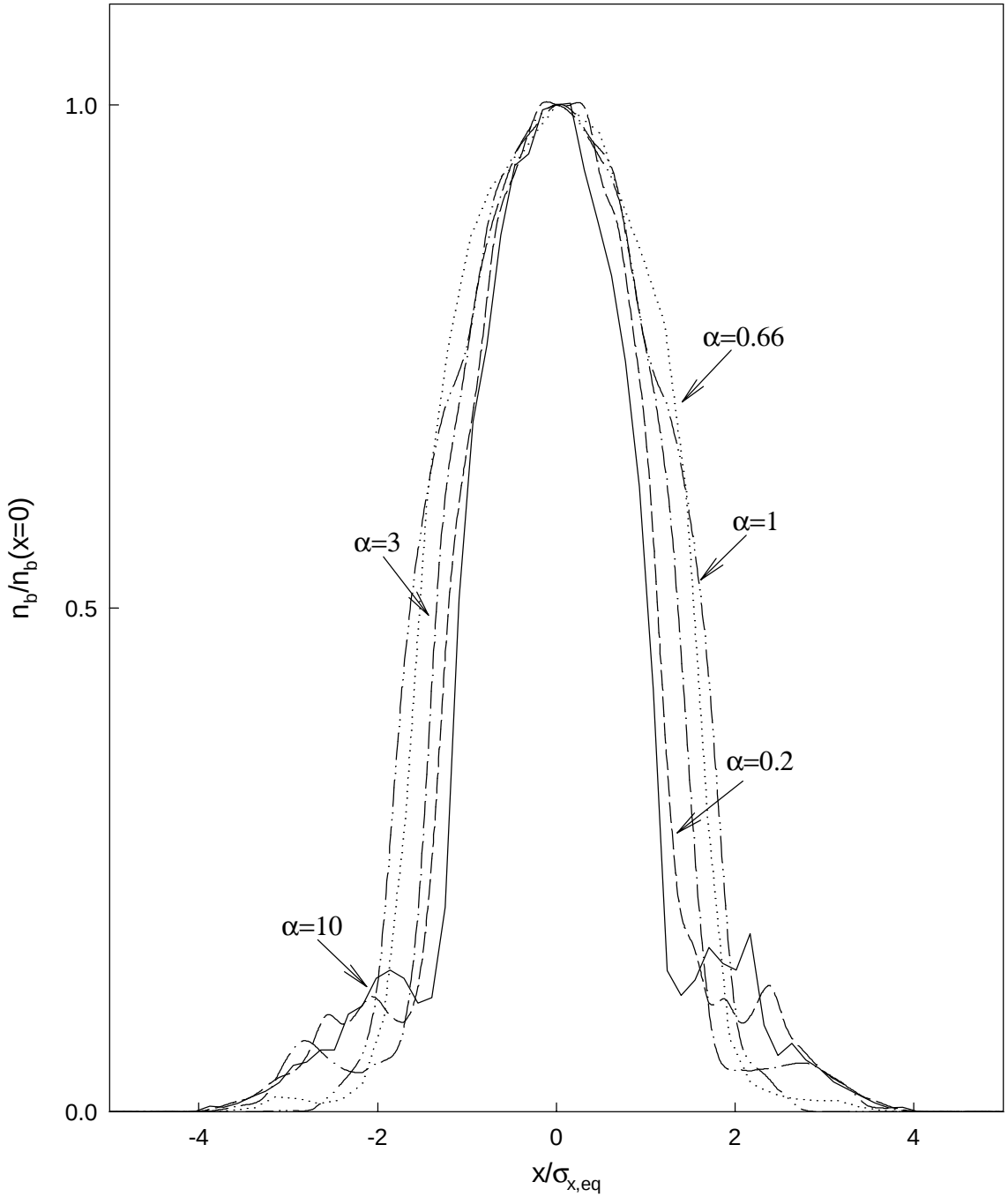

Figure 5.6: Final density profiles for the initially uniform beam with $\alpha = 0.2$ (- - - -), $\alpha = 0.66$ ($\cdot\cdot\cdot\cdot$), $\alpha = 1.1$ (— — —), $\alpha = 3$ (— $\cdot$ — $\cdot$ — $\cdot$) and $\alpha = 10$ (——). Density is normalized to its value at $x = 0$, and spatial variable is normalized by the final beam size at each given α.

that obtained for the initially gaussian beam can be seen. Densities of slightly mismatched beams have a bell-like shape, while the profiles of highly mismatched beams have a core-halo structure.

The temperature profiles $T_b(x)$ are presented in Fig. 5.7 for the same initial conditions. Profiles show the same general dependence as for the initially gaussian beams. Temperature is a monotonically decreasing function of the spatial variable x for beams with a slight mismatch. Hot regions away from the beam center appear for the highly mismatched beams. These regions coincide with the transitions from the core to the halo of the beam.

5.3 Comparison of Numerical Stationary Results with the Previous Theory

In this Section, we compare previous theoretical predictions (in particular, these of Refs. [6] and [2]) with the numerical results of the last section. For completeness, we also briefly review the theory presented in Ref. [7]. Due to the freedom in the selection of the averaging operator (determined by the unknown at present details of the relaxation) no comparison is made with the numerical results. The interested reader can find studies for a number of different guesses of the averaging operator in Ref. [8].

A pioneering paper was that of Lynden-Bell's theory of the coarse-grained equilibrium state reached as a result of collisionless relaxation process. In this model, the collisionless dynamics can be considered as a mixing process of an initially uniform phase-space distribution patch f_o with the surrounding fluid with $f = 0$. However, complete mixing forbidden by the macroscopic constraint of the conservation of energy. Another constraint preventing a final uniform distribution is the conservation of phase-space density in the incompressible dynamics governed by a collisionless Vlasov equation. This leads to the consideration of the dynamics of the coarse-grained, or averaged distribution function, that we denote by $\bar{f}$. The mixing can only decrease the value of $\bar{f}$ of the patch due to the fact that every cell used as an averaging volume now incorporates both the initial particles and regions of the vacuum. Therefore, a constraint $\bar{f} \leq f_o$ is applied to the averaged distribution function everywhere. This constraint gives rise to the exclusion principle resulting in a Fermi-Dirac equilibrium distribution for the coarse-grained equilibrium.

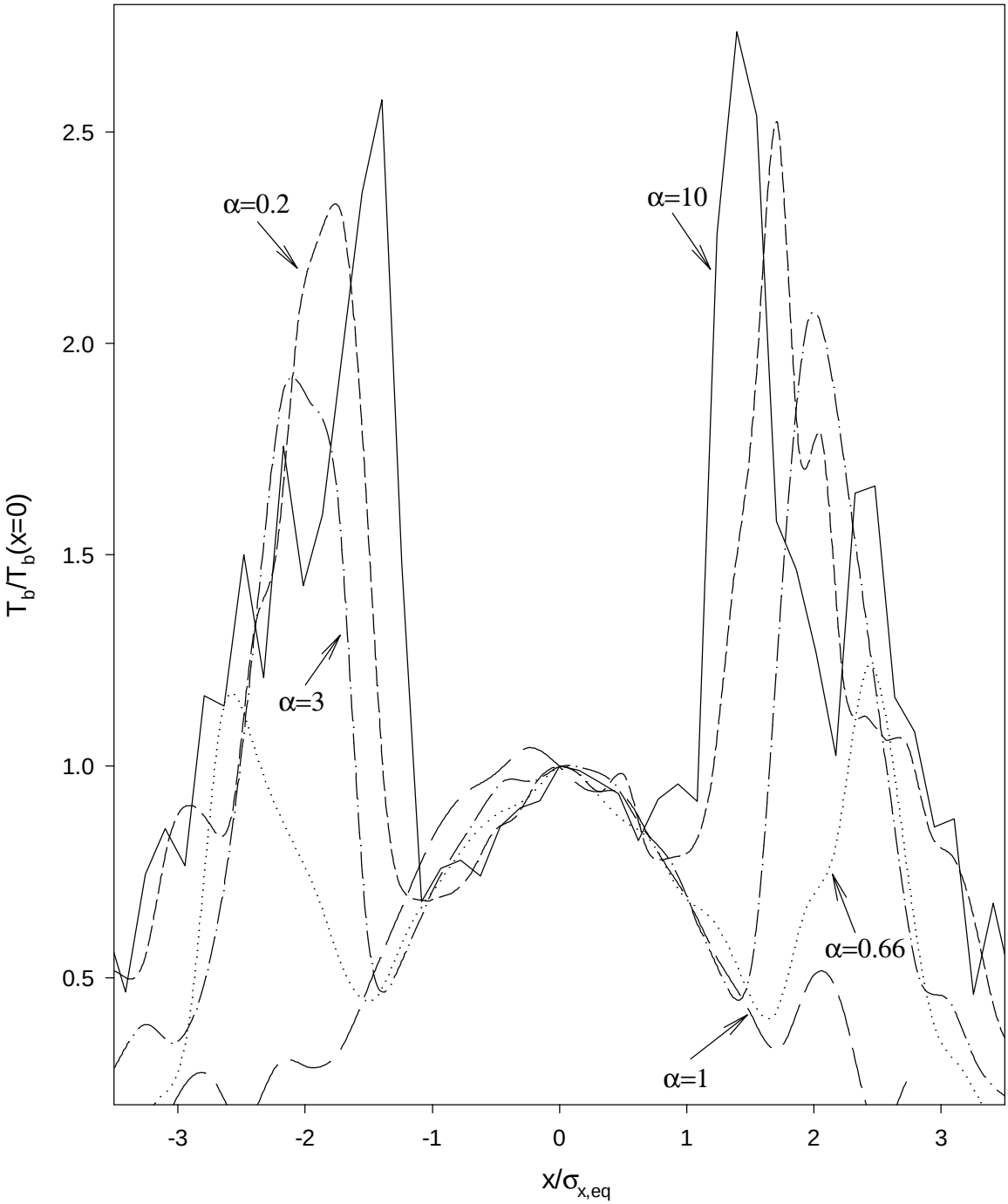

Figure 5.7: Final temperature profiles for the initially uniform beam with $\alpha = 0.2$ (- - - -), $\alpha = 0.66$ ($\cdots\cdots$), $\alpha = 1.1$ (— — —), $\alpha = 3$ (— · — · — ·) and $\alpha = 10$ (——). Temperature is normalized to its value at $x = 0$, and spatial variable is normalized by the final beam size for each given α.

This result can also be derived explicitly by a variational method. According to Lynden-Bell, the most likely distribution that is reached at equilibrium can be obtained by maximizing the mixing entropy defined as

$$S = -\int [\rho \ln \rho + (1-\rho)\ln(1-\rho)] dx dv_x, \tag{5.1}$$

where the density function is introduced as $\rho(x, v_x) = \bar{f}(x, v_x)/f_o$. The entropy is maximized under the macroscopic constraints of energy and total number of particles conservation. The resulting averaged equilibrium distribution has the following form

$$\bar{f} = \frac{f_o}{1 + e^{\beta(E-E_F)}}, \tag{5.2}$$

where $E(x) = m\gamma v_x^2/2 - q_b v_z A_z$ is the particle energy and E_F is a constant equivalent to the Fermi energy for Fermi-Dirac equilibrium distribution. Another parameter β arises from the Lagrange multiplier of the energy constraint. The result for the equilibrium state given by Eq. (5.2) was obtained for a special case with the initially uniform distribution. Reference [6] also makes a prediction for initially non-uniform states as a superposition of Fermi-Dirac distributions given by Eq. (5.2).

Two distinct limits are usually considered which allow for a significant simplification of the distribution function. As the particle energy $E(x)$ is an increasing function of x ($dA_z/dx < 0$), for sufficiently large x $e^{\beta(E-E_F)} > 1$, and the distribution function takes the familiar Maxwell-Boltzmann form

$$\bar{f} \simeq f_o e^{-\beta(E-E_F)}. \tag{5.3}$$

This limit is usually referred to as 'non-degenerate' or 'diluted'. In Lynden-Bell's theory, at distances far enough from the center of the beam, the distribution always takes the Maxwell-Boltzmann shape of Eq. (5.3). In the second (the so called 'degenerate' limit), $E \ll E_F$ for most of the particles of the beam, resulting in the distribution function

$$\bar{f} \simeq f_o, \quad \text{for} \;\; E \leq E_F \tag{5.4}$$

The explicit spatial dependence of $\bar{f}$ can be found as follows. The distribution depends on the vector potential A_z, which is determined as a solution of Poisson equation

$$\frac{\partial^2 A_z}{\partial x^2} = -q_b v_z \mu_0 \int_{-\infty}^{\infty} dv_x \bar{f}(x, v_x). \tag{5.5}$$

Substituting Eq. (5.2) into Poisson equation (5.5), the equilibrium solution for the vector potential is obtained. Due to the presence of the boundaries at $x = \pm L$ in our PIC simulation, Eq. (5.5) is solved subject to a boundary condition $A_z|_{x=\pm L} = 0$. The constants β and E_F can be determined from the constraints of the number of particles and energy conservation.

To make a comparison between the prediction of Lynden-Bell theory and a PIC simulation, consider a specific example of the initially uniform beam with $\alpha = 5$. The theoretical prediction is obtained in the following way. First, some start-up values of parameters β and E_F are chosen. Equation (5.5) is solved numerically as an initial value problem for the vector potential with $A_z|_{x=\pm L} = 0$ and $\partial A_z/\partial x|_{x=\pm L} = -q_b v_z \mu_0 N/2$. Equation (5.2) is used for the distribution function. After the solution for A_z is found, the distribution function can be easily reconstructed. The total number of particles and the energy of the beam are calculated and compared with the initial values for the system under consideration. The values of the parameters β and E_F are adjusted and the distribution function is recalculated. This iteration procedure is repeated until a desired accuracy in the conservation relation is achieved.

The results obtained for the density and temperature of the beam with an initial mismatch of $\alpha = 5$ are presented in Fig. 5.8 with a dashed line. The predictions of the PIC simulation are also plotted for comparisons in the same graph with a solid line. The initial density and temperature are presented with dotted lines for a reference. All quantities are normalized by their initial values at $x = 0$. The spatial scale is normalized by the initial value of the rms beam size. Significant discrepancies can be seen between the analytical prediction and the numerical result. A more pronounced difference in the density behavior in the core and halo regions can be seen. The analytical prediction for the temperature resembles that of the PIC simulation in the core but no rise of T_b in the transition region between the core-halo regions results from Lynden-Bell theory.

Comparisons were also performed for cases with other values of the initial mismatch. The results were similar to that presented in Fig. 5.8. Significant disagreements with results of PIC simulations were observed. A few remarks are in place here about the general behavior of the beam density and temperature in Lynden-Bell final state. A core-halo structure is usually observe with the core corresponding to the degenerate region of the distribution and halo - to the Maxwell-Boltzmann part of the beam. While a monotonic decay of the temperature as a function of the distance from the center of the beam takes

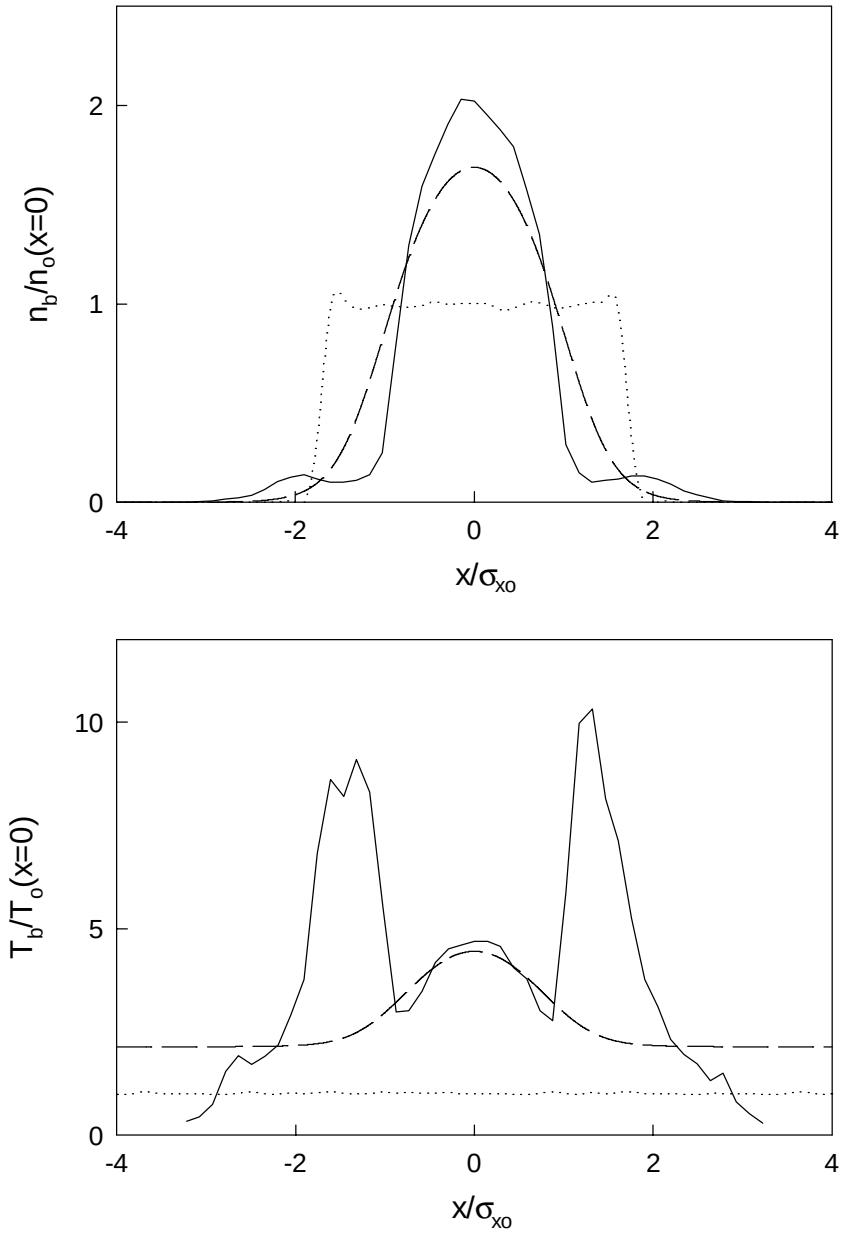

Figure 5.8: Comparisons between Lynden-Bell predictions (- - - - -) and PIC simulation ($-\ -\ -\ -\ -\ -\ -\ -$) for the final density and temperature profiles for the initially uniform beam with $\alpha = 5$. The initial profiles ($\cdots\cdots$) are plotted as a reference.

place in the degenerate beam core, a constant temperature is established in the tail of the beam. No increase in the temperature at the transition region or gradual decrease of T_b inside the core are observed in the analytical prediction. We thus conclude that Lynden-Bell prediction for the uniform initial patch in the phase-space is not realized in numerical simulations.

We next compare analytical predictions derived in Ref. [2] with results of PIC simulations. Rosenzweig and Chen [2] considered this problem in the context of the beam propagating through a plasma, and approximated the final coarse-grained distribution with a thermal distribution already considered in Ch. 2 and given by Eq. (2.35). The distribution is characterized by two parameters b and u_B, which define the spatial and velocity scales of the beam. The density corresponding to this equilibrium distribution is given by a modified Bennett profile for a slab beam

$$n_B(x) = \frac{N}{2b}\frac{1}{\cosh^2 x/b}. \tag{5.6}$$

The unknown parameters b and u_B are specified using the conservation laws for the system. Rosenzweig and Chen suggested to use the conservation of the total number of particles and the invariance of $f(x = 0, v_x = 0, t)$ to determine the unknown parameters.

The comparisons are performed for cases with both initially gaussian and uniform distributions. Using Eqs. (2.13) and (2.16) for the theoretical predictions of Ref. [2] for the final beam size of the initially gaussian and uniform beams respectively and the relation $b = 2\sqrt{3}\sigma_{x,eq}/\pi$ for Bennett profile of Eq. (5.6), the parameter b can be easily found. Equations (2.14) and (2.17) are then used to determine $u_B \equiv \sigma_{v,eq}$. The results for the final density and temperature of the initially gaussian beam with the mismatch of $\alpha = 5$ are presented in Fig. 5.9. Analogous result for the initially uniform beam of the mismatch of $\alpha = 5$ can be seen in Fig. 5.10. As expected, a serious disagreement between the predicted and numerical temperature profiles in the final state is observed. Owing to the assumption of the thermal character of the distribution in the final state, the analytical prediction for T_b is a constant function of the spatial variable. Thus, no prediction is obtained for the observed temperature 'bumps' in the stationary state. The predicted density profile resembles that of the PIC simulation especially in the case of the initially gaussian beam. However, no core-halo structure is predicted. A closer inspection of the results reveals significant discrepancies in the density profiles at the tail of the beam for both initial distributions. Thus, the theoretical prediction of Ref. [2] can be used to obtain

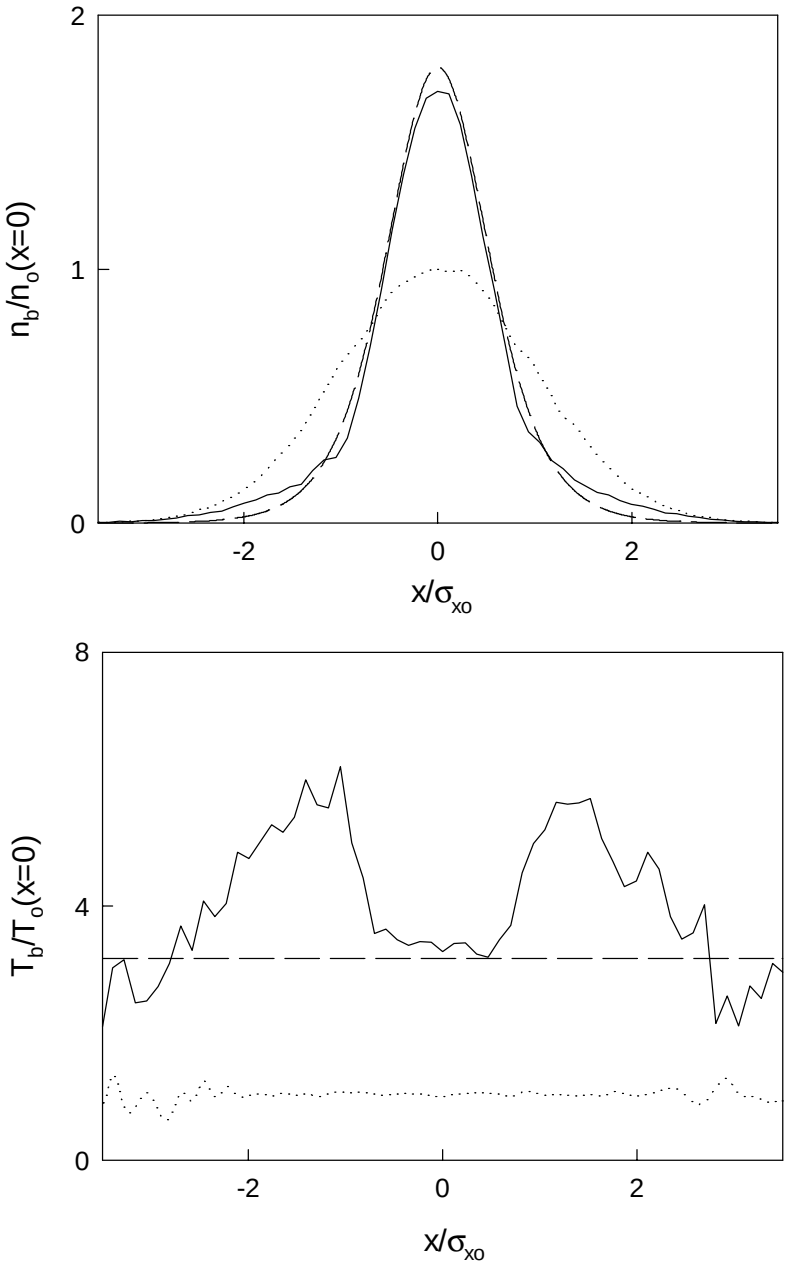

Figure 5.9: Comparisons between predictions of Ref. [2] (– – – –) and PIC simulation (—— –) for the final density and temperature profiles for the uniform gaussian beam with $\alpha = 5$. Corresponding initial profiles (· · · · ·) are plotted as a reference.

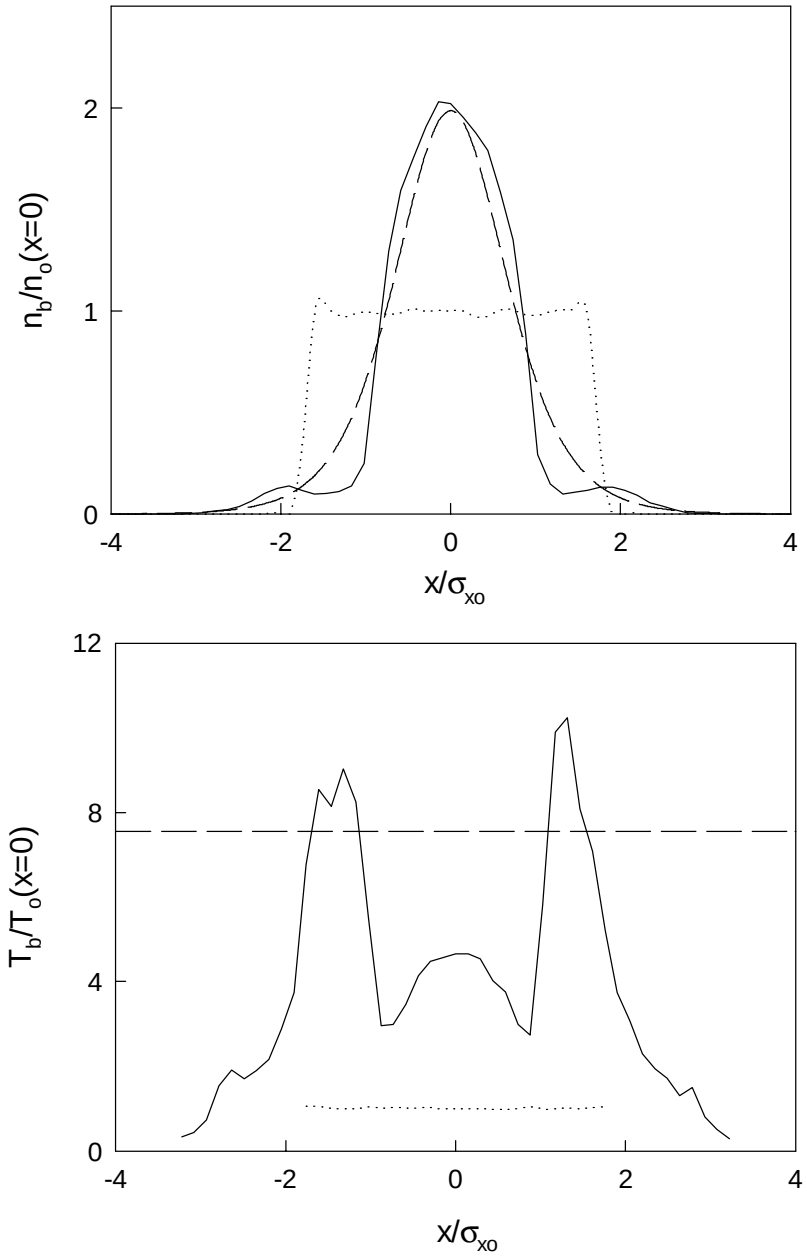

Figure 5.10: Comparisons between predictions of Ref. [2] (– – – –) and PIC simulation (———) for the final density and temperature profiles for the initially gaussian beam with $\alpha = 5$. Corresponding initial profiles ($\cdot\cdot\cdot\cdot\cdot$) are plotted as a reference.

estimates of the density profiles if the behavior at the beam tail is irrelevant for the particular investigation but it can not be used in studies of beam halo. The theory can not be used to determine the distribution of the beam temperature, and many important aspects of the final coarse-grained distribution are lost in the analysis, such as the appearance of the space-velocity correlations in the phase-space. It also does not shed light on the origin of these correlations, the change in the behavior of the beam temperature with the change in the initial mismatch parameter or help to determine the relative scales of the beam core and halo.

Lastly, we briefly mention the theory of Wiechen et al. developed in Refs. [7] and [8]. There, the following technique is suggested to find the final coarse-grained state of the system. The exact dynamics of the system conserves the phase-space density of the distribution. This fact can be expressed qualitatively by the invariance of the function $\phi(g)$ defined as

$$\phi(g) = \int dx dv_x \Theta[f(x, v_x) - g], \tag{5.7}$$

where Θ stands for the Heavyside step function. Only states with $\phi(g)$ equivalent to $\phi_o(g)$ of the initial state are accessible within the incompressible Vlasov dynamics. The function $\phi(g)$ can be inverted to result in $g(\phi) \equiv \phi^{-1}(g)$ which is usually referred to as a memory function. The paper postulates that the globally stable equilibrium state within the collisionless dynamics is the minimum energy state of all possible states with the same memory function. Due to the fact that non-equilibrium states have a higher energy, the globally stable states are not accessible from the initially non-equilibrium state due to the conservation of the energy. However, it is stated that the equilibrium states may be reachable on the macroscopic (or averaged) scales. It is assumed that the filamentation and mixing change the memory function so that the averaged distribution function corresponds to the lowest energy state. The final coarse-grained equilibrium is then the lowest energy state with energy equal to that of the initial state but corresponding to the distribution with the memory function equal to the transformed by mixing function $\bar{g}(\phi)$.

The real draw back of this procedure is in the unknown transformation experienced by the memory function due to the filamentation. Wiechen and Ziegel suggested to use a self-similar transformation given by

$$\bar{g}(\phi) = \frac{1}{\delta} g(\phi/\delta), \tag{5.8}$$

where δ is the parameter related to the mixing scale for cases with strong and uniform filamentation. Models for the transformation of g for cases with non-uniform mixing were also suggested [55]. However, no model derived from the first principles for the transformation experienced by the memory function is known. This ambiguity in the construction of $\bar{g}$, which is crucial to obtaining results for the final beam properties, prevents us from performing direct comparisons of this theory with the numerical simulation.

5.4 Non-thermal Character of the Final Coarse-grained Equilibrium

Theory of Ref. [2], developed by Rosenzweig and Chen, assumes that the beam becomes thermalized in the coarse-grained equilibrium state. The PIC results for the asymptotic temperature profiles presented in Sec. 5.2 and final values of the correlation ratio presented in Sec. 3.2 clearly indicate that the equilibrium coarse-grained distribution has a non-thermal character. This conclusion can also be reached considering the dynamical invariants of the system.

Consider, for example, the initially gaussian distribution given by Eq. (2.3). To find whether it is possible to reach a thermal equilibrium state in the averaged sense, we assume a Bennett distribution for the coarse-grained function in a final state. The relations between the beam size and velocity spread in asymptotic Bennett equilibrium and initial gaussian states were derived in Sec. 2.3 and are given by Eqs. (2.33) and (2.38). The derivation was based on the use of the equilibrium condition and the constraint of energy conservation. Our system, however, possesses other dynamical invariants. Consider the Vlasov equation for the distribution function $f(0,0)$ evaluated at the origin of the phase-space

$$\frac{\partial f(0,0)}{\partial t} - \frac{q_b v_z B_y(0)}{m_b \gamma} \frac{\partial f(0,0)}{\partial v_x} = 0. \tag{5.9}$$

Due to the even symmetry of the beam density, $(n_b(x) = n_b(-x))$, the magnetic field vanishes at the origin. Thus, the value of $f(0,0)$ is conserved in the dynamics of the beam. Making an assumption based on the insignificant filamentation at the origin that the coarse-grained distribution at the origin is approximately equal to the exact distribution function, the conservation of the averaged distribution at the origin results. Using expressions for the assumed initial and final distributions given by Eqs. (2.3) and (2.35), the condition for the

invariance of the distribution function at the origin can be explicitly written as

$$f_0(0,0) = \frac{N}{2\pi}\frac{1}{\sigma_{xo}\sigma_{vo}} = \bar{f}_B(0,0) = \frac{N}{4\sqrt{6}}\frac{\sqrt{\pi}}{\sigma_{x,eq}\sigma_{v,eq}}. \tag{5.10}$$

Substituting the values of the final beam properties $\sigma_{x,eq}$ and $\sigma_{v,eq}$ given by Eqs. (2.33) and (2.38) into Eq. (5.10), and defining a function

$$R(\alpha) = \frac{2\sqrt{2}}{3\pi\sqrt{3}}\frac{(1+2\alpha)^{3/2}}{\alpha}. \tag{5.11}$$

the following condition

$$R(\alpha) = 1 \tag{5.12}$$

is obtained. Thus, when the condition of Eq. (5.12) is satisfied the equilibrium state preserves both invariants (*i.e.*, energy and number of particles at the origin) of the system.

The plot of the function $R(\alpha)$ *vs* α is presented in Fig. 5.11. It indicates that the

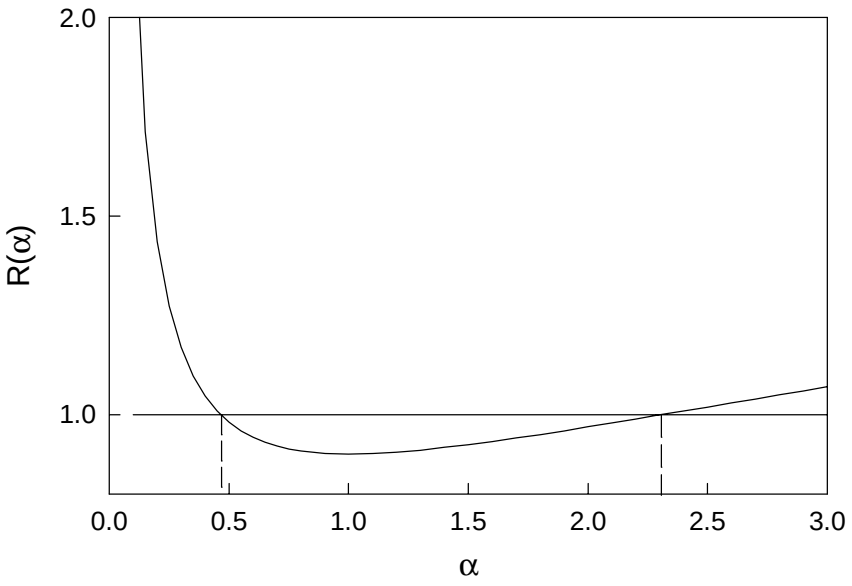

Figure 5.11: Function $R(\alpha)$ defined by Eq. (5.11).

condition of Eq. (5.12) is satisfied only at specific values of the initial mismatch parameter α. In particular, two initial distributions with $\alpha = 0.47$ and $\alpha = 2.34$ result in $R(\alpha) = 1$ and

thus possibly allow for the final thermal distribution. While we can not make a statement that these values of the initial mismatch parameter result in the thermalization of the distribution, we can conclusively state that the establishment of the thermal equilibrium is impossible for all other values of α. This theoretical conclusion is supported by the numerical results. Indeed, the temperature profiles of the asymptotic state show the spatial dependence for most initial conditions considered. The value of the correlation ratio is different from unity as well indicating the non-thermal character of the distribution.

5.5 Simple Analytical Model for the Asymptotic State

A great interest exists in the prediction of the final coarse-grained state bypassing the evolution of the system towards the equilibrium state. As discussed in Secs. 5.1 and 5.3, a significant amount of previous work was devoted to this subject. Unfortunately, no analytical theory exists that provides good predictions of the asymptotic distribution. Such theory could also shed light on the physics governing the selection of the final state.

We have obtained the estimates of the beam bulk properties (*i.e.* beam size and velocity spread) in the final coarse-grained equilibrium, as shown in Sec. 2.3. Good agreement with PIC simulations was observed for mismatches from $\alpha = 0.2$ to $\alpha = 10$. We now consider the problem of predicting the values of higher order moments which, in principle, can be used to reconstruct the whole distribution function profile. The values of only a few higher order moments, such as 4^{th} order, can be used to make conclusions about the general properties of the distribution such as the degree of space-velocity correlations. Due to the complexity of the problem, we do not attempt to make detailed accurate predictions but instead concentrate on obtaining the main observed effects and understanding their physical mechanism. These effects include the correlated nature of the final distribution function, the increase of the degree of the space-velocity correlation as the initial mismatch parameter is increased, and a change in the asymptotic beam density profile as α changes which can be seen in the change of the ration of $\langle x^4 \rangle / \langle x^2 \rangle^2$.

Toward this goal, a simple analytical model is derived that provides us with estimates of the final values of higher order moments. To our knowledge, analytic estimates of higher order moments have not been previously obtained. The theoretical predictions contain main features of the asymptotic state. The analytical treatment requires some simplifying assumptions. In evaluating virial integrals of the form $\langle x^p v_x^q F_x \rangle$, F_x is approx-

imated by an external time-independent linear force. While the spatial nonlinearity of the force is very important in the rate of decay of the coarse-grained distribution towards the equilibrium state through phase mixing and filamentation, we expect it to play a minor role in determining the final state of the beam. We expect, given the above simplifications, only a qualitative agreement between the theoretical model and PIC results.

Although estimates of the beam size and temperature for the equilibrium state were already obtained in Sec. 2.3, we begin by reevaluating the results using the assumptions of the simplified model. These estimates are later used to obtained predictions for higher order moments. We start with the dynamical equations for the evolution of second order moments, given by Eqs. (2.19)-(2.21). We rewrite them here for convenience:

$$\frac{d\langle x^2\rangle}{dt} = 2\langle xv_x\rangle, \tag{5.13}$$

$$\frac{d\langle xv_x\rangle}{dt} = \langle v_x^2\rangle - \frac{q_b v_z}{m_b\gamma}\langle xB_y\rangle, \tag{5.14}$$

$$\frac{d\langle v_x^2\rangle}{dt} = -2\frac{q_b v_z}{m_b\gamma}\langle v_xB_y\rangle. \tag{5.15}$$

We now assume that the magnetic field of the beam needed to evaluate the averages $\langle xB_y\rangle$ and $\langle v_xB_y\rangle$, can be approximated by a linear time-independent function. Explicitly, we approximate the force by

$$\frac{q_b v_z}{m_b\gamma}B_y(x) = \beta x. \tag{5.16}$$

Now Eqs. (5.13)-(5.15) take the following form

$$\frac{d\langle x^2\rangle}{dt} = 2\langle xv_x\rangle, \tag{5.17}$$

$$\frac{d\langle xv_x\rangle}{dt} = \langle v_x^2\rangle - \beta\langle x^2\rangle, \tag{5.18}$$

$$\frac{d\langle v_x^2\rangle}{dt} = -2\beta\langle xv_x\rangle. \tag{5.19}$$

The direct integration of these simplified dynamical equations, which are now closed within the second order moment system, will show no relaxation. This is not surprising since the spatial linearity of the force was assumed along with a lack of coupling to higher order moments. However, we anticipate that the state around which the oscillations take place can serve as an approximation for the equilibrium. From Eq. (5.18), we conclude that in this equilibrium state

$$\langle v_x^2\rangle_{eq} = \beta\langle x^2\rangle_{eq}. \tag{5.20}$$

Equation (5.20) is equivalent to the equilibrium condition used in Sec. 2.3. It can be obtained directly from Eq. (2.22) by substituting Eq. (5.16) for the magnetic field. From Eqs. (5.17) and (5.19) we also conclude that during the dynamics

$$\frac{d}{dt}(\beta\langle x^2\rangle + \langle v_x^2\rangle) = 0. \tag{5.21}$$

This equation is equivalent to the simplified conservation of energy relation for the linearized force. However, it can not be obtained from the conservation of energy given by Eq. (2.30). The difference comes from the assumption of the external force and, therefore, a lack of self-consistency in the problem. The conservation of energy relation can be used to specify the equilibrium state as

$$\beta\langle x^2\rangle_{eq} + \langle v_x^2\rangle_{eq} = \beta\langle x^2\rangle_o + \langle v_x^2\rangle_o. \tag{5.22}$$

Using the definition of the initial mismatch parameter given by Eq. (2.5), we find

$$\alpha = \frac{q_b v_z \langle xB_y\rangle_o}{m\gamma\langle v_x^2\rangle_o} = \frac{\beta\langle x^2\rangle_o}{\langle v_x^2\rangle_o}, \tag{5.23}$$

where Eq. (5.16) is used for the force acting on the beam particles. Substituting Eq. (5.20) into Eq. (5.22) and expressing $\langle v_x^2\rangle_o$ through the initial mismatch parameter and the beam size, we obtain

$$2\beta\langle x^2\rangle_{eq} = \beta\langle x^2\rangle_o + \frac{\beta}{\alpha}\langle x^2\rangle_o. \tag{5.24}$$

Simplification of the last equation yields

$$\langle x^2\rangle_{eq} = \frac{(1+\alpha)}{2\alpha}\langle x^2\rangle_o. \tag{5.25}$$

Using the equilibrium condition and the definition of α we obtain the velocity spread in equilibrium

$$\langle v_x^2\rangle_{eq} = \frac{(1+\alpha)}{2}\langle v_x^2\rangle_o. \tag{5.26}$$

The final emittance can now be easily computed; it is given by

$$\varepsilon_{eq} = \frac{(1+\alpha)}{2\sqrt{\alpha}}\varepsilon_o. \tag{5.27}$$

Equations (5.25)-(5.27) differ from more general results given by Eqs. (2.33), (2.38) and (2.40) derived in Sec. 2.3 for an initially gaussian beam. This discrepancy arises from

the approximation of a linear, external force. Note that due to these approximations, the estimates for the beam size and emittance normalized to their initial values do not depend on the initial density profile. Rather, they are determined by the value of the mismatch parameter.

The comparison between numerical PIC results, predictions of Sec. 2.3 and current estimates is presented for an initial beam with a gaussian distribution in Fig. 5.12 and for an initially uniform beam in Fig. 5.13. The comparisons indicate that even a simple theory with an external linearized force predicts a correct dependence of the final bulk properties on the initial mismatch parameter. However, due to the simplifications, the agreement with PIC results is not as good as it is in the case of a more sophisticated model of Sec. 2.3.

A virtue of this simplified model is that it allows us to estimate the values of higher order moments in the asymptotic state. Let us consider the system of dynamical equations for the forth order moments

$$\begin{aligned}
\frac{d\langle x^4\rangle}{dt} &= 4\langle x^3 v_x\rangle, \\
\frac{d\langle x^3 v_x\rangle}{dt} &= 3\langle x^2 v_x^2\rangle - \frac{q_b v_z}{m_b\gamma}\langle x^3 B_y\rangle, \\
\frac{d\langle x^2 v_x^2\rangle}{dt} &= 2\langle x v_x^3\rangle - 2\frac{q_b v_z}{m_b\gamma}\langle x^2 v_x B_y\rangle, \\
\frac{d\langle x v_x^3\rangle}{dt} &= \langle v_x^4\rangle - 3\frac{q_b v_z}{m_b\gamma}\langle x v_x^2 B_y\rangle, \\
\frac{d\langle v_x^4\rangle}{dt} &= -4\frac{q_b v_z}{m_b\gamma}\langle v_x^3 B_y\rangle. \qquad (5.28)
\end{aligned}$$

Using approximation of Eq. (5.16), the last system can be rewritten as

$$\begin{aligned}
\frac{d\langle x^4\rangle}{dt} &= 4\langle x^3 v_x\rangle, \qquad (5.29) \\
\frac{d\langle x^3 v_x\rangle}{dt} &= 3\langle x^2 v_x^2\rangle - \beta\langle x^4\rangle, \qquad (5.30) \\
\frac{d\langle x^2 v_x^2\rangle}{dt} &= 2\langle x v_x^3\rangle - 2\beta\langle x^3 v_x\rangle, \qquad (5.31) \\
\frac{d\langle x v_x^3\rangle}{dt} &= \langle v_x^4\rangle - 3\beta\langle x^2 v_x^2\rangle, \qquad (5.32) \\
\frac{d\langle v_x^4\rangle}{dt} &= -4\beta\langle x v_x^3\rangle. \qquad (5.33)
\end{aligned}$$

Equations (5.30) and (5.32) immediately provide the equilibrium conditions

$$\langle x^4\rangle = \frac{3}{\beta}\langle x^2 v_x^2\rangle, \qquad (5.34)$$

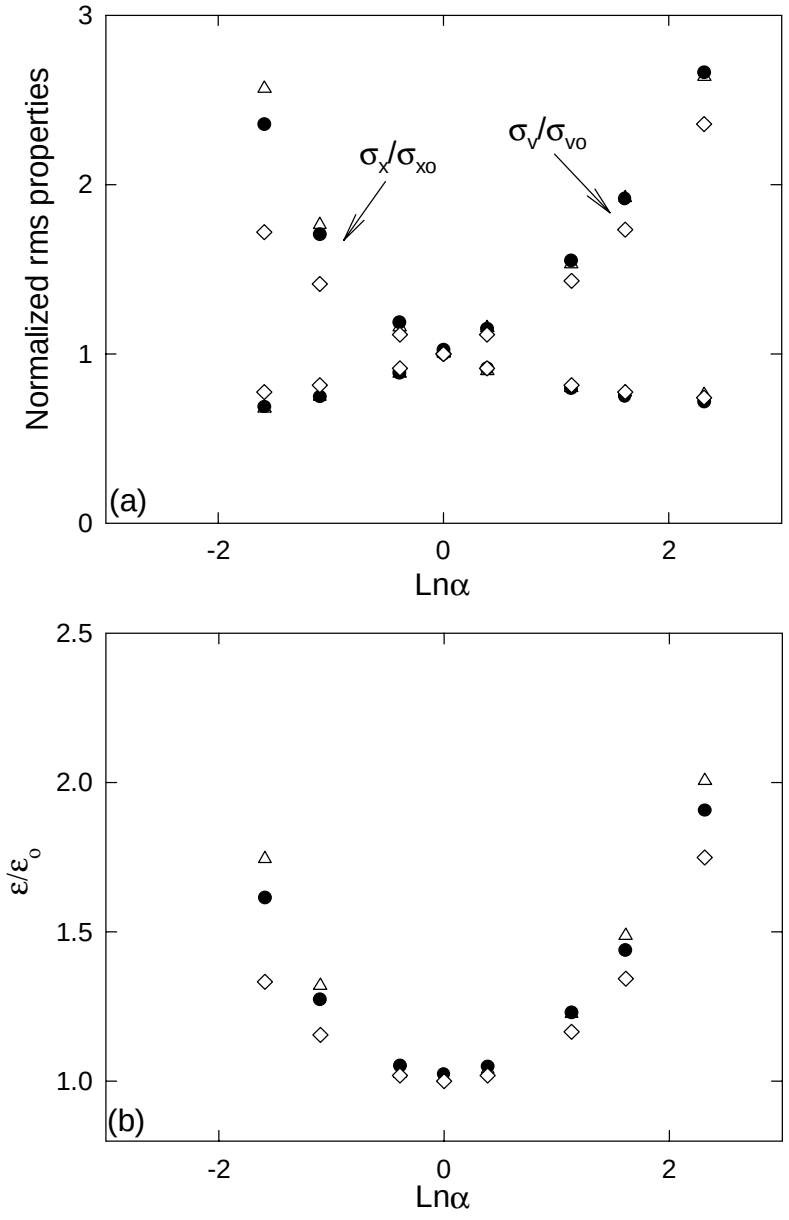

Figure 5.12: Comparison between the simple analytical predictions given by Eqs. (5.25)-(5.27) ($\diamond$), predictions of Eqs. (2.33), (2.38) and (2.40) ($\bullet$) and PIC results ($\triangle$) for (a) the rms beam properties and (b) the emittance *vs* the initial mismatch α of the initially gaussian beam.

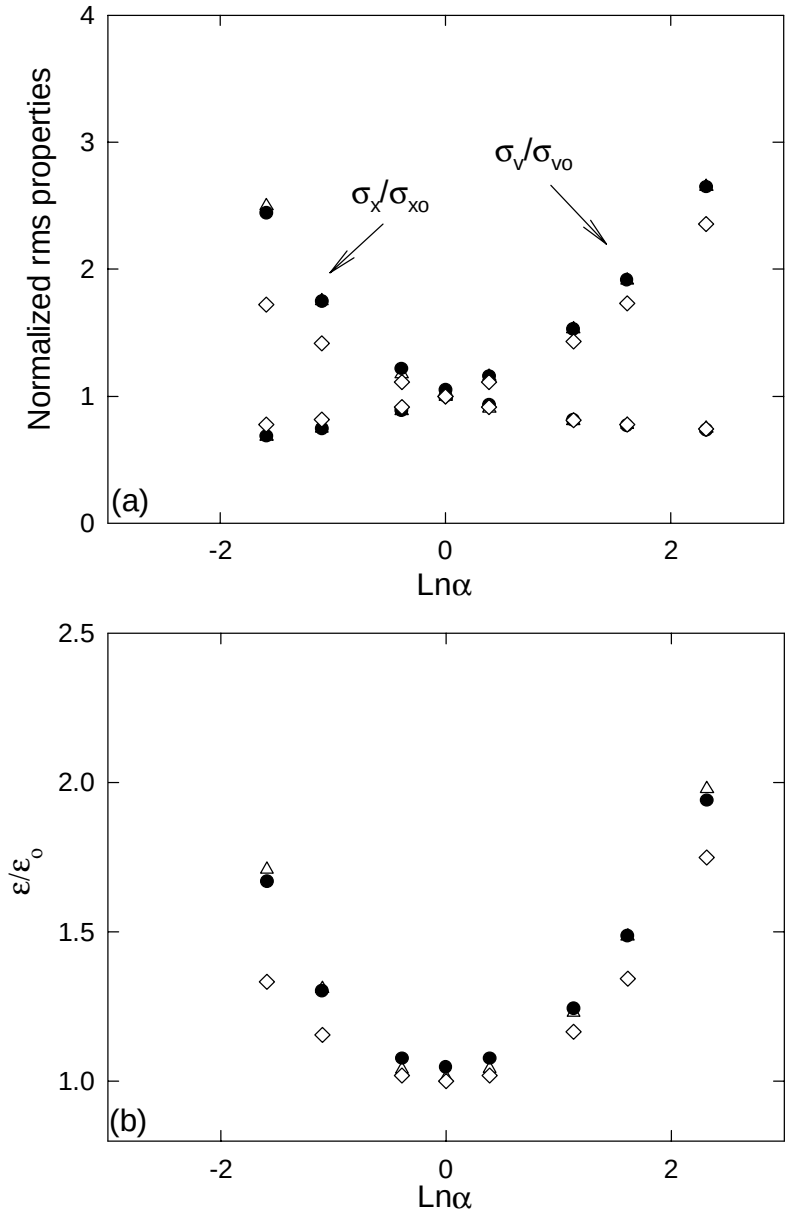

Figure 5.13: Comparison between the simple analytical predictions given by Eqs. (5.25)-(5.27) ($\diamond$), predictions of Eqs. (2.33), (2.39) and (2.41) ($\bullet$) and PIC results ($\triangle$) for (a) the rms beam properties and (b) the emittance *vs* the initial mismatch α of the initially uniform beam.

$$\langle v_x^4 \rangle \quad = \quad 3\beta \langle x^2 v_x^2 \rangle. \tag{5.35}$$

Combining Eqs. (5.29), (5.31) and (5.33) yields a conservation law for the dynamical evolution

$$\frac{d}{dt}\left(\beta \langle x^4 \rangle + 2\langle x^2 v_x^2 \rangle + \frac{1}{\beta}\langle v_x^4 \rangle \right) = 0. \tag{5.36}$$

Using this conservation law, the relation between 4^{th} order moments in the final and initial state can be easily obtained as

$$\beta \langle x^4 \rangle_{eq} + 2\langle x^2 v_x^2 \rangle_{eq} + \frac{1}{\beta}\langle v_x^4 \rangle_{eq} = \beta \langle x^4 \rangle_o + 2\langle x^2 v_x^2 \rangle_o + \frac{1}{\beta}\langle v_x^4 \rangle_o. \tag{5.37}$$

Using the equilibrium conditions given by Eqs. (5.34)-(5.35), the conservation relation can also be written as

$$8\langle x^2 v_x^2 \rangle_{eq} = \beta \langle x^4 \rangle_o + 2\langle x^2 v_x^2 \rangle_o + \frac{1}{\beta}\langle v_x^4 \rangle_o. \tag{5.38}$$

To further specify the relations between second and forth order moments, let us consider two particular examples of the initially gaussian and uniform beams. We begin with a case of a gaussian beam. Using explicit expressions for the gaussian density, the following relations can be easily obtained

$$\begin{aligned} \langle x^4 \rangle_o &= 3\sigma_{xo}^4, \\ \langle v_x^4 \rangle_o &= 3\sigma_{vo}^4. \end{aligned} \tag{5.39}$$

Substitution of these expressions into the conservation relation given by Eq. (5.38) and use of Eq. (5.23) for the initial mismatch parameter α yields

$$\frac{\langle x^2 v_x^2 \rangle_{eq}}{\sigma_{xo}^2 \sigma_{vo}^2} = \frac{3\alpha^2 + 2\alpha + 3}{8\alpha}. \tag{5.40}$$

Using relations between the equilibrium and initial beam size and velocity spread, given by Eqs. (5.25) and (5.26), the theoretical prediction for the correlation ratio takes the form

$$\frac{\langle x^2 v_x^2 \rangle_{eq}}{\sigma_{x,eq}^2 \sigma_{v,eq}^2} = \frac{3\alpha^2 + 2\alpha + 3}{2(1+\alpha)^2}. \tag{5.41}$$

The equilibrium condition of Eq. (5.34) combined with Eq. (5.40) or Eq. (5.41) results in an estimate for the fourth order spatial moment

$$\frac{\langle x^4 \rangle_{eq}}{\sigma_{x,eq}^4} = \frac{3}{2}\frac{(3\alpha^2 + 2\alpha + 3)}{(1+\alpha)^2}, \tag{5.42}$$

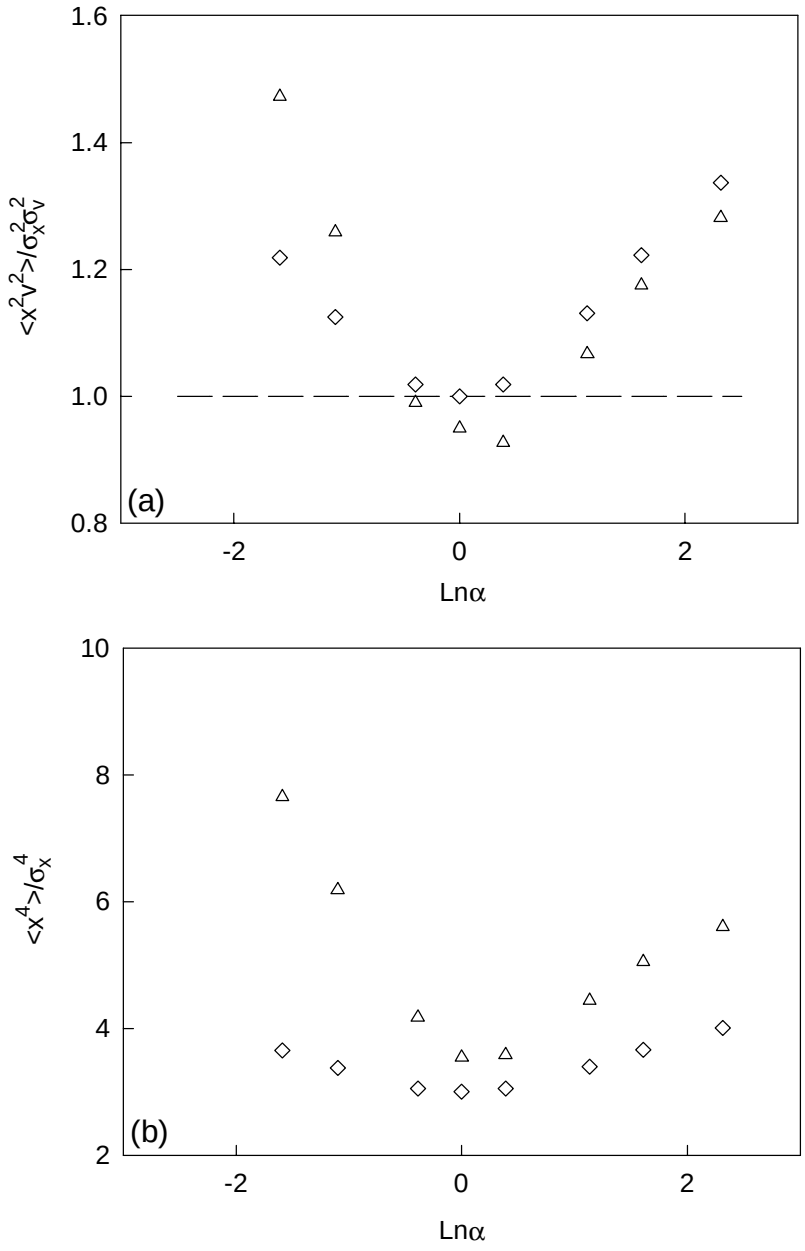

Figure 5.14: Comparison between the simple analytical predictions given by Eqs. (5.41)-(5.42) ($\diamond$) and PIC results ($\triangle$) for (a) the correlation ratio $\langle x^2 v_x^2 \rangle_{eq} / \sigma_{x,eq}^2 \sigma_{v,eq}^2$ (b) the spatial ratio $\langle x^4 \rangle_{eq} / \sigma_{x,eq}^4$ for the initially gaussian beam *vs* the mismatch parameter α. The correlation ratio for the decorrelated distribution is also plotted as a reference (- - - -).

where the expression for the initial mismatch parameter is used.

Comparisons between the analytical predictions and PIC simulation results for fourth order moments are presented in Fig. 5.14. The figure clearly indicates that the theoretical estimates show the correct trend in the dependence of the correlation ratio and the ratio of the fourth order spatial moment to σ_x^4 on the initial mismatch parameter. The prediction of Eq. (5.41) becomes notably different from unity for beams with a significant initial mismatch. The approximations made in the model make the discrepancies observed between the analytical estimates and PIC results unsurprising.

Analogous relations can also be obtained for the initially uniform beam. For such a beam, the fourth order moments are related to the second order moments by

$$\begin{aligned} \langle x^4 \rangle_o &= 1.8\sigma_{xo}^4, \\ \langle v_x^4 \rangle_o &= 1.8\sigma_{vo}^4. \end{aligned} \tag{5.43}$$

Repeating the procedure already used for the initially gaussian beam, the correlation ratio in the asymptotic state is estimated to be

$$\frac{\langle x^2 v_x^2 \rangle_{eq}}{\sigma_{x,eq}^2 \sigma_{v,eq}^2} = \frac{1.8\alpha^2 + 2\alpha + 1.8}{2(1+\alpha)^2}. \tag{5.44}$$

The ratio of the spatial fourth order moment to the square of the beam size can also be evaluated, and it is given by

$$\frac{\langle x^4 \rangle_{eq}}{\sigma_{x,eq}^4} = \frac{3}{2}\frac{(1.8\alpha^2 + 2\alpha + 1.8)}{(1+\alpha)^2}. \tag{5.45}$$

Note that in contrast to the estimates for the second order moments, the predictions for the fourth order moments depend on the initial density profile.

Comparisons between Eqs. (5.44)-(5.45) and PIC results for the initially uniform beam are plotted in Fig. 5.15. We observe a similar dependence of the theoretical estimates and the numerical predictions on the initial mismatch parameter. Some significant discrepancies are also seen as a consequence of the approximations. The simple analytical predictions for the fourth order moments obtained in this section can be used to make fast estimates for the general properties of the distribution.

The obtained predictions for the forth order moments together with the results of PIC simulations indicate that the final coarse-grained equilibrium shows some dependence on the initial beam parameters. For example, the value of the correlation ratio shows a

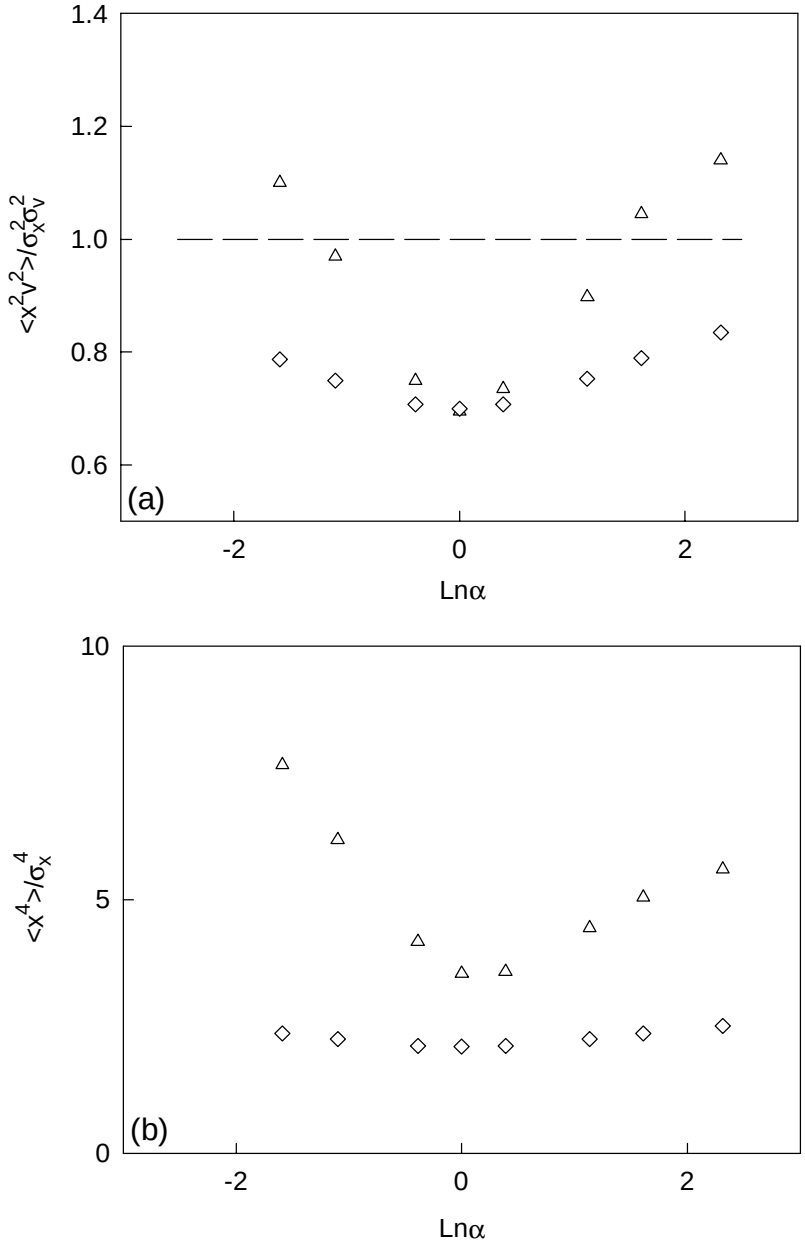

Figure 5.15: Comparison between the simple analytical predictions given by Eqs. (5.41)-(5.42) ($\diamond$) and PIC results ($\triangle$) for (a) the correlation ratio $\langle x^2 v_x^2 \rangle_{eq} / \sigma_{x,eq}^2 \sigma_{v,eq}^2$ (b) the spatial ratio $\langle x^4 \rangle_{eq} / \sigma_{x,eq}^4$ for the initially uniform beam *vs* the initial mismatch parameter α. The correlation ratio for the decorrelated distribution is also plotted as a reference (- - - -).

strong connection to the initial beam mismatch. The value of the spatial ratio $\langle x^4 \rangle_{eq} / \sigma_{x,eq}^4$ also shows the dependence on the initial mismatch pointing towards a change in the beam density profile. The results for the two ratios are also different for the initially gaussian and uniform beams. In contrast with the viscous systems that always tend to the same final distribution (*i.e.* thermal), these results indicate that a certain degree of memory is present in the system.

The calculation can be continued to predict the values of higher order beam moments in the stationary state. In principle, the properties of the final coarse-grained distribution function can then be reconstructed, and different system properties of interest such as density and temperature can be computed. However, due to the observed discrepancies in the fourth order moments, we do not expect a good agreement between the numerical and analytical predictions. We, therefore, stop with the simplified theory presented in this section, and investigate a different approach to evaluating the final beam density.

5.6 Density Profile in the Asymptotic State of a System with an External Force

A real interest exists in the prediction of the density of the system after the coarse-grained equilibrium is reached. Unfortunately, the exact physical mechanism that determines the distribution of the beam after the mixing process is completed is still unknown. Due to the complexity of the problem, we do not attempt to make predictions for the coarse-grained distribution function of the exact problem. Instead, we treat a simpler problem of a beam propagating in a system with an external nonlinear force. The force is chosen to retain some essential features of the exact system of a beam propagating in an overdense plasma. In particular, the force is taken to be equal to the initial self-consistent force of the beam but is assumed to remain constant throughout the propagation.

The lack of time-dependence of the force allows for an infinite set of macroscopic conservation laws that can be used to specify the final state. These conservation laws originate from the invariance of energy of every beam particle. While no assumption can be made about the form of the distribution function in the equilibrium and infinite number of conservation laws can be used to specify the exact profile of the distribution, we follow

an easier path and begin by assuming that equilibrium $\bar{f}$ can be represented as

$$\bar{f}_f(x,v_x) = C(x)n_b(x)[1 + s(x)v_x^2 + t(x)v_x^4 + d(x)v_x^6 + g(x)v_x^8]e^{-v_x^2/\beta^2}, \tag{5.46}$$

where $n_b(x)$ represents the beam density. Thus,

$$\int_{-\infty}^{\infty} dv_x \bar{f}(x,v_x) = n_b(x), \tag{5.47}$$

and $C(x)$ is a normalization function, β is a parameter, and $s(x)$, $t(x)$, $d(x)$ and $g(x)$ are unknown functions of the spatial variable. The expression for the distribution function given by Eq. (5.46) can be considered as a truncated expansion of the distribution function multiplied by the factor $e^{v_x^2/\beta^2}$ in the power series over velocity. The equilibrium conditions and conservation laws are then used to specify the unknown functions $s(x)$, $t(x)$, $d(x)$ and $g(x)$ and a parameter β. First, we use Eq. (5.47) to determine $C(x)$. Integrating $f_f(x,v_x)$ over velocities and using Eq. (5.47), we obtain

$$C(x) = \frac{1}{\beta\sqrt{\pi}} \frac{1}{1 + \frac{1}{2}s(x)\beta^2 + \frac{3}{4}t(x)\beta^4 + \frac{15}{8}d(x)\beta^6 + \frac{105}{16}g(x)\beta^8}. \tag{5.48}$$

Substitution of $C(x)$ into the representation of the distribution function results in

$$\bar{f}_f(x,v_x) = \frac{n_b(x)}{\beta\sqrt{\pi}} \frac{1 + s(x)v_x^2 + t(x)v_x^4 + d(x)v_x^6 + g(x)v_x^8}{1 + \frac{1}{2}s(x)\beta^2 + \frac{3}{4}t(x)\beta^4 + \frac{15}{8}d(x)\beta^6 + \frac{105}{16}g(x)\beta^8} e^{-v_x^2/\beta^2}. \tag{5.49}$$

To specify the unknown functions $s(x)$, $t(x)$, $d(x)$ and $g(x)$, we make use of the equilibrium conditions for the system. In the asymptotic state, the coarse-grained distribution function $\bar{f}_f(x,v_x)$ becomes stationary and thus satisfies the time-independent Vlasov equation. This condition can be written using Eq. (3.1) as

$$v_x \frac{\partial \bar{f}_f}{\partial x} - \frac{q_b v_z B_y}{m_b \gamma} \frac{\partial \bar{f}_f}{\partial v_x} = 0. \tag{5.50}$$

Substituting the expression for the averaged distribution function given by Eq. (5.49) and equating corresponding powers of velocity, the following equations result

$$\begin{aligned} n_b' &= n_b(x) \frac{\frac{\beta^2}{2}s' + \frac{3\beta^4}{4}t' + \frac{15\beta^6}{8}d' + \frac{105\beta^8}{16}g'}{1 + \frac{1}{2}s(x)\beta^2 + \frac{3}{4}t(x)\beta^4 + \frac{15}{8}d(x)\beta^6 + \frac{105}{16}g(x)\beta^8} \\ &- \frac{2}{\beta^2}\frac{q_b v_z B_y}{m_b \gamma} n_b(x) + 2n_b(x)s(x)\frac{q_b v_z B_y}{m_b \gamma}, \end{aligned} \tag{5.51}$$

$$s' = -2s^2(x)\frac{q_b v_z B_y}{m_b \gamma} + 4t(x)\frac{q_b v_z B_y}{m_b \gamma}, \tag{5.52}$$

$$t' = -2s(x)t(x)\frac{q_b v_z B_y}{m_b\gamma} + 6d(x)\frac{q_b v_z B_y}{m_b\gamma}, \tag{5.53}$$

$$d' = -2s(x)d(x)\frac{q_b v_z B_y}{m_b\gamma} + 8g(x)\frac{q_b v_z B_y}{m_b\gamma}, \tag{5.54}$$

$$g' = -2s(x)g(x)\frac{q_b v_z B_y}{m_b\gamma}. \tag{5.55}$$

Here, the notation $'$ denotes the spatial derivative d/dx. These equilibrium conditions ensure that the distribution function given by Eq. (5.49) does not vary in time. If values of these functions are specified in one point in x, the set of ODE can be integrated as an initial value problem and $n_b(x)$, $s(x)$, $t(x)$, $d(x)$ and $g(x)$ can be determined. The required values of the functions at one point on the x-axis can be determined using the appropriate number of conservation laws. Without loss of generality, the point is chosen at the origin $x = 0$. Then, six unknown parameters $n_b(0)$, $s(0)$, $t(0)$, $d(0)$, $g(0)$ and β are used to specify a particular equilibrium state and need to be determined using conservation laws.

The following six conservation laws are utilized: invariance of the value of the distribution function at the origin, conservation of the total number of particles and 4 macroscopic relations stemming from the conservation of energy of every particle. First, the invariance of the value of $\bar{f}(x = 0, v_x = 0, t)$ is used to determine $n_b(x = 0)$ in the asymptotic state. Equating $\bar{f}_f(x = 0, v_x = 0) = f_o(x = 0, v_x = 0)$, where $f_o(x, v_x)$ stands for the phase-space distribution of the initial state, we obtain

$$n_b(0) = \beta\sqrt{\pi} f_o(0,0)(1 + \frac{1}{2}s(0)\beta^2 + \frac{3}{4}t(0)\beta^4 + \frac{15}{8}d(0)\beta^6 + \frac{105}{16}g(0)\beta^8). \tag{5.56}$$

The remaining five conservation laws have a form of integral relations. First, we derive the relations originating from the conservation of particle energy. Consider the dynamical equation for the velocity spread of the beam. The derivation is similar to that of the conservation of energy presented in Sec. 2.3, but is given to show how the present differences in the assumptions affect the result. A self-consistent force was considered in Sec. 2.3, while a simplified system that is acted upon with an external time independent force is investigated here.

We begin with the dynamical equation for the beam temperature given by Eq. (2.21) that we rewrite here for clarity

$$\frac{d\langle v_x^2\rangle}{dt} = -2\frac{q_b v_z}{m_b\gamma}\langle v_x B_y\rangle. \tag{5.57}$$

After substituting $B_y = -\partial A_z/\partial x$ and integrating by parts, Eq. (5.57) becomes

$$\frac{d\langle v_x^2\rangle}{dt} = -2\frac{q_b v_z}{N m_b \gamma}\int dx dv_x\ A_z v_x \frac{\partial f}{\partial x} = 2\frac{q_b v_z}{N m_b \gamma}\frac{d}{dt}\langle A_z\rangle, \tag{5.58}$$

where the Vlasov equation is used, the common boundary condition $f|_{v_x\to-\infty}^{\to+\infty} = f|_C = 0$ is applied, and an integration over v_x is performed. We have also explicitly used the time independence of the external field. The resulting conservation relation can be written as

$$\langle v_x^2\rangle - 2\frac{q_b v_z}{N m_b \gamma}\langle A_z\rangle = C_2, \tag{5.59}$$

where C_2 is a constant.

The next conservation law is obtained from the dynamical equation for the next order velocity moment which is written as

$$\frac{d\langle v_x^4\rangle}{dt} = -4\frac{q_b v_z}{m_b \gamma}\langle v_x^3 B_y\rangle. \tag{5.60}$$

Following the same analysis, we obtain

$$\begin{aligned}\frac{d\langle v_x^4\rangle}{dt} &= -4\frac{q_b v_z}{N m_b \gamma}\int dx dv_x\ A_z v_x^3 \frac{\partial f}{\partial x} \\ &= 4\frac{q_b v_z}{N m_b \gamma}\frac{d}{dt}\langle v_x^2 A_z\rangle - 4\left(\frac{q_b v_z}{N m_b \gamma}\right)^2 \int dx dv_x\ A_z^2 \frac{df}{dt},\end{aligned} \tag{5.61}$$

Taking into account the time independence of the external force, the last equation can be written in the form of the conservation law as follows

$$\langle v_x^4\rangle - 4\frac{q_b v_z}{N m_b \gamma}\langle v_x^2 A_z\rangle + 4\left(\frac{q_b v_z}{N m_b \gamma}\right)^2 \langle A_z^2\rangle = C_4, \tag{5.62}$$

where C_4 is a constant.

This procedure can also be used to obtain higher order conservation laws from the dynamical equations that govern the evolution of higher order velocity moments, $\langle v_x^{2n}\rangle$. Only two more relations are needed to specify the distribution function. As the technique of obtaining the conservation relations is clear, we only quote the final results

$$\langle v_x^6\rangle - 6\frac{q_b v_z}{N m_b \gamma}\langle v_x^4 A_z\rangle + 12\left(\frac{q_b v_z}{N m_b \gamma}\right)^2 \langle v_x^2 A_z\rangle - 8\left(\frac{q_b v_z}{N m_b \gamma}\right)^3 \langle A_z^3\rangle = C_6, \tag{5.63}$$

$$\begin{aligned}\langle v_x^8\rangle &- 8\frac{q_b v_z}{N m_b \gamma}\langle v_x^6 A_z\rangle + 24\left(\frac{q_b v_z}{N m_b \gamma}\right)^2 \langle v_x^4 A_z\rangle - 32\left(\frac{q_b v_z}{N m_b \gamma}\right)^3 \langle A_z^3\rangle \\ &+ 16\left(\frac{q_b v_z}{N m_b \gamma}\right)^4 \langle A_z^4\rangle = C_8.\end{aligned} \tag{5.64}$$

We now have four conservation laws given by Eqs. (5.58), (5.62), (5.63) and (5.64) that can be used to specify $s(0)$, $t(0)$, $d(0)$ and $g(0)$ based on the initial distribution. These invariance relations are the result of the conservation of energy of every particle in the distribution given by

$$E_i(x^{(i)}, v_x^{(i)}) = {v_x^{(i)}}^2 - 2\frac{q_b v_z}{N m_b \gamma} A_z(x^{(i)}), \tag{5.65}$$

where i stand for the index identifying a particle. They can also be obtained directly from the particle energy conservation as averages of

$$\langle E_i^{2n} \rangle \equiv \frac{1}{N} \int\int dx dv_x E^{2n}(x, v_x) f(x, v_x) = C_{2n} \tag{5.66}$$

over the distribution.

The last conservation law that is used to specify the parameters of the final coarse-grained distribution is the invariance of the total number of particles that can be written as

$$N \equiv \int_{-\infty}^{\infty} \int_{-\infty}^{\infty} dx dv_x f_o(x, v_x) = \int_{-\infty}^{\infty} dx n_b(x). \tag{5.67}$$

To find $s(0)$, $t(0)$, $d(0)$, $g(0)$ and β, we use an iterative procedure. First, some starting values of the parameters are assumed. The functions $n_b(x)$, $s(x)$, $t(x)$, $d(x)$ and $g(x)$ are evaluated as a numerical solution of equilibrium conditions given by Eqs. (5.51-(5.55). Then the evaluated distribution function is used to calculate quantities required for the conservation laws. For example, the value of the velocity spread needed for Eq. (5.58) is computed as follows

$$\begin{aligned} \langle v_x^2 \rangle_f &\equiv \int\int dx dv_x v_x^2 \bar{f}_f(x, v_x) = \int dx C(x) n_b(x) \int dv_x v_x^2 [1 + s(x) v_x^2 + t(x) v_x^4 \\ &+ d(x) v_x^6 + g(x) v_x^8] e^{-v_x^2/\beta^2}. \end{aligned} \tag{5.68}$$

Evaluation of the integral over velocities results in

$$\langle v_x^2 \rangle_f = \beta^2 \int dx n_b(x) \frac{1 + \frac{3}{2} s(x)\beta^2 + \frac{15}{4} t(x)\beta^4 + \frac{105}{8} d(x)\beta^6 + \frac{945}{16} g(x)\beta^8}{1 + \frac{1}{2} s(x)\beta^2 + \frac{3}{4} t(x)\beta^4 + \frac{15}{8} d(x)\beta^6 + \frac{105}{16} g(x)\beta^8}. \tag{5.69}$$

The remaining integral over the spatial variable is evaluated numerically using the computed functions $n_b(x)$, $s(x)$, $t(x)$, $d(x)$ and $g(x)$. The values of the conserved quantities are calculated for the assumed form of the distribution function and compared with the unknown initial values. In the next step, the parameters $s(0)$, $t(0)$, $d(0)$, $g(0)$ and β are adjusted,

and the distribution function and conserved quantities are reevaluated. The iterations are continued until convergence to a desired accuracy in the invariant relations is achieved.

The predictions obtained using the technique are compared with PIC results for the asymptotic temperature and density of a beam propagating in the external, time-independent field that is equal to the self-field of the initial distribution. The analysis is performed for the initially gaussian beam with a range of the mismatch parameter. Consider the results obtained for a beam with $\alpha = 5$. The parameters of the initial beam are taken the same as these used in Sec. 2.1. Different starting values for $s(0)$, $t(0)$, $d(0)$, $g(0)$ and β result in the same final values after the iterations are completed. As a result of the iterations, the following final values of the parameters are obtained

$$\begin{aligned} s(0) &= -0.03197, \qquad t(0) = 0.07633, \\ d(0) &= -0.00859, \qquad g(0) = 0.001132, \\ &\beta = 1.334. \end{aligned} \tag{5.70}$$

The conservation relations are satisfied with the accuracy of 10^{-6}. To illustrate the dependence of the unknown spatial functions on x, the solutions of the equilibrium Eqs. (5.51)-(5.55) are plotted in Fig. 5.16 for the solution of Eq. (5.70). It can be seen from the plot that a convergence of the expansion in the powers of v_x is observed in all points in x. The predicted final density and temperature profiles are presented in Fig. 5.17 together with PIC results. The initial profiles are also plotted for reference. Figure 5.17 indicates that the theoretical prediction is in excellent agreement with PIC results. The temperature dependence shows a presence of 'hotter' regions at a distance from the beam center.

Some additional comparisons between the analytical theory and PIC simulations for the final beam properties are presented in the next three figures. Final density and temperature profiles for a beam with $\alpha = 0.33$ are presented in Fig. 5.18, with $\alpha = 1.5$ are plotted in Fig. 5.19, and with $\alpha = 10$ are shown in Fig. 5.20. A very good agreement can be seen in all cases considered.

A theory developed in this Section provides with good predictions for the final beam density and temperature profiles when an external, time-independent nonlinear force is acting on the system. While comparisons were presented here for a restricted system with initial gaussian density and the external force was taken as equal to the self-field of the initial distribution, the tests, performed for other initial conditions and forces, showed good agreement with PIC results. We now modify the technique in the attempt to predict

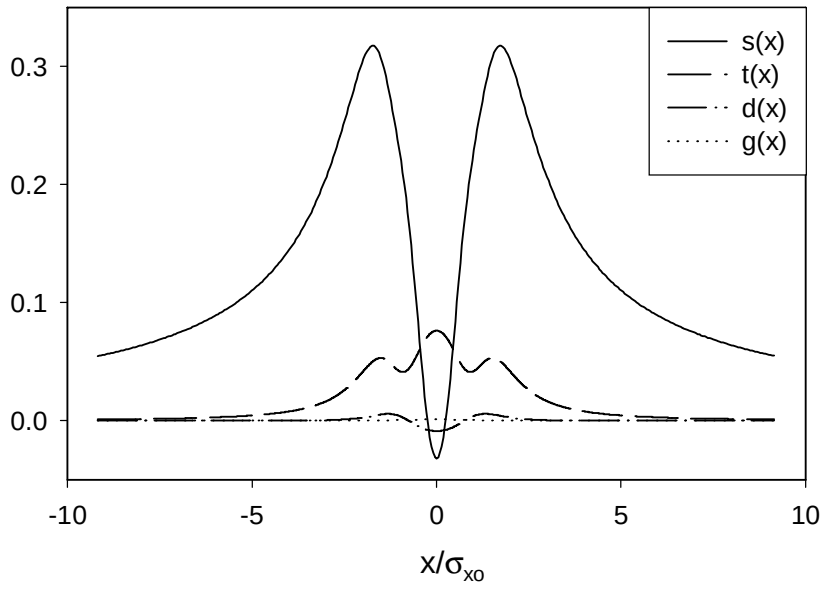

Figure 5.16: The iterative solutions for the unknown equilibrium functions $s(x)$, $t(x)$, $d(x)$ and $g(x)$ corresponding to the initial gaussian beam with $\alpha = 5$.

the asymptotic beam properties for a system with a *self-consistent* force that is the main subject of this thesis. Due to a lack of an exact procedure to determine the final state of such a system, we use an approximate technique based on the method presented above. This analysis also sheds light on the importance of the self-consistency of the force in determining the asymptotic state.

The following successive approximations method is proposed to determine a final state of a system with a nonlinear, self-consistent force. In the first iteration, the coarse-grained equilibrium of a system with an external, time-independent force equal to the self-consistent force of the initial beam is determined using the methodology outlined in this Section. In the following iteration, a final state of a system with an external, time-independent force is again sought but now the force is taken as that of a distribution found in the first iteration. The procedure is carried on up until a convergence in the distribution properties (*i.e.*, α, $s(0)$, $t(0)$, $d(0)$ and $g(0)$) is achieved to a desired accuracy. Following this procedure, an attempt is made to account for an averaged force acting on the beam

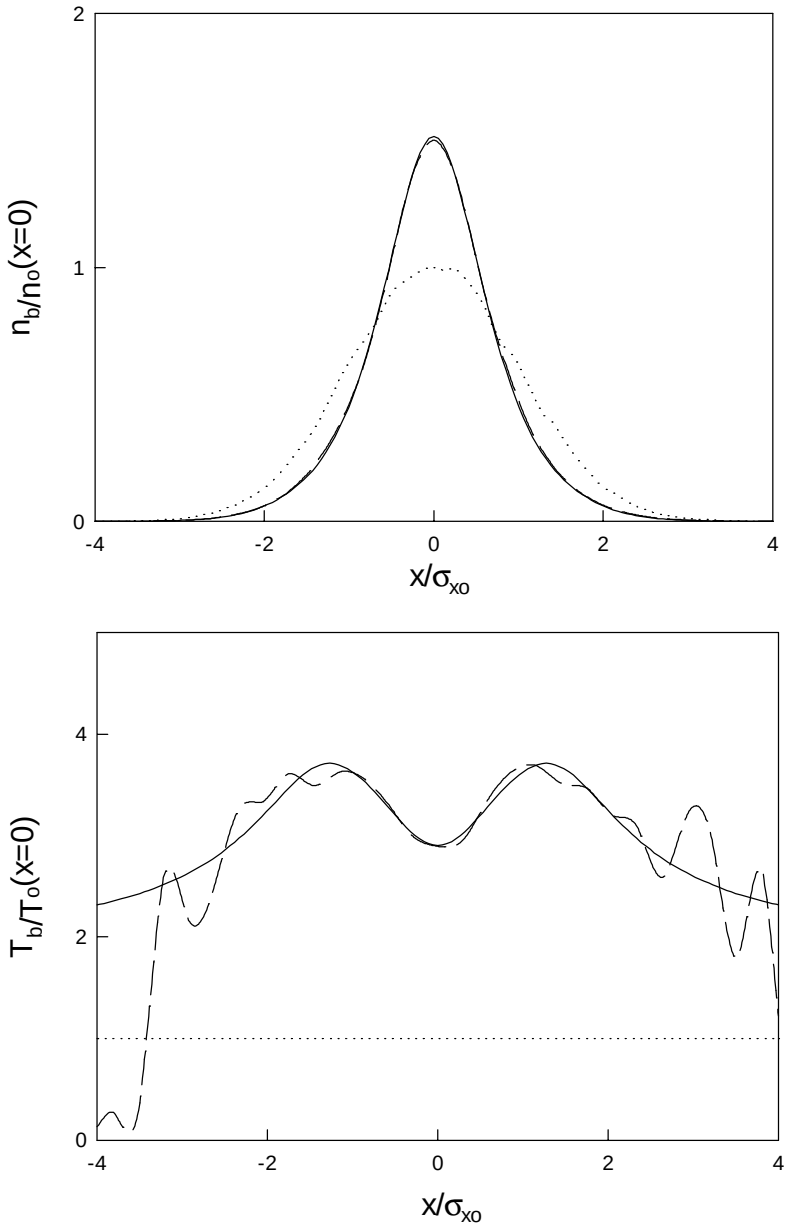

Figure 5.17: Theoretical (———) and PIC (- - - -) final density and temperature profiles for the initially gaussian beam with $\alpha = 5$ acted upon with an external force. The initial profiles ($\cdots\cdots$) are plotted as a reference.

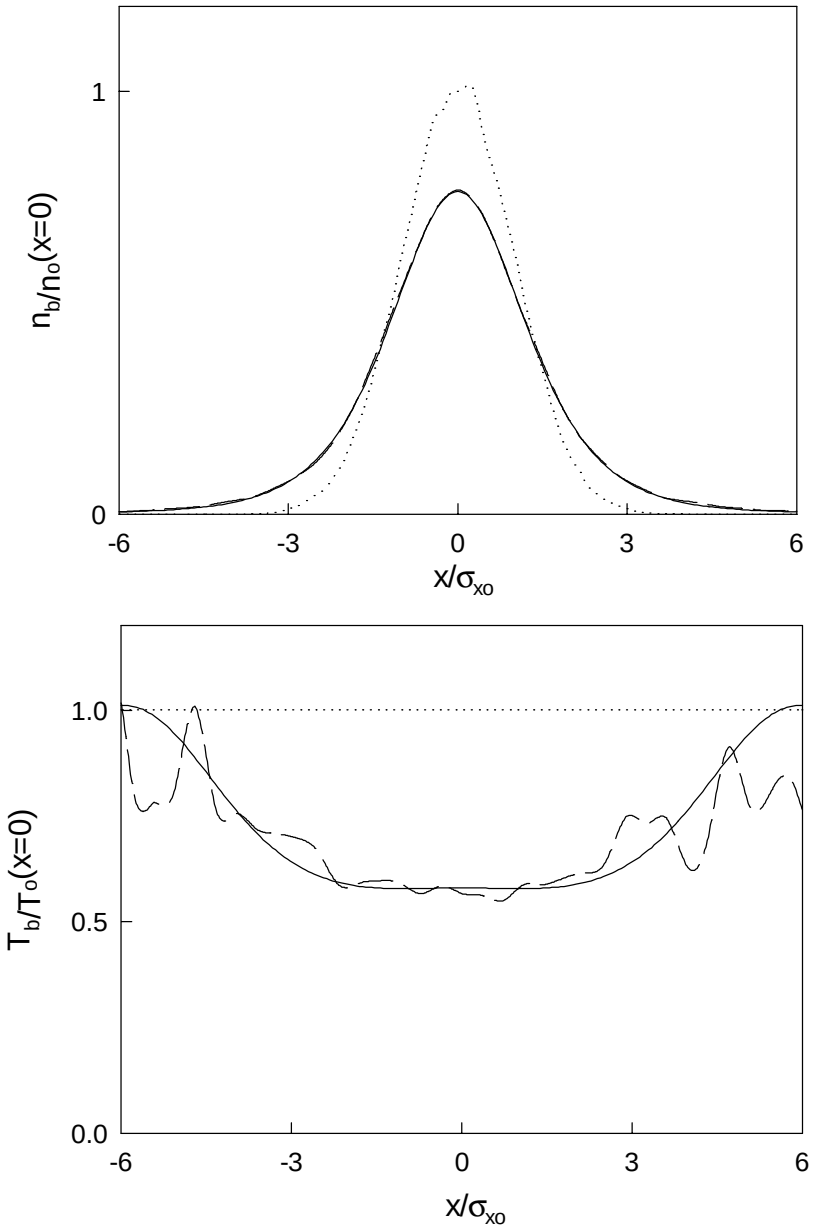

Figure 5.18: Theoretical (———) and PIC (- - - -) final density and temperature profiles for the initially gaussian beam with $\alpha = 0.33$ acted upon with an external force. The initial profiles ($\cdots\cdots$) are plotted as a reference.

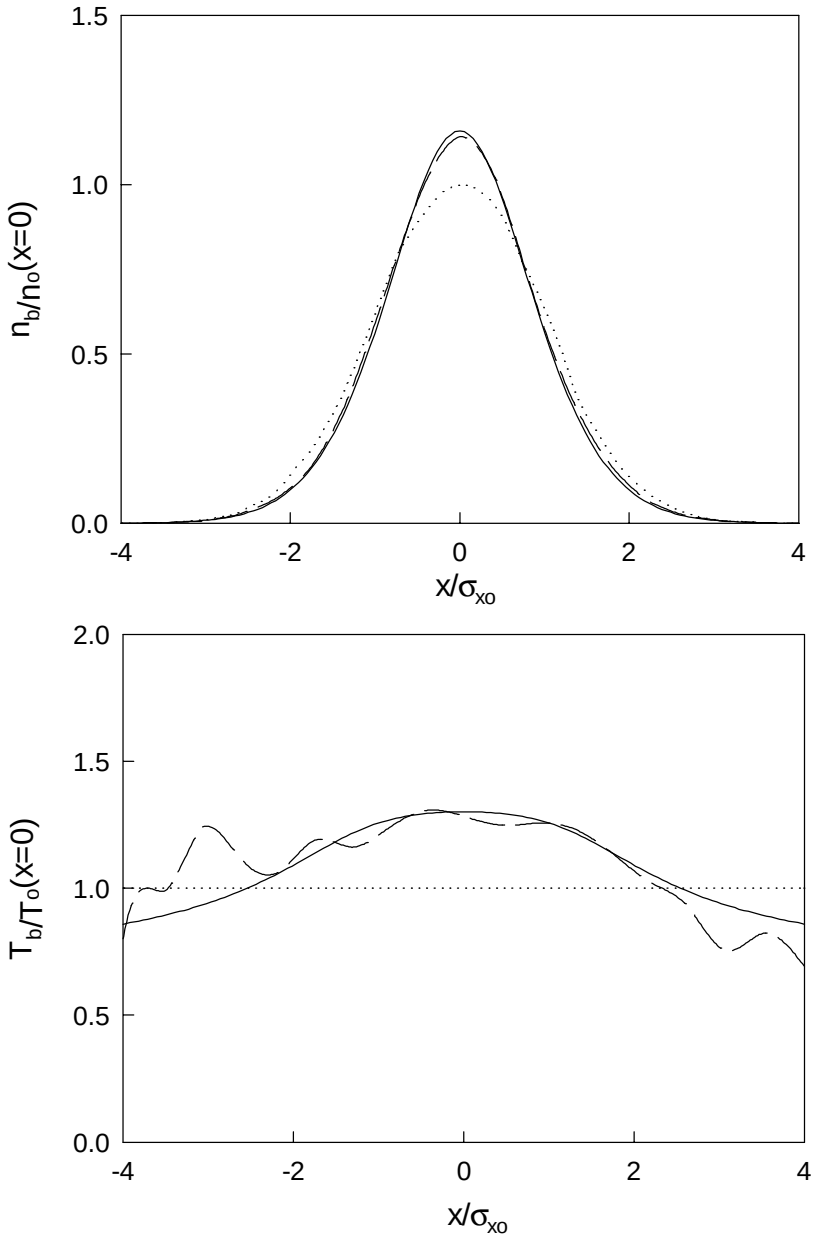

Figure 5.19: Theoretical (———) and PIC (- - - -) final density and temperature profiles for the initially gaussian beam with $\alpha = 1.5$ acted upon with an external force. The initial profiles ($\cdots\cdots$) are plotted as a reference.

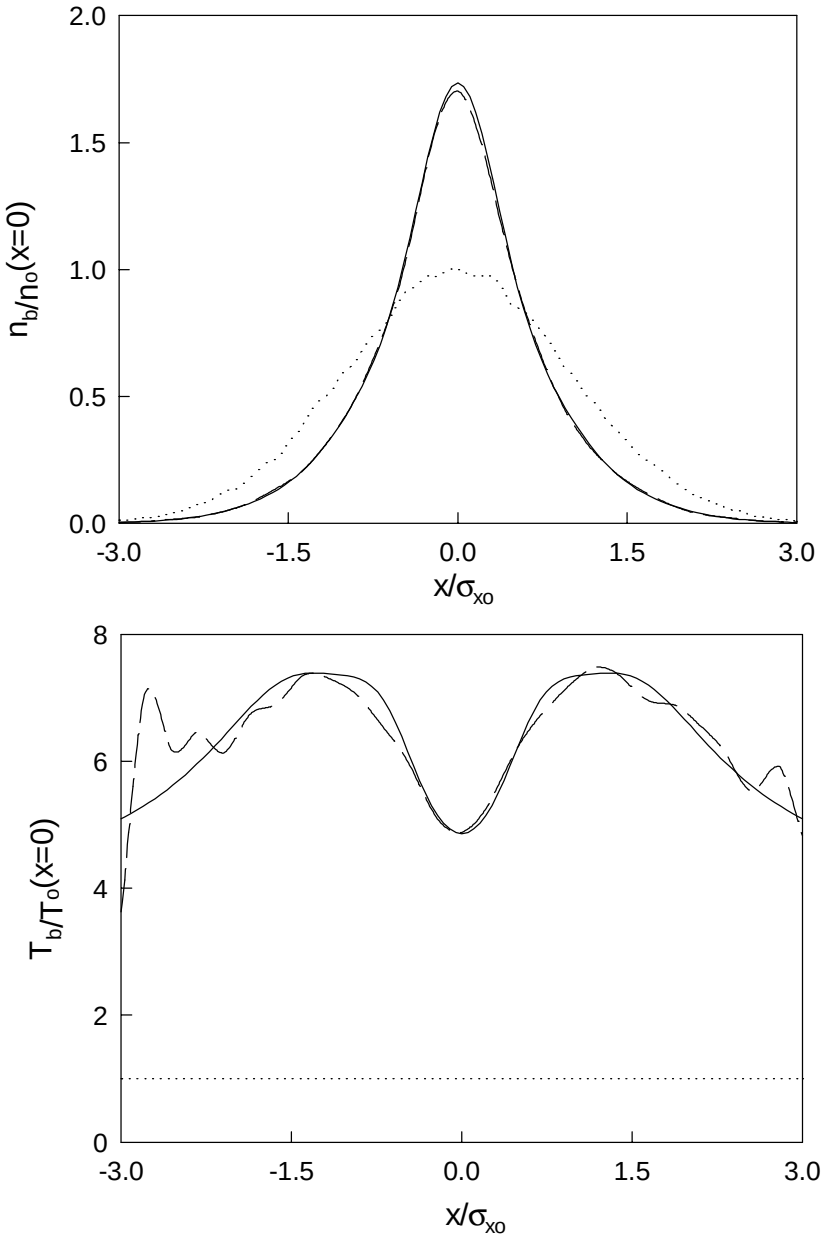

Figure 5.20: Theoretical (———) and PIC (- - - -) final density and temperature profiles for the initially gaussian beam with $\alpha = 10$ acted upon with an external force. The initial profiles ($\cdots\cdots$) are plotted as a reference.

in the process of its evolution. We want to emphasize that no rigorous proof is presented here of the fact that the procedure would result in convergence to a particular distribution. The distribution found in this way would correspond to a true equilibrium solution of the Vlasov equation (due to the use of the equilibrium Eqs. (5.51)-(5.55)).

The results obtained for a system with a self-consistent force are compared with PIC predictions in the next four figures. Initial density and temperature profiles, as well as results obtained for the time-independent, external force equal to that of the initial beam are also plotted as a reference. Predictions are presented for the initially gaussian beam with different values of the initial mismatch parameter. In particular, results for $\alpha = 0.33$, $\alpha = 1.5$, $\alpha = 5$ and $\alpha = 10$ are plotted. Convergence up to the accuracy 10^{-5} in the distribution parameters is achieved in all cases considered.

Predictions for an initially gaussian beam with $\alpha = 0.33$ are presented in Fig. 5.21. The results for the density and temperature profiles obtained using the iterative model (———) and a PIC simulation (- - - -) are plotted together with the initial beam profile ($\cdots\cdots$) and theoretical predictions obtained for a system acted upon with an external force equal to the self-consistent force of the initial beam (— · — · — ·). It can be seen that the iterative model offers only a slight change over the results for the time-independent force equal to that of the initial beam. PIC results indicate that the final beam density and temperature resemble the results obtained with a time-independent force.

The predictions for the asymptotic properties for a self-consistent evolution of a beam with the initial mismatch of $\alpha = 1.5$ are presented in Fig. 5.22. The results of the iterations appear to be very similar to the predictions for the calculation with a force acting on the initial beam. Dynamical PIC results for the asymptotic properties again show that the final profiles are not greatly affected by the variations in the force.

Results for the initial gaussian beam with $\alpha = 5$ are plotted in Fig. 5.23. We again observe that the iteration technique produces results similar to these obtained for a beam acted upon with the initial force. However, PIC simulation indicates that the density and especially temperature profiles become significantly different for this case compared to the time independent force result. In particular, we observe a much more significant variation in the beam temperature between the beam core and hot exterior regions. This can also be seen in the density plot as a sharp transition between the core and the halo of the beam. The theoretical prediction, obtained using the iteration procedure, does not show a pronounced transition between the core and the halo in the density plot and underestimates

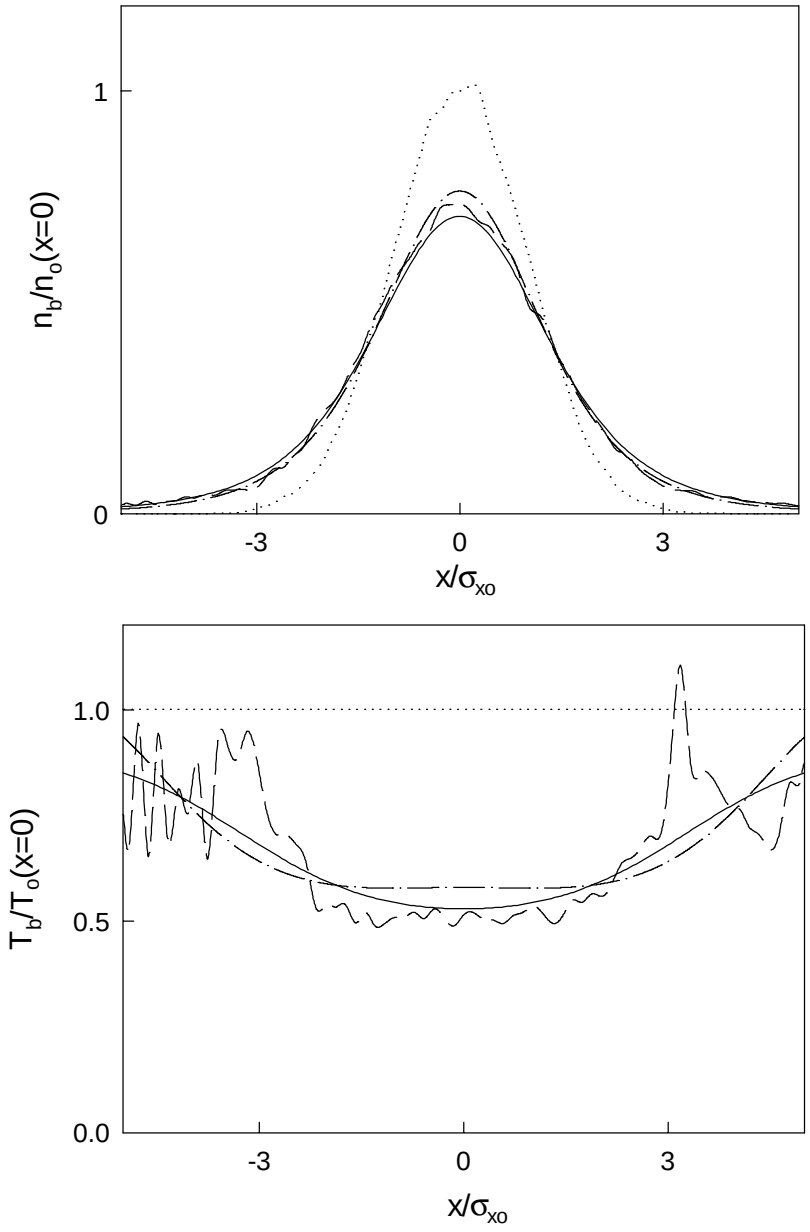

Figure 5.21: Comparison between theoretical (———) and PIC predictions (- - - -) for a beam acted upon with a self-consistent force. The initial profiles for a gaussian beam with $\alpha = 0.33$ ($\cdots\cdots$) together with the theoretical prediction for the external, time-independent force equal to the self-consistent force of the initial beam (— · — · — ·) are plotted as a reference.

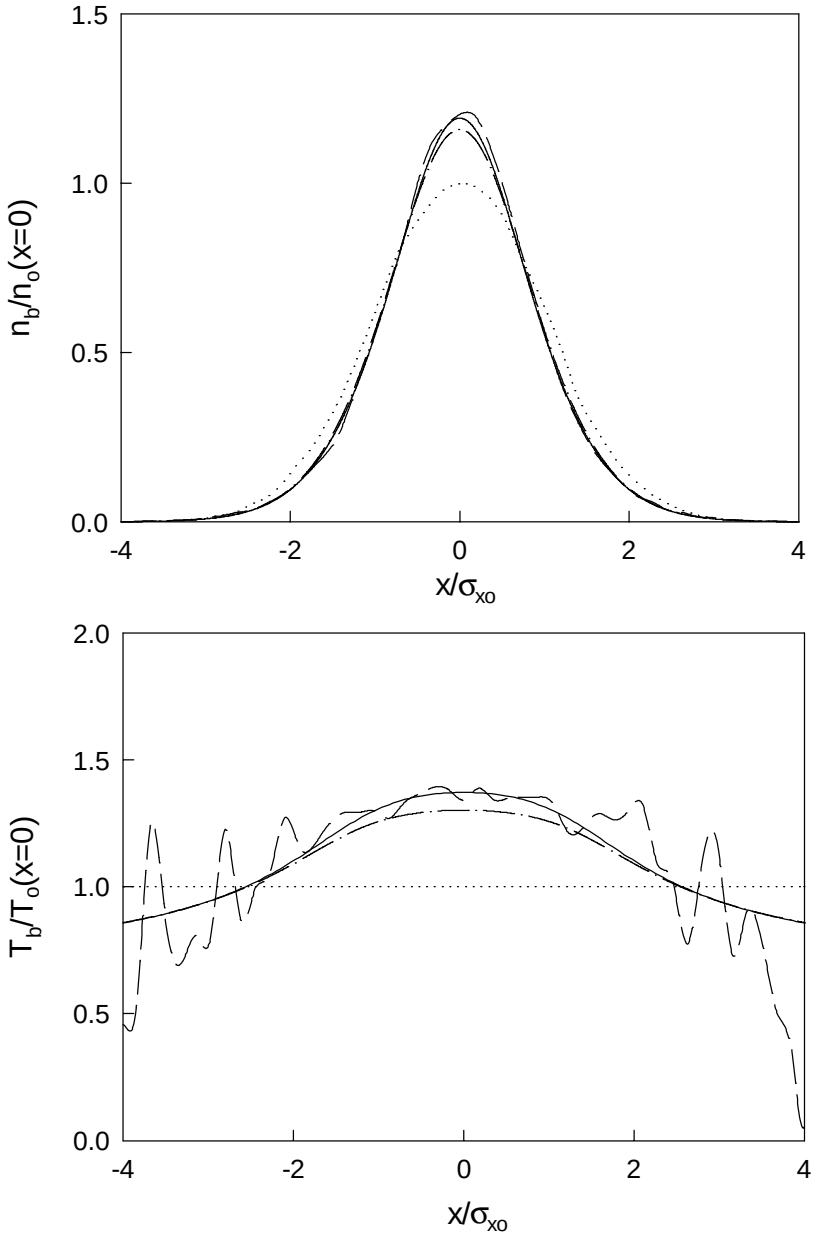

Figure 5.22: Comparison between theoretical (———) and PIC predictions (- - - -) for a beam acted upon with a self-consistent force. The initial profiles for a gaussian beam with $\alpha = 1.5$ ($\cdot\cdot\cdot\cdot\cdot$) together with the theoretical prediction for the external, time-independent force equal to the self-consistent force of the initial beam (— $\cdot$ — $\cdot$ — $\cdot$) are plotted as a reference.

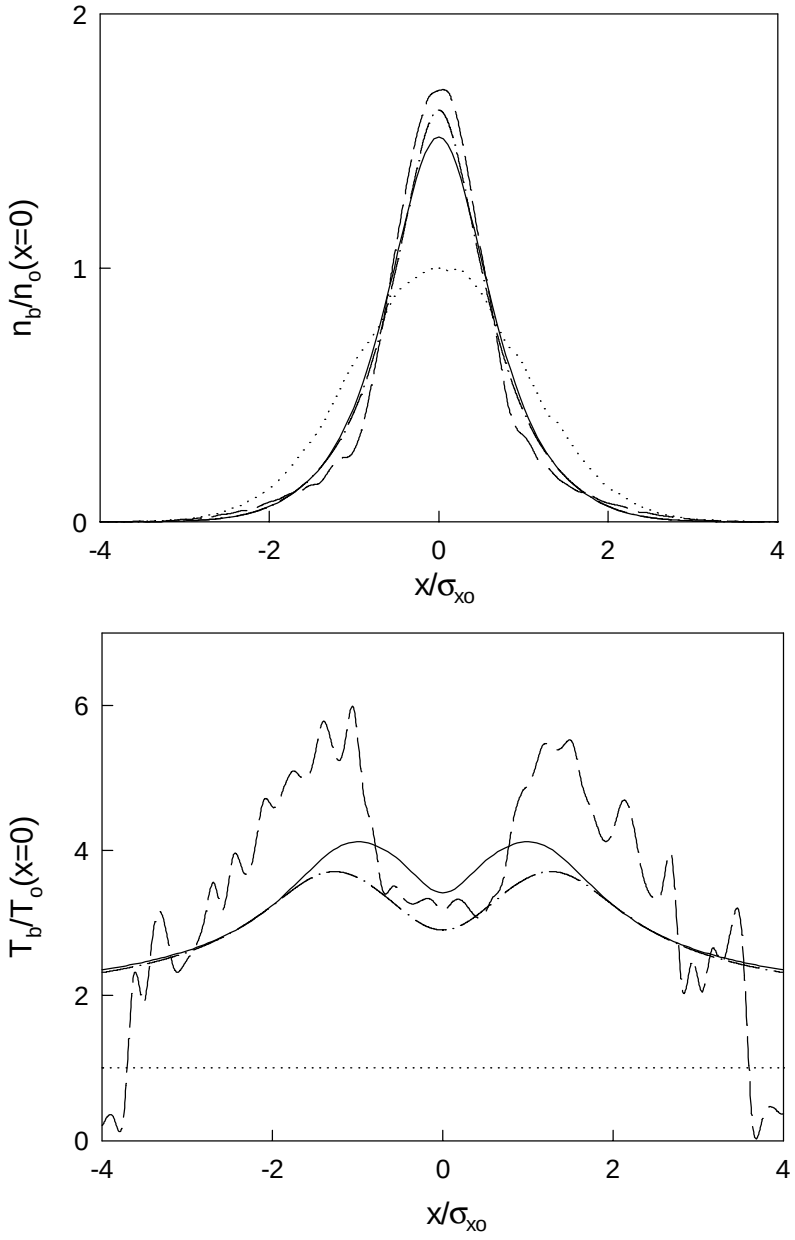

Figure 5.23: Comparison between theoretical (———) and PIC predictions (- - - -) for a beam acted upon with a self-consistent force. The initial profiles for a gaussian beam with $\alpha = 5$ ($\cdot\cdot\cdot\cdot$) together with the theoretical prediction for the external, time-independent force equal to the self-consistent force of the initial beam (— · — · — ·) are plotted as a reference.

the temperature of the hot halo particles.

Finally, comparisons of the theoretical and PIC predictions for the beam with the initial mismatch of $\alpha = 10$ are presented in Fig. 5.24. The results are similar to these for the gaussian beam with $\alpha = 5$.

The results of this Section show that the predictions of the theory developed for the final states of the systems with external, spatially nonlinear, time-independent forces agree well with the numerical dynamical results for such beams. The comparisons also indicate that, at least for systems with the self-consistent force of the type given by Eq. (2.2) and for some but not all initial cases, the variations of the force along the beam propagation result in significant changes for the final beam properties compared to the same beam acted upon with a force of the initial beam. While the technique proposed in this thesis predicts correctly the main features of the final distribution, it does not provide us with good predictions of the asymptotic beam properties for a system with a self-consistent force.

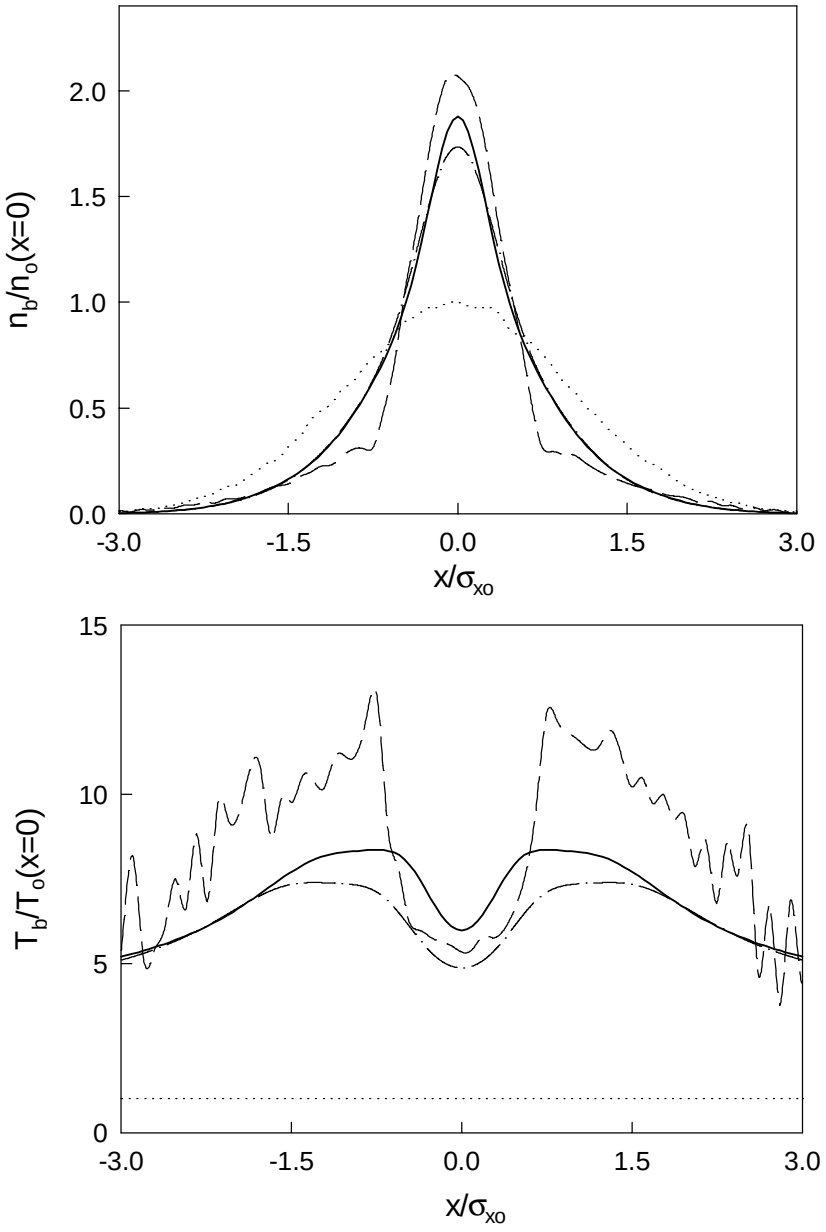

Figure 5.24: Comparison between theoretical (———) and PIC predictions (- - - -) for a beam acted upon with a self-consistent force. The initial profiles for a gaussian beam with $\alpha = 10$ ($\cdots\cdots$) together with the theoretical prediction for the external, time-independent force equal to the self-consistent force of the initial beam (— · — · — ·) are plotted as a reference.

Chapter 6

Conclusions

A comprehensive study of the collisionless relaxation of a mismatched beam propagating through an overdense plasma has been presented. This general process takes place in a variety of different physical systems with nonlinear forces (both self-consistent and external) and negligible dissipation, so that many of our results apply to systems found in plasma physics, beam physics, astrophysics, fluid mechanics and elsewhere. The problems of modeling such a system as well as physics of lossless relaxation and asymptotic properties were investigated. The main results of this thesis are now summarized.

The first main result of this thesis is the development of a new theoretical framework that can be used to predict the evolution of rms beam properties, in particular relaxation of a particle beam propagating through an overdense plasma. In the course of beam propagation, indications of collisionless relaxation can be seen in the evolution of different macroscopic beam quantities. On a short time scale, a few betatron periods, the decay of oscillation amplitudes of rms beam properties such as beam size and temperature is seen together with a subsequent establishment of stationary values. This relaxation of rms oscillations is attributed to the mixing of the initial distribution in the phase-space. While the evolution of bulk beam quantities obtained using PIC simulations appears to be very simple, no previous theoretical analysis was able to accurately describe the decay apart from full particle or kinetic simulations. For example, the widely used envelope equation model does not predict any relaxation of betatron oscillations or the observed emittance growth.

A new technique was developed in this thesis and used to predict the dynamics of low order beam moments with a simple numerical computation involving 100-200 equations.

The CME model is based on the expansion of the distribution function over the asymmetrically weighted Hermite polynomial basis with a subsequent truncation of the series. The model was used to study the evolution of second order beam moments $\langle x^2 \rangle$, $\langle xv \rangle$ and $\langle v_x^2 \rangle$.

The numerical CME computations were performed for gaussian and uniform initial distributions over a wide range of parameters corresponding to beams both colder and hotter than in equilibrium. The dynamical results for the evolution of second and forth order moments were compared with PIC simulations and showed excellent agreement for all cases. All the details of the low order moment dynamics, including amplitude of the betatron oscillations, frequency, the relaxation time, and asymptotic values were fully reproduced by CME simulations. The density and temperature profiles in equilibrium were also compared; they showed some discrepancies stemming from the insufficient number of expansion coefficients kept in the CME integration.

Numerical integrations of CME equations were usually performed with an artificial attenuation term added to the dynamics. Integration of CME showed an unlimited growth of the dynamical variables which was cured by the addition of sufficient attenuation into the system. A special form of the attenuation term introduced in this work depends on the order of the amplitude that is been damped. No artificial damping was introduced into the dynamics of second order coefficients connected to the evolution of the second order beam moments. A detailed study of the CME system together with the numerical investigation of normalization and truncation properties presented in this work outlines a sensible choice of numerical parameters and can serve as a guideline for future studies.

The CME equations, transformed into a specially chosen basis, also shed light into the mechanism of collisionless relaxation. The so-called decoupled basis, corresponding to the eigenvalue basis of the system with interactions between different orders turned of, proved to be very useful in understanding the nature of the amplitude decay. The spectrum of the decoupled basis showed that different orders contain eigenmodes with frequencies that are very close in value. The numerical examples indicate that the interactions of these resonant modes lead to the rapid relaxation of the initial betatron oscillations. The nonlinearity of the force controls the strength of the coupling between different resonant modes. The investigation of this dependence for a hypothetical system with a nonlinear external force shows a direct relation between the nonlinearity and the relaxation time for the second order moment oscillations. A simple estimate of the relaxation time, based on the coupling between the lowest order resonant modes, was developed and was found to be

in a satisfactory agreement with results of PIC simulations.

The question of the asymptotic beam state was addressed in the thesis. In particular, simple estimates of the second order moments achieved in the asymptotic state were obtained using an equilibrium condition and the conservation of energy. Comparisons between the analytical results and PIC simulations were performed for initially gaussian and uniform beams over a wide range of the initial mismatch. Very good agreement between the theoretical and numerical results was seen in all cases. The more complicated issue of the final beam density and temperature profiles, which are established on a much longer time scale, was also investigated. Interesting features of the stationary coarse-grained equilibrium, some of which were known from previous work and some first pointed out in this thesis, such as the development of the core-halo structure in the density profile and the appearance of 'hotter' regions away from the beam center, were studied.

Detailed comparisons of PIC simulations with existing theoretical predictions showed significant discrepancies. In particular, the comparison with Lynden-Bell's prediction of Ref. [6] revealed disagreement. Although Lynden-Bell's result predicted a core-halo structure for the final beam density, the details such as the width of the beam and the value of the density at the origin showed a disparity between the theoretical and PIC results. No 'hot' regions in the asymptotic beam were predicted by the theory. Comparisons with the results of Ref. [2] were also presented. While the theoretical prediction for the final beam density resembled the numerical result, especially for the initially gaussian beam, the temperature profiles showed unrepairable differences. The underlying assumption, namely the establishment of thermal equilibrium through collisionless relaxation, contradicts the results of PIC simulations which show highly non-thermal final states.

The question of the possibility to establish a thermal equilibrium state was addressed separately to investigate the peculiarities of the not-so-well understood collisionless equilibria compared to the classical viscous relaxation. A simple analysis based on the use of conservation laws of the system showed that the thermalization of the distribution is only possible in a few exceptional cases. This result supports the main conclusions reached based on the PIC studies.

Finally, the asymptotic beam density and temperature, were predicted. In this theory, the self-consistent force was replaced by an appropriately chosen fixed external force. An approximate model based on the use of the dynamical invariants was developed that allowed to predict the stationary state of the system using the initial beam properties.

The results showed an excellent agreement with PIC simulations performed for the initially gaussian beams with different mismatch. A modification of the theory was also proposed to predict the final fluid properties of a beam with a self-consistent force. The theory is based on the iterative scheme accounting for an averaged effect of the self-consistent, changing force. The results for gaussian beams closely resemble the predictions for the final density and temperature of the same initial beam acted upon with the unchanging, initial force. PIC simulations indicate that the self-consistency of the force becomes increasingly important for cases with large initial mismatch, and iterative procedure fails to predict some important features of the distribution.

The theory developed in this thesis can easily be extended to study similar phenomena in other systems. First, it is well suited to perform fast numerical computations for the propagation of high brightness beams in linear focusing channels. The problem of emittance growth observed in such beam propagation has attracted a significant attention in the last two decades (for an excellent review and discussion of the problem see Ref. [38]). A simple addition of a term corresponding to a spatially linear force would allow for a study of a long term propagation of a beam with significant self-consistent force. The CME model of this thesis can be easily used to verify many existing theoretical predictions for the emittance growth and final beam properties. The model can also be extended to study the evolution of bulk beam properties of the cylindrical beams. This extension might involve a use of a different expansion basis due to a different cylindrical geometry. Some further investigations into the possibility of predicting the final coarse-grained equilibrium distribution using a model similar to that of Sec. 5.6 are needed.

Appendix A

CME derivation through the evolution of beam moments.

As it was pointed out in Sec. 3.1, the set of the expansion coefficients $\{a_{kl}\}$ with $k+l \leq j_{max}$ is intimately connected with the set of normalized beam moments $\{\langle X^p V^q \rangle\}$ with $p+q \leq j_{max}$. This fact can be used to derive the CME equations.

We begin with the general evolution equation for the beam moment $\{\langle X^p V^q \rangle\}$, which can be written in the following form

$$\frac{d}{d\tau}\langle X^p V^q \rangle = p\langle X^{p-1} V^{q+1} \rangle + q\kappa \langle X^p V^{q-1} F \rangle, \tag{A.1}$$

where the particle equation of motion $\dot{V} = \kappa F$ written in normalized variables is used. Evaluating the last term on the right-hand side of Eq. (A.1) using the expansion for the distribution function given by Eq. 3.10 and the expression for the force as in Eq. (3.20), we obtain

$$\langle X^p V^q F \rangle = \sum_{klm} a_{kl} a_{m0} Q_{pkm} M_{ql}, \tag{A.2}$$

where the following notations are used

$$\begin{aligned} Q_{pk0} &= -\frac{\sqrt{\pi}}{2} M_{pk}, \\ Q_{pkm} &= \int_{-\infty}^{\infty} dY \, \frac{H_k(Y) H_{m-1}(Y) e^{-2Y^2}}{\pi^{1/4}\sqrt{2^{k+m} k! m!}} Y^p, \quad m \neq 0. \end{aligned} \tag{A.3}$$

Substituting Eq. (3.14) (which expresses the beam moments through the coefficients a_{kl})

and Eq. (A.2) into the right-hand side of Eq. (A.1), the evolution equation takes the form

$$\frac{d}{d\tau}\langle X^p V^q\rangle = p\sum_{k,l=0}^{\infty} a_{kl} M_{p-1,k} M_{q+1,l} + q\kappa \sum_{k,l,m=0}^{\infty} a_{kl} a_{m0} Q_{pkm} M_{q-1,l}. \tag{A.4}$$

Inverting Eq. (3.14), the dynamics of $\{a_{kl}\}$ (for $k+l>0$) can be easily found as

$$\frac{da_{kl}}{d\tau} = \sum_{p,q=0}^{\infty} M^{-1}_{kp} M^{-1}_{lq} \frac{d}{d\tau}\langle X^p V^q\rangle. \tag{A.5}$$

Bibliography

[1] J. B. Rosenzweig and P. Chen. Transverse Equilibria in Linear Collider Beam-Beam Collisions. *Workshop on Beam-Beam and Beam-Radiation Interactions. High intensity and nonlinear effects*, page 18, 1991.

[2] J. B. Rosenzweig and P. Chen. Transverse Equilibria and luminosity enhancement in linear collider beam-beam collisions. *Phys. Rev. E.*, 50:526, 1994.

[3] B.B. Kadomtsev and O.P. Pogutse. Collisionless relaxation in systems with Coulomb interactions. *Phys. Rev. Lett.*, 25:1155, 1970.

[4] S. Cuperman, A. Harten and M. Lecar. The collective relaxation of two-phase-space-density collisionless one-dimensional self gravitating systems. *Astroph. and Sp. Sc.*, 13:425, 1971.

[5] R.N. Henriksen and L.M. Widrow. Self-similar relaxation of self-gravitating collisionless particles . *Phys. Rev. Lett.*, 78:3426, 1997.

[6] D. Lynden-Bell. Statistical Mechanics of Violent Relaxation in Stellar Systems. *Mon. Not. Roy. Astron. Soc.*, 136:101, 1967.

[7] H. Wiechen, H.J. Ziegler, K. Schindler. Relaxation of collisionless self-gravitating matter: the lowest energy state. *Mon. Not. Roy. Astron. Soc.*, 232:623, 1988.

[8] H.J. Ziegler and H. Wiechen. Relaxation of collisionless self-gravitating matter: the final state. *Mon. Not. Roy. Astron. Soc.*, 238:1261, 1989.

[9] E. Esarey, P. Sprangle, J. Krall and A. Ting. Overview of plasma-based accelerator concepts. *IEEE Trans. Plasma Sci.*, page 252, 1996.

[10] M.J. Hogan, R. Assman, F.-J. Decker, R. Iverson, P. Raimondi, S. Rokni, R.H. Siemann, D. Walz, D. Whittum, B. Blue, C.E. Clayton, E. Dodd, R. Hemker, C. Joshi, K.A. Marsh, W.B. Mori, S. Wang, T. Katsouleas, S. Lee, P. Muggli, P. Catravas, S. Chattopadhyay, E. Esarey, W.P. Leemans. E-157: A 1.4-m-long plasma wake field acceleration experiment using a 30 GeV electron beam from the Stanford Linear Accelerator Center Linac. *Phys. Plasmas*, 7:2241, 2000.

[11] R. Assman, P. Chen, F.-J. Decker, R. Iverson, M.J. Hogan, S. Rokni, R.H. Siemanu, D. Walz, D. Whittum, P. Catravas, S. Chattopadhyay, E. Esarey, W.P. Leemans, P. Volfbeyn, C. Clayton, R. Hemker, C. Joshi, K. Marsh, W.B. Mori, S. Wang, T. Katsouleas, S. Lee, P. Muggli. Progress towards E-157: a 1 GeV plasma wakefield accelerator. *Proceedings of the 1999 Particle Accelerator Conference*, page 330, 1999.

[12] S.E. Graybill and S.V. Nablo . Observations of magnetically self-focusing electron beams. *Appl. Phys. Lett.*, 8:18, 1966.

[13] P. Chen. A possible final focusing mechanism for linear colliders. *Particle Accelerators*, 20:171, 1987.

[14] G. Hairapetian, P. Davis, C.E. Clayton, C. Joshi, C. Pellegrini, and T. Katsouleas. Experimental demonstration of dynamic focusing of a relativistic electron bunch by an overdense plasma lens. *Phys. Rev. Lett.*, 72:2403, 1995.

[15] R. Govil, W. P. Leemans, E. Yu. Backhaus and J. S. Wurtele. Observation of return current effects in passive plasma lenses. *Phys. Rev. Lett.*, 83:3202, 1999.

[16] D. Prono, B. Ecker, N. Bergstrom, and J. Benford . Plasma-return-current heating by relativistic electron beams with $\nu/\gamma \sim 10$. *Phys. Rev. Lett.*, 35:438, 1975.

[17] R. B. Miller. *An introduction to the physics of intense charged particle beams.* Plenum Press, New York, 1982.

[18] J. R. Pierce. *Travelling Wave Tubes.* D.Van Nostrand, New York, 1950.

[19] S.E. Graybill . Observation of energetic ions from a beam-generated plasma. *J. Appl. Phys.*, 41:236, 1970.

[20] R. Keinings and M.E. Jones . Two-dimensional dynamics of the plasma wakefield accelerator . *Phys. Fluids*, 30:252, 1987.

[21] D.A. Hammer and N. Rostoker. Propagation of high current relativistic electron beam. *Phys. Fluids*, 13:1831, 1970.

[22] J.L. Cox, Jr. and W.H. Bennett. Reverse current induced by injection of a relativistic electron beam into a pinched plasma. *Phys. Fluids*, 13:182, 1970.

[23] R. Lee and R.N. Sudan. Return current induced by a relativistic beam propagating in a magnetized plasma. *Phys. Fluids*, 14:1213, 1971.

[24] D.A. MacArthur and J.W. Poukey. Return current induced by a relativistic electron beam propagating into neutral gas. *Phys. Rev. Lett.*, 27:1765, 1971.

[25] L.S. Levine, I.M. Vitkovitsky, D.A. Hammer, and M.L. Andrews. Propagation of an intense relativistic electron beam theough a plasma background . *J. Appl. Phys.*, 42:1863, 1971.

[26] M.N. Lebedev. Equilibrium model analysis of a high-current relativistic electron beam in a dense plasma. *Sov. Phys. - Tech. Physics*, 37:1171, 1992.

[27] O. Buneman. Dissipation of currents in ionized media. *Phys. Rev.*, 115:503, 1959.

[28] L.E. Thode and R.N. Sudan . Plasma heating by relativistic electron beams. I. Two-stream instability . *Phys. Fluids*, 18:1552, 1975.

[29] L.E. Thode and R.N. Sudan . Plasma heating by relativistic electron beams. II. Return current interaction. *Phys. Fluids*, 18:1564, 1975.

[30] L.E. Thode. Energy lost by a relativistic electron beam due to two-stream instability. *Phys. Fluids*, 19:305, 1976.

[31] L.E. Thode. Plasma heating by scattering relativistic electron beams: Correlations among experiment, simulation, and theory. *Phys. Fluids*, 19:831, 1976.

[32] P.G. de Jagher, F.W. Sluijter, and H.J. Hopman. Relativistic electron beams and beam-plasma interaction. *Phys. Rep.*, 167:177, 1988.

[33] G. Wallis, K. Sauer, D. Sunder, S.E. Rosinskii, A.A. Rukhadze, and V.G. Rukhlin. Injection of high-current relativistic electron beam into plasma and gas . *Sov. Phys. Usp.*, 17:492, 1975.

[34] G. Contopoulos. Collisionless stellar dynamics. *Astroph. and Sp. Sc.*, 13:377, 1971.

[35] J. Binney and S. Tremaine. *Galactic Dynamics.* Princeton University Press, Princeton, 1987.

[36] P. M. Lapostolle. Possible emittance increase through filamentation due to the space charge in continuous beams. *IEEE Trans. Nucl. Sci.*, 18:1101, 1971.

[37] F. J. Sacherer. RMS envelope equations with space charge. *IEEE Trans. Nucl. Sci.*, 18:1105, 1971.

[38] M. Reiser. *Theory and Design of Charged Particle Beams.* John Wiley, New York, 1994.

[39] T. P. Wangler, K. R. Crandall, R. S. Mills, and M. Reiser. Relation between field energy and RMS emittance in intense particle beams. *IEEE Trans. Nucl. Sci.*, page 2562, 1985.

[40] T. P. Wangler, K. R. Crandall, and R. S. Mills. Emittance growth from charge density changes in high-current beams. *AIP Conference Proceedings, International Conference on Heavy Ion Inertial Fusion.*

[41] E. P. Lee and S. S. Yu. Model of Emittance growth in a self-pinched beam. *LLNL Report*, 1979.

[42] E. P. Lee, S. S. Yu, and W. A. Barletta . Phase-space distortion of a heavy-ion beam propagating through a vacuum reactor vessel. *Nucl. Fus.*, 21:961, 1981.

[43] P. J. Channell. The moment approach to charged particle beam dynamics. *IEEE Trans. Nucl. Sci.*, 30:2607, 1983.

[44] P. J. Channell, L. M. Healy and W. P. Lysenko. The moment code BEDLAM. *IEEE Trans. Nucl. Sci.*, 32:2565, 1985.

[45] B. A. Shadwick and J. S. Wurtele. General Moment Model of Beam Transport. *Proceedings of the 1999 Particle Accelerator Conference*, page 2888, 1999.

[46] F. C. Grant and M. R. Feix. . *Phys. Fluids*, 10:696, 1967.

[47] J. W. Schummer and J. P. Holloway . Vlasov simulations using velocity-scaled hermite representations . *J. Comp. Phys.*, 144:626, 1998.

[48] P. H. Chavanis. On the 'coarse-grained' evolution of collisionless stellar systems. *Mon. Not. R. Astron. Soc.*, 300:981, 1998.

[49] F.H. Shu. On the statistical mechanics of violent relaxation . *Astrophys. J.*, 225:83, 1978.

[50] F. Hohl and M. R. Feix. Numerical Experiments with a One-Dimensional Model for a Self-Gravitating System.

[51] J. Tanekusa. Statistical theory of violent relaxation. *Publs Astr. Soc. Japan.*, 39:425, 1987.

[52] T. S. Van Albada. Dissipationless galaxy formation and $r^{1/4}$ law. *Mon. Not. Roy. Astron. Soc.*, 201:939, 1982.

[53] T. A. McGlynn. Dissipationless collapse of galaxies and initial conditions. *Astrophys. J.*, 281:13, 1984.

[54] H. Wiechen and H.J. Ziegler. Relaxation of collisionless plasmas. *J. Plasma Physics*, 51:341, 1994.

[55] H.J. Ziegler, H. Wiechen and U. Arendt . Non-uniform mixing in collisionless self-gravitating systems. *Mon. Not. Roy. Astron. Soc.*, 266:263, 1994.

[56] H. E. Kandrup. Violent relaxation, phase mixing, and gravitational Landau damping. *ApJ*, 500:120, 1998.

[57] A. May and T.S. Albada. Dynamical constraints during violent relaxation and their effects on the final state. *Mon. Not. Roy. Astron. Soc.*, 209:15, 1984.

[58] W. H. Bennett. Magnetically self-focused streams. *Phys. Rev.*, 45:890, 1934.

[59] W. H. Bennett. *Phys. Rev*, 98:1584, 1955.

[60] Z. Yoshida. A self-consistent equilibrium model of plasma-beam systems. *Phys. Fluids B*, 1:1702, 1989.

[61] I.A. Kotel'nikov and V.N. Khudik . Plasma equilibrium during the injection of a rigid beam of charged particles. *Pl. Phys. Reports*, 23:130, 1997.

[62] E. P. Lee. Kinetic theory of a relativistic beam. *Phys. Fluids*, 19:60, 1976.

[63] J. Krall and G. Joyce. Transverse equilibrium and stability of the primary beam in the plasma wake-field accelerator. *Phys. Plasmas*, 2:1326, 1995.

[64] K.V. Lotov. Simulation of ultrarelativistic beam dynamics in plasma wake-field accelerator. *Phys. Plasmas*, 5:785, 1998.

[65] S.T. Ivanov and K.A. Reshetnikova . Nonlinear equilibrium state of relativistic electron beam and EM waves of large amplitude in a plasma . *Plas. Phys.*, 25:865, 1983.

[66] E. Yu. Backhaus and J. S. Wurtele. Coupled Moment Expansion model for the dynamics in a beam plasma system. *Phys. Plasmas*, 7:1, 2000.

[67] S. Humphries, Jr. *Charged particle beams* . Wiley, New York, 1990.

[68] UC Berkeley EECS Plasma Simulation Group is headed by prof. C. K. Birdsall. More information about the group and available codes can be found at http://ptsg.eecs.berkeley.edu.

[69] C. K. Birdsall and A. B. Langdon. *Plasma Physics via computer simulation.* McGraw-Hill, New York, 1985.

[70] E. P. Lee. Determination of the radius of a self pinched beam from its energy integral. *LLNL Report*, 1980.

[71] G. Knorr and M. Shoucri. Plasma simulation as eigenvalue problem. *J. Comp. Phys.*, 14:1, 1974.

[72] G. Severne and M. Luwel. Dynamical theory of collisionless relaxation. *Astroph. and Sp. Sc.*, 72:293, 1980.

[73] P. H. Chavanis and J. Sommeria. Degenerate equilibrium states of collisionless stellar systems. *Mon. Not. R. Astron. Soc.*, 296:569, 1998.

[74] T. Nozakura . On the cores of collisionless self-gravitating systems. *Mon. Not. Roy. Astron. Soc.*, 257:455, 1992.